EDGEWOOD CHEMICAL BIOLOGICAL CENTER
U.S. ARMY RESEARCH, DEVELOPMENT AND ENGINEERING COMMAND
Aberdeen Proving Ground, MD 21010-5424

ECBC-TR-1534

BASELINING STRUCTURE-REACTIVITY RELATIONSHIPS FOR SELECTED METAL-ORGANIC FRAMEWORK AND METAL OXIDE CATALYSTS FOR ADSORPTION AND DECOMPOSITION

Christopher J. Karwacki
Matthew A. Browe
John J. Mahle
George W. Wagner
Monica McEntee
Alex Balboa
Wesley O. Gordon
Jared B. DeCoste
Gregory W. Peterson

RESEARCH AND TECHNOLOGY DIRECTORATE

Gregory Mogilevsky

DYNOLOGY CORPORATION
Vienna, VA 22182-6218

July 2018

Approved for public release: distribution unlimited.

DISCLAIMER

The findings in this report are not to be construed as an official Department of the Army position unless so designated by other authorizing documents.

REPORT DOCUMENTATION PAGE

Form Approved
OMB No. 0704-0188

Public reporting burden for this collection of information is estimated to average 1 hour per response, including the time for reviewing instructions, searching existing data sources, gathering and maintaining the data needed, and completing and reviewing this collection of information. Send comments regarding this burden estimate or any other aspect of this collection of information, including suggestions for reducing this burden to Department of Defense, Washington Headquarters Services, Directorate for Information Operations and Reports (0704-0188), 1215 Jefferson Davis Highway, Suite 1204, Arlington, VA 22202-4302. Respondents should be aware that notwithstanding any other provision of law, no person shall be subject to any penalty for failing to comply with a collection of information if it does not display a currently valid OMB control number. **PLEASE DO NOT RETURN YOUR FORM TO THE ABOVE ADDRESS.**

1. REPORT DATE *(DD-MM-YYYY)*	2. REPORT TYPE	3. DATES COVERED *(From - To)*
XX-07-2018	Final	Oct 2014–Nov 2017

4. TITLE AND SUBTITLE
Baselining Structure-Reactivity Relationships for Selected Metal-Organic Framework and Metal Oxide Catalysts for Adsorption and Decomposition

5a. CONTRACT NUMBER

5b. GRANT NUMBER

5c. PROGRAM ELEMENT NUMBER

6. AUTHOR(S)
Karwacki, Christopher J.; Browe, Matthew A.; Mahle, John J.; Wagner, George W.; McEntee, Monica; Balboa, Alex; Gordon, Wesley O.; DeCoste, Jared B.; Peterson, Gregory W. (ECBC); Mogilevsky, Gregory (Dynology Corp.)

5d. PROJECT NUMBER
CB3934

5e. TASK NUMBER

5f. WORK UNIT NUMBER

7. PERFORMING ORGANIZATION NAME(S) AND ADDRESS(ES)
Director, ECBC, ATTN: RDCB-DRP, APG, MD 21010-5424
Dynology Corporation; 8000 Towers Crescent Drive, Suite 1525, Vienna, VA 22182-6218

8. PERFORMING ORGANIZATION REPORT NUMBER
ECBC-TR-1534

9. SPONSORING / MONITORING AGENCY NAME(S) AND ADDRESS(ES)
Defense Threat Reduction Agency, 8725 John J. Kingman Road, MSC 6201, Fort Belvoir, VA 22060-6201

10. SPONSOR/MONITOR'S ACRONYM(S)
DTRA

11. SPONSOR/MONITOR'S REPORT NUMBER(S)

12. DISTRIBUTION / AVAILABILITY STATEMENT
Approved for public release: distribution unlimited.

13. SUPPLEMENTARY NOTES

14. ABSTRACT-LIMIT 200 WORDS
Complete structure-activity relationships were elucidated with 3 metal-organic frameworks and 4 metal oxides against a broad spectrum of chemical warfare agents and simulants. Major findings and implications for future work are discussed.

15. SUBJECT TERMS
Chemical warfare agent (CWA)
Nuclear magnetic resonance (NMR)
Referee material
Diffuse reflectance IR spectroscopy (DRIFTS)
Dose extraction
Simulant

16. SECURITY CLASSIFICATION OF:			17. LIMITATION OF ABSTRACT	18. NUMBER OF PAGES	19a. NAME OF RESPONSIBLE PERSON
a. REPORT	b. ABSTRACT	c. THIS PAGE			Renu B. Rastogi
U	U	U	UU	174	19b. TELEPHONE NUMBER *(include area code)* (410) 436-7545

Standard Form 298 (Rev. 8-98)
Prescribed by ANSI Std. Z39.18

Blank

PREFACE

The work described in this report was authorized under Defense Threat Reduction Agency (Fort Bervoir, VA) project number CB3934. This work was started in October 2014 and completed in November 2017.

The use of either trade or manufacturers' names in this report does not constitute an official endorsement of any commercial products. This report may not be cited for purposes of advertisement.

The text of this report is published as received and was not edited by the Technical Releases Office, U.S. Army Edgewood Chemical Biological Center.

This report has been approved for public release.

Blank

CONTENTS

PREFACE iii
LIST OF FIGURES vii
LIST OF TABLES xiv
ACRONYMS xv
ABSTRACT/EXECUTIVE SUMMARY xvii

1. INTRODUCTION 1

2. MOTIVATION FOR SELECTED MATERIALS 2

3. SELECTION OF CHEMICAL AGENTS AND RELATED COMPOUNDS 2

4. CHARACTERIZATION TECHNIQUES, METHODS, AND EXPERIMENT 2

4.1 X-ray Diffraction 4
4.2 Scanning Electron Microscopy 5
4.3 Thermogravimetric Analysis 6
4.4 Differential Scanning Calorimetry 7
4.5 Attenuated Total Reflectance Fourier Transform Infrared Spectroscopy 7
4.6 Raman Spectroscopy 8
4.7 UV-Vis Spectroscopy 9
4.8 Fluorescence Spectroscopy 12
4.9 N_2 Isotherm 13
4.10 Water Isotherm 14
4.11 Potentiometric Titration 17
4.12 Chemical Dose-Extraction Removal Ability 18
4.13 Nuclear Magnetic Resonance Spectroscopy 22
4.14 Diffuse Reflectance Infrared Fourier Transform Spectroscopy 23

5. RESULTS 24

5.1 Titania (P25) 24
5.1.1 Physical Properties 24
5.1.2 Surface Chemical Properties 26
5.1.3 Electronic and Optical Properties 27
5.1.4 Adsorption and Reaction Characterization 29
5.1.5 Chemical Dose and Extraction Technique 31
5.1.6 NMR 31
5.1.7 DRIFTS 37
5.2 Zirconium hydroxide 41
5.2.1 Physical Properties 41
5.2.2 Surface Chemical Properties 43
5.2.3 Electronic and Optical Properties 45
5.2.4 Adsorption and Reaction Characterization 47
5.2.5 Chemical Dose and Extraction Technique 49
5.2.6 NMR 49
5.2.7 DRIFTS 59
5.3 Ferrihydrite and goethite 64

5.3.1 Physical Properties 64
5.3.2 Surface Chemical Properties 66
5.3.3 Electronic and Optical Properties 67
5.3.4 Adsorption and Reaction Characterization 69
5.3.5 Chemical Dose and Extraction Technique 71
5.3.6 NMR 71
5.3.7 DRIFTS 74
5.4 UiO-66 79
5.4.1 Physical Properties 79
5.4.2 Surface Chemical Properties 81
5.4.3 Electronic and Optical Properties 82
5.4.4 Adsorption and Reaction Characterization 84
5.4.5 Chemical Dose and Extraction Technique 86
5.4.6 NMR 86
5.4.7 DRIFTS 93
5.5 UiO-66-NH_2 95
5.5.1 Physical Properties 97
5.5.2 Surface Chemical Properties 99
5.5.3 Electronic and Optical Properties 100
5.5.4 Adsorption and Reaction Characterization 100
5.5.5 Chemical Dose and Extraction Technique 103
5.5.6 NMR 104
5.5.7 DRIFTS 109
5.6 NU-1000 111
5.6.1 Physical Properties 114
5.6.2 Surface Chemical Properties 116
5.6.3 Electronic and Optical Properties 117
5.6.4 Adsorption and Reaction Characterization 119
5.6.5 Chemical Dose and Extraction Technique 121
5.6.6 NMR 122
5.6.7 DRIFTS 125

6. ANALYSIS AND DISCUSSION 126

6.1 Chemical Sensing 116
6.1.1 Assessment of Spectral Properties of Simulant-Exposed Materials 117
6.2 Chemical Performance 116
6.2.1 Comparison of Dose-Extraction Simulant Data to Dose-Extraction Agent Data 117
6.2.1.1 Comparison by Chemical Set 116
6.2.1.1.1 Comparison of CEES to HD 117
6.2.1.1.2 Comparison of DMMP, DFT, DMCP to GB and GD 130
6.2.1.1.3 Comparison of Malathion to VX 133
6.2.1.2 Comparison by Material 117
6.2.2 Comparison of NMR Agent Data to Dose-Extraction Agent Data 117

6.3 Chemical Reaction Mechanisms 117

7. LITERATURE CITED 132

APPENDIX A – Raman and FTIR Data of Simulants 149

FIGURES

Figure 1. Structures of simulants and corresponding agents used in this study 3
Figure 2. X-ray diffraction mechanism 5
Figure 3. SEM setup 6
Figure 4. TGA setup 6
Figure 5. ATR schematic 7
Figure 6. Raman spectroscopy schematic 8
Figure 7. Diagram of raman scattering lines 9
Figure 8. Electronic transitions of sigma, pi, and nonbonding electrons 9
Figure 9. Band transition representation for (a) direct-allowed, (b) direct-forbidden, and (c) indirect electronic transitions[1]. E_v and E_c represent the valence band and conduction band energy levels, respectively 10
Figure 10. Fluorescence schematic 13
Figure 11. Fluorescence spectroscopy schematic 13
Figure 12. Schematic of Water Isotherm Apparatus 14
Figure 13. Autosampler vials 19
Figure 14. Microdispenser, autosampler vials and vortex tube 20
Figure 15. Centrifuge, UV lamp and vortexer 20
Figure 16. Agilent 6890 with autosampler 21
Figure 17. Extraction Method Block Diagram 21
Figure 18. Crystalline structures of rutile and anatase polymorphs of TiO_2 24
Figure 19. XRD pattern of P25, with allocation of peaks to the anatase or rutile phase 25
Figure 20. SEM image of P25 25
Figure 21. TGA and DSC profile of P25 26
Figure 22. Raman spectra of P25 27
Figure 23. UV-Vis spectra of P25 27
Figure 24. Tauc plot of P25 28
Figure 25. UV-Vis spectra of simulant-exposed P25 samples 28
Figure 26. Fluorescence emission spectra of P25 29
Figure 27. Fluorescence emission spectra of simulant-exposed P25 29
Figure 28. N_2 isotherm of P25 30
Figure 29. Water isotherm of P25 30
Figure 30. pKa distribution of P25 31
Figure 31. Select 31P NMR spectra obtained for 2.6 µL GD added to 0.7 mg P25 titania in 0.75 mL 0.5 M EM buffer at the indicated times 32
Figure 32. Plot of [GD] vs. time for 31P NMR spectra obtained for 2.6 µL GD added to 0.7 mg P25 titania in 0.75 mL 0.5 M EM buffer 32
Figure 33. Select 31P NMR spectra obtained for 2.6 µL GD added to 0.75 mL 0.5 M EM buffer (control) at the indicated times 33
Figure 34. Plot of [GD] vs. time for 31P NMR spectra obtained for 2.6 µL GD added to 0.75 mL 0.5 M EM buffer (control) 33
Figure 35. Select 31P NMR spectra obtained for 3.9 µL VX added to 0.7 mg P25 titania in 0.75 mL 0.5 M EM buffer at the indicated times 34

Figure 36. Plot of [VX] vs. time for 31P NMR spectra obtained for 3.9 µL VX added to 0.7 mg P25 titania in 0.75 mL 0.5 M EM buffer 34
Figure 37. Select 31P NMR spectra obtained for 3.9 µL VX added to 0.75 mL 0.5 M EM buffer (control) at the indicated times 35
Figure 38. Plot of [VX] vs. time for 31P NMR spectra obtained for 3.9 µL VX added to 0.75 mL 0.5 M EM buffer 35
Figure 39. Select 31P NMR spectra obtained for 3.9 µL VX added to 0.7 mg P25 titania in 0.75 mL water at the indicated times 36
Figure 40. Plot of [VX] vs. time for 31P NMR spectra obtained for 3.9 µL VX added to 0.7 mg P25 titania in 0.75 mL water. 36
Figure 41. GD and VX Reactions Observed With P25 Titania 37
Figure 42. DRIFTS spectra of CEES on P25 38
Figure 43. DRIFTS spectra of HD on P25 38
Figure 44. DRIFTS spectra of DMMP on P25 39
Figure 45. DRIFTS spectra of DMCP on P25 39
Figure 46. DRIFTS spectra of GB on P25 40
Figure 47. DRIFTS spectra of Malathion on P25 40
Figure 48. Proposed Structure of Zr(OH)4. Sheet-like structures (a) form with a combination of bridging and terminal hydroxyl groups. These sheets combine (b) to form a pseudo-porosity, featuring a variety of surface hydroxyl functionalities (c) 41
Figure 49. PXRD Data for Type B $Zr(OH)_4$ 42
Figure 50. Scanning Electron Microscopy image of Type B $Zr(OH)_4$ 42
Figure 51. TGA/DSC Data for Type B $Zr(OH)_4$ 43
Figure 52. XPS Data for Type B $Zr(OH)_4$ 43
Figure 53. ATR-FTIR Spectra for Type B $Zr(OH)_4$ 44
Figure 54. Raman Spectra for Type B $Zr(OH)_4$ 44
Figure 55. UV/Vis Data for Type B $Zr(OH)_4$ 45
Figure 56. Tauc Plot of $Zr(OH)_4$ 45
Figure 57. UV/Vis Data for Simulant-exposed Type B $Zr(OH)_4$ 46
Figure 58. Fluorescence Data for Type B $Zr(OH)_4$ 46
Figure 59. Fluorescence data for simulant-exposed $Zr(OH)_4$ 47
Figure 60. Nitrogen Isotherm Data for Type B $Zr(OH)_4$ 47
Figure 61. Water Isotherm Data for Type B $Zr(OH)_4$ 48
Figure 62. pKa distribution of $Zr(OH)_4$ 49
Figure 63. Hydroxyl group arrangements on zirconium hydroxide[2] 49
Figure 64. Select ^{31}P NMR spectra obtained for 2.6 µL GD added to 1.5 mg $Zr(OH)_4$ in 0.75 mL 0.5 M EM buffer at the indicated times 50
Figure 65. Plot of [GD] vs. time for ^{31}P NMR spectra obtained for 2.6 µL GD added to 1.5 mg $Zr(OH)_4$ in 0.75 mL 0.5 M EM buffer 50
Figure 66. Select ^{31}P NMR spectra obtained for 3.9 µL VX added to 1.5 mg $Zr(OH)_4$ in 0.75 mL 0.5 M EM buffer at the indicated times 51
Figure 67. Plot of [VX] vs. time for ^{31}P NMR spectra obtained for 3.9 µL VX added to 1.5 mg $Zr(OH)_4$ in 0.75 mL 0.5 M EM buffer 51
Figure 68. Select ^{31}P NMR spectra obtained for 3.9 µL VX added to 1.5 mg $Zr(OH)_4$ in 0.75 mL water 52
Figure 69. Plot of [VX] vs. time for ^{31}P NMR spectra obtained for 3.9 µL VX added to 1.5 mg $Zr(OH)_4$ in 0.75 mL water 52
Figure 70. Select ^{13}C NMR spectra obtained for 20 µL HD added to 100 mg $Zr(OH)_4$ 53
Figure 71. Plot of [HD] vs. time for ^{13}C NMR NMR spectra obtained for 20 µL HD added to 100 mg $Zr(OH)_4$ 53

Figure 72. ^{13}C NMR spectra obtained for CH_3CN-extracts of 20 µL HD added to 100 mg $Zr(OH)_4$ 54
Figure 73. Plot of [HD] vs. time for ^{1}H NMR spectra obtained for CH_3CN-extractions of 20 µL HD added to 100 mg $Zr(OH)_4$ 54
Figure 74. Select ^{13}C NMR spectra for 20 µL HD/160 µL CH_3CN added to 100 mg $Zr(OH)_4$ 55
Figure 75. Plot of [HD] vs. time for ^{13}C NMR spectra obtained for 20 µL HD/160 µL CH_3CN added to 100 mg $Zr(OH)_4$ 55
Figure 76. Select ^{13}C NMR spectra obtained for 20 µL HD/160 µL $CHCl_3$ added to 100 mg $Zr(OH)_4$ 56
Figure 77. Plot of [HD] vs. time for ^{13}C NMR NMR spectra obtained for 20 µL HD/160 µL $CHCl_3$ added to 100 mg $Zr(OH)_4$ 56
Figure 78. HD Reaction with $Zr(OH)_4$ 57
Figure 79. Select ^{13}C NMR spectra obtained for 180 µL $CHCl_3$ added to microcentrifuge tube (see text) 58
Figure 80. ^{1}H (left) and ^{13}C (right) NMR spectra obtained for the $CHCl_3$ extract of the microcentrifuge tube.EtOH presence was confirmed by spiking with authentic EtOH ... 58
Figure 81. DRIFTS spectra of CEES on $Zr(OH)_4$ 59
Figure 82. DRIFTS spectra of HD on $Zr(OH)_4$ 59
Figure 83. DRIFTS spectra of DMMP on $Zr(OH)_4$ 60
Figure 84. DRIFTS spectra of DFP on $Zr(OH)_4$ 60
Figure 85. DRIFTS spectra of DMCP on $Zr(OH)_4$ 61
Figure 86. DRIFTS spectra of dry GB on $Zr(OH)_4$ 61
Figure 87. DRIFTS spectra of wet GB on $Zr(OH)_4$ 62
Figure 88. DRIFTS spectra of malathion on $Zr(OH)_4$ 62
Figure 89. DRIFTS spectra of VX on $Zr(OH)_4$ 63
Figure 90. Unit cell of goethite 64
Figure 91. XRD patterns of ferrihydrite (left) and goethite (right) 65
Figure 92. SEM of ferrihydrite (left) and goethite (middle), with goethite crystal structure on right[3] 65
Figure 93. TGA and DSC profiles of ferrihydrite (left) and goethite (right) 66
Figure 94. FTIR spectra of ferrihydrite (left) and goethite (right) 66
Figure 95. Raman spectra of ferrihydrite (left) and goethite (right) 67
Figure 96. UV-Vis spectra of ferrihydrite (left) and goethite (right) 68
Figure 97. Tauc plots of ferrihydrite (left) and goethite (right) 68
Figure 98. UV-Vis spectra of simulant-exposed ferrihydrite (left) and goethite (right) 68
Figure 99. Fluorescence emission spectra of ferrhydrite (left) and goethite (right) 69
Figure 100. Fluorescence emission spectra of simulant-exposed ferrhydrite (left) and simulant-exposed goethite (right) 69
Figure 101. N_2 isotherms of ferrihydrite (left) and goethite (right) 70
Figure 102. Water isotherms of ferrihydrite (left) and goethite (right) 70
Figure 103. pKa distributions for ferrihydrite (left) and goethite (right) 71
Figure 104. ^{31}P NMR spectra obtained for 2.5 µL DMMP added to 2.5 mg ferrihydrite; 1-h reaction 72
Figure 105. ^{31}P NMR spectra obtained for 2.5 µL DMMP added to 2.5 mg ferrihydrite; 2-month reaction 73
Figure 106. Hydrolysis of DMMP to MMPA 73
Figure 107. ^{31}P (left) and ^{1}H (right) NMR spectra obtained for 2.5 µL DMMP in 0.75 mL 0.2 N HCl (top) and 0.75 mL 1.9 N NaOH (bottom; see text) 74
Figure 108. ^{31}P NMR spectra obtained for 0.2 N HCl extract of the 2-month DMMP/ferrihydrite reaction sample before (left) and after (right) spiking with authentic MMPA 74
Figure 109. DRIFTS spectra of CEES on ferrihydrite 75

Figure 110. DRIFTS spectra of HD on ferrihydrite 75
Figure 111. DRIFTS spectra of DMMP on ferrihydrite 76
Figure 112. DRIFTS spectra of DFP on ferrihydrite 76
Figure 113. DRIFTS spectra of DMCP on ferrihydrite 77
Figure 114. DRIFTS spectra of malathion on ferrihydrite 77
Figure 115. DRIFTS spectra of DMMP on goethite 78
Figure 116. DRIFTS spectra of GB on goethite 78
Figure 117. Depiction of UiO-66[4] 79
Figure 118. XRD pattern of UiO-66 80
Figure 119. SEM of UiO-66 80
Figure 120. TGA/DSC profile of UiO-66 81
Figure 121. FTIR spectra of UiO-66 81
Figure 122. Raman spectra of UiO-66 82
Figure 123. UV-Vis spectra of UiO-66 82
Figure 124. Tauc plot of UiO-66 83
Figure 125. UV-Vis spectra of simulant-exposed UiO-66 83
Figure 126. Fluorescence spectra of UiO-66 84
Figure 127. Fluorescence spectra of simulant-exposed UiO-66 84
Figure 128. N_2 isotherm of UiO-66 85
Figure 129. Water isotherm of UiO-66 85
Figure 130. pKa distribution of UiO-66 86
Figure 131. Types of protons on UiO-66[5] 86
Figure 132. Select ^{31}P NMR spectra obtained for 2.6 µL GD added to 2.5 mg UiO-66 in 0.75 mL 0.5 M EM buffer 87
Figure 133. Plot of [GD] vs. time for ^{31}P NMR spectra obtained for 2.6 µL GD added to 2.5 mg UiO-66 in 0.75 mL 0.5 M EM buffer 87
Figure 134. Select ^{31}P MAS NMR spectra obtained for 5 µL GD added to 100 mg UiO-66 88
Figure 135. Plot of [GD] vs. time for ^{31}P MAS NMR spectra obtained for 5 µL GD added to 100 mg UiO-66 88
Figure 136. Select ^{13}C NMR spectra obtained for 20 µL HD added to 50 mg UiO-66 at the indicated times 89
Figure 137. Plot of [HD] vs. time for ^{13}C NMR spectra obtained for 20 µL HD added to 50 mg UiO-66 90
Figure 138. Select ^{13}C NMR spectra obtained for 20 µL HD/160 µL $CHCl_3$ added to 50 mg UiO-66 at the indicated times 90
Figure 139. Plot of [HD] vs. time for ^{13}C NMR spectra obtained for 20 µL HD/160 µL $CHCl_3$ added to 50 mg UiO-66 91
Figure 140. Select ^{13}C NMR spectra obtained for 20 µL HD/160 µL CH_3CN added to 50 mg UiO-66 at the indicated times. The large peak near 5 ppm is due to the CH_3CN solvent. 91
Figure 141. Plot of [HD] vs. time for ^{13}C NMR spectra obtained for 20 µL HD/160 µL CH_3CN added to 50 mg UiO-66 92
Figure 142. ^{13}H NMR spectra obtained for 20 µL HD to 50 mg UiO-66 and CH_3CN-extracted at the indicated times 92
Figure 143. Plot of [HD] vs. time for ^{13}C NMR spectra obtained for CH_3CN-extractions 92
Figure 144. DRIFTS spectra of CEES on UiO-66 93
Figure 145. DRIFTS spectra of HD on UiO-66 94
Figure 146. DRIFTS spectra of DMMP on UiO-66 94
Figure 147. DRIFTS spectra of DMCP on UiO-66 95
Figure 148. DRIFTS spectra of GB on UiO-66 95
Figure 149. DRIFTS spectra of malathion on UiO-66 96
Figure 150. DRIFTS spectra of VX on UiO-66 96

Figure 151. Structure of UiO-66-NH_2 97
Figure 152. XRD pattern of UiO-66-NH_2 98
Figure 153. SEM image of UiO-66-NH_2 98
Figure 154. TGA and DSC profiles of UiO-66-NH_2 99
Figure 155. FTIR spectra of UiO-66-NH_2 99
Figure 156. Raman spectra of UiO-66-NH_2 100
Figure 157. UV-Vis spectra of UiO-66-NH_2 100
Figure 158. Tauc plot of UiO-66-NH_2 101
Figure 159. UV-Vis spectra of simulant-exposed UiO-66-NH_2 101
Figure 160. Fluorescence spectra of UiO-66-NH_2 102
Figure 161. Fluorescence spectra of simulant-exposed UiO-66-NH_2 102
Figure 162. N_2 isotherm of UiO-66-NH_2 102
Figure 163. Water isotherm of UiO-66-NH_2 103
Figure 164. pKa distribution of UiO-66-NH_2 103
Figure 165. Select ^{31}P NMR spectra obtained for 2.6 μL GD added to 2.6 mg UiO-66-NH_2 in 0.75 mL 0.5 M EM buffer 104
Figure 166. Plot of [GD] vs. time for ^{31}P NMR spectra obtained for 2.6 μL GD added to 2.6 mg UiO-66-NH_2 in 0.75 mL 0.5 M EM buffer 105
Figure 167. Select ^{31}P NMR spectra obtained for 2.6 μL GD added to 2.6 mg UiO-66-NH_2 in 0.75 mL water 105
Figure 168. Plot of [GD] vs. time for ^{31}P NMR spectra obtained for 2.6 μL GD added to 2.6 mg UiO-66-NH_2 in 0.75 mL water 106
Figure 169. Select ^{31}P MAS NMR spectra obtained for 5 μL GD added to 100 mg UiO-66-NH_2 106
Figure 170. Plot of [GD] vs. time for ^{31}P MAS NMR spectra obtained for 5 μL GD added to 100 mg UiO-66-NH_2 107
Figure 171. Select ^{13}C NMR spectra obtained for 5 μL HD added to 41 mg UiO-66-NH_2. Arrows indicate the two HD peaks (see text) 107
Figure 172. Plot of [HD] vs. time for ^{13}C NMR spectra obtained for 5 μL HD added to 41 mg UiO-66-NH_2 107
Figure 173. Select ^{1}H NMR spectra obtained for 5 μL HD added to 5 mg UiO-66-NH_2 in 0.75 mL CD_3CN. Integrals are shown for the two HD peaks (see text) 108
Figure 174. Plot of [HD] vs. time for ^{1}H NMR spectra obtained for 5 μL HD added to 5 mg UiO-66-NH_2 in 0.75 mL CD_3CN 108
Figure 175. DRIFTS spectra of CEES on UiO-66-NH_2 109
Figure 176. DRIFTS spectra of HD on UiO-66-NH_2 109
Figure 177. DRIFTS spectra of DMMP on UiO-66-NH_2 110
Figure 178. DRIFTS spectra of dry GB on UiO-66-NH_2 111
Figure 179. DRIFTS spectra of wet GB on UiO-66-NH_2 111
Figure 180. DRIFTS spectra of GD on UiO-66-NH_2 112
Figure 181. DRIFTS spectra of malathion on UiO-66-NH_2 112
Figure 182. DRIFTS spectra of VX on UiO-66-NH_2 113
Figure 183. Structure of NU-1000 114
Figure 184. XRD spectra of NU-1000 115
Figure 185. SEM images of NU-1000 115
Figure 186. TGA profile of NU-1000 116
Figure 187. FTIR spectra of NU-1000 116
Figure 188. Raman spectra of NU-1000 117
Figure 189. UV-Vis spectra of NU-1000 117
Figure 190. Tauc plot of NU-1000 118
Figure 191. UV-Vis spectra of simulant-exposed NU-1000 118
Figure 192. Fluorescence spectra of NU-1000 119

Figure 193. Fluorescence spectra of simulant-exposed NU-1000 119
Figure 194. N_2 isotherm of NU-1000 120
Figure 195. Water isotherm for NU-1000 120
Figure 196. pKa distribution of NU-1000 121
Figure 197. Select ^{31}P NMR spectra obtained for 2.6 μL GD added to 3.3 mg NU1000 in 0.75 mL 0.5 M EM buffer 122
Figure 198. Plot of [GD] vs. time for ^{31}P NMR spectra obtained for 2.6 μL GD added to 3.3 mg NU-1000 in 0.75 mL 0.5 M EM buffer 122
Figure 199. Select ^{31}P NMR spectra obtained for 2.6 μL GD added to 3.3 mg NU-1000 in 0.75 mL water 123
Figure 200. Plot of [GD] vs. time for ^{31}P NMR spectra obtained for 2.6 μL GD added to 3.3 mg NU-1000 in 0.75 mL water 123
Figure 201. Select ^{31}P NMR MAS NMR spectra obtained for 5 μL GD added to 19.4 mg NU-1000 124
Figure 202. Plot of [GD] vs. time for ^{31}P NMR MAS NMR spectra obtained for 5 μL GD added to 100 mg NU-1000 124
Figure 203. DRIFTS spectra of CEES on NU-1000 125
Figure 204. DRIFTS spectra of DMMP on NU-1000 126
Figure 205. DRIFTS spectra of DMCP on NU-1000 126
Figure 206. DRIFTS spectra of malathion on NU-1000 127
Figure 207. DRIFTS spectra of VX on NU-1000 127
Figure 208. CEES and HD dose-extraction removal data for referee materials 129
Figure 209. Differential data between CEES and HD dose-extraction removal percentage 130
Figure 210. Plot of CEES dose-extraction removal versus HD dose-extraction removal. A line of slope equal to one passing through the origin is included to represent perfect correlation 130
Figure 211. DMMP, DFP, DMCP, and GB dose-extraction removal data for referee materials 131
Figure 212. Differential data between DMMP, DFP, and DMCP and GB dose-extraction removal percentage 131
Figure 213. Plot of DMMP, DFP, and DMCP dose-extraction removal versus GB dose-extraction removal. A line of slope equal to one passing through the origin is included to represent perfect correlation 132
Figure 214. DMMP, DFP, DMCP, and GD dose-extraction removal data for referee materials 132
Figure 215. Differential data between DMMP, DFP, and DMCP and GD dose-extraction removal percentage 132
Figure 216. Plot of DMMP, DFP, and DMCP dose-extraction removal versus GD dose-extraction removal. A line of slope equal to one passing through the origin is included to represent perfect correlation 133
Figure 217. Malathion and VX dose-extraction removal data for referee materials 133
Figure 218. Differential data between malathion and VX dose-extraction removal percentage 134
Figure 219. Plot of malathion dose-extraction removal versus VX dose-extraction removal. A line of slope equal to one passing through the origin is included to represent perfect correlation 134
Figure 220. Dose-extraction removal data for all referee materials 135
Figure 221. Differential data of dose-extraction removal percentages for all simulant-agent combinations for all referee materials 135
Figure 222. Comparison of NMR half-life for HD in $CHCl_3$ versus HD dose-extraction percent remaining for applicable referee materials 136
Figure 223. Comparison of NMR half-life for GD in a 0.5M ethylmorpholine buffer at pH 10 versus GD dose-extraction percent remaining for applicable referee materials 137

Figure 224. Comparison of NMR half-life for VX in a 0.5M ethylmorpholine buffer at pH 10 versus VX dose-extraction percent remaining for applicable referee materials 137
Figure 225. Raman spectra of neat CEES 149
Figure 226. FTIR spectra of neat CEES 149
Figure 227. Raman spectra of neat DMMP 149
Figure 228. FTIR spectra of neat DMMP 150
Figure 229. Raman spectra of neat DMCP 150
Figure 230. FTIR spectra of neat DMCP 150
Figure 231. Raman spectra of neat malathion 151
Figure 232. FTIR spectra of neat malathion 151

TABLES

Table 1. Physical properties of 25 30
Table 2. Dose-extraction results for P25 31
Table 3. Reactions of GD and VX with P25 titania 37
Table 4. Surface Area and Pore Volume for Type B Zirconium Hydroxide 48
Table 5. Dose-extraction performance data for $Zr(OH)_4$ 49
Table 6. Reactions of GD, VX, and HD with $Zr(OH)_4$ 57
Table 7. Physical properties of Ferrihydrite and Goethite 70
Table 8. Dose-extraction results for ferrihydrite 71
Table 9. Dose-extraction results for goethite 72
Table 10. Physical properties of UiO-66 85
Table 11. Dose-extraction results for UiO-66 86
Table 12. Reactions with UiO-66 89
Table 13. Physical properties of UiO-66-NH_2 103
Table 14. Dose-extraction results for UiO-66-NH_2 104
Table 15. Results for Reactions of GD and HD with UiO-66-NH_2 108
Table 16. Physical properties of NU-1000 120
Table 17. Dose-extraction results for NU-1000 121
Table 18. Reactivity of GD with NU-1000 125

ACRONYMS

ATR	Attenuated Total Reflectance
BDC	1,4-benzenedicarboylate
BET	Brunauer, Emmett, and Teller
BJH	Barrett, Joyner, and Halenda
CASARM	Chemical Agent Standard Analytical Reference Material
CEES	Chloroethyl Ethylsulfide
CWA	Chemical Warfare Agent
DFP	Diisopropyl Fluorophosphate
DMCP	Dimethyl Chlorophosphate
DMF	Dimethyl Formamide
DMMP	Dimethyl Methylphosphonate
DMSO	Dimethyl Sulfoxide
DRIFTS	Diffuse Reflectance Infrared Fourier Transform Spectroscopy
DSC	Differential Scanning Calorimetry
DTRA	Defense Threat Reduction Agency
ECBC	Edgewood Chemical and Biological Center
EM	Ethylmorpholine
EMPA	Ethyl Methylphosphonic Acid
FID	Flame Ionization Detector
FTIR	Fourier Transform Infrared Spectroscopy
GB	sarin
GC	Gas Chromatography
GD	soman
HD	mustard gas
HOMO	Highest Occupied Molecular Orbital
LC	Liquid Chromatography
LUMO	Lowest Unoccupied Molecular Orbital
MAS	Magic Angle Spinning
MCT	Mercury-Cadmium-Telluride
MFC	Mass Flow Controller
MMPA	(2-Methyl)propyl Methyl Phosphonic Acid
MOF	Metal-Organic Framework
MS	Mass Spectrometry

NMR	Nuclear Magnetic Resonance
NU	Northwestern University
PL	Photoluminescence
PT	Potentiometric Titration
SAIEUS	Sorbent Adsorption Integral Equation Using Splines
SALI	Solvent-Assisted Ligand Incorporation
SBU	Secondary binding unit
SCCM	Standard Cubic Centimeters per Minute
SEM	Scanning Electron Microscopy
TGA	Thermogravimetric Analysis
TIC	Toxic Industrial Chemical
UiO	University of Oslo
UV	Ultraviolet
VX	*O*-ethyl *S*-[2-(diisopropylamino)ethyl] methylphosphonothioate
XRD	X-Ray Diffraction

ABSTRACT/EXECUTIVE SUMMARY

This report provides measured data on the physical properties and reaction chemistry of P25 titania, zirconium hydroxide, goethite, and ferrihydrite, UiO-66, UiO-66-NH_2, and NU-1000 with chemical agents and simulants (HD, GB, GD, and VX and simulants chloroethyl ethyl sulfide, dimethyl methylphosphate, dimethyl chlorophosphate, diisopropyl fluorophosphates, and malathion). The objective of this investigation was to provide a benchmark on emerging catalysts with the aim to advance the understanding of the structure-activity relationships and mechanisms related to sorbent-agent interactions.

Blank

BASELINING STRUCTURE-REACTIVITY FOR SELECTED METAL-ORGANIC FRAMEWORK AND METAL OXIDE CATALYSTS FOR ADSORPTION AND DECOMPOSITION

1. INTRODUCTION

Metal organic frameworks (MOFs) and metal oxides (MOs) are two important classes of heterogeneous catalysts that show promise for removal and decomposition of traditional chemical warfare agents (CWAs) and emerging chemical hazards for defense-related protection and decontamination applications. MOFs are constructed of metal nodes and organic linkers and as such offer a high degree of tunability affecting the materials porosity, surface area and reaction chemistry. Bulk MOs have a long history in catalysis however in recent years new forms of these materials at subnanometer dimensions have attracted significant attention in low temperature reaction applications.

Catalyst design requires a systematic and thorough understanding of the relationship between a material's structure and it's chemical activity that must be extended from the bench level to operationally relevant environments. In this work catalyst design efforts involving MOF and MO are focused on understanding mass transport, adsorption, surface chemistry, environmental factors and dynamics under relevant operating conditions (*in operando*). The process from concept to validation is inherently complex and demands rigorous characterization centered on surfaces and interfacial phenonmena with increasing length scales that ultimately result in a highly optimized bulk material. The chemical activity of a catalyst is perhaps the most important benchmark that can be used to assess the feasibility of a material for a variety of protection and decontamination applications, where adsorption and decomposition of hazardous chemicals is the preferred route for mitigation of contaminated environments. However there are many parameters that contribute, negatively or positively, to the observed activity of a catalyst, defined most importantly by the electronic properties and chemistry of the surface and at greater length scales the porosity and network of pores that facilitate mass transport, adsorption and overall reaction capacity. Today there are numerous experimental and theoretical techniques to promote the understanding of key properties, activity and dynamics of catalysts in native and composite form under pristine and operationally relevant conditions. Unlike traditional empirical efforts, it is viewed that a rational design approach to catalyst design, grounded in first principles, is critical to successful transition, development and implementation of active materials for the modern warfighter. It is anticipated that knowledge of these parameters and methodologies from both classes of materials can be employed to rapidly engineer functional forms of single or multi-catalyst composites tailored to respond to a broad spectrum of chemical hazards.

The U.S. Army Edgewood Chemical Biological Center (Aberdeen Proving Ground, MD) has an established history in the design, development and transition to manufacture reactive adsorbents that has served the needs of the DoD Chemical Biological Defense program.[ref CCC reports, TIC, Zr]. For the past century the leading technology has been activated impregnated carbon where its chemistry and adsorption evolved with changes in filtration requirements. In general the design goals have centered on high adsorption capacities for low vapor pressure chemicals such as organophosphorus and thiol compounds, and chemisorption and decomposition of high vapor pressure chemicals, such as cynides and othe acid forming chemicals. In recent years there has been interest to pursue catalytically active materials that can decompose all classes of adsorbed chemicals. Although, in the near term, the primary focus is on organophosphorus and thiol compounds and select toxic industrial chemicals there is a longer term strategy to incorporate chemistries that would be effective towards emerging classes of chemical hazards. As such the Defense Threat Reduction Agency has tasked the U.S. Army Edgewood Chemical Biological Center to lead the materials research phase focused on discovery and early engineering of new solid phase catalysts.

The primary focus areas are:

- Solid Catalyst Discovery
- Synthesis and Preparation of Porous Catalysts
- Adsorption and Mass Transport Characterization
- Reaction Chemistry/Mechanisms with CWA and Simulants
- Surface Chemistry/Mechanisms with Ambient Contaminants
- Engineering and Maturation of Composite Structures

In this work, we report on promising catalyst materials that serve as a benchmark for future material improvements with the aim to establish a record of *quantitative measurement* for early generation materials in native form. The selected catalysts are: TiO_2, Zr(OH)4, FeO/FeOH, UiO66, UiO66-NH2 and NU-1000 and the chemical warfare agents and simulants are: HD, CEES, DFP, DMC, GB, GD, VX, DMMP and malathion.

2. MOTIVATION FOR SELECTED MATERIALS

This reports provides measured data on the fundamental properties and activity measurement of TiO_2, Zr(OH)4, FeO/FeOH, UiO66, UiO66-NH2 and NU-1000 in their primitive (powder/granular) form. The materials chosen for this effort exemplify the new types of materials that are emerging from various research efforts supported by our academic collaborators. They represent different types of materials, specifically metal organic frameworks and metal oxides/hydroxides. Metal oxides are binary metal – oxygen systems that have crystalline structures. They are characterized by their surfaces, which include ewis and Brønsted acid and base sites, responsible for reactivity. Additionally, some of these materials have been shown to have photocatalytic activities, generating photoinduced superoxide states. Metal hydroxides are metal – hydroxide complexes that are characterized by a surplus of hydroxyl groups of various pKa values. These hydroxide groups are responsible for hydrolysis activities. Finally, metal organic frameworks (MOFs) are ordered structures that possess metal or metal oxide clusters with organic linking molecules holding the structures together. The materials possess a very high surface area and porosity compared to metal oxide materials. Also, the organic linkers can be tailored towards specific functionalities.

3. SELECTION OF CHEMICAL AGENTS AND RELATED COMPOUNDS

The chemicals selected for this study include the vesicant sulfur mustard (HD), the G-series nerve agents sarin (GB) and soman (GD) and the V-series nerve agent *O*-ethyl *S*-[2-(diisopropylamino)ethyl] methylphosphonothioate (VX). These materials have a widespread history of nefarious use from World War II to modern times and are among the most devastating chemical weapons known in the mainstream scientific community. The G-series and V-series agents are acetylcholinesterase inhibitors that lead to rapid respiratory depression upon exposure at the parts per billion (ppb) level.

A set of simulants was chosen to mimic the vesicant and nerve agents selected in the study in a less toxic medium and gauge their performance characteristics on the referee materials for comparison. The simulant 2-chloroethyl ethylsulfide (CEES) was chosen to mimic HD, the simulant malathion was chosen to mimic VX, and the simulants dimethyl methylphosphonate (DMMP), dimethyl chlorophosphonate (DMCP), and diisopropyl fluorophosphonate (DFP) were chosen to mimic the G-series agents soman and sarin. Structures of all simulants and nerve agents tested are shown in Figure xx.

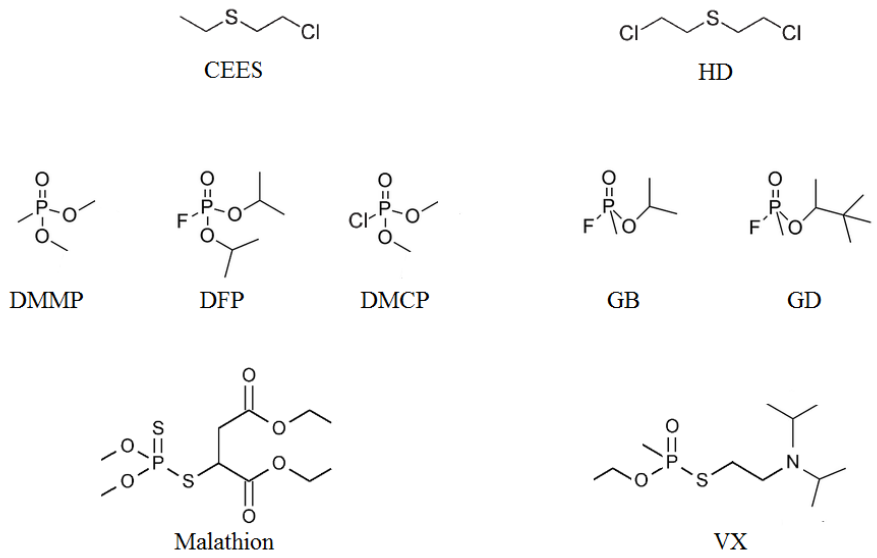

Figure 1. Structures of simulants and corresponding agents used in this study.

4. CHARACTERIZATION TECHNIQUES, METHODS, AND EXPERIMENT

The selected catalysts were characterized for their bulk physical properties, surface chemical structure properties, electronic properties, and potential for chemical reactivity. Chemical activity data were measured on the catalysts against selected nerve agents and simulants of interest. The physical properties of the materials were characterized by their crystal structure and morphological characteristics (surface area, porosity, pore distribution, etc.). Powder x-ray diffraction (XRD) determines the crystallographic and structural information of the material. The Miller indices associated with the powder diffraction peaks, along with their full width at the half-maximum, determine the structure and size of the crystalline domains through Bragg's Law and the Scherrer Equation. Scanning electron microscopy (SEM) shows the visual representation of the material and its morphology. Thermogravimetric Analysis (TGA) yields information on the bulk chemical makeup of the material, and Digital Scanning Calorimetry (DSC) identifies thermodynamic characteristics of the material and determines potential phase transitions.

Raman and Fourier Transform Infrared (FTIR) spectroscopies yield chemical structure information of the surface of the material. FTIR spectroscopy provides a vibrational analysis of structural components that have a permanent dipole moment, and raman spectroscopy analyzes structural components that have no permanent dipole moment but are polarizeable. These complementary tools are necessary in tandem to fully analyze all vibrational components of these materials.

The optical and electronic description of the material yields information on its electronic structure. UV-vis spectroscopy determines the optical band gap of the material and the wavelength at which a photocatalytic material will absorb light for optimum photoexcitation. Photoluminescence (PL) spectroscopy measurements determine the energy levels that exist within the material and reveal any defect states. The optical properties of materials can change when the material is exposed to a chemical challenge. For example, adsorption of a chemical can introduce defect states and photon absorption sites that will perturb the UV-vis and PL spectra. Therefore, the optical measurement techniques can be used as a self-reporting probe if their spectra are changed upon exposure to chemical threats, leading way to the development of sensing materials.

The potential for chemical reactivity of the primitive materials is explored by focusing the study on the surface properties. Nitrogen (N_2) isotherm measurements determine the surface area and porosity of the material, therefore quantifying the morphological properties. Water isotherm measurement yield an analysis of how water interacts with the material and sheds insight to potential hydrolytic activity, which is a common removal mechanism for agents and simulants. Potentiometric titration measurements characterize the pKa of the surface species and aids in the calculation of the point of zero charge of the material.

Performance data of the materials was first collected via a dose-extraction technique to measure bulk reactivity against selected liquid-phase agents and simulants. Reaction products on selected high performers was then measured via 1H Nuclear Magnetic Resonance (NMR) spectroscopy, which yields information on protons within structure, mainly surface hydroxyls for metal oxides, and linker information for MOFs. Lastly, time-dependent evolution of reaction products was measured via diffuse reflectance infrared fourier transform spectroscopy (DRIFTS) in order to begin to decipher the underlying mechanisms of reaction.

4.1 X-RAY DIFFRACTION

X-ray diffraction (XRD) is used as a characterization technique to identify the degree of crystallinity, the specific crystalline phase, and the structural orientation properties of a material. XRD utilizes fundamental properties of crystalline materials in that their atoms can often be oriented in several different planes with unique interatomic spacing, d. When these planes interact with incident x-rays, the x-rays are scattered in a manner that can produce either destructive or constructive interference, depending on whether the diffracted wavelengths move in phase or out of phase with each other. This gives rise to selection rules for specific lattices, and the constructive interference x-rays produce peaks associated, recorded on the XRD instrument. In a typical experiment, incident x-rays are bombarded onto a sample surface at an angle 2θ with the average surface of the material, and the corresponding intensity of the diffracted X-ray at angle 2θ is measured and plotted against the diffraction angle. In this study, attenuation in this scattering of a material relative to its pure-form pattern could be anticipated upon chemical exposure due to structural integrity of the material being compromised during the adsorption and reaction process. The relationship between the angle of the x-ray beam diffracting from a crystalline surface and the interatomic spacing of that surface is given by Bragg's Law in Equation 1,

$$2d\sin\theta = n\lambda \tag{1}$$

where
λ = wavelength of the x-ray
θ = scattering angle
n = integer representing the order of the diffraction peak; 1 is used here
d = inter-plane distance of atoms

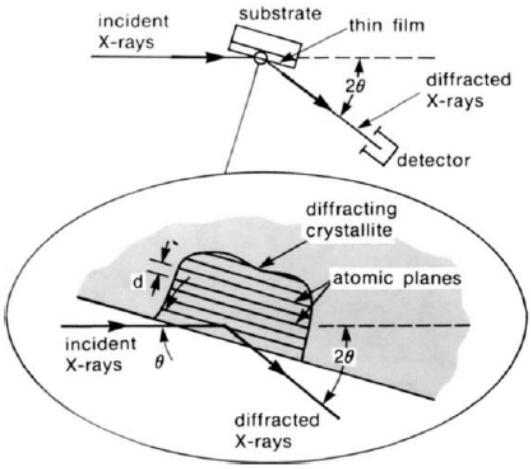

Figure 2. X-ray diffraction mechanism

XRD pattern measurements were performed with a Rigaku MiniFlex 600 x-ray diffractometer equipped with a D/teX x-ray detector with Cu Kα radiation (λ = 1.54 A) at 40 kV voltage and 15 mA current. MiniFlex Guidance software was used for data acquisition, and PDXL 2 diffraction analysis software was used to process the measured data and subtract the background. Samples were loaded onto Rigaku 906165 Flush Si 510 zero-background sample holders coated with an ultrathin layer of laboratory-grade Vaseline and scanned from a 2θ range of 3 to 90 degrees at a rate of 5 degrees/min with a 0.02 degree step size.

4.2 SCANNING ELECTRON MICROSCOPY

Scanning electron microscopy (SEM) is an imaging technique used to provide general topographical and surface composition information of a material. SEM is utilized here to generate baseline images of the referee materials as a gauge for particle size, morphology, and distribution. In the instrument, a source of electrons is focused in vacuum into a probe that rasterizes the sample surface. Various interactions occur between the electrons and sample surface that can result in emission of electrons or photons from or through the surface, which involve either inelastic scattering of the high-energy electron with atomic electrons of the sample or elastic scattering of the electron with atomic nuclei of the sample. A fraction of the emitted electrons, called secondary electrons, are collected by appropriate detectors, and the output is used to moderate the brightness of a cathode ray tube (CRT) to produce an image. Images produced in this manner are secondary electron images, backscattered electron images, or elemental X-ray maps. Resolution of the SEM can approach a few nanometers, and it can operate at magnifications from 10x-300,000x.

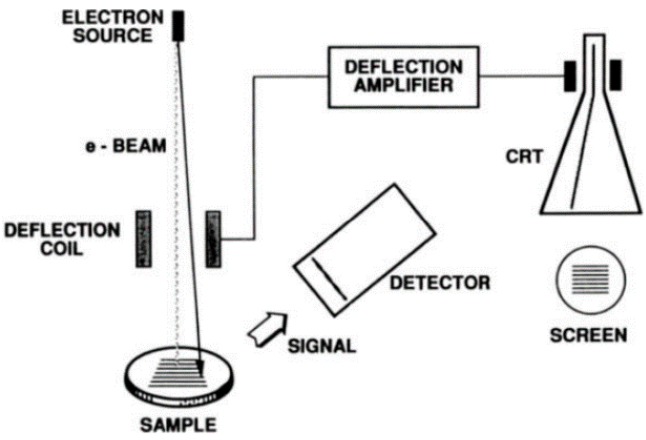

Figure 3. SEM setup

In the outlined study, SEM images of the materials were obtained using a JEOL JCM-5700 Scanning Electron Microscope. Samples were supported on double-sided carbon tape, and sputter coated with approximately 50 Angstroms of gold. The instrument was operated in high vacuum mode using an accelerating voltage of 15 kV at a nominal working distance of 10 mm.

4.3 THERMOGRAVIMETRIC ANALYSIS

Thermogravimetric analysis (TGA) is a thermal analysis process in which a sample is heated with constant heat rate under nitrogen or synthetic air, while the mass evolution during the process is measured. The system typically consists of a microthermobalance and a high temperature furnace. A mass loss indicates that a degradation of the measured substance is taking place. Mass gain indicates that a chemical reaction is causing a conversion of a material to another form, for example a metal reacting with oxygen to create an oxide under oxygen flow. Thermal stability and sample composition information of a material can be derived from this data, indicated specifically by the exact temperature values at which a loss in mass is observed.

A TGA Q500-1323 instrument was used for TGA measurements. About 20 mg of each sample was placed in a tared platinum pan and heated from 23 C to 800 C at a rate of 2 C/min, followed by equilibration to 25 C. Percent weight and derivative weight were calculated at each measurement.

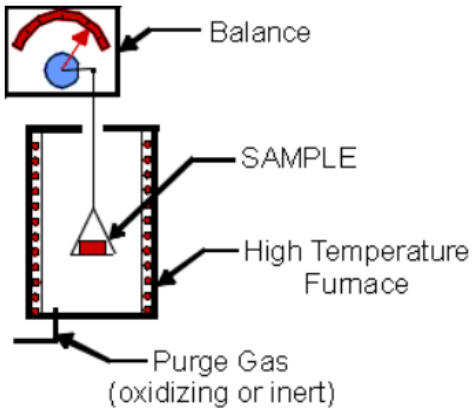

Figure 4. TGA setup

4.4 DIFFERENTIAL SCANNING CALORIMETRY

Differential scanning calorimetry (DSC) is used as a thermal analysis technique that measures the temperatures and heat flows associated with transitions in materials as a function of time and temperature in a controlled atmosphere. These measurements provide quantitative and qualitative information about physical and chemical changes that involve endothermic or exothermic processes, or changes in heat capacity. Among other properties, DSC can measure glass transitions, melting and boiling points, crystallization time and temperature, heats of fusion and reactions, specific heat capacity, and purity of a material. The area of an individual peak produced is directly proportional to the enthalpy change of the sample, and the direction of the peak, pointing up or down, indicates whether the thermal event is exothermic or endothermic, respectively.

Differential scanning calorimetry measurements were conducted on a TA Instruments SDT Q600 with aluminum pans. The temperature was ramped from 25 C to 600 C at a rate of 10 C/min after an initial 10 minute hold at ambient temperature. Nitrogen was used as a carrier gas and flowed at 20 mL/min.

4.5 ATR-FTIR

Attenuated total reflection Fourier transform infrared (ATR-FTIR) spectroscopy is used as a vibrational spectroscopy method to probe excitations of various vibrational modes of chemical bonds present in the IR absorption wavelength range of 4000-400 cm^{-1} and to provide quantitative chemical identification of species in a material. In order for a vibrational mode to be detectable with FTIR spectroscopy, it must generate a change in the dipole moment of the molecule. In Attenuated Total Reflectance (ATR) mode, as utilized in this effort and diagramed in figure x, the infrared beam is directed into an ATR crystal. Exploiting the principles of a waveguide, the change in refractive index at the crystal surface causes the beam to be back-reflected several times as it propagates down the length of the crystal before reaching the detector. If the sample is put into contact with the crystal surface, the beam will interact weakly with the sample at several points. Since the propagating beam in the crystal barely penetrates through the surface of the sample adjacent to the crystal, signals at a sample surface can be enhanced as well, which is the focus of this effort as reactivity against challenge chemicals is expected to be a surface phenomenon.

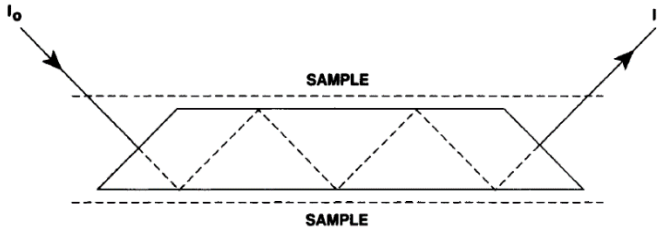

Figure 5: ATR schematic

A Bruker Tensor 27 Fourier Transform Infrared (FTIR) Spectrometer equipped with a diamond Bruker Platinum ATR accessory and OPUS software was used for infrared spectroscopy measurements. Samples were scanned at a resolution of 2 cm^{-1}, utilizing 16 scans for the sample and background over a range of 4000 to 400 cm^{-1} with a quartz beam splitter, an aperture of 6 mm, and a scanner velocity of 10 kHz. Measurements were collected on three different sets of data: the unexposed and dried at 80 C referee materials, the referee materials exposed to agent with no further treatment, and the referee materials exposed to agent, washed 3 times with acetonitrile, and dried overnight at 80 C.

4.6 RAMAN SPECTROSCOPY

Raman spectroscopy is used as an alternative vibrational structural characterization tool to FTIR. Raman spectroscopy arises from indirect coupling of high-frequency radiation with the electron clouds that comprise the chemical bonds in a sample. While a sample requires a permanent dipole moment to be FTIR-active, Raman activity is dependent on the polarizability of the material, thus making it potentially more favorable for analyzing non-polar materials, such as certain metal oxides. Raman spectroscopy is also primarily a structural characterization tool that is more sensitive to lengths, strengths, and arrangements of bonds in a material than it is to chemical composition. Thus, a Raman spectrum of an ordered solid would show greater differences with defects and disorder than to trace chemical impurities.

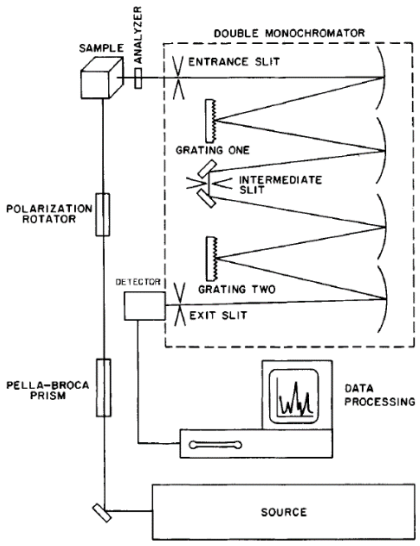

Figure 6. Raman spectroscopy schematic

In the Raman scattering experiment, an intense monochromatic light is exposed to the sample. The electric field from the light distorts the electron clouds that comprise the sample's chemical bonds and stores energy. When the electric field reverses upon the wave passing, the distorted electron clouds relax, and the stored energy is reradiated. Most of the stored energy is reradiated at the same frequency as that of the incident exciting light, referred to as Rayleigh scattering, but a small percentage of it is transferred to the sample, exciting its vibrational modes. The vibrational energies are then deducted from the energy of the incident beam and weak side bands appear in the spectrum at frequencies less than that of the incident beam/Rayleigh line. The separation of these weak side bands from the Rayleigh line directly correlates to the Raman vibrational frequencies of the sample. This Raman process that excites molecular vibrations is referred to as Stokes scattering.

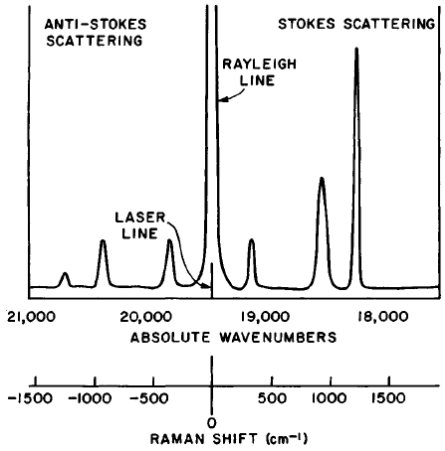

Figure 7. Diagram of raman scattering lines

Raman spectra were measured using an Inphotonics Echelle spectrograph. A filtered fiber optics probe was used to illuminate the samples with 785 nm excitation light and also collect the Raman scattered light. The near-infrared excitation wavelength of 785 nm was used since its relatively low energy photons excite less fluorescence than visible wavelengths. The laser power used was ~100 mW. For some of the particularly dark-colored samples, the powders were spun under the laser beam to reduce laser-induced burning of the samples.

4.7 UV-VIS SPECTROSCOPY

Absorption of ultraviolet (UV) and visible radiation by a material is evaluated to gauge the excitation of its outer electrons. This typically involves transitions involving either pi, sigma, and nonbonding electrons, charge-transfer electrons, or d-orbital and f-orbital electrons. Pi, sigma, and nonbonding electron transitions are more common in organic species, charge-transfer transitions are more common in metal-ligand complexes, d-orbital transitions occur among elements in the first and second transition metal series, and f-orbital transitions occur among elements in the lanthanide and actinide series. Among pi, sigma, and nonbonding electrons, only n -> π^* and π-> π^* transitions occur within the wavelength region typically employed by UV-Vis spectroscopy (200-800 nm). Elucidation of these electronic transitions observed at a given applied wavelength provides valuable information related to the sensing abilities of a particular material.

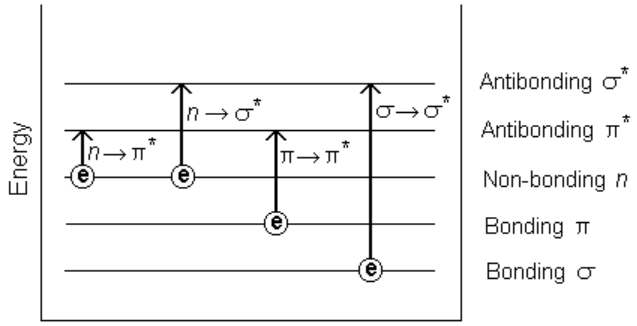

Figure 8. Electronic transitions of sigma, pi, and nonbonding electrons

Further, data from the UV-Vis spectra of a material can be used to estimate its band gap through generating a profile called a Tauc plot. Tauc plots utilize the concept that the optical absorption edge energy

in a UV-Vis spectrum represents the minimum energy required for highest occupied molecular orbital to lowest unoccupied molecular orbital (HOMO-LUMO) transition of a valence electron in a material. This transition can occur in either a direct or indirect manner; direct transitions only require a photon to excite the electron, while indirect transitions also require a change in the crystal momentum of the material, involving concerted vibrations and energy from the its lattice (phonons)[6]. The energy dependence of the absorption coefficient of a material in the region near this absorption edge in shown in Equation 2.

$$\alpha = \frac{C(hv-E_0)^n}{\mathrm{hv}} \tag{2}$$

In Equation (2), hv is the energy of the incident photon, E_0 is the optical absorption edge energy, C is a constant, and the exponent n is dependent on the type of optical transition instigated by photon absorption; n is ½ for direct-allowed transitions, n is 3/2 for direct-forbidden transitions, n is 2 for indirect-allowed transitions, and n is 3 for indirect-forbidden transitions[6]. A representation of these band transitions is depicted in Figure 9. Previous work on many of the materials or analogues of the materials in this study has shown reliable electronic properties obtained using correlations for direct-allowed transitions[7, 8], while ferrihydrite and goethite have shown evidence of both direct and indirect electronic transitions[9, 10], and so a selection of n = ½, corresponding to direct-allowed transitions, will be made here for simplicity. Thus, for the materials considered here, Equation 2 can be rewritten as Equation 3.

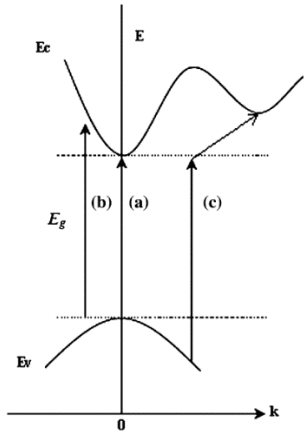

Figure 9. Band transition representation for (a) direct-allowed, (b) direct-forbidden, and (c) indirect electronic transitions[1]. E_v and E_c represent the valence band and conduction band energy levels, respectively.

$$(\alpha \mathrm{hv})^2 = \mathrm{C}(\mathrm{hv} - E_0) \tag{3}$$

The E_0 term also represents the band gap of the material and can thus be obtained graphically by plotting $(\alpha hv)^2$ versus hv, the Tauc plot. This plot typically will have a component parallel to the abscissa at low hv values, followed by a component that sharply increases linearly. Extrapolation of this linear component to the abscissa yields the band gap of the material. First, however, a calculation of the absorption coefficient must be obtained. The absorption coefficient at each wavelength of light in the UV-Vis spectrum can be estimated using the Beer-Lambert law. Among the postulates of this law is that the intensity of light transmitted through a sample is related to the intensity of the incident light as in Equation 4

$$I = I_0 e^{-ux} \tag{4}$$

where I_0 is the intensity of the incident light, I is the intensity of the transmitted light, x is the thickness of the sample, and u is the attenuation coefficient, which, for low scattering/reflection of the incident light (which is expected in most cases), is approximately equal to the absorption coefficient of the material. Further, the absorbance of the material is known as the logarithm of the ratio of the intensity of the incident light to the intensity of the transmitted light as shown in Equation 5

$$\mathrm{A} = log\left(\frac{I_0}{I}\right) = log\left(\frac{I_0}{I_0\, e^{-ux}}\right) \tag{5}$$

therefore,

$$\mathrm{A} = log\left(\frac{I_0}{I}\right) \approx log\left(\frac{I_0}{I_0 e^{-\alpha x}}\right) = \log(e^{\alpha x}) = \ \alpha x\ log(e) \tag{6}$$

and

$$\alpha = \left(\frac{A}{x\log(e)}\right) \tag{7}$$

where α is the absorption coefficient. Since the thickness of the sample is constant throughout the UV-Vis experiment, equation 7 can be written for the purposes of this study as

$$\alpha = \left(\frac{A}{C\prime}\right) \tag{8}$$

where C' equals x log(e) and is a constant in these experiments. Thus, equation 3 now becomes

$$(\frac{\mathrm{A}}{C\prime}\mathrm{hv})^2 = \mathrm{C}(\mathrm{hv} - \ E_0) \tag{9}$$

which simplifies to

$$(\mathrm{Ahv})^2 = \mathrm{C}"(\mathrm{hv} - \ E_0) \tag{10}$$

where C" equals C*(C')^2 and is another constant. Thus, the linear portion of a plot of (Ahv)^2 versus hv extrapolated to the abscissa is sufficient for band gap calculation, as the absolute scaling of the ordinate does not affect this extrapolated value. The photon energy can be calculated from the UV-Vis wavelength using Equation 11

$$hv = E = h\left(\frac{c}{\lambda}\right) \tag{11}$$

where h is Planck's constant and c is the speed of light. If given λ in micrometers (um) and calculating E in electronvolts, equation 11 approximates as

$$E(eV) = \left(\frac{1.2398}{\lambda(um)}\right) \tag{12}$$

Therefore equation 10 now may be written as

$$(\mathrm{A}\left(\frac{1.2398}{\lambda(um)}\right))^2 = \mathrm{C}"(\left(\frac{1.2398}{\lambda(um)}\right) - \ E_0(\mathrm{eV})) \tag{13}$$

and UV-Vis absorbance data can quickly be used to generate a Tauc plot by profiling $[(A(1.2398/(\lambda))]^2$ versus $(1.2398/\lambda)$, with λ in um and A representing the fractional absorbance of the material at corresponding wavelength λ. This methodology was used with all referee materials to plot $(Ahv)^2$ versus hv and calculate a band gap for the baseline material. While the Tauc plot method most strictly applies to semiconductor metal oxides, its use in literature has extended to metal-organic frameworks as well[8], and thus it will be utilized in this work to evaluate properties of all the baseline referee materials.

UV-Vis measurements were conducted with a Jasco V-650 UV-Vis spectrophotometer equipped with a ILV-724 150mm integrating sphere for solid phase analysis and SpectraManager software for data acquisition. The unexposed, and agent-exposed-and-washed referee materials were scanned from 200-800 nm in continuous scan mode in the range 200-800 nm, with a source change wavelength of 340 nm, a data pitch of 1.0 nm, and a band width of 5.0 nm. Both the virgin and simulant-exposed referee materials were characterized in this manner, with the simulant-exposed materials washed three times with distilled water. Each washing step consisted of the material placed in a 4 mL vial, the vial being filled with distilled water and vortexed for 1 minute, the sample being centrifuged for 1 minute, and the supernatant being removed via pipette. Washed samples were then dried at 80 C prior to analysis.

4.8 FLUORESCENCE SPECTROSCOPY

Fluorescence measurements were conducted on the unexposed, simulation-exposed, and agent-exposed and washed materials with a Jasco FP-8300 fluorimeter in conjunction with SpectraManager software. Measurements were conducted using an excitation wavelength determined from the maximum absorbance wavelength of the corresponding UV-Vis spectra greater than or equal to 280 nm and was uniform for each material set. An excitation and emission bandwidth of 1 nm was used in a measurement range from 5 nm greater than the excitation wavelength to 750 nm, with a Xe light source, a data internal of 0.5 nm, a response of 0.5 seconds, and a scan speed of 500 nm/min.

In general luminescence, a material gains energy by absorbing light at a given wavelength to promote a valence electron from its ground state to an excited state. The system is then subject to nonradiative internal relaxation involving interaction with its vibrational and rotational modes, and the excited electron is transferred to a more stable excited level. In insulators and semiconductors, this can lead to the formation of a bound state between the excited electron and the resulting valence level "hole" left by its migration, called an exciton. Fluorescence spectroscopy explores these excited levels to look for distinct and characteristic electronic energy states within the band gap of a material.

For fluorescent materials, this energy is at least partially released in the form of light, which is referred to as radiative relaxation. This emitted light has a longer wavelength than the incident light and is detected as fluorescence, with the spectral dependence of its intensity providing information about the properties of the material. With this study specifically, we are aiming to distinguish if a material can be self-indicating upon agent exposure through these fluorescence phenomena. Both the virgin and simulant-exposed referee materials were characterized in this manner, with the simulant-exposed materials washed three times with distilled water. Each washing step consisted of the material placed in a 4mL vial, the vial being filled with distilled water and vortexed for 1 minute, the sample being centrifuged for 1 minute, and the supernatant being removed via pipette. Washed samples were then dried at 80 C prior to analysis.

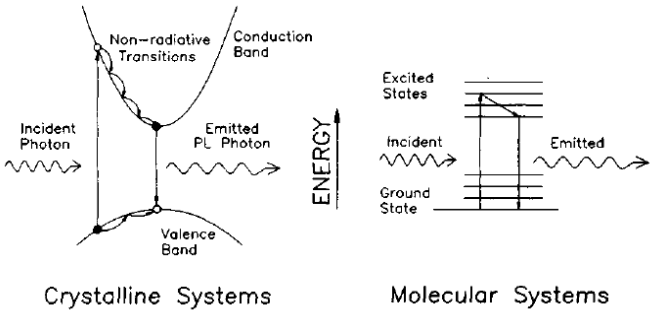

Figure 10. Fluorescence schematic

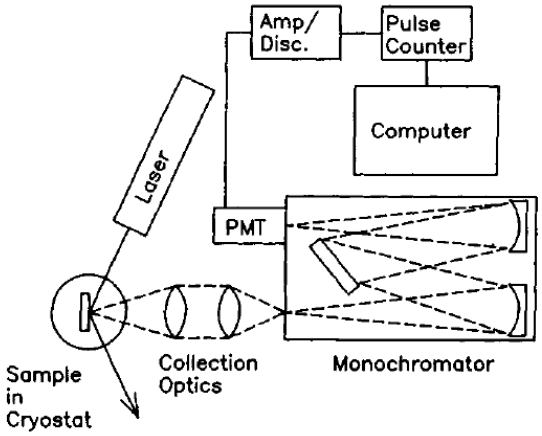

Figure 11. Fluorescence spectroscopy schematic

4.9 N_2 ISOTHERM

The nitrogen (N_2) absorption isotherm is the predominant method used for complete characterization of the physical properties of a material. In the method, a material is off-gassed in vacuum overnight and then exposed to N_2 gas. Nitrogen uptake is measured as a function of pressure and converted to a graphical distribution in the form of the nitrogen isotherm.

BET surface areas and pore size distributions were obtained by nitrogen adsorption isotherms at 77 K using a Quantachrome Autosorb-1 porosity analyzer. A relative pressure range of 10^{-4} to $p_{sat} = 1$ was measured for the adsorption branch, followed by a desorption branch to indicate the type and degree of hysteresis. All samples were outgassed under vacuum for 20 h. Brunauer-Emmett-Teller (BET) specific surface areas were derived from a linear region of the isotherm between relative pressures from 0.03 to 0.3 based on parameters described by Rouquerol et al. Total pore volume was calculated using a nonlinear density functional theory (NLDFT) method for all materials. Micropore volume was calculated using the Dubinin-Astakov method for goethite and ferrihydrite and the de Boer t-plot method for all other materials.

4.10 WATER ISOTHERM

The principle of a water adsorption isotherm of a material is to determine its water content at a full range of relative humidities. The amount of water vapor that can be absorbed by a material depends on its chemical composition, physical-chemical state, and physical structure. Consequently, the isotherm shape is unique to each material due to differences in capillary, surface, and colligative effects. This can profoundly impact the reactivity of a material, namely its potential for hydrolytic properties.

Water isotherms were collected at 25°C. Water was delivered from a saturator cell to a temperature-controlled microbalance containing the sorbent to be evaluated. The concentration of moisture in the air, or relative humidity, was systematically increased (or decreased) by changing the temperature of the saturator cell. By measuring the change in weight, the amount of water adsorbed on the material was calculated.

Shown in
Figure 12 is a schematic of the automated apparatus built to measure adsorption isotherm data. An isotherm is obtained by measuring the adsorbed phase concentration (loading) as a function of the vapor phase concentration at a constant temperature. The isotherm apparatus is comprised of three subsystems, (1) the vapor phase concentration control system, (2) the adsorbed phase measurement system, and (3) the temperature control system. The operation of all three subsystems is computer-controlled.

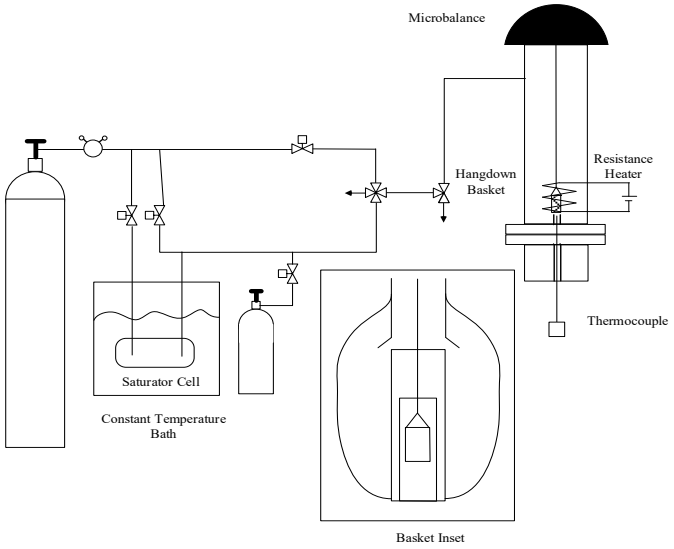

Figure 12: Schematic of Water Isotherm Apparatus

The vapor phase concentration control system is used to generate and monitor the concentration of chemical vapor over the adsorbent. It consists of a programmable flow controller network, a specially designed vapor-liquid equilibrator cell, and a MIRAN infrared (IR) analyzer. The flow control network directs flows to the appropriate devices and precisely controls the flow rates of each of these streams. The vapor-liquid equilibrator cell is used to saturate the desired flow stream with chemical vapor. This saturated flow stream is then mixed with a chemical free diluent gas stream to produce a predictable and controlled vapor-phase chemical concentration. The IR is used as an independent measure of the vapor-phase concentration.

A series of normally-closed mass flow controllers (MFCs) are used to direct the various clean gas streams to either the vapor-liquid equilibrator cell or the temperature-controlled test chamber. MFCs #1, #2, and #3 (10, 100, 1000 standard cubic centimeters per minute (SCCM) full scale) are used to control the gas flow rate through the equilibrator cell. The choice of the MFC to be used depends on the selected vapor-

phase concentration. MFC#4, MFC #5, and MFC #6 are all 0 - 10 standard liters per minute (SLPM) used to control the flow rates of the diluent stream, the Cahn balance purge stream, and the IR purge stream, respectively.

The vapor-liquid equilibrator system is designed for maximum efficiency and safety and consists of four main parts: a liquid reservoir, an aluminum oxide wick, an inlet, and an outlet. The liquid reservoir is designed to accommodate a maximum of 10 ml of liquid and is filled from the inlet port. A cylindrical aluminum oxide tube, located in the reservoir, serves as a wick and absorbs the liquid. The tube's purpose is to provide sufficient mass transfer area to insure the flowing vapor stream is equilibrated at the selected water bath temperature. Dry air enters the equilibrator at a rate determined by the mass flow controller(s) and is passed over the liquid-laden wick in a double-pass configuration. The first pass is through the inside of the cylindrical wick and the second pass is over the outside of the wick. The saturated vapor exits the cell and mixes with dry, diluent gas from MFC #4. The design of the equilibrator cell virtually insures that no aerosols are formed. A circulating water bath (Water Bath #1) is used to precisely control the temperature (+ 0.1 °C) of the equilibrator cell. The bath is kept below room temperature in order to prevent the saturated vapor from condensing downstream.

The final component of the vapor-phase concentration-control system is an infrared spectrometer, (Miran Model 80, Foxboro/Wilks, S. Norwalk, CT). The IR analyzer non-destructively measures the concentration of the chemical vapor stream just prior to entering the adsorbent bed. This concentration value is corrected to standard temperature and pressure (STP). It is used to verify the vapor-phase concentration.

The adsorbed-phase concentration measurement system is the most important subsystem. The most significant component is the microbalance (Model D-200, Cahn Instruments, Cerritos, CA). The Cahn microbalance has the capability to measure weight changes on the order of 1.0 ug. The adsorbent sample rests in a small, stainless steel, mesh basket suspended from an arm of the Cahn microbalance by a thin wire. The wire and basket are located in the central cavity of the test chamber as seen in Figure 12. The chemical-laden feed vapor is passed through the adsorbent bed and weight measurements are periodically made. After passing through the adsorbent, any chemical remaining in the effluent stream is removed by a high capacity carbon filter.

The states (i.e., on or off) of the switching valves, the vapor-liquid equilibrator flow solenoids, and the desorption heating coil are controlled through a series of electromechanical relays and a personal computer. Internally-developed application software controls the above relays as well as the RS-232 communications to the Miran analyzer, the Cahn microbalance, and the MFC's. The computer program also controls all of the required steps to measure isotherm data. Operational parameters such as the target vapor-phase concentrations and the volumetric flow rate of the diluent air for each equilibrium point, and the number and order of equilibrium points desired are selected by the operator and saved in a setup file.

The main objectives of this automated gravimetric procedure are; (1) to measure adsorption equilibrium data in the most time-efficient manner and (2) to improve the data accuracy compared to the more tedious, non-automated, methodologies. The isotherm measurement system has three basic operations, (1) system initialization, (2) chemical feed (challenge) and (3) adsorbate strip. Prior to the start of the experiment, the initial adsorbent weight is determined. Isotherm measurements begin at the highest vapor-phase concentration. After equilibrium is established, an adsorbate strip procedure is started. This is the most unique feature of this system since it dramatically reduces the equilibration time required for strongly adsorbed vapors. To use this feature effectively, target loadings for each vapor-phase concentration need to be determined. It is critical to set these target loadings so the adsorbent is stripped below its equilibrium loading at the next vapor-phase concentration. The system then alternates between the challenge/equilibration and the strip operation until all of the desired isotherm points are measured.

The samples are dried overnight in a convection oven at 105°C. The sample is then removed from the oven and placed in a desiccator and allowed to cool to room temperature. The samples are sealed in airtight containers to ensure that they remained dry. A 30 to 50-mg sample is arranged as a monolayer in the sample holder to promote rapid mass transfer. The sample holder is then attached to the Cahn microbalance.

Dry air is introduced into the system through MFC #5 and was directed through the adsorbent bed at a selected flow rate between 1 and 4 SLPM for one hour. Valve 1 is changed from its orientation shown in Figure 12 to allow air from the PSA dryer to pass over the adsorbent and exit through valve 2. The bed temperature is increased to 125 °C during this step to ensure that the material is dry prior to the start of the experiment.

After completing the drying step, the temperature of the bed is returned to the desired experimental temperature by deactivating the relay that controls the current to the NiCr wire. The purge air is diverted away from the bed by changing the position of valve 2 to isolate the adsorbent from all flow streams. Water bath #2, which maintains the chamber temperature, is set to the desired temperature of the isotherm. The microbalance is allowed to stabilize for approximately one minute and the initial dry adsorbent weight is recorded.

Once the starting weight is obtained, the computer directs the appropriate subsystems to begin the isotherm experiment. The first desired chemical vapor-phase concentration and the total volumetric flow rate over the adsorbent are read in from an operator-created data file. Valves 1 and 2 of the circulation system are aligned as shown in Figure 1. The appropriate vapor-liquid equilibrator and diluent flow rates are calculated using the vapor pressure of the feed chemical. The mass flow controllers are programmed with the calculated flow rates and the appropriate solenoid valves are opened to begin all flows. The feed vapor is transferred sent through the circulation system (containing the in-line IR), then through the adsorbent sample basket. The challenge mode continues for a predefined interval of time, usually about 30 minutes.

Every 15 minutes, the program records the output of the IR to monitor the chemical feed concentration. IR absorbance data and concentration values are saved to a data file. The controlling computer program continuously displays a graph of these data as a function of time with each IR update. Additional recorded information includes the target concentration, flow rates for MFC#1, MFC#2, MFC#3, and MFC#4, and the elapsed time of the experimental run.

After 30 minutes of chemical exposure, the computer program changes the position of Valve 2 to isolate the adsorbent. After a one-minute wait time to allow the basket to stabilize, the sample is weighed. The loading (mg of water/mg of sample) is calculated by taking the difference between the current and initial dry weight and dividing by the initial dry adsorbent weight. The program continuously displays a graph of the loading with time. This cycle is repeated until three loading measurements have been made.

After the third adsorbent loading is determined, the program calculates an average loading using the three most recent measurements. If the current loading falls within a 0.02% of the average loading, then it is assumed that equilibrium between the vapor-phase and adsorbed-phase has been achieved. The experiment continues to cycle between vapor challenges and weighing until this equilibrium criterion is met.

After the first equilibrium point is achieved, the system starts a "strip" mode. In this mode, the adsorbent bed is heated, using NiCr wire, to a pre-determined temperature for a selected time interval. Previously adsorbed chemical is desorbed using a previously set flow rate of clean, dry carrier gas. As mentioned previously, the stripping operation is a unique feature of this system. However, to take full advantage of this approach, it is necessary to strip below the equilibrium loading value for the next selected vapor-phase concentration. Target loadings for each point are selected with this requirement in mind.

When the strip mode is initiated, Valve 1 is switched from the orientation shown in Figure 1 to allow dry air to pass over the adsorbent. The adsorbent bed temperature is usually higher during the strip mode to decrease the number of strip cycles required to reach the loading target. However, the temperature must not be set too high to avoid problems with chemical reaction.

After 5 minutes in the strip mode, the power to the NiCr wire is shut off. Purge air continues to flow over the adsorbent while the system cools back down to the test chamber temperature. The cooling portion of the stripping cycle is continued for 15 minutes. Cooling times are modified based upon the heat capacity of the components within the chamber and the purge gas flow rate.

After 15 minutes of sample cooling, the adsorbent is isolated from all flow streams by changing the positions of Valves 1 and 2. The sample basket is once again allowed to stabilize prior to a weight

measurement. Once stable, the Cahn microbalance measures the weight of the adsorbent. This weight is converted to a loading and then compared with the target loading established for the next vapor-phase concentration. If the measured loading after stripping is less than or equal to the target loading, the chemical challenge mode is initiated. If the measured loading is greater than the target loading, the controlling computer program begins another strip cycle.

4.11 POTENTIOMETRIC TITRATION

Potentiometric titration (PT) measurements are used to identify the pKa and relative amount of surface species in a material as well as the point of zero charge of the material. It has been well-documented that basic surface species are essential for reaction with HD and G agents[2], and PT is a very suitable tool for gauging this potential. Potentiometric titrations were performed with a Metrohm 907 Titrando automatic titrator equipped with Dosino 800 20 mL dosing units and Tiamo 2.2 software, with 0.1 M $HClO_4$ and 0.1 M NaOH used as titrants. A mass of 100 mg of material was added to 50 mL of 0.01 M $NaNO_3$ and stirred in a closed cell overnight, with a N_2 feed bubbled through the solution continuously to eliminate the acidic influence of atmospheric CO_2. After a steady pH was obtained in the resulting solution, the base addition component of the titration was then immediately commenced via dosing of the 0.1 M NaOH up to a pH of 11 using the instrument settings of maximum signal drift of 1 mV/min and a waiting time of 300-600 seconds between doses to prevent disingenuous titrant effects from being recorded. The instrument was set to measure the equilibrium pH after each addition according to the aforementioned parameters. The resulting data was compiled into a proton binding isotherm of net charge per gram, Q, vs pH, representative of the total amount of protonated sites in the material, which is given by the Equation 14:

$$Q(pH) = \frac{(C_b - C_a + [H^+] - [OH^-])V}{m} \tag{14}$$

Where

$$[H^+] = \frac{10^{-pH}}{\gamma} \tag{15}$$

$$[OH^-] = \frac{10^{-pOH}}{\gamma} = \frac{10^{-(14-pH)}}{\gamma} \tag{16}$$

$$\log(\gamma) = -0.5115\left(\frac{\sqrt{I}}{1+\sqrt{I}} - 0.3I\right) \tag{17}$$

The terms C_b and C_a are the base and acid concentrations, respectively, in the suspension after each titrant addition, V is the total volume of the suspension, and m is the mass of solid material used in the titration, which is 100 mg for all cases in this study. The hydronium and hydroxide ion concentrations, $[H^+]$ & $[OH^-]$, are calculated by utilizing the pH of the solution and dividing by ionic-strength-dependent activity coefficients calculated using the Davies equation, as shown in equations 15, 16, and 17. A plot of Q(pH) vs pH for a given material typically assumes a sigmoidal profile, and the pH at the inflection point of this profile, the location at which the second derivative of the equation of the best-fit line to the data points is equal to zero, is considered the pH corresponding to the point of zero charge of the material.

This profile was then also used to construct the pK_a distribution of the material, represented as a profile of $f(pK_a)$ versus pK_a, using the Sorbent Adsorption Integral Equation Using Splines (SAIEUS) numerical procedure[11], which applies regularization combined with non-negativity constraints to iteratively solve Equation 18. Only the Q(pH) data from 4 < pH < 10 was used for this construction, as the concentration of free H^+ or OH^- ions typically exceeds that of H^+ or OH^- ions consumed by the titrated sample outside of this range, which is known to create spurious contributions to the resulting pKa profiles[12]. This phenomenon is also referred to as the buffering effect of water. This pK_a distribution provides a general representation of the pK_a and relative amount at each pK_a of surface species present on the material and offers direct insight into the potential acid-base chemistries that could be utilized.

$$Q(pH) = \int_{-\infty}^{\infty} q(pH, pK_a) f(pK_a) dpK_a \quad (18)$$

4.12 CHEMICAL DOSE-EXTRACTION REMOVAL ABILITY

An internally-developed chemical dose-extraction method is utilized as a baseline technique to gauge the reactive potential of referee materials against a neat, liquid-phase challenge of select simulants and agents. Presentation of an appropriate rationale for the development of the method requires a sufficient exploration of the physical and chemical processes that govern traditional adsorption phenomena. Briefly, the filtration of low-volatility vapors is traditionally accomplished using microporous adsorbents. Physical adsorption alone, however, has the limitation that the adsorbed vapor can elute through the bed or off-gas uncontrollably. This is of particular concern for the filtration of toxic vapors such as chemical warfare agents (CWAs). Reaction of toxic chemicals to non-toxic products is a more desirable alternative and requires the discrimination between adsorption phenomena and reaction. Therefore, in order to assess this reactivity, this dosing and extraction method has been developed. The low volatility chemical is dosed to a solid sorbent as a liquid. After thorough mixing and exposure time, the dosed chemical and any reaction products can be extracted and analyzed. Organic species can be identified using coupled gas chromatography/mass spectrometry methods (GC/MS), while ionic species can be analyzed using liquid chromatography (LC/MS).

In contrast to other techniques such as solid state nuclear magnetic resonance (NMR) which allow analysis of the sorbent-sorbate interaction, the extraction technique does not report any properties of the sorbent. GC analysis using a flame ionization detector (FID) is capable of following the disappearance of the chromatographic peak of all the chemical agents and simulants. Reaction products formed by sorbate interaction, if soluble in the extraction solvent, can be identified using a GC/MS. Insoluble components may be identified by analysis using LC/MS or by NMR. This method is similar to that described by Roy et al.[13] analyzing the degradation of HD and CEES on CuBTC.

Commercial chemicals used in this study were obtained from several sources. Chloroethyl ethyl sulfide (CEES) 98%, dimethyl chlorophosphonate (DMCP) 96%, dimethyl methylphosphonate (DMMP) 97% and diisopropylfluorophosphate (DFP) were obtained from Sigma-Aldrich. Malathion was obtained from the Spectrum division of United Industries and distilled to 93% purity. Chemical agents GB, GD, VX and HD were Chemical Agent Standard Analytical Reference Material (CASARM) quality. Note when using chemical agents that care must be taken and only qualified operators are permitted. Adsorbent materials studied were obtained from a variety of sources. Materials evaluated with this method included many different matrices, including commercial high porosity adsorbents, fabrics, and experimental crystalline and formulated powders. A large number of samples needed to be processed and disposed; therefore, a low-cost commercially-available reaction vessel, the standard 2 ml GC autosampler vial (Alltech Associates Inc 2 ml clear snap seal vial) was selected. These autosampler vials are available with either snap-on or screw-on caps. The snap on tops were used for non-toxic testing but are only design for single use. The screw-on caps provide a better seal against vapor loss. If the sample vials were to be vortexed, additional seal integrity could be achieved by wrapping the cap with electrical tape.

The tare weight of each empty vial was recorded. The desired amount of the sorbent sample was then added to the vial, and the net weight was recorded. The target sample weight was between 10-50 mg. The vials were then placed in a convection oven and dried for 1 hour at 90 C. The dry weight of the sample was then recorded. If the samples were to be humidified, then one of two methods was used. In the first approach, the open vials containing sample were placed in a vessel which was purged overnight using a controlled humidity stream. The vials were then reweighed and capped. In the second approach, liquid doses of water were added to the sample vial. Approximately 10-20 wt% liquid water, 5-10 ul, was used. In all cases, the water content was in molar excess of the reactive chemical substrate. The vial was capped

and vortexed for one minute. The former approach was preferred because this was considered to most closely simulate filter media operation.

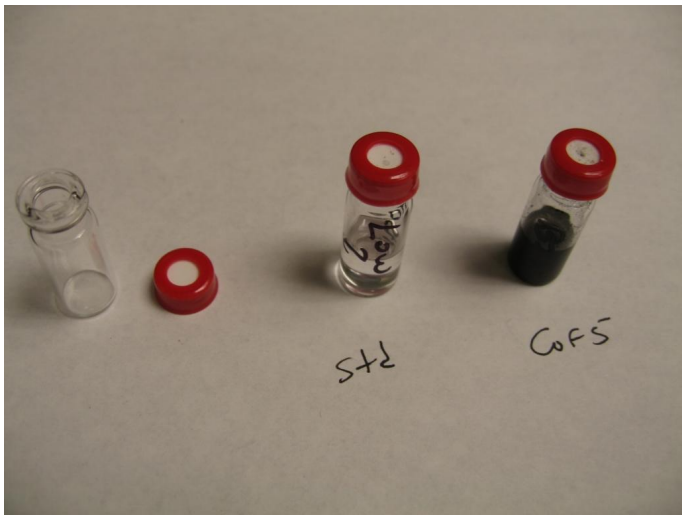

Figure 13. Autosampler vials

The reactive chemical was added to the humidified 2 mL sample vial as a liquid dose using a 10 uL digital microdispenser by Drummond Scientific (Broomall, PA) depicted in Figure 14. In order to promote spreading of the chemical on the sorbent, the reactive species was first mixed with solvent carrier in a separate vial. Chloroform was chosen as the solvent for two reasons. First, its relatively high volatility, exemplified by its boiling point of 61.7 C, meant that it would not be strongly adsorbed and compete for adsorption sites with the chemical of interest. Second, it was relatively unreactive compared to other solvents such as acetone. The volumetric mixing ratio of solvent to reactive chemical was chosen as 8:1. Aliquots of the reactive species/solvent mixture were then dosed to the sorbent- containing vials. The sample vials were then vortexed with a Fisher Scientific Touch-Mix model 231 vortexer for one minute and allowed to stand for a reaction period of approximately 60 minutes.

Following the reaction period and any other treatment, the reactive chemical and soluble products were then extracted from the solid matrix by adding 1.5 ml of acetonitrile solvent to the sample vial, followed by a one minute vortex. This mixture was then separated to halt the reaction by first centrifuging the mixture vial, using a Fisher Scientific Model 225 centrifuge operating at 6000 rpm for 5 minutes, then transferring the solvent layer to a clean vial.

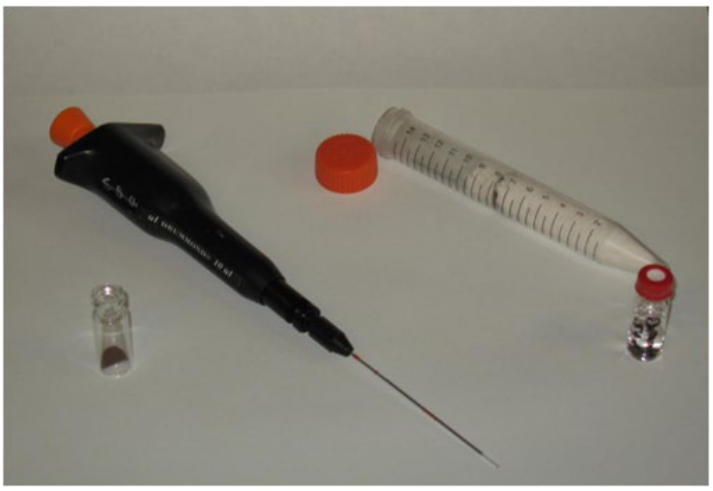

Figure 14. Microdispenser, autosampler vials and vortex tube.

Figure 15. Centrifuge, UV lamp and vortexer

Samples were analyzed using an Agilent 6890 gas chromatograph (GC), Figure 16, equipped with a 7383B autosampler and an Agilent flame ionization (FID) detector. A RTX-1701 30-meter column of 1 um film thickness or a DB-5 15-meter column of 1 um film thickness was used with a heating rate of 13 C/min. A guard column was installed because of the mixed matrix and non-volatile components in the injection sources. The autoinjector used a 10 ul syringe and 5 ul injections. Additional analysis was conducted using an Agilent 6890 gas chromatograph (GC) equipped with an Agilent 6973 Mass Selective Detector and a 7383B autosampler. The mass spectrometer used an HP 5MS column, 30m x 0.25 mm with 0.5um film thickness with a heating rate of 15 C/min.

Figure 16. Agilent 6890 with autosampler

A summary of the method and analysis is shown in Figure 17. Inconsistent results were obtained on some initial trials. A pre and post rinse step was shown to be required to obtain clean injections. Also, some early trials conducted with an RTX column instead of the 1701 resulted in peak broadening. The solvent peak in all cases eluted well ahead of the analyte. The size and retention time of the solvent peak was monitored to give an indication of the repeatability of the method. The characteristic retention times for CEES, DMMP, DMCP, DFP, and malathion using the GC column parameters outlined were 3.5, 3.7, 4.0, 4.3, and 5.8 minutes, respectively.

The density varied significantly among the many sorbent materials considered. The maximum sample mass for each adsorbent was selected to be no greater than 50 mg but typically 25 mg. In order to maintain an approximately similar volume of sorbent the mass was varied so that the adsorbent covered the bottom of the vial or else the mass was limited by the quantity of available sorbent. The latter was an issue with some experimental materials. In all cases, the volume of reactive chemical delivered to the mixture was maintained at the ratio of 0.1 ul of chemical per 1 mg of sorbent, corresponding roughly to a 10% by weight dosing of the chemical on the sorbent. This was chosen to ensure adequate sorbent to allow for complete reaction. The extraction step was performed at the end of the exposure period by adding 1.5 ml of solvent, vortexing for 1 minute, centrifuging at 1000 rpm for 1 minute, and pipetting the supernatant salutation from the vial for analysis with the GC.

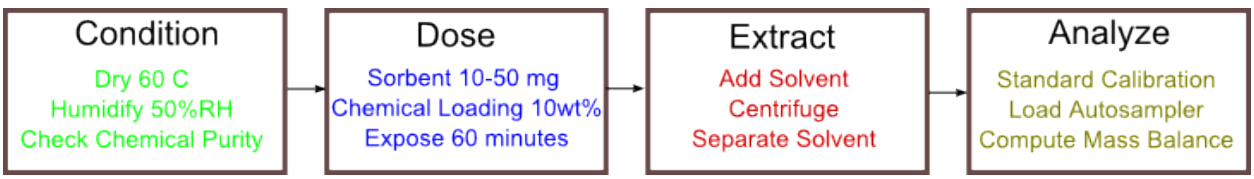

Figure 17. Extraction Method Block Diagram

Calibration standards were prepared each day by dosing a known volume, usually 2.5 ul, of the test chemical, into an autosampler vial with 1.5 ml extraction solvent, usually acetonitrile. Acetonitrile is

less reactive than other possible solvents for this application, such as chloroform, and has an intermediate polarity. Percent removal for a given sorbent-agent combination was determined by calculating the percent depletion of the integral under the GC profile peak for the acetonitrile-agent supernatant discussed at the end of section 1.2 at the characteristic retention time of the agent in question as compared to that agent's corresponding calibration standard. It was assumed that the addition of solvent stopped the reaction on the sorbent. In cases of high conversion this possibility was assessed by solid-phase magic angle spinning (MAS) NMR analysis.

4.13 NUCLEAR MAGNETIC RESONANCE SPECTROSCOPY

Nuclear Magnetic Resonance (NMR) spectroscopy is used to ultimately decipher specific reaction products formed and associated kinetics upon chemical exposure to referee materials. Materials downselected for NMR showed ostensibly high reactivity during the dose-extraction experiments, as decrease of the reactant in dose-extraction was the first step in determining whether a material shows promise for CWA detoxification. NMR was utilized at this juncture to elucidate wither the original toxic chemical was indeed chemically reacted or whether it was not extracted efficiently and was still physisorbed on the referee material matrix. In NMR spectroscopy, a sample is immersed in a strong magnetic field of strength 1-12 Tesla, splitting the degeneracy of the spin states of the nuclei in the sample that have either an odd mass or odd atomic number and thus would possess a permanent magnetic moment, which applies to isotopes of roughly half the elements in the periodic table. Excitation among these magnetic level is performed by absorption of radiofrequency radiation, and by measuring this energy at which the absorptions occur, the energy differences between the spin states are determined. The nuclear magnetic moments and electronic environment surrounding the target atoms exert an influence on this, which splits the absorption energies into multiple lines and shifts peak positions. These effects allow the local chemical environment of the target atoms to be evaluated, including coordination number, neighboring functional groups, and bond distances. For many simulants and CWAs, this target atom is phosphorous in the form of ^{31}P, with carbon in form of ^{13}C or hydrogen as ^{1}H used as supplementary probes.

NMR experiments were divided into two distinct efforts. The first effort characterized formation of products on simulant-exposed referee materials, and the second effort served as a supplementary measurement of degree of conversion for high-performing materials from the dose-extraction measurements. For the measurements of simulant-exposed MOFs UiO-66 and UiO-66-NH_2, approximately 5 mg of each MOF sample was digested in 750 microliters of a 10% by volume HF/d6-DMSO solution and studied using ^{1}H nuclear magnetic resonance (NMR). A Varian INOVA 300 NMR spectrometer was utilized for the experiments. A 10 ms pulse followed by a 4 s acquisition time and a 1 s delay were performed for 64 iterations. Spectra were referenced to the internal DMSO peak at $\delta = 2.5$ ppm.

For the percent conversion measurements, ^{31}P NMR spectra were measured with a Varian INOVA 400 NMR spectrometer equipped with a DOTY Scientific SuperSonic 7-mm VT-MAS probe. 128 scans per spectrum were performed using 30 pulses, a 0.5 s acquisition time, and 4 s delay between scans. Spectra were referenced to an external 85% H_3PO_4 (0 ppm, 31P) standard. A pH of 10, accomplished with a 0.45 M N-ethylmorpholine buffer solution, was selected to provide a basic environment that would facilitate reaction. An agent-to-sorbent ratio was selected so that the number of moles of active catalyst sites is equal to 6% of the number of moles of agent.

A third set of conditions was used to measure DMMP composition on ferrihydrite. Because of the strong magnetic field that is required for NMR operation, in-situ analysis of ferromagnetic materials, such as those based on iron, is impossible. Therefore, to test the chemical properties of the toxic chemicals and their products that were exposed to the iron-based materials requires extraction of the products and analysis of the extract.

For the NMR experiments involving DMMP decomposition, samples were evaluated in both as-received form and equilibrated at 50% RH. For both samples, 2.5 μL DMMP was added to 25 mg

ferrihydrite in a 4-mL vial. The vial was capped and allowed to stand for 1 hour. The sample was then extracted with 1.5 mL CH_3CN and analyzed by ^{31}P NMR.

4.14 DIFFUSE REFLECTANCE INFRARED FOURIER TRANSFORM SPECTROSCOPY

Diffuse Reflectance Infrared Fourier Transform Spectroscopy (DRIFTS) is used as another infrared spectroscopy technique in which infrared light on a sample is reflected and transmitted depending on the bulk properties of the material. While FTIR generates information on steady-state surface species formed after chemical exposure and a sufficient equilibration time, DRIFTS will generate information on the transient surface species generated during the reaction process and arguably provide the greatest elucidation of the complete reaction mechanism. The diffuse reflection in DRIFTS is produced by the sample's rough surfaces' reflection of the light in all directions and is collected by use of an ellipsoid or paraboloid mirror.

In the DRIFTS procedure, the sample was first prepared by adding a known mass of dry powder to a ceramic sample cup and conditioning the setup overnight in a pure nitrogen atmosphere of flow 1.25 mL/min at 25 C. A ThermoScientific Nicolet 6700 FTIR with a 40 mL cell was equipped with an external mercury-cadmium-telluride (MCT) detector (Infrared Associates) cooled with liquid nitrogen and a PIKE DiffusIR Model 198-2509 accessory with UV port, gold optics, heated chamber model 162-4140, and a KBr beamsplitter. A gain of 2.0, an optical velocity of 3.7974, an aperture of 65, a resolution of 2 cm^{-1}, a data spacing of 0.964 cm^{-1}, and range limits of 600-4200 cm^{-1} were used. A total of 1024 scans were used for the background, and either 256, 512, 1024, or 2048 scans were used for the experimental collection, depending on the vapor exposure time frame. Samples were analyzed at 25 C. A sampling interval of 117.70 seconds was used. Happ-Genzel apodization, Mertz phase correction, and Kubelka-Munk conversion methods were used in processing the spectra.

5. RESULTS

5.1 TITANIA (P25)

Of all metal oxides considered for catalytic and photocatalytic applications, titanium dioxide (TiO_2) is most heavily studied due to unique surface properties, chemical stability, and reactivity. TiO_2 exists in three major crystalline structures, which are (in order of natural occurrence) rutile, anatase, and brookite. All these phases possess different surface properties and electronic structures, leading to different applications based on the choice of the crystalline form. It was recently discovered that mixed crystalline phase (anatase + rutile) polymorphs of TiO_2 show enhanced photocatalytic functionality under ultraviolet irradiation. The most important property of TiO_2 in most applications is the chemistry of the exposed surfaces and associated defects. Any emerging titania materials developed for catalytic applications must have their surface structure and chemistry optimized, characterized, and well-defined. For example, it is not enough to proclaim that anatase nanoparticles were synthesized. It is equally important to characterize which surface ((001) vs. (101)) is exposed and how saturated it is with either bridging or terminal hydroxyl groups. The benchmark material chosen to compare the emerging titania (and other binary transition metal oxides such as ZrO_2 and CeO_2) is P25 TiO_2 material, produced by Aeroxide (Formerly Degussa). P25 is TiO_2 with 75-80% anatase and 20-25% rutile, with exact percent compositions varying based on the lot. The material has shown widespread abilities as a photocatalyst[14], with well-defined surface strutures, morphology, and other properties.

5.1.1 PHYSICAL PROPERTIES

The crystal structures in Figure 18 depict the rutile and anatase TiO_2. Typically, P25 contains a molar ratio of 25% rutile to 75% anatase. This is reflected in the x-ray diffraction pattern, which clearly shows diffraction peaks due to anatase and rutile phases coexisting. The anatase phase exhibits peaks at 2-theta values of 25 degrees (101 surface), 38 degrees (004 surface), 48 degrees (200 surface), 54 degrees (105 surface), 55 degrees (211 surface), 62 degrees (204 surface), 69 degrees (116 surface), 70 degrees (220 surface), 75 degrees (215 surface), and 83 degrees (224 surface). The rutile phase exhibits peaks at 2-theta value of 27 degrees (110 surface), 36 degrees (101 surface), 42 degrees (111 surface), and 44 degrees (210 surface)[15].

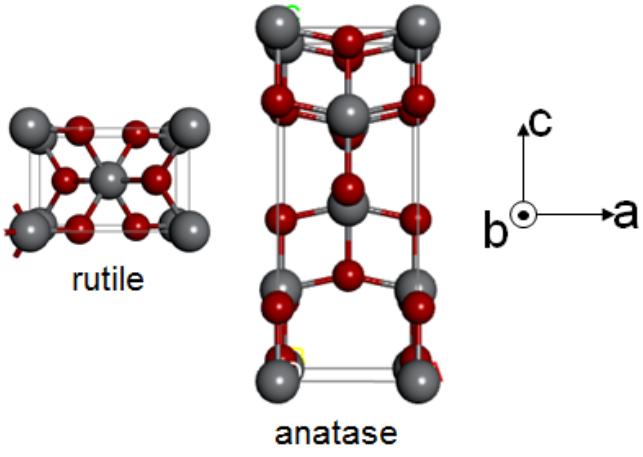

Figure 18. Crystalline structures of rutile and anatase polymorphs of TiO_2.

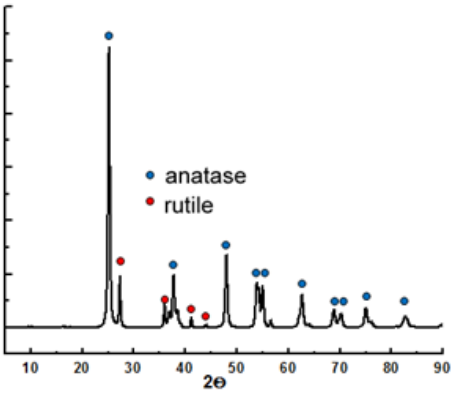

Figure 19. XRD pattern of P25, with allocation of peaks to the anatase or rutile phase

Quantitative analysis of the XRD pattern allows for determination of the mass fraction (XA) of anatase within the sample. Calculation of the mass fraction of anatase in the sample is performed using Equation 19. Since the molar mass of both anatase and rutile are the same, as both components are TiO_2, the mass fraction in this case is the same as the mole fraction.

$$X_A = \frac{1}{1+1.26\frac{I_R}{I_A}} \tag{19}$$

I_R is the intensity of the rutile (110) peak, occurring at $2\Theta \approx 28^{o}$, while I_A is the intensity of the anatase (101) peak, occurring at $2\Theta \approx 25^{o}$. The calculation determines that the mass fraction of anatase is 0.812, while the mass fraction of rutile is 0.188. The SEM image, shown in Figure 20, confirms that the P25 material consists of 30-50 nm nanoparticles, forming larger aggregates, which is consistent with observations in literature[16].

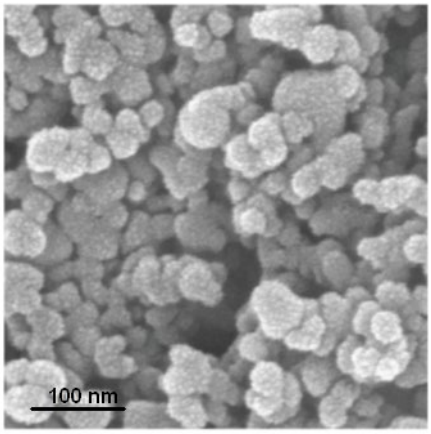

Figure 20. SEM image of P25

Thermal analysis results show the phase transitions of TiO_2 and the associated loss of adsorbed water. It is seen in the TGA graph that there is a two percent drop of weight, occurring prior to 150°C. This indicates that a low amount of bulk water is adsorbed on the surface, which is all driven away. The small amount of water absorbed in the TGA is partially caused by the fact that the total surface area of the material is only 40-50 m^2/g and that the morphology of the material is dominated by macropores, with little to no microporosity. The DSC plot shows that P25's anatase phase experiences a slow phase transition from anatase to rutile starting at around 450°C, and ending at around 550°C. This is commonly attributed to the fact that the phase transition of TiO_2 from anatase to rutile occurs over a period of time, with nucleation and growth of rutile clusters in the anatase material[17].

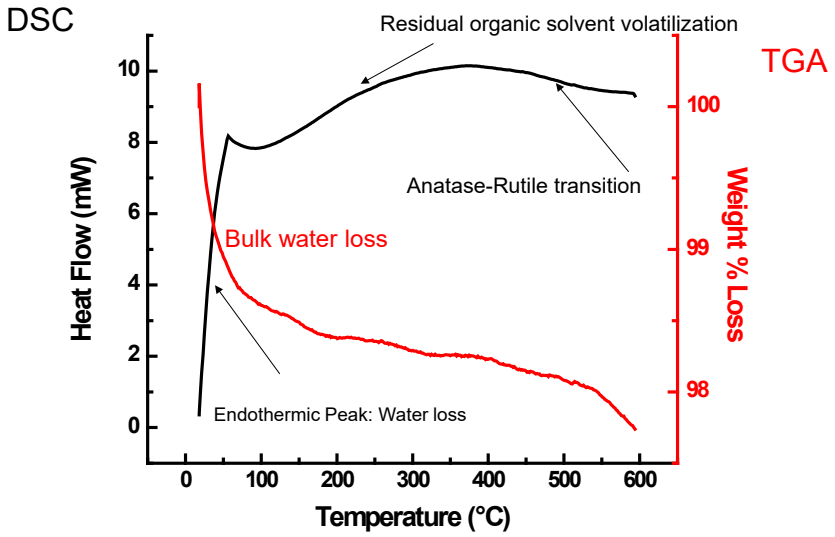

Figure 21. TGA and DSC profile of P25.

5.1.2 SURFACE PROPERTIES

Raman and FTIR spectra provide information on the surface properties of P25. The broad peak at approximately 440 cm^{-1} in the Raman spectrum of P25 comes from rutile phase TiO_2, specifically the E_g mode[18], while the three high intensity peaks (395, 513, and 634 cm^{-1}) are from the anatase phase[19], corresponding to the $B_{1g(1)}$, A_{1g}+$B_{1g(2)}$, and $E_{g(2)}$ anatase modes, specifically[18, 20]. Other rutile Raman modes cannot be deconvoluted from the high intensity anatase peaks. The broad FTIR bands at 1000 cm^{-1} correspond to the bending and stretching vibrations between Ti-O and Ti-O-Ti bridging stretching modes[21]. The peaks at 1640 cm^{-1} and between the 3600-2600 cm^{-1} range all correspond to physically absorbed water[21].

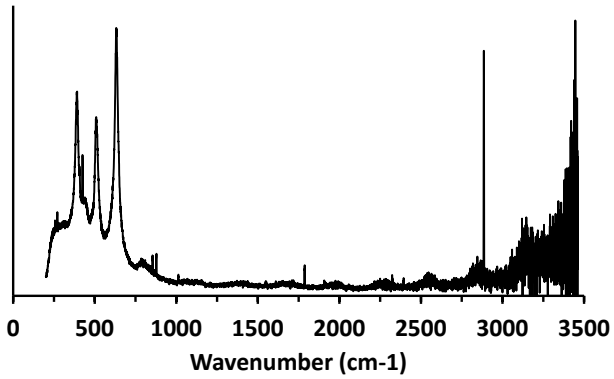

Figure 22. Raman spectra of P25

5.1.3 ELECTRONIC AND OPTICAL PROPERTIES

P25 titania was characterized for its electronic and optical properties. These properties have been documented both in peer-reviewed literature and by the manufacturer. However, these measurements were taken in-house to help build the understanding of this baseline material. The UV-Vis spectra of P25 aligned well with literature values as it matched the reported absorption edge of 403 nm[22]. Band gaps were calculated from absorption edges in the UV-Vis spectra, as consistent with literature methods[22]. Tauc plot analysis of the UV-vis spectra indicates that the band gap of the material is around 3.2 eV, corresponding to the accepted literature value[23].

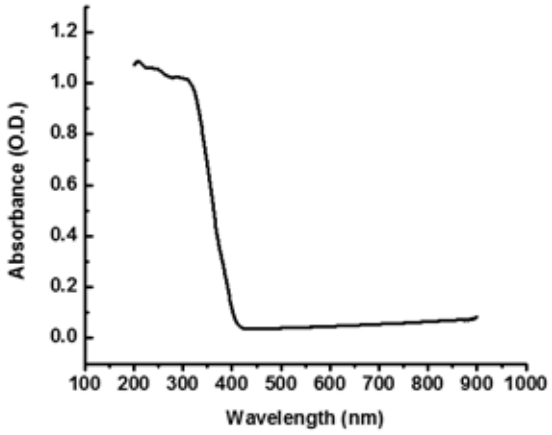

Figure 23. UV-Vis spectra of P25.

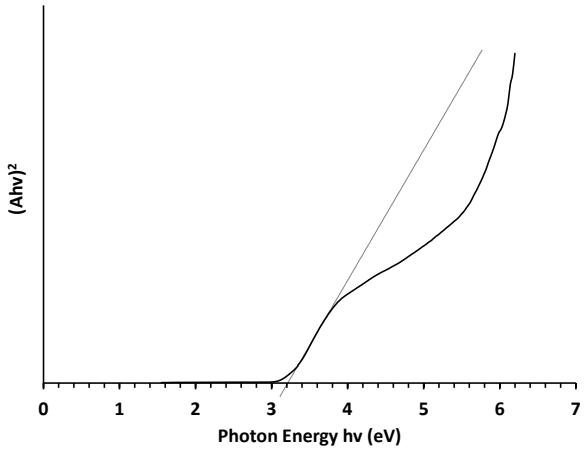

Figure 24. Tauc plot of P25.

Additionally, it is determined that the band gap of P25 is that of direct, allowed variety, further confirming the literature properties of non-quantum-confined titania. After exposure to the chemical agent simulants, the following UV-vis spectra were collected in Figure 25.

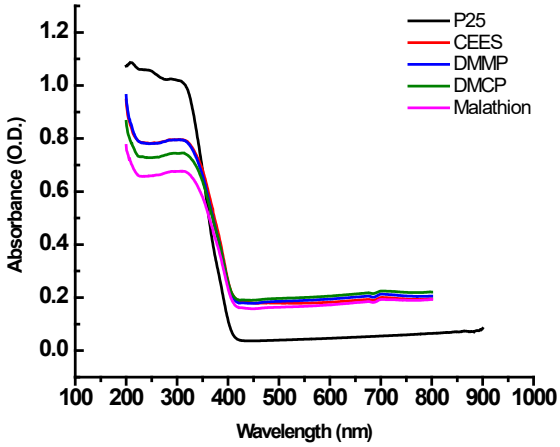

Figure 25. UV-Vis spectra of simulant-exposed P25 samples.

Exposure to simulant in general truncated the adsorbance in the ultraviolet region, but overall, no chemical-specific changes in the UV-vis spectra were observed, indicating that the adsorbed chemicals did not alter the band structure or introduce any new electron states. This also means that the chemicals did create any new molecular orbitals, meaning no chemical adsorption took place.

Fluorescence measurement of P25 was performed under sub-bandgap excitation of 285 nm, and the fluorescence spectra of P25 is shown in Figure 26. The spectrum shows low-intensity emission as a broad band around 400-500 nm. This is attributed to radiative recombination of excitons of shallow traps identified with oxygen vacancies and Ti^{4+} adjacent to oxygen vacancies[24]. Fluorescence spectra of simulant-exposed P25 is shown in Figure 27. No discernable change is observed in the fluorescence spectra for any of the exposed samples, indicating that no changes in band structure occurred.

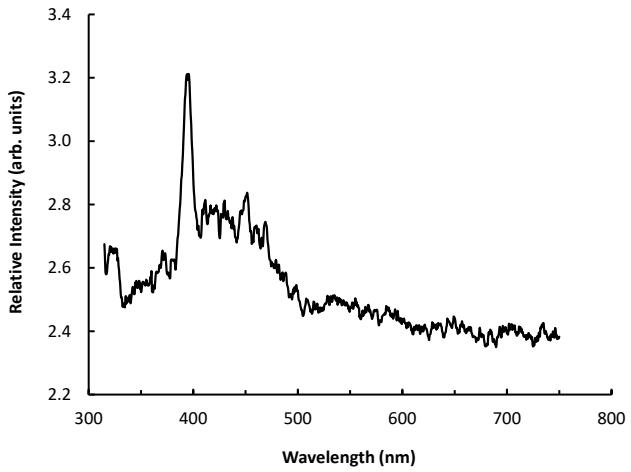

Figure 26. Fluorescence emission spectra of P25.

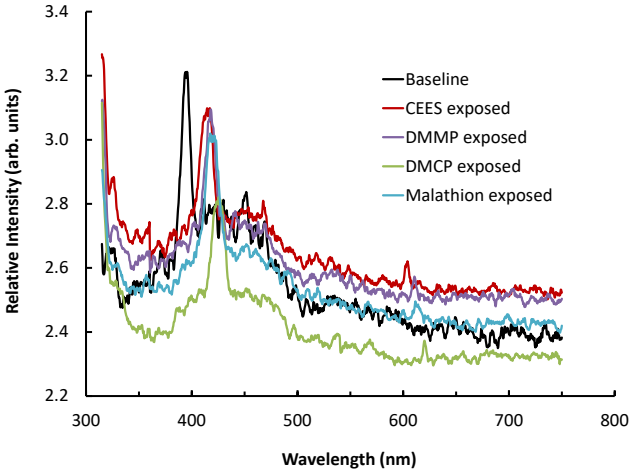

Figure 27. Fluorescence emission spectra of simulant-exposed P25

5.1.4 ADSORPTION AND REACTION CHARACTERIZATION

The N_2 isotherm of P25 is shown in Figure 28. P25 TiO_2 exhibited a type II isotherm with a small H3 hysteresis loop and a BET surface area of approximately 50 m^2/g, all of which is typical of this material[25].

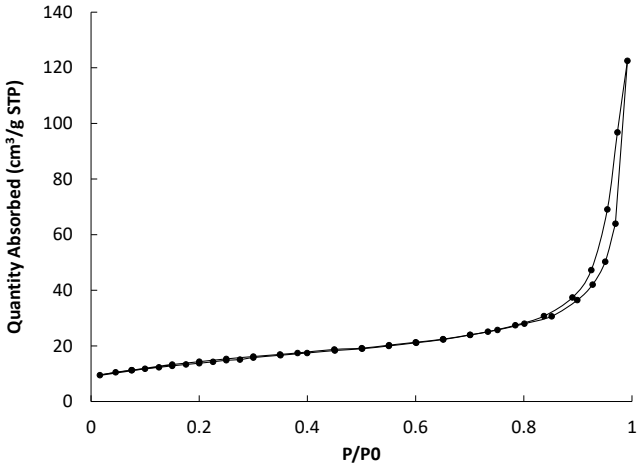

Figure 28. N_2 isotherm of P25.

Table 1. Physical properties of P25.

BET SA (m^2/g)	Total PV (cc/g)	Micropore Volume (cc/g)
48.8	0.1897	0.0016

The water isotherm of P25 is shown in Figure 29. P25 TiO_2 exhibited low water uptake across the range of pressures evaluated, which is expected due to its very low surface area and lack of excessive surface functional groups that would interact with water via forces such as hydrogen bonding.

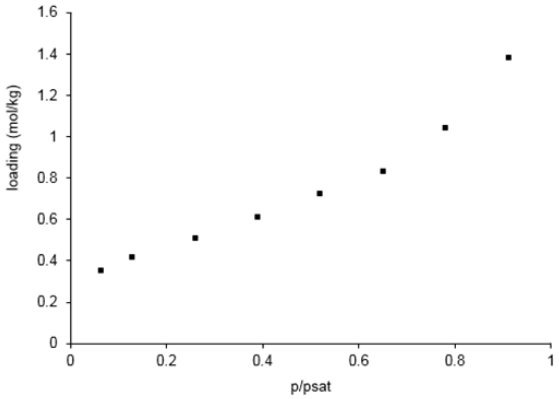

Figure 29. Water isotherm of P25

Potentiometric titration data for P25 is shown in Figure 30. Three distinct peaks are observed in the pKa distribution. The peaks around pKa of 5.0 and 9.0 have been assigned primarily to the anatase phase of titania, and the peak around pKa 6.5 is assigned to a nearly even contribution from anatase and rutile phases[12,26]. Specifically, the peaks represent proton affinity constants on the metal oxide surface. For anatase, contributions occur from one-step proton binding constants of monodentate hydroxo-groups at pKa 5.40, bidentate oxo-groups at pKa 7.75, and monodentate oxo-groups at pKa 9.46[27]. For rutile, contributions occur from the following proton affinity constants predicted for its surface[12,28]:

$$(=Ti\text{-})_2\text{-}O^{-2/3} + H^+ \leftrightarrow (=Ti\text{-})_2\text{-}OH^{+1/3}, \quad pKa = 5.3$$
$$\equiv Ti\text{-}OH^{-1/3} + H^+ \leftrightarrow \equiv Ti\text{-}OH_2^{+2/3}, \quad pKa = 6.3$$

Thus, the P25 peak at pKa of 5.0 results from major contributions to the anatase proton binding constant of monodentate hydroxo-groups and minor contributions from proton affinity constant 1 of the rutile phase, the peak at pKa of 6.5 results from significant contributions from proton affinity constant 2 of the rutile phase and the anatase proton binding constant of bidentate oxo-groups, and the peak at pKa of 9.0 results from the anatase proton binding constant of monodentate oxo-groups. The calculated point of zero charge of 6.7 was within range of literature values scaling from 6.0 to 6.8[29].

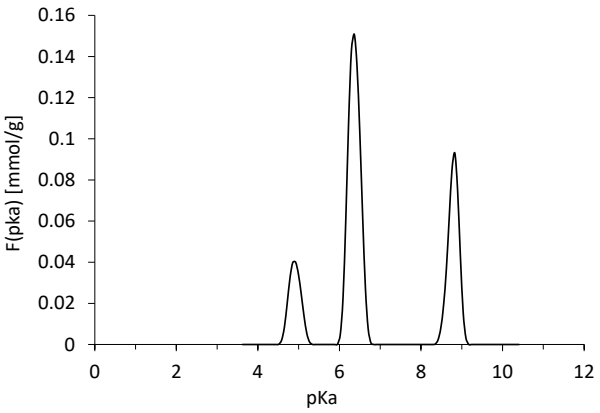

Figure 30. pKa distribution of P25

5.1.5 CHEMICAL DOSE-EXTRACTION TECHNIQUE

P25 has shown in literature to have exceptional room-temperature reactivity against CEES and organophosphates in photocatalytic applications due to its low band gap and surface structure allowing for the ability to produce reactive hydroxyl and superoxide radicals upon irradiation with ultraviolet light[30, 31], but under the dark ambient conditions of this experiment, it exhibited low removal abilities, less than 25%, against all simulants in the dose-extraction experiments with the exception of DMCP. Removal ability was higher among some of the agents, however, as P25 exceeded 60% removal with GB and approached 90% removal with VX.

Table 2. Dose-extraction results for P25

CEES		HD		DMCP		DFP		DMMP		GB		GD		Malathion		VX	
%R	SD	%R	SD	%R	SD	%R	SD	%R	SD	%R	SD	%R	SD	%R	SD	%R	SD
14.5	0.9	1.8	n/a	71.5	5.0	15.2	3.9	21.4	5.7	60.1	n/a	4.7	1.1	5.3	2.6	87.5	n/a

5.1.6 NMR

^{31}P NMR was used to investigate the catalytic activity of P25 titania for GD in 0.5 M (pH 10) ethylmorpholine (EM) buffer (Figure 31) and for VX in 0.5 M EM buffer (pH 10) and neutral water (pH 7; Figures 35, 39). Kinetic plots are also shown (Figures 32, 36, 40). As controls, the background reactions of GD and VX were run in 0.5 M EM buffer (Figures 33, 37; kinetic plots, Figures 34, 38). Kinetic parameters found are shown in Table 1. Observed reactions are shown in Scheme 1.

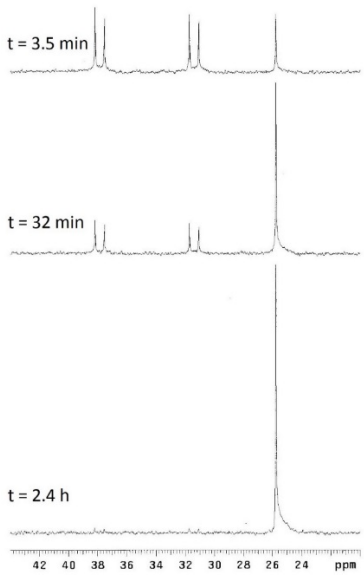

Figure 31. Select ^{31}P NMR spectra obtained for 2.6 µL GD added to 0.7 mg P25 titania in 0.75 mL 0.5 M EM buffer at the indicated times.

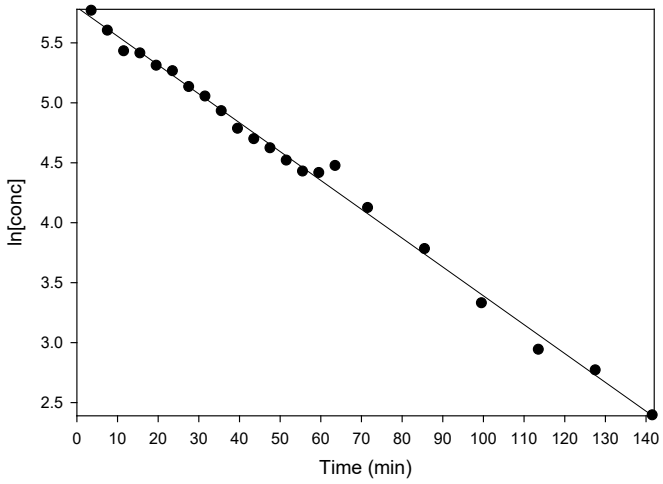

Figure 32. Plot of [GD] vs. time for ^{31}P NMR spectra obtained for 2.6 µL GD added to 0.7 mg P25 titania in 0.75 mL 0.5 M EM buffer.

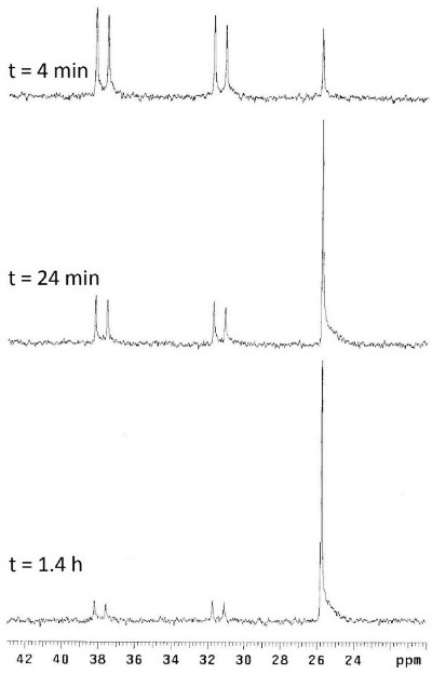

Figure 33. Select ^{31}P NMR spectra obtained for 2.6 µL GD added to 0.75 mL 0.5 M EM buffer (control) at the indicated times.

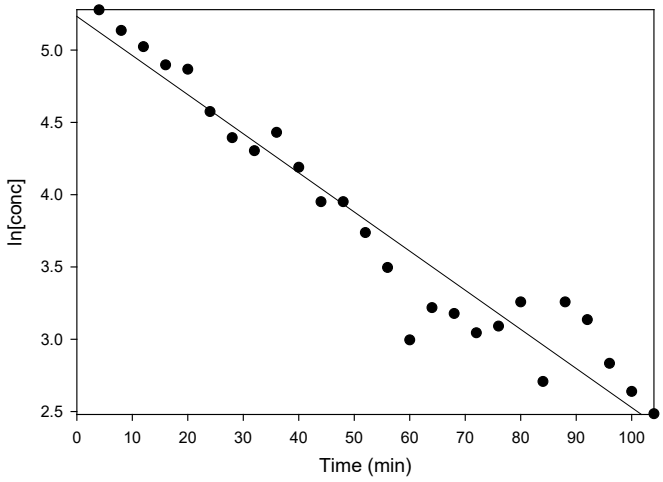

Figure 34. Plot of [GD] vs. time for ^{31}P NMR spectra obtained for 2.6 µL GD added to 0.75 mL 0.5 M EM buffer (control).

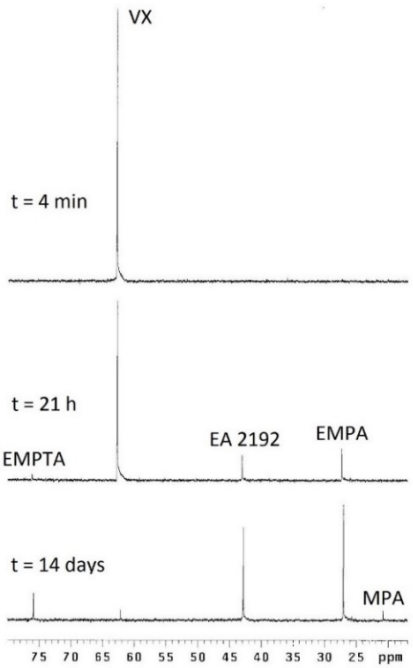

Figure 35. Select ^{31}P NMR spectra obtained for 3.9 µL VX added to 0.7 mg P25 titania in 0.75 mL 0.5 M EM buffer at the indicated times.

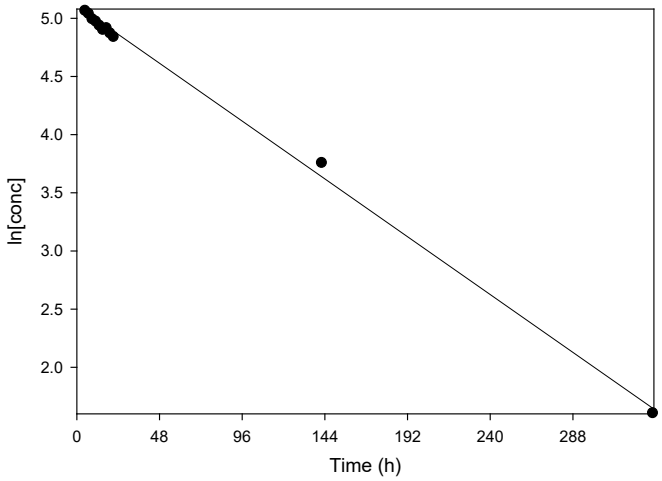

Figure 36. Plot of [VX] vs. time for ^{31}P NMR spectra obtained for 3.9 µL VX added to 0.7 mg P25 titania in 0.75 mL 0.5 M EM buffer.

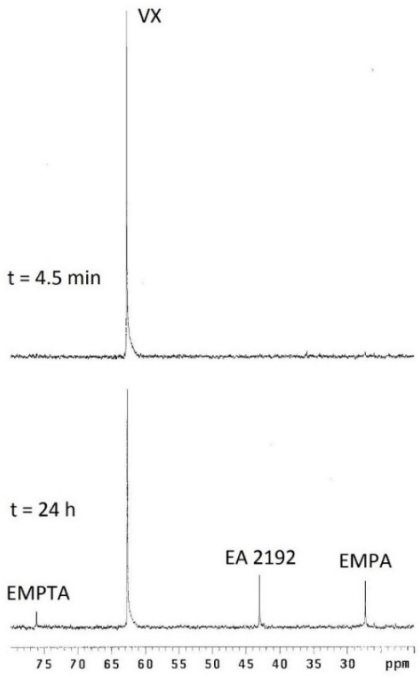

Figure 37. Select ^{31}P NMR spectra obtained for 3.9 µL VX added to 0.75 mL 0.5 M EM buffer (control) at the indicated times.

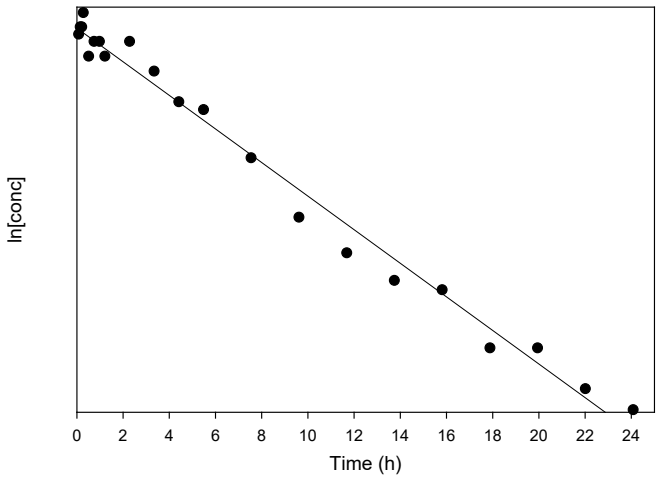

Figure 38. Plot of [VX] vs. time for ^{31}P NMR spectra obtained for 3.9 µL VX added to 0.75 mL 0.5 M EM buffer.

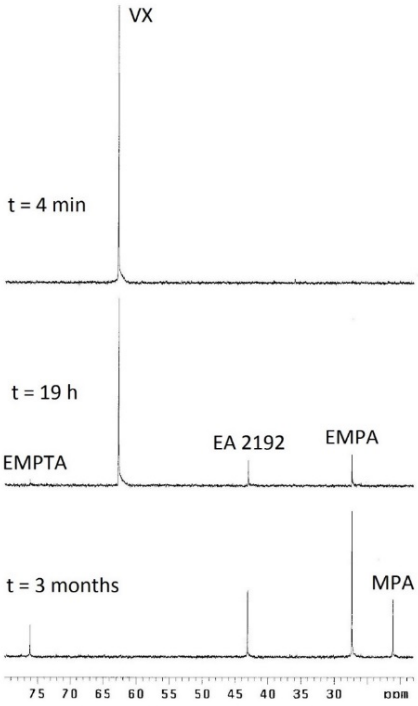

Figure 39. Select ^{31}P NMR spectra obtained for 3.9 µL VX added to 0.7 mg P25 titania in 0.75 mL water at the indicated times.

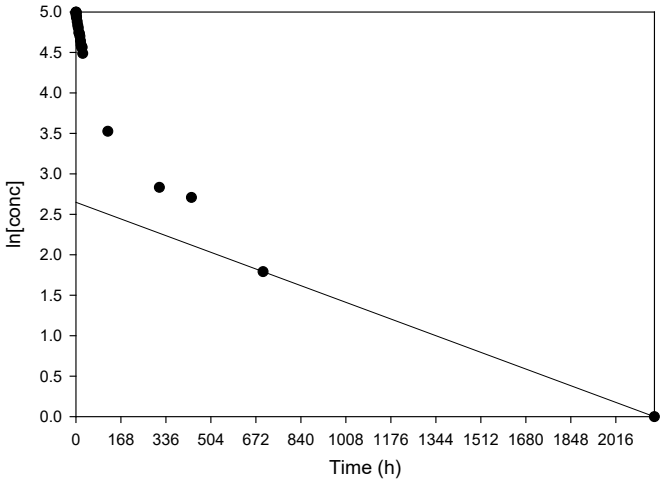

Figure 40. Plot of [VX] vs. time for ^{31}P NMR spectra obtained for 3.9 µL VX added to 0.7 mg P25 titania in 0.75 mL water.

Table 3. Reactions of GD and VX with P25 Titania.

Chemical and Conditions	Performance with P25 Titania	Performance with buffer only
GD, pH 10 EM Buffer	$t_{1/2}$ = 29 min	$t_{1/2}$ = 26 min
VX, pH 10 EM Buffer	$t_{1/2}$ = 2.8 days	$t_{1/2}$ = 1.7 days
VX, Neutral Water	$t_{1/2}$ = 24 days	–

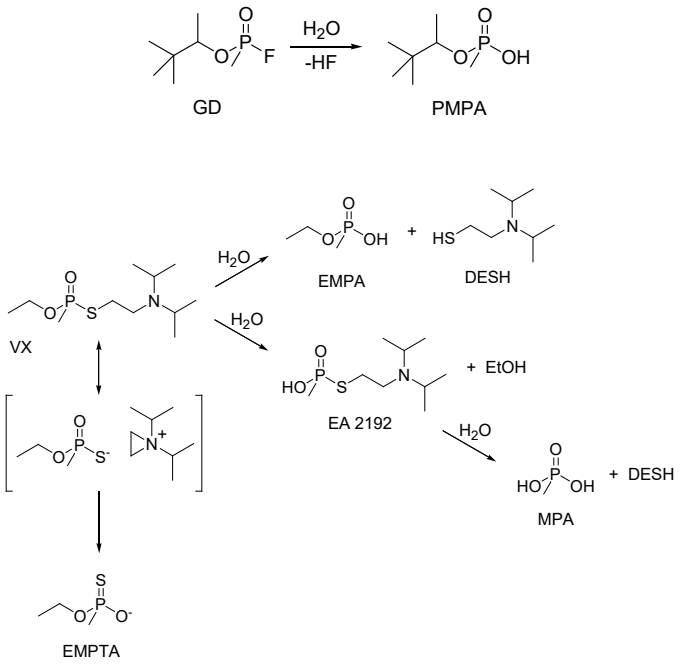

Figure 41. GD (top) and VX (bottom) Reactions Observed With P25 Titania

No catalytic activity is exhibited for GD as the rate is comparable to the background reaction in pH 10 EM buffer alone (Table 1). GD is hydrolyzed to non-toxic PMPA (Figure 41, top). For VX with P25 titania in pH 10 EM buffer, the reaction (Figure 41, bottom) is slower than that of the background reaction in buffer alone. For both VX cases, in addition to non-toxic EMPA and EMPTA, toxic EA 2192 is formed. However, in the presence of P25 titania, slow, secondary hydrolysis of EA 2192 to non-toxic MPA is observed. For VX with P25 in neutral water, the reaction continually slowed, eventually exhibiting a half-life of 24 days. Toxic EA 2192 was again formed, which also slowly hydrolyzed to non-toxic MPA.

5.1.7 DRIFTS

The DRIFTS spectra of CEES on P25 is shown in Figure 42. The loss at 3680 cm^{-1} is assigned to Ti-OH stretching modes. Increasing peaks around 1460 cm^{-1} and 1420 cm^{-1} are assigned to in-plane CH_3 bending modes, increasing peaks at 1210 cm^{-1} and 1300 cm^{-1} are assigned to out-of-plane CH_2 bending (wagging) modes, and the increasing peak at 1150 cm^{-1} is assigned to out-of-plane S-CH_2 bending (wagging) modes.

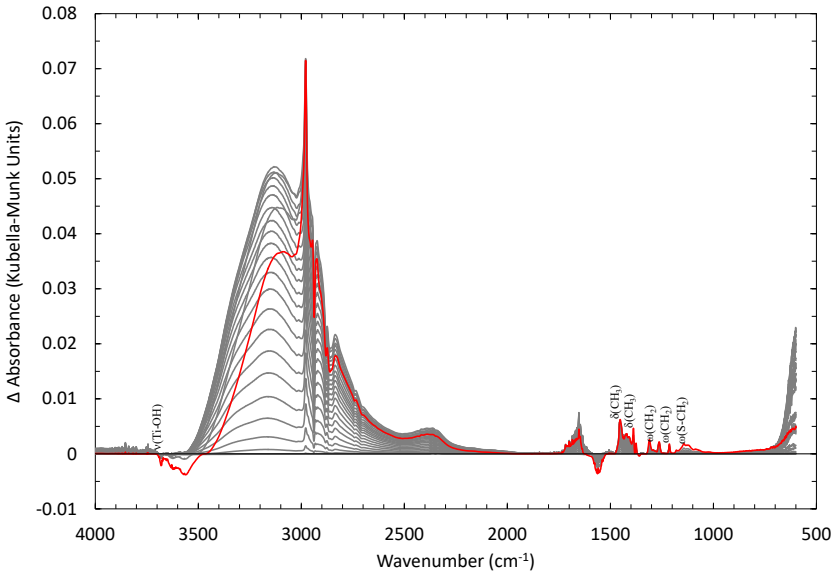

Figure 42. DRIFTS spectra of CEES on P25.

The DRIFTS spectra of HD on P25 is depicted in Figure 43. The increasing peak at 3700 cm^{-1} is assigned to terminal Ti-OH stretching modes, and the loss at 3670 cm^{-1} is assigned to bridging Ti-OH stretching modes.

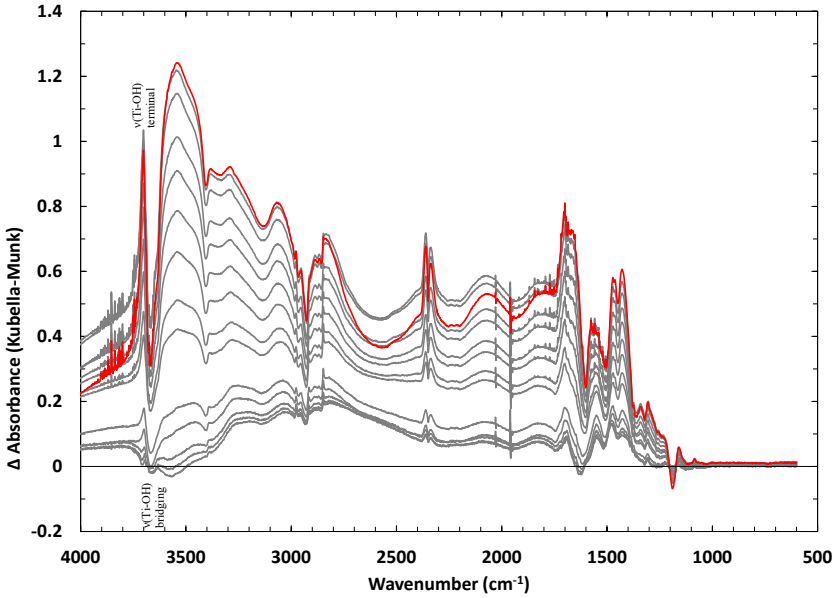

Figure 43. DRIFTS spectra of HD on P25.

The DRIFTS spectra of DMMP on P25 is shown in Figure 44. Losses at 3680 cm^{-1}, 3550 cm^{-1}, and 1620 cm^{-1} are assigned to Ti-OH stretching modes, H_2O stretching modes, and in-plane H_2O bending

modes, respectively. Increasing peaks at 1460 cm^{-1}, 1310 cm^{-1}, and 1210 cm^{-1} are assigned to CH_3 bending modes, P-CH_3 bending modes, and P=O stretching modes, respectively. There is clear decomposition of DMMP at early times/low coverage, as Ti-OCH_3 is observed. At higher coverage, the amount of decomposition drops and DMMP is more physisorbed.

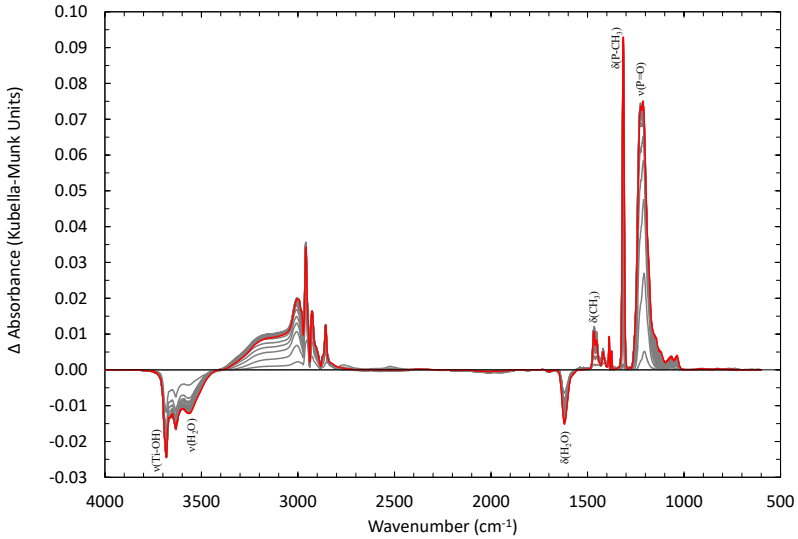

Figure 44. DRIFTS spectra of DMMP on P25.

DRIFTS spectra of DMCP on P25 is shown in Figure 45. Negative peaks at 3630 cm^{-1}, 3570 cm^{-1}, and 1620 cm^{-1} are assigned to Ti-OH stretching modes, H_2O stretching modes, and in-plane H_2O bending modes, respectively. Increasing peaks at 1450 cm^{-1} and 1220 cm^{-1} are assigned to in-plane CH_3 bending modes and P=O stretching modes, respectively.

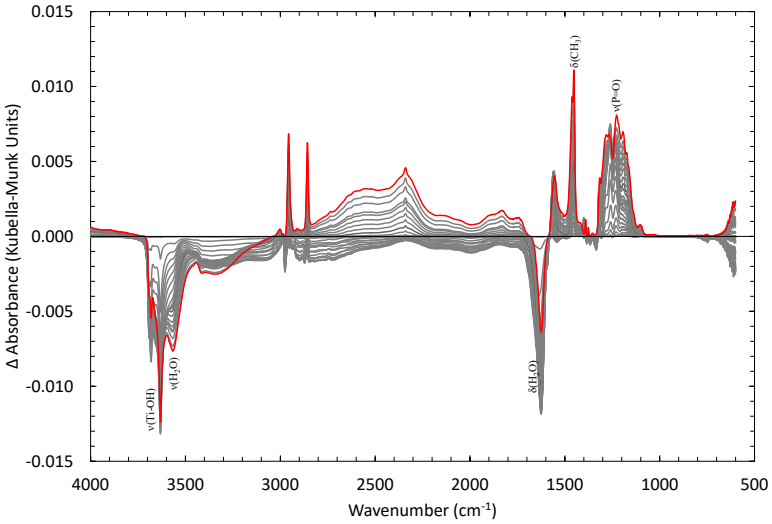

Figure 45. DRIFTS spectra of DMCP on P25.

DRIFTS spectra of GB on P25 is shown in Figure 46. The loss at 3690 cm^{-1} is assigned to Ti-OH stretching modes, and the positive peaks at 1460 cm^{-1} and 1310 cm^{-1} are assigned to in-plane CH_3 bending modes and in-plane P-CH_3 bending modes, respectively.

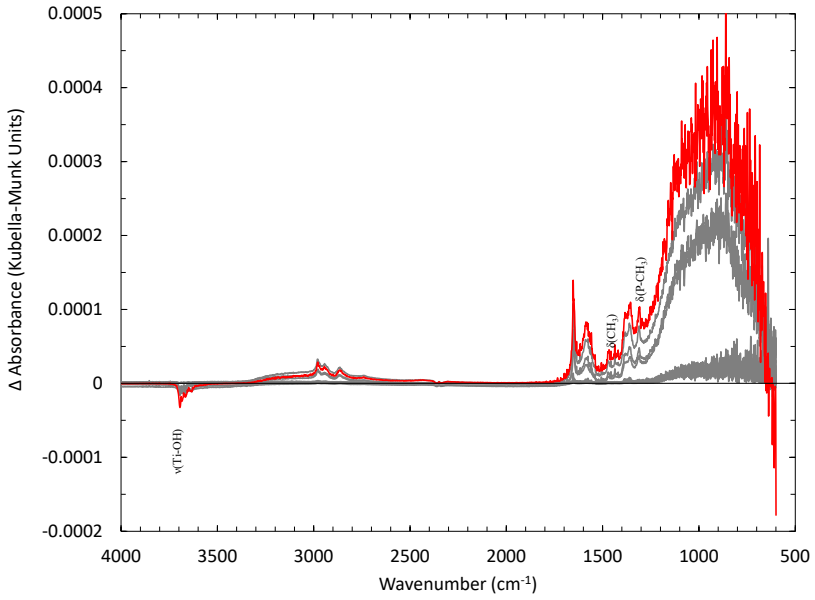

Figure 46. DRIFTS spectra of GB on P25.

DRIFTS spectra of malathion on P25 is shown in Figure 47. Losses at 3680 cm^{-1} and 1620 cm^{-1} are assigned to Ti-OH stretching modes and H_2O stretching modes, respectively. Increasing peaks at 2950 cm^{-1}, 1450 cm^{-1}, 1190 cm^{-1} and 1090 cm^{-1} are assigned to both CH_3 and CH_2 stretching modes, in-plane CH_3 bending modes, P=S modes, and P-S modes, respectively.

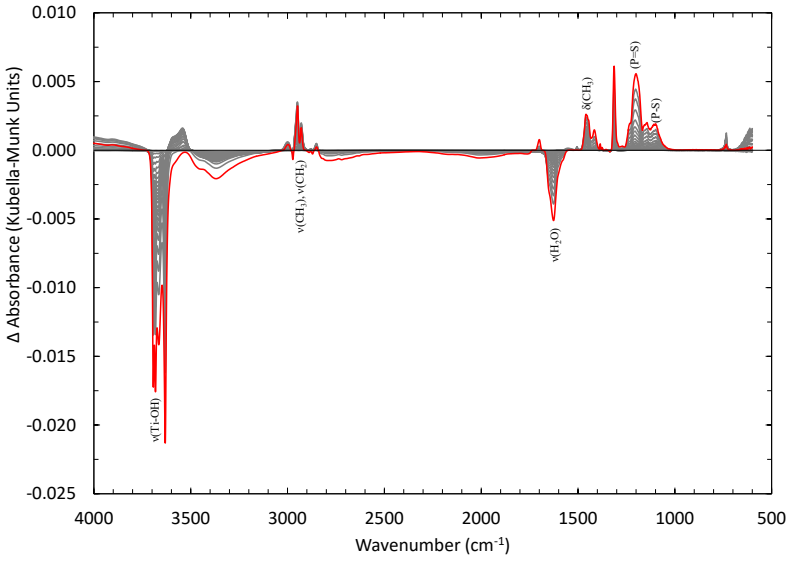

Figure 47. DRIFTS spectra of malathion on P25.

5.2 ZIRCONIUM HYDROXIDE

Zirconium hydroxide, $Zr(OH)_4$, is a versatile material that has been investigated by ECBC over the past several years in various applications. Initially, the material was used as the baseline substrate for CoZZAT, a metal hydroxide containing additives such as cobalt, zinc, silver, and triethylenediamine. During transition of CoZZAT, investigations led to the development of new decontamination materials containing $Zr(OH)_4$, settling on Type B as the most reactive among over half a dozen varieties studied due to its high surface area and high ratio of bridging to terminal hydroxyl groups, both of which have shown to be suitable for hydrolyzing nerve agents[2].

5.2.1 PHYSICAL PROPERTIES

Type B $Zr(OH)_4$ is manufactured at the ton scale by MEL Chemicals (Flemington, NJ) using a proprietary process. Typical $Zr(OH)_4$ materials are made using a metal salt (e.g. zirconium oxychloride, zirconium oxynitrate, zirconium sulfate) precipitated in an aqueous solution with a base (e.g. KOH). In the early 2000s, Southon described potential structures of $Zr(OH)_4$ materials, as described in Figure 48a[32]. Typically this is a somewhat easy task to accomplish, but $Zr(OH)_4$ is amorphous to X-rays, making structural determination extremely difficult. In fact, this is the focus of an ongoing effort. A combination of terminal hydroxyl groups are connected by bridging hydroxyl groups, forming small crystallites/plates that then agglomerate into larger structures. On the surface, a variety of groups are available, giving a wide range of Bronsted and Lewis acidity[33].

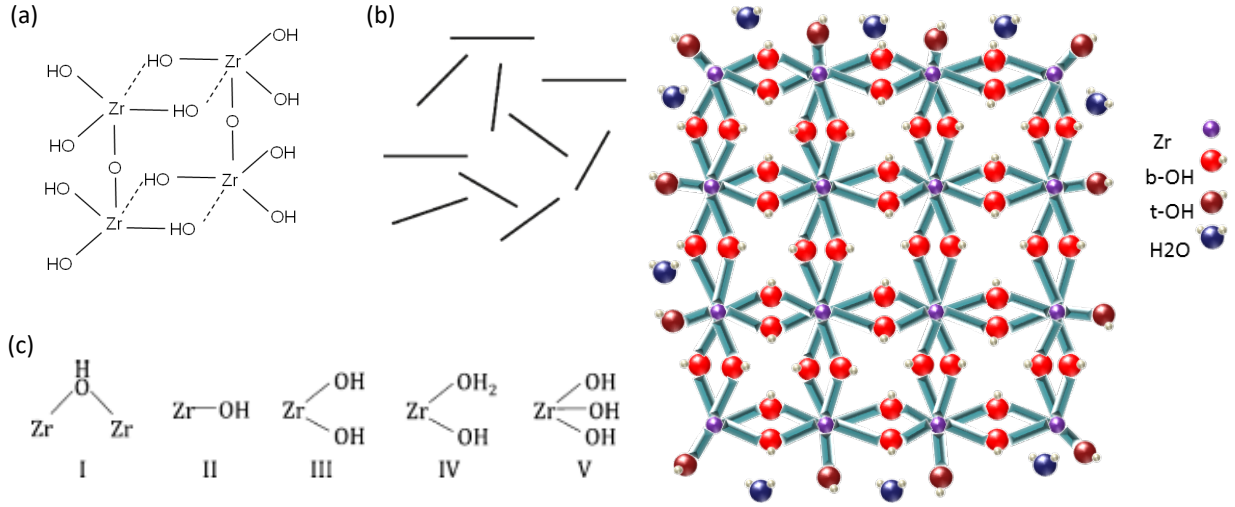

Figure 48. Proposed Structure of $Zr(OH)_4$. Sheet-like structures (a) form with a combination of bridging and terminal hydroxyl groups. These sheets combine (b) to form a pseudo-porosity, featuring a variety of surface hydroxyl functionalities (c).

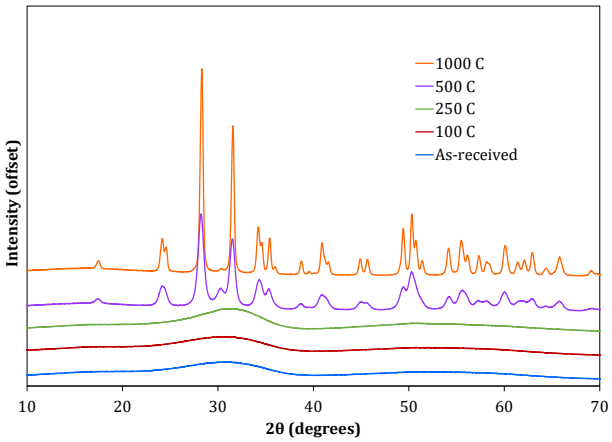

Figure 49. PXRD Data for Type B $Zr(OH)_4$.

The SEM image shown in Figure 50 illustrates the microstructure of Type B $Zr(OH)_4$. The material is made up of nanocrystals that agglomerate into larger particles greater than 1 µm. The overall roughness of the material is indicative of defects, which are likely one main reason for the reactivity of the material.

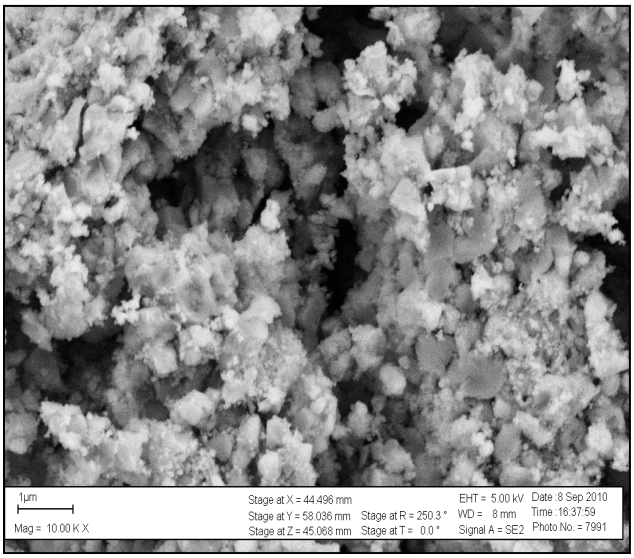

Figure 50. Scanning Electron Microscopy image of Type B $Zr(OH)_4$.

Thermogravimetric data, shown in Figure 51, shows that initial mass losses are endothermic, resulting from the loss of water from the surface. As temperature increases, hydrogen-bonded water continues to off-gas until crystallization to ZrO_2 occurs at approximately 400-450°C, corresponding to the strong exothermic peak in the DSC profile[34]. Samples were calcined at various temperatures to confirm the crystallization process; PXRD data are shown in Figure xx. The as-received material is amorphous to X-rays, as expected. Not until calcination at 500°C do we see reflections in the patterns; these reflections are commensurate of a mainly monoclinic crystal structure, with a potential intermixed tetragonal phase ZrO_2.

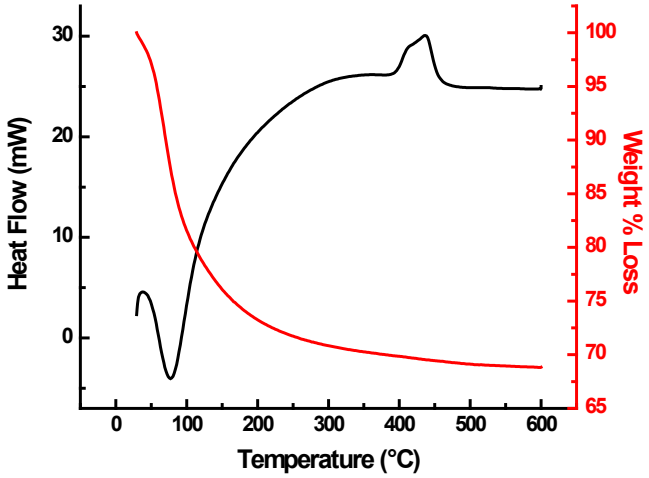

Figure 51. TGA/DSC Data for Type B $Zr(OH)_4$.

5.2.2 SURFACE PROPERTIES

XPS data have been collected in the past for $Zr(OH)_4$ and are shown in Figure 52. Of particular note is the oxygen 1s region, shown below in Figure xx. Deconvolution of the spectra shows two distinct peaks at 529.9 and 531.7 eV. The lower energy peak corresponds to bridging hydroxyls, while the higher energy peak corresponds to terminal hydroxyls. The availability of these peaks is paramount to the reactivity of the material, as we have previously demonstrated[35-37].

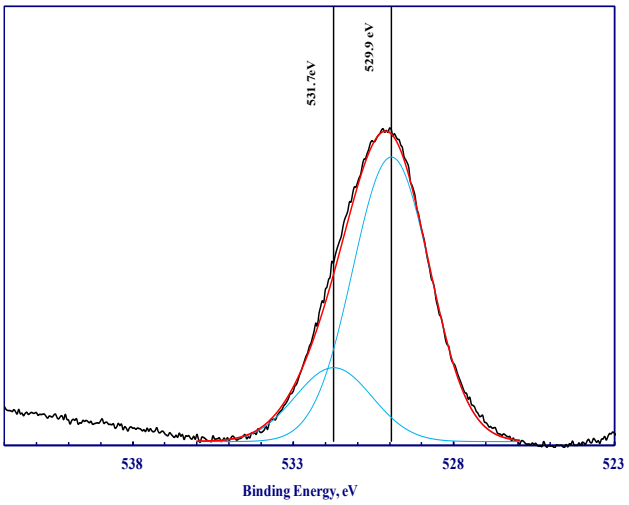

Figure 52. XPS Data for Type B $Zr(OH)_4$.

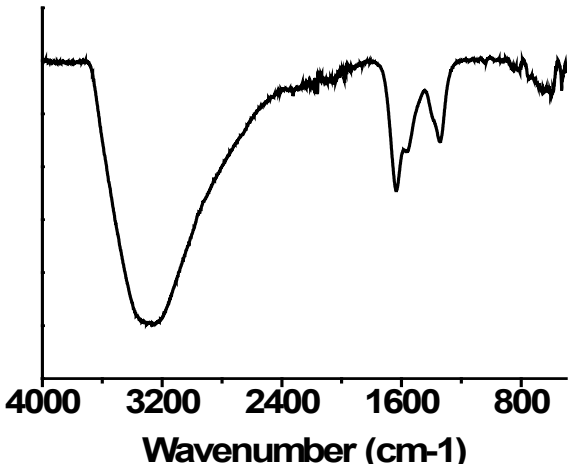

Figure 53. ATR-FTIR Spectra for Type B $Zr(OH)_4$.

The ATR-FTIR spectra of $Zr(OH)_4$ has a wide peak around 3300 cm^{-1}, indicative of OH stretching modes from its abundance of bridging and terminal hydroxyl groups, as well as physisorbed water, which masks the detailed signature of its true hydroxyl group profile. It also has major peaks at 1300 cm^{-1} and 1600 cm^{-1}, commonly attributed to modes involving C-O-Zr bonds of adsorbed carbonate species in the material; specifically, the peak at 1300 cm^{-1} is attributed to "side-on" coordination of CO_2 to unsaturated Zr^{+4} sites, and the peak at 1600 cm^{-1} is indicative of CO_2 interactions with terminal hydroxyl groups, forming a bicarbonate species on the surface[36]. The small broad peak around 700 cm^{-1} is consistent with Zr-O-Zr stretching modes[38] and consistent with results previously reported in literature[39].

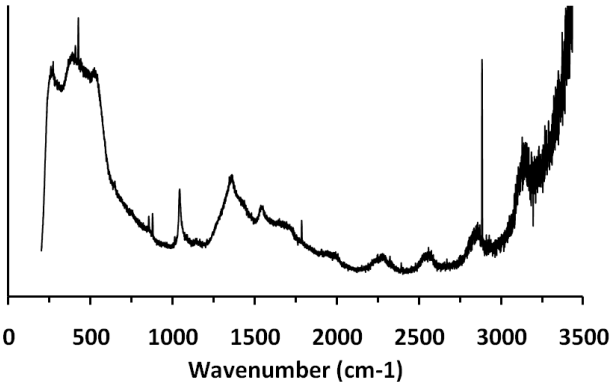

Figure 54. Raman Spectra for Type B $Zr(OH)_4$.

The raman spectra of $Zr(OH)_4$ is shown in Figure 54. Raman spectroscopy has been typically used with this material to differentiate the allotropic forms of zirconia (cubic, monoclinic, tetragonal) due to their distinct patterns in the 200-800 cm^{-1} region[40], but the results here show mixed phases present. The peak at 465 cm^{-1} corresponds to tetragonal zirconia, the peak at 490 cm^{-1} corresponds to cubic zirconia, and peaks around 250 cm^{-1}, 420 cm^{-1}, 515 cm^{-1}, 543 cm^{-1}, and 1063 cm^{-1} correspond to monoclinic zirconia[41].

5.2.3 ELECTRONIC AND OPTICAL PROPERTIES

UV-Vis spectra of $Zr(OH)_4$ is depicted in Figure 55, and fluorescence emission spectra is shown in Figure 58. A mild UV absorption peak around 290 nm is observed and can be attributed to valence band to conduction band transition in zirconia species[42]. Tauc plot analysis in Figure 56 calculates a band gap of about 5.05 eV, larger than the literature band gap of $Zr(OH)_4$ of 3.5 eV but well within accepted values of ZrO_2, which range from 3.0 eV to 6.0 eV[43]. No visible region peaks were detected for the zirconium hydroxide species in fluorescence spectra. UV-vis spectra and fluorescence spectra of simulant-exposed $Zr(OH)_4$ are shown in Figures 57 and 59. Malathion-exposed $Zr(OH)_4$ does not possess the 290 nm peak, resulting in a higher-wavelength absorption edge and possibly lower band gap of the resulting material, but no other exposed samples yielded significantly different spectra than the baseline material.

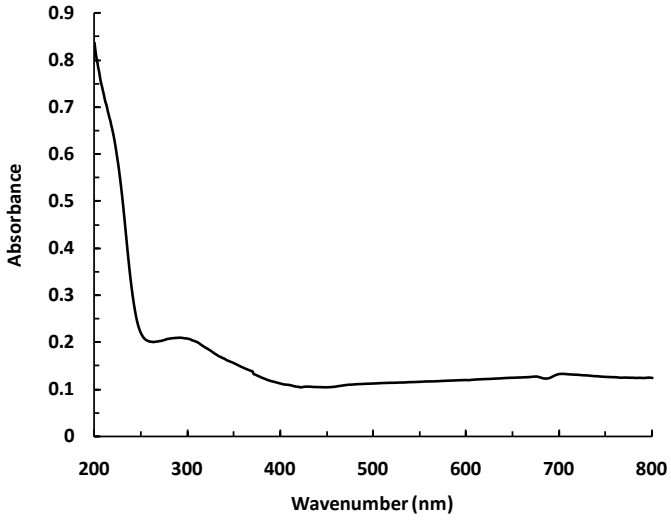

Figure 55. UV/Vis Data for Type B $Zr(OH)_4$.

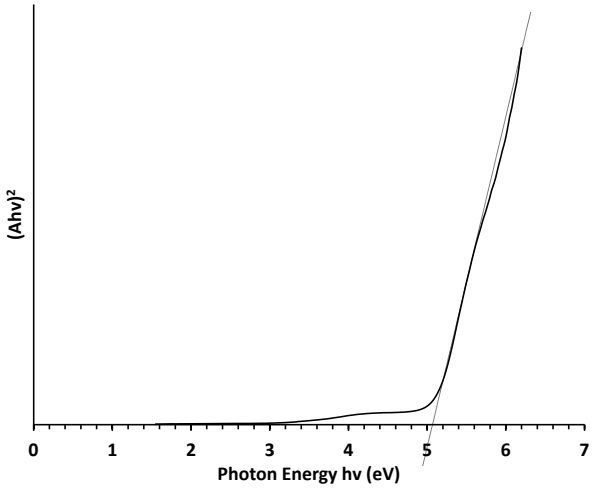

Figure 56. Tauc Plot of $Zr(OH)_4$

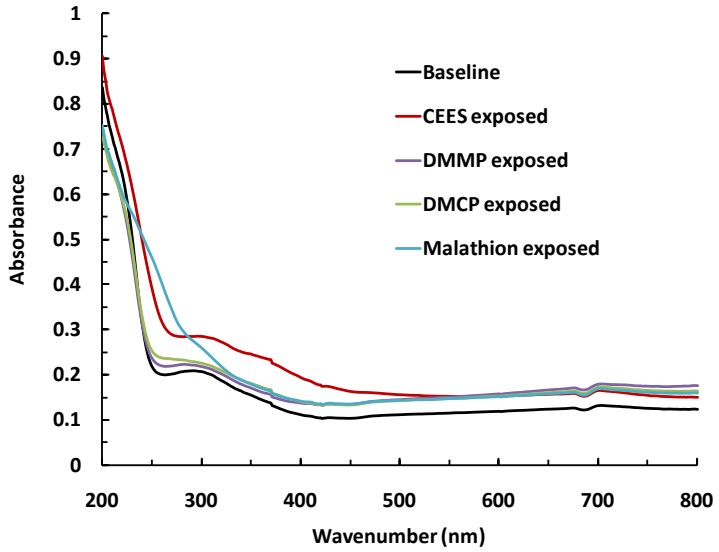

Figure 57. UV/Vis Data for Simulant-exposed Type B $Zr(OH)_4$.

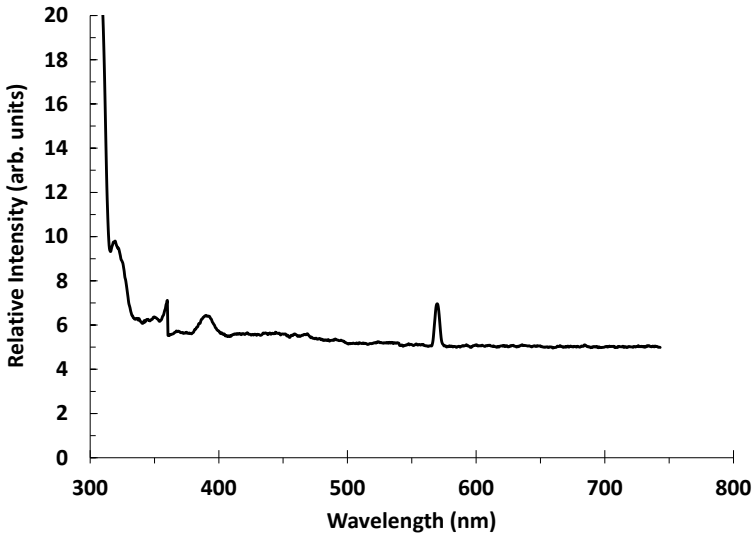

Figure 58. Fluorescence Data for Type B $Zr(OH)_4$.

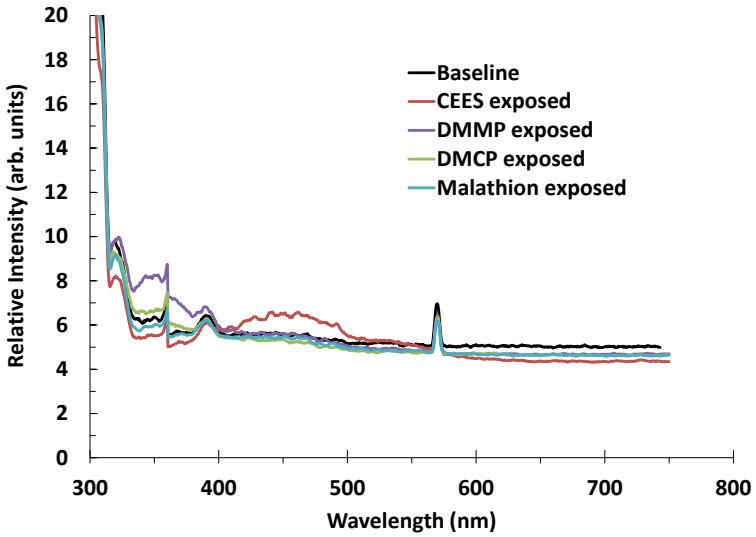

Figure 59. Fluorescence data for simulant-exposed $Zr(OH)_4$

5.2.4 ADSORPTION AND REACTION CAPABILITIES CHARACTERIZATION

Nitrogen isotherm data, shown in Figure 60, demonstrates the relatively high nitrogen uptake of $Zr(OH)_4$ as compared to other metal oxyhydroxides. Low partial pressure data indicate a large micropore region; indeed, BET surface area and micropore volumes confirm this, with values of 453 m^2/g and 0.17 cc/g, respectively. The micropore volume is almost half of the total pore volume of 0.38 cc/g. Of note is the presence of some mesoporosity, as seen by the interesting hysteresis loop between relative pressures of approximately 0.4-0.6. Data near saturation show the presence of some macroporosity as well, likely due to gaps between agglomerated crystallites.

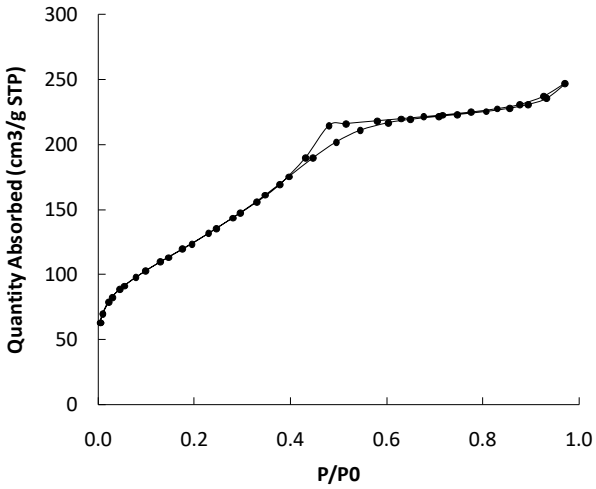

Figure 60. Nitrogen Isotherm Data for Type B $Zr(OH)_4$.

Table 4. Surface Area and Pore Volume for Type B Zirconium Hydroxide

$Zr(OH)_4$	BET SA (m^2/g)	Total PV (cc/g)	Micropore Volume (cc/g)
Type B	453	0.3816	0.1709

Water isotherm data, shown in Figure 61, shows the hydrophilic nature of $Zr(OH)_4$. This is not surprising, as the surface is mostly hydroxyl sites, providing areas for water to hydrogen bond. Even at low relative pressures, the amount of water loaded on the surface is significant, and the material reaches a saturation loading of almost 14 mol/kg.

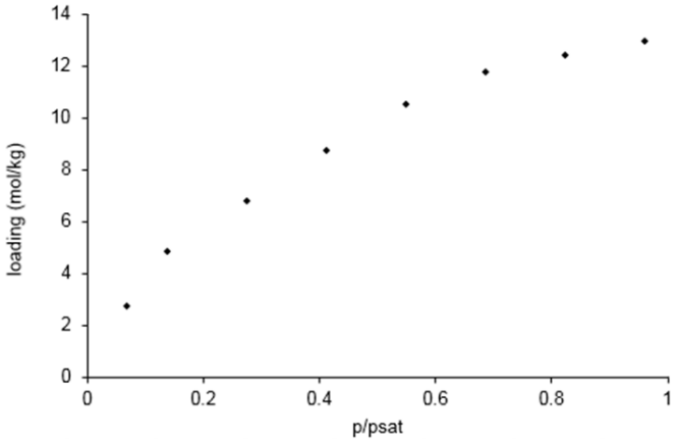

Figure 61. Water Isotherm Data for Type B $Zr(OH)_4$.

Potentiometric titration data for $Zr(OH)_4$ is shown in Figure 62. The pKa distribution essentially reflects the 5 main types of hydroxyl arrangements on zirconium hydroxide, represented in Figure 63. Arrangements I, II, III, IV, and V correspond to peaks at pKa of 4.5, 5.5, 6.5, 8, and 9, respectively, with the pKa 8 peak shifted to a pKa of 7 in the distribution of Figure 62. The peak at 10.5 is attributed to water molecules coordinated to these hydroxyl groups[2]. Therefore, the pKa distribution in Figure 62 suggests that the material is comprised principally of bridging hydroxyl arrangement I and terminal hydroxyl arrangement II. The calculated point of zero charge was found at a pH of 7.6, which was within literature values which range from 4.0 to 8.6[44].

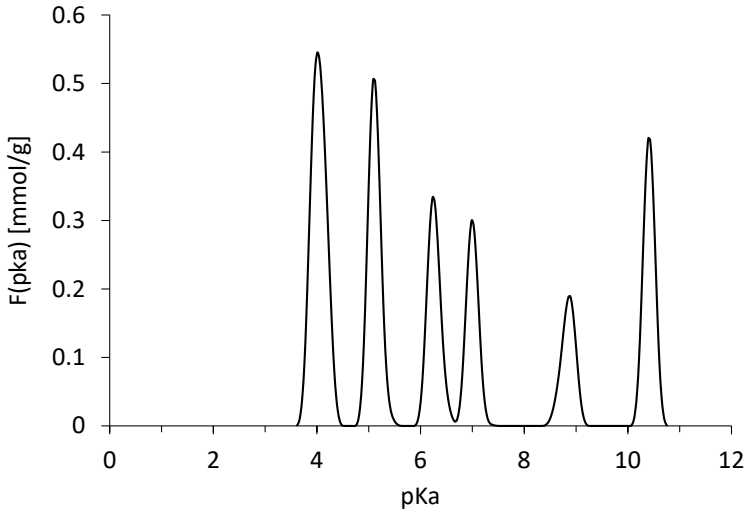

Figure 62. pKa distribution of $Zr(OH)_4$

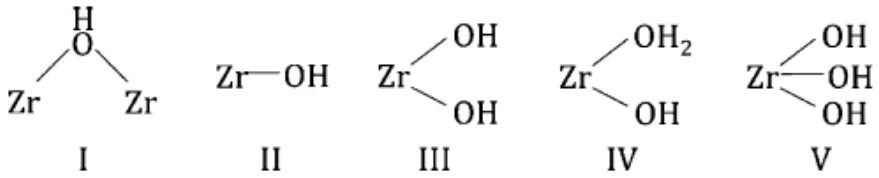

Figure 63. Hydroxyl group arrangements on zirconium hydroxide[2]

5.2.5 CHEMICAL DOSE-EXTRACTION TECHNIQUE

Table 5. Dose-extraction performance data for $Zr(OH)_4$

CEES		HD		DMCP		DFP		DMMP		GB		GD		Malathion		VX	
%R	SD	%R	SD	%R	SD	%R	SD	%R	SD	%R	SD	%R	SD	%R	SD	%R	SD
69.3	8.5	24.5	2.0	100	n/a	96.5	n/a	61.4	5.3	98.0	n/a	95.0	n/a	47.3	10.0	100	n/a

Zirconium hydroxide demonstrated high reactivity across nearly the entire spectrum of simulants and agents, as shown in Table 5. Reactivity among the G simulants progressed in the order DMMP < DFP < DMCP, with the DFP reactivity most closely mimicking the performance of GB and GD. CEES reactivity greatly overpredicted HD reactivity, and malathion reactivity greatly underpredicted VX reactivity. Hydrolysis of VX is a function of its more acidic bridging hydroxyl groups, whereas hydrolysis of GB is due to its more basic terminal hydroxyl groups[2]. The broad-spectrum simulant and agent chemistry of zirconium hydroxide is well-documented in literature, as its bridging hydroxyl groups provide for active sites for hydrolysis reactions of all agents, vesicants, and simulants[2]. With CEES and HD, the terminal hydroxyl groups provide active sites for elimination reactions to diethyl sulfide (DES)[2], though the reactivity was lower than for G-series and V-series agents due to the higher viscosity and oily properties of the vesicants impeding their ability to diffuse efficiently on the hydrophilic zirconium hydroxide surface[2].

5.2.6 NMR

NMR was used to investigate the catalytic activity of $Zr(OH)_4$ for VX, GD, and HD. ^{31}P NMR spectra for $Zr(OH)_4$ with GD in 0.5 M (pH 10) ethylmorpholine (EM) buffer are shown in Figure 64, and with VX in 0.5 M EM buffer (pH 10) and neutral water (pH 7) in Figures 66 and 68. Kinetic plots are also shown (Figures 65, 67, 69). Kinetic parameters found are shown in Table 6. Additionally, HD was also run under various conditions: Neat on the $Zr(OH)_4$ sorbent (Figures 70-71); by extraction from the $Zr(OH)_4$ sorbent with CH_3CN (Figures 72-73); and on the $Zr(OH)_4$ sorbent in the presence of CH_3CN and $CHCl_3$ solvents (Figures 74-77).

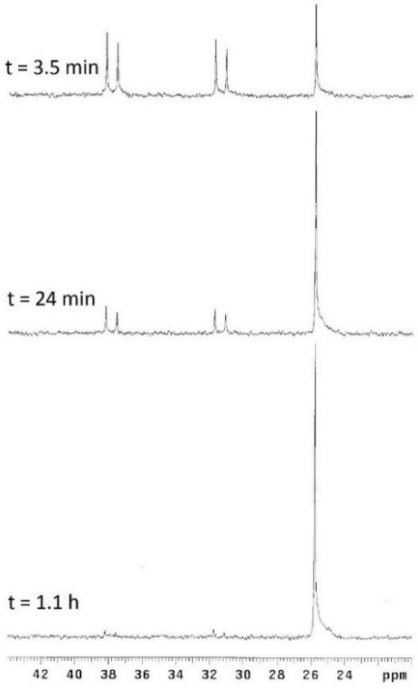

Figure 64. Select ^{31}P NMR spectra obtained for 2.6 µL GD added to 1.5 mg $Zr(OH)_4$ in 0.75 mL 0.5 M EM buffer at the indicated times.

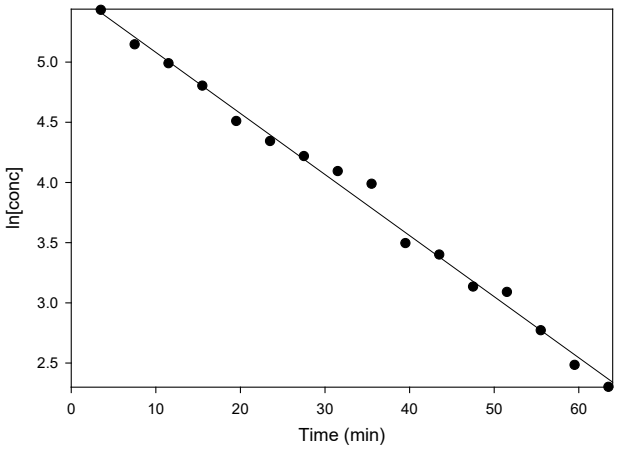

Figure 65. Plot of [GD] vs. time for ^{31}P NMR spectra obtained for 2.6 µL GD added to 1.5 mg $Zr(OH)_4$ in 0.75 mL 0.5 M EM buffer.

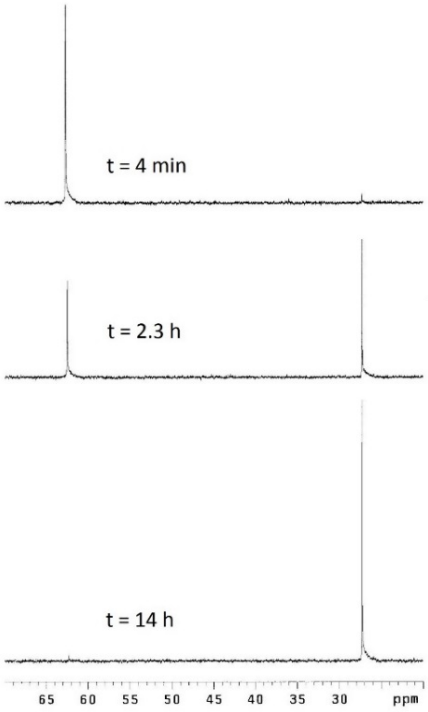

Figure 66. Select ^{31}P NMR spectra obtained for 3.9 µL VX added to 1.5 mg $Zr(OH)_4$ in 0.75 mL 0.5 M EM buffer at the indicated times.

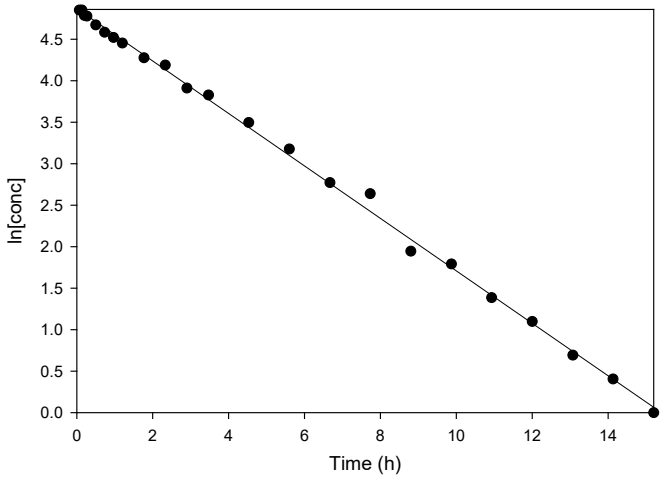

Figure 67. Plot of [VX] vs. time for ^{31}P NMR spectra obtained for 3.9 µL VX added to 1.5 mg $Zr(OH)_4$ in 0.75 mL 0.5 M EM buffer.

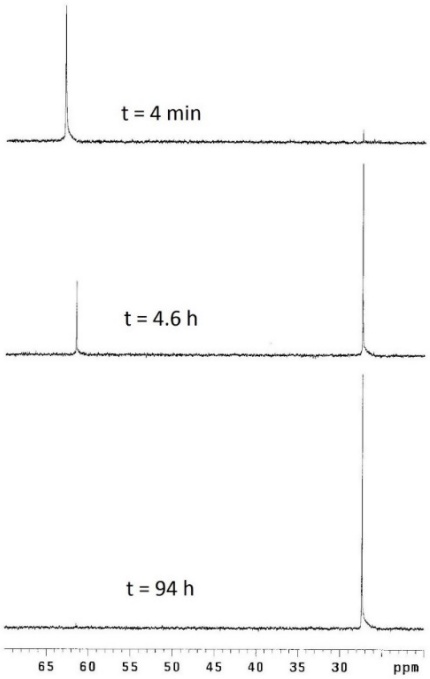

Figure 68. Select ^{31}P NMR spectra obtained for 3.9 µL VX added to 1.5 mg $Zr(OH)_4$ in 0.75 mL water.

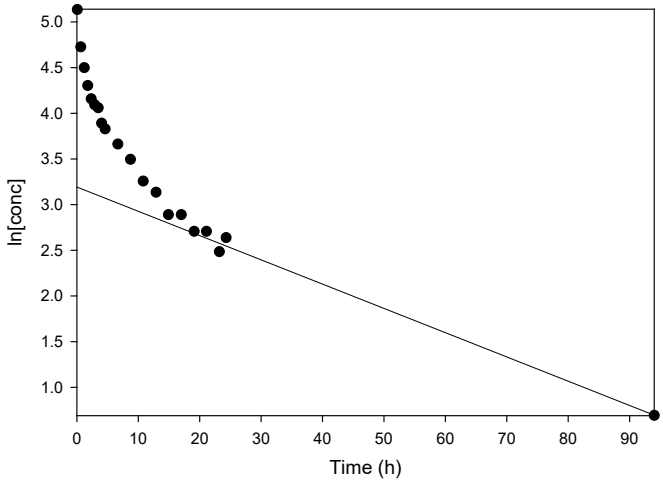

Figure 69. Plot of [VX] vs. time for ^{31}P NMR spectra obtained for 3.9 µL VX added to 1.5 mg $Zr(OH)_4$ in 0.75 mL water.

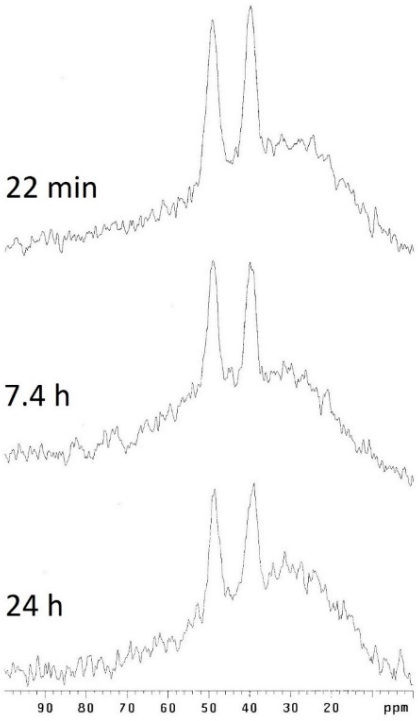

Figure 70. Select ^{13}C NMR spectra obtained for 20 µL HD added to 100 mg $Zr(OH)_4$.

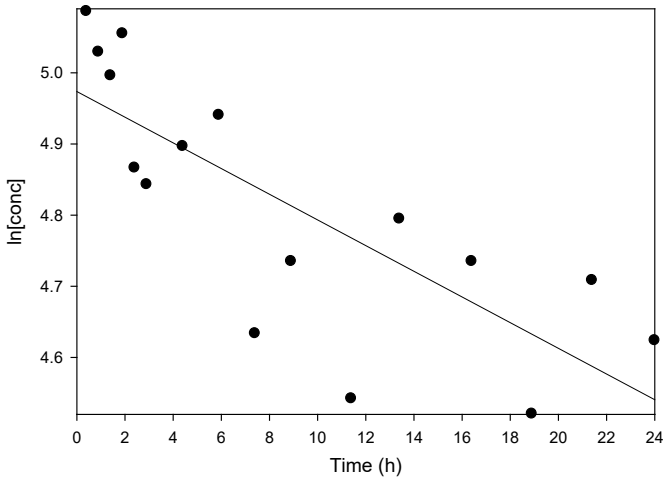

Figure 71. Plot of [HD] vs. time for ^{13}C NMR NMR spectra obtained for 20 µL HD added to 100 mg $Zr(OH)_4$.

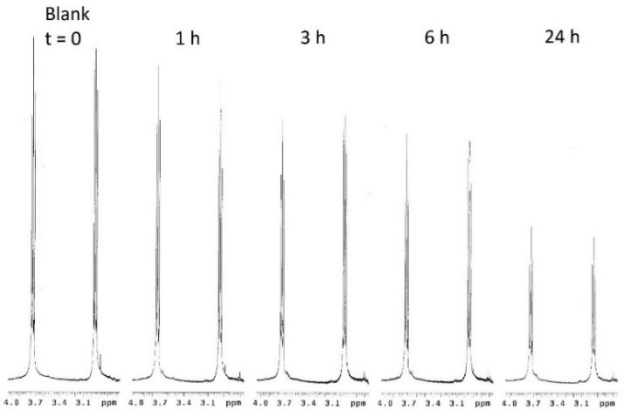

Figure 72. ^{13}C NMR spectra obtained for CH_3CN-extracts of 20 µL HD added to 100 mg $Zr(OH)_4$.

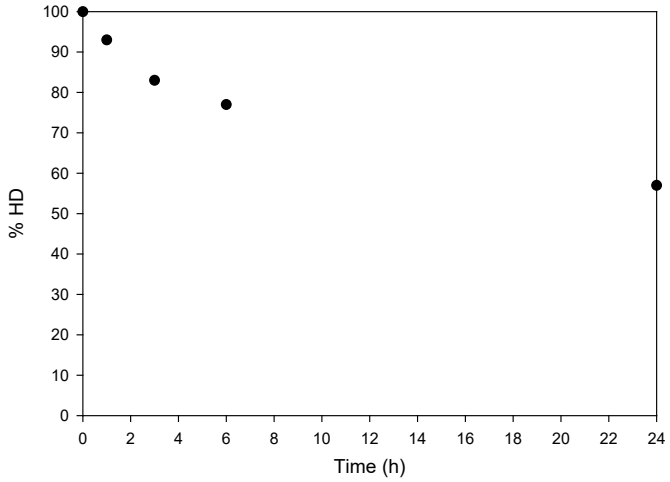

Figure 73. Plot of [HD] vs. time for ^1H NMR spectra obtained for CH_3CN-extractions of 20 µL HD added to 100 mg $Zr(OH)_4$.

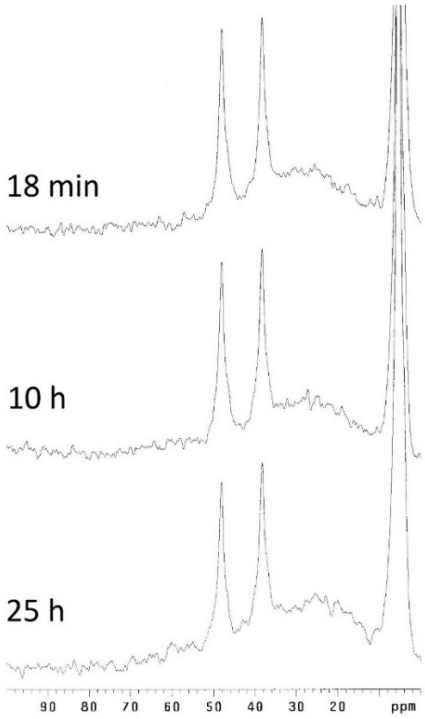

Figure 74. Select ^{13}C NMR spectra for 20 μL HD/160 μL CH_3CN added to 100 mg $Zr(OH)_4$.

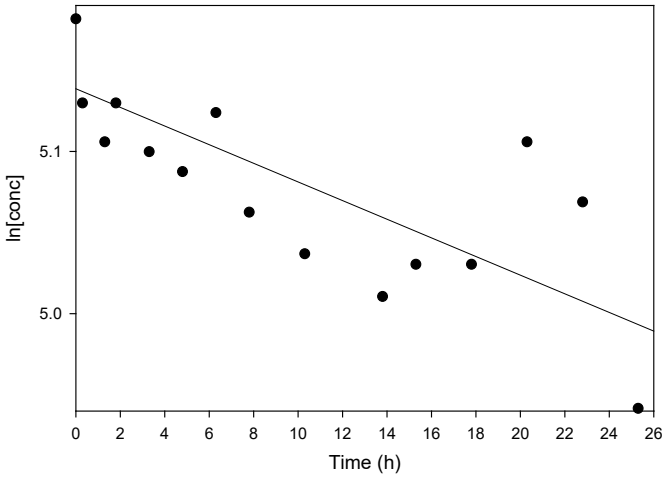

Figure 75. Plot of [HD] vs. time for ^{13}C NMR spectra obtained for 20 μL HD/160 μL CH_3CN added to 100 mg $Zr(OH)_4$.

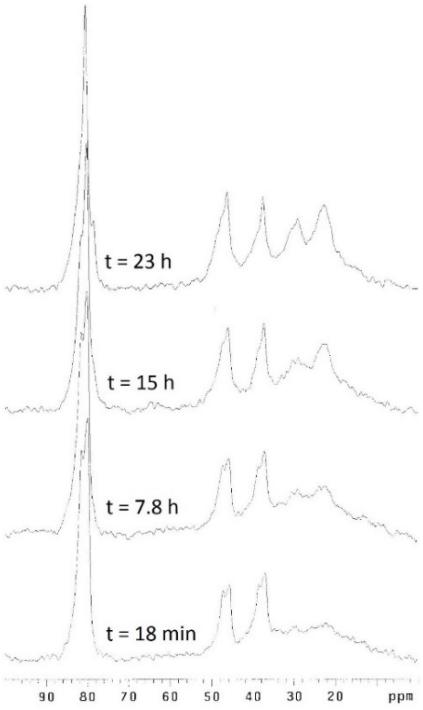

Figure 76. Select ^{13}C NMR spectra obtained for 20 μL HD/160 μL $CHCl_3$ added to 100 mg $Zr(OH)_4$.

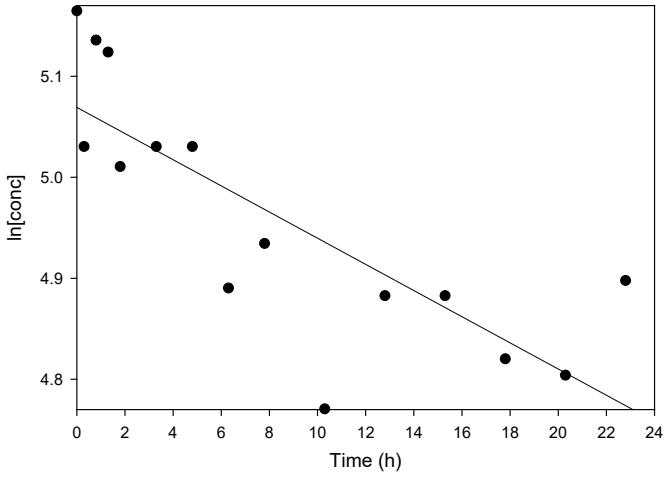

Figure 77. Plot of [HD] vs. time for ^{13}C NMR NMR spectra obtained for 20 μL HD/160 μL $CHCl_3$ added to 100 mg $Zr(OH)_4$.

Table 6. Reactions of GD, VX, and HD with $Zr(OH)_4$

Chemical and Conditions	Perfomance with $Zr(OH)_4$	Performance with buffer only
GD, pH 10 EM Buffer	$t_{1/2}$ = 14 min	$t_{1/2}$ = 26 min
VX, pH 10 EM Buffer	$t_{1/2}$ = 2.2 h	$t_{1/2}$ = 1.7 days
VX, Neutral Water	Final $t_{1/2}$ = 1.1 days	-
HD, Neat	$t_{1/2}$ = 1.6 days	-
HD, Neat, Extracted with CH_3CN	57 % remaining @ 24 h[a]	-
HD in CH_3CN	$t_{1/2}$ = 5.0 days	-
HD in $CHCl_3$	$t_{1/2}$ = 2.3 days	-

[a] ln plot not linear; % remaining after 24 h given.

Some catalysis by $Zr(OH)_4$ is observed for GD in pH 10 EM buffer as its half-life is shorter in the presence of $Zr(OH)_4$ (14 min) compared to buffer alone (26 min). GD is hydrolyzed to non-toxic PMPA, as noted above for P25 TiO_2 (Section 6.1.6, Figure 41(top)). VX hydrolysis is also catalyzed by $Zr(OH)_4$ in the presence of pH 10 EM buffer. Furthermore, with the presence of $Zr(OH)_4$ in the buffer, toxic EA 2192 is not formed; only non-toxic EMPA hydrolysis product is present. The slow hydrolysis of VX in the presence of $Zr(OH)_4$ in neutral water also avoids forming toxic EA 2192, with only non-toxic EMPA being observed. Unlike P25 titania, which allows toxic EA 2192 to form but subsequently hydrolyzes it to non-toxic MPA, $Zr(OH)_4$ prevents formation of toxic EA 2192 in the first place (if EA 2192 were formed and subsequently hydrolyzed, MPA would be formed; MPA is not detected as in the case of P25 titania).

Regarding HD, 20 μL neat HD added to 100 mg $Zr(OH)_4$ exhibited a half-life of 1.6 days. The previously characterized[2] reaction of HD with $Zr(OH)_4$ is shown in Figure 78. For extraction experiments done on a series of samples similarly containing 20 μL HD on 100 mg $Zr(OH)_4$ first order behavior was not observed – precluding calculation of a half-life – but 57% HD remained after 24 h, i.e. nearly half the HD reacted in one day, consistent with the 1.6-h half-life observed for the above in situ sample. For 20 μL HD in 160 μL CH_3CN in contact with 100 mg $Zr(OH)_4$ the observed half-life was longer at 5 h. When $CHCl_3$ solvent was used – 20 μL HD in 160 μL $CHCl_3$ – a shorter half-life of 2.3 days was observed.

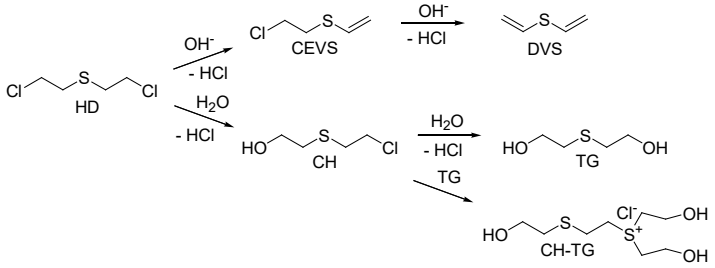

Figure 78. HD Reaction with $Zr(OH)_4$

For the $CHCl_3$ solvent, the extra peaks emerging over time in the 13C NMR spectrum are due to $CHCl_3$ (but not CH_3CN) apparently extracting EtOH from the plastic microcentrifuge tube used to contain the sample. This extraction was confirmed by adding $CHCl_3$ itself to a microcentrifuge tube, as shown in Figure 80, where the extracted EtOH – and $CHCl_3$ as well – yielded doublet peaks ($CHCl_3$: 80.1, 79.2 ppm; EtOH CH_2 group: 48.8, 48.0 ppm; EtOH CH_3 group: 29.7, 23.6 ppm). Decanting the $CHCl_3$/EtOH extract from the microcentrifuge tube into a fresh NMR tube yielded the normal, single peaks for EtOH (and

$CHCl_3$) in both ^{1}H and ^{13}C NMR spectra. The presence of EtOH in the extract was confirmed by spiking with authentic EtOH.

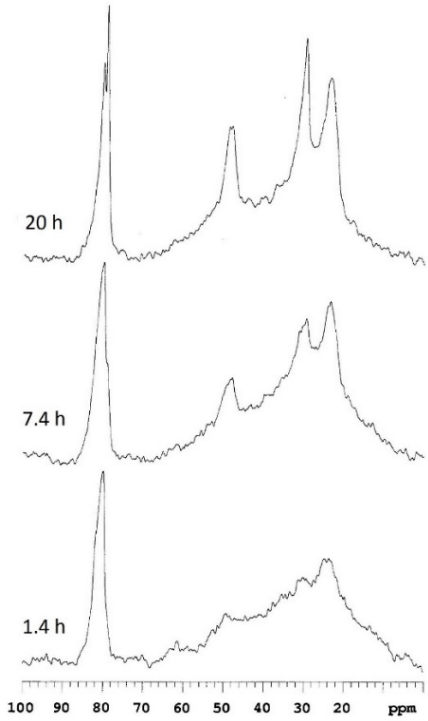

Figure 79. Select ^{13}C NMR spectra obtained for 180 µL $CHCl_3$ added to microcentrifuge tube (see text).

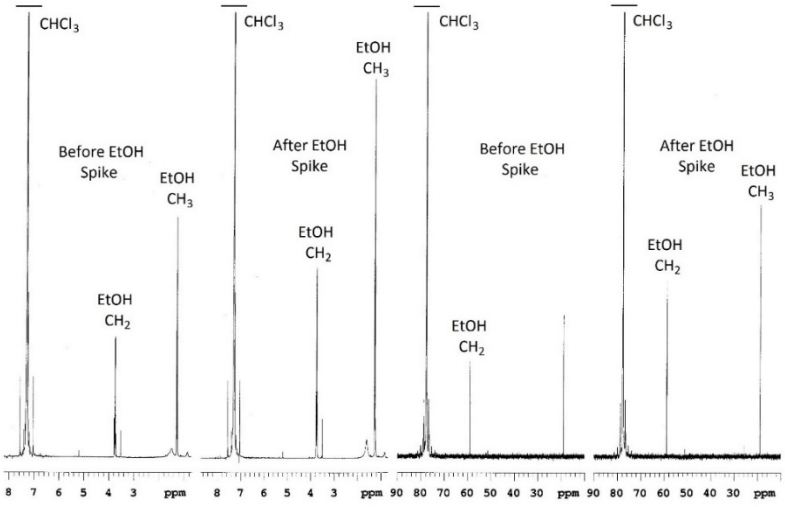

Figure 80. ^{1}H (left) and ^{13}C (right) NMR spectra obtained for the $CHCl_3$ extract of the microcentrifuge tube. EtOH presence was confirmed by spiking with authentic EtOH.

5.2.7 DRIFTS

The DRIFTS spectra of CEES on $Zr(OH)_4$ is shown in Figure 81. Losses at 3680 cm^{-1}, 2940 cm^{-1}, 2890 cm^{-1}, 1430 cm^{-1}, 1260 cm^{-1}, 1230 cm^{-1}, 1200 cm^{-1}, and 690 cm^{-1} are assigned to Zr-OH stretching modes, CH_2 stretching modes, CH_2 stretching modes, in-plane CH_3 bending modes, out-of-plane CH_2 bending (wagging) modes, out-of-plane CH_2 bending (wagging) modes, out-of-plane S-CH_2 bending (wagging) modes, and C-Cl stretching modes, respectively.

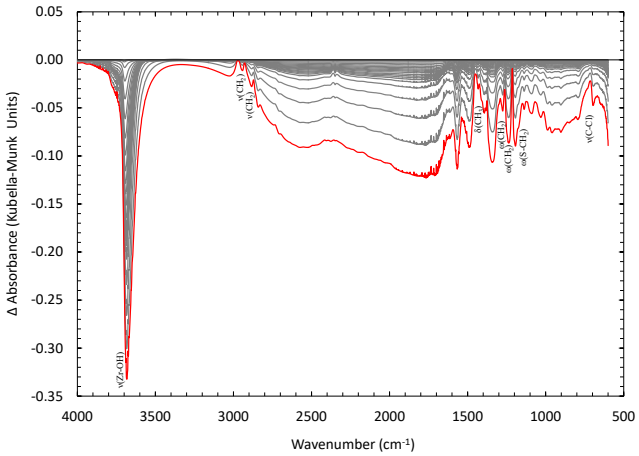

Figure 81. DRIFTS spectra of CEES on $Zr(OH)_4$

The DRIFTS spectra of HD on $Zr(OH)_4$ is shown in Figure 82. Losses at 3670 cm^{-1}, 2090 cm^{-1}, 2850 cm^{-1}, and 1330 cm^{-1} are attributed to Zr-OH stretching modes, CH_2 stretching modes, CH_2 stretching modes, and out-of-plane CH_2 bending (wagging) modes, respectively. The increasing peak at 1190 cm^{-1} is assigned to both in-plane $S(CH_2)$ bending modes and in-plane $Cl(CH_2)$ bending modes.

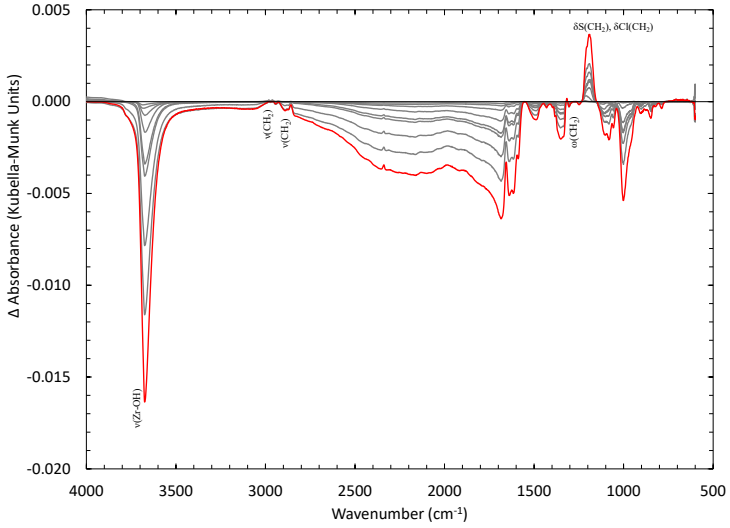

Figure 82. DRIFTS spectra of HD on $Zr(OH)_4$

The DRIFTS spectra was collected for DMMP on $Zr(OH)_4$ and is shown in Figure 83. Adsorption of DMMP on $ZrOH_4$ in the IR spectra shows a loss in the isolated OH band indicating one adsorption site. Adsorption of DMMP can be seen by the increase and redshift in the P=O band down to 1200 cm^{-1}. The DMMP molecule looks to also decompose as peaks can be seen for isolated methoxy groups as well as formate (-OOCH), formaldehyde ($-OCH_2$) and carbonate ($-CO_3$) bands.

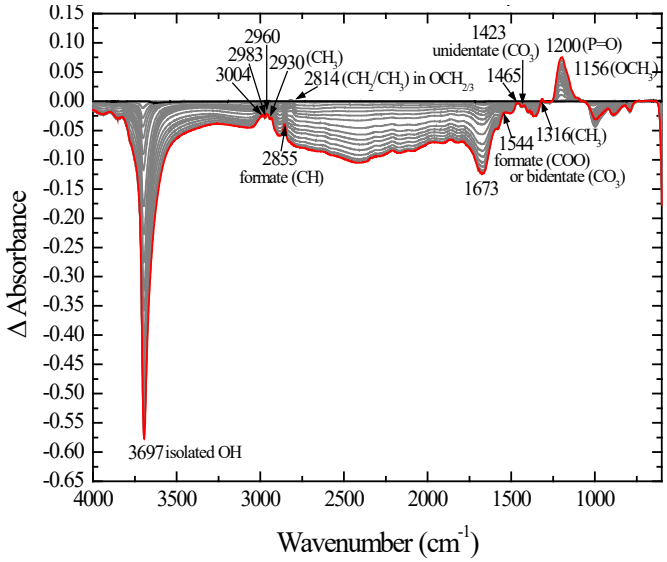

Figure 83. DRIFTS spectra of DMMP on $Zr(OH)_4$

The DRIFTS spectra of DFP on Zr(OH)4 is shown in Figure 84. Losses at 3680 cm^{-1}, 3610 cm^{-1}, and 1610 cm^{-1} are attributed to Zr-OH stretching modes, H_2O stretching modes, and in-plane H_2O bending modes, respectively. Increasing peaks at 2940 cm^{-1}, 2870 cm^{-1}, 1410 cm^{-1}, 1290 cm^{-1}, and 1030 cm^{-1} are assigned to CH_3 stretching modes, CH stretching modes, in-plane CH_3 bending modes, P=O stretching modes, and C-O stretching modes, respectively.

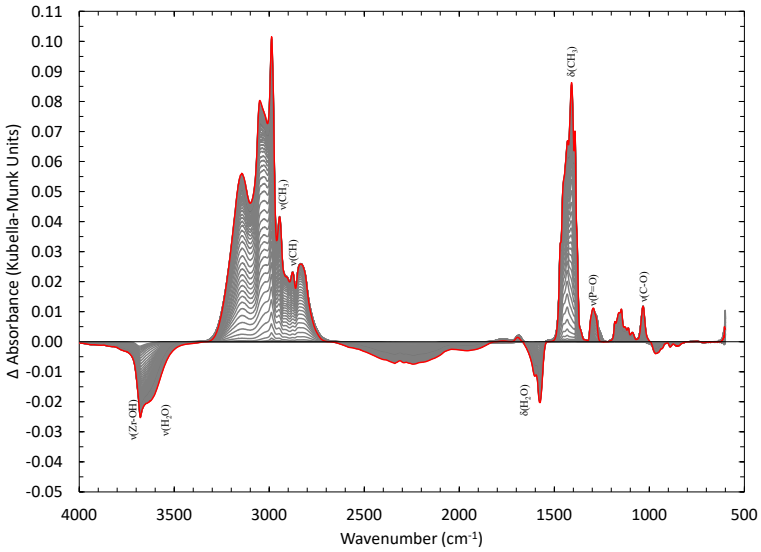

Figure 84. DRIFTS spectra of DFP on $Zr(OH)_4$

The DRIFTS spectra of DMCP on $Zr(OH)_4$ is shown in Figure 85. The loss at 3660 cm^{-1} is attributed to Zr-OH stretching modes. Increasing peaks at 1450 cm^{-1}, 1300 cm^{-1}, and 1210 cm^{-1} are assigned to in-plane CH_3 bending modes, in-plane P-CH_3 bending modes, and P=O stretching modes, respectively.

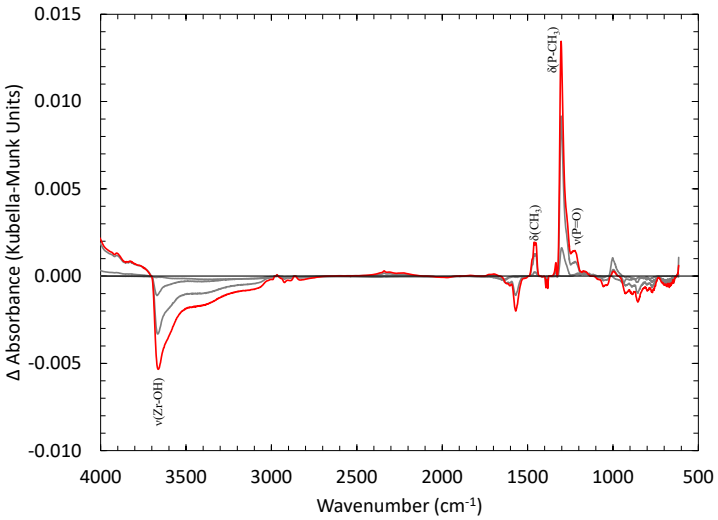

Figure 85. DRIFTS spectra of DMCP on $Zr(OH)_4$

The DRIFTS spectra of dry GB on $Zr(OH)_4$ is shown in Figure 86. Losses at 3700 cm^{-1}, 2960 cm^{-1}, and 1440 cm^{-1} are attributed to Zr-OH stretching modes, CH_3 stretching modes, and in-plane CH_3 bending modes, respectively. Increasing peaks at 1380 cm^{-1} and 1200 cm^{-1} are assigned to in-plane CH_3 bending modes and P=O stretching modes, respectively.

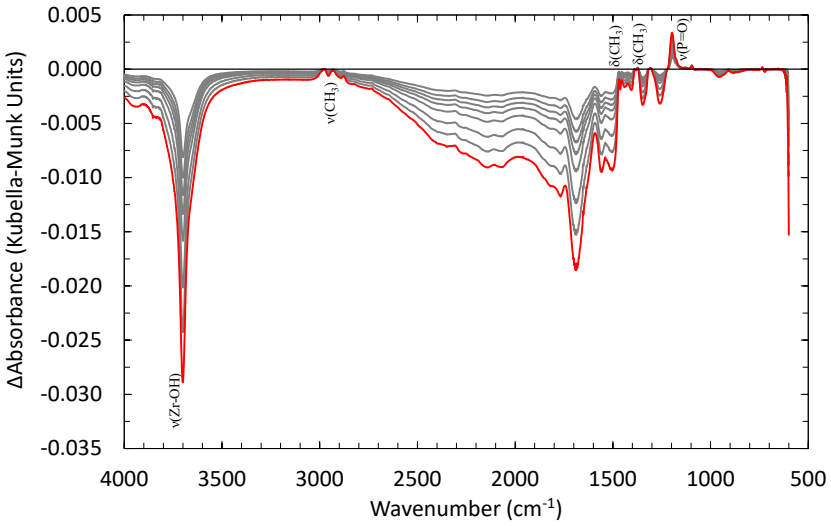

Figure 86. DRIFTS spectra of dry GB on $Zr(OH)_4$

The DRIFTS spectra of wet GB on $Zr(OH)_4$ is shown in Figure 87. Losses at 3700 cm^{-1}, 2950 cm^{-1}, 1410 cm^{-1}, and 1400 cm^{-1} are attributed to Zr-OH stretching modes, CH_3 stretching modes, in-plane CH_3 bending modes, and in-plane CH_3 bending modes, respectively. The increasing peak at 1210 cm^{-1} is assigned to P=O stretching modes.

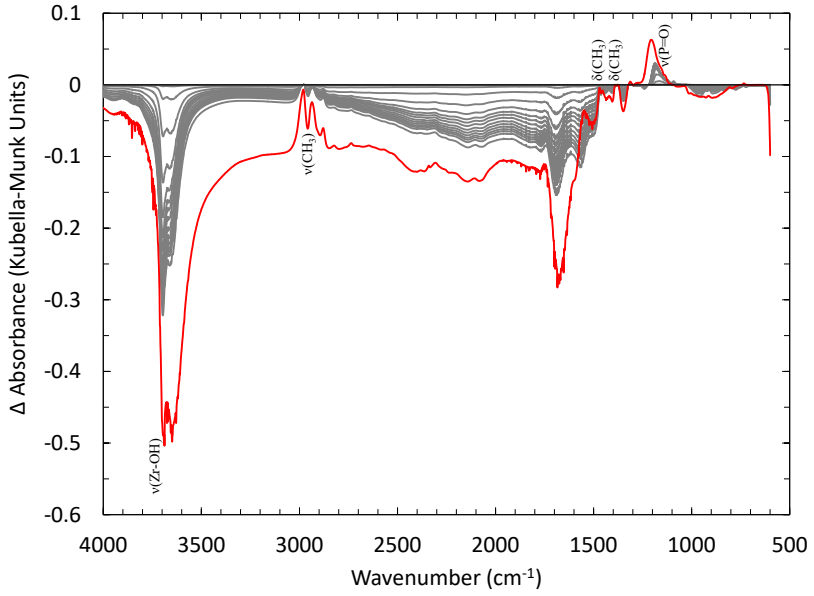

Figure 87. DRIFTS spectra of wet GB on $Zr(OH)_4$

The DRIFTS spectra of malathion on $Zr(OH)_4$ is shown in Figure 88. Losses at 3690 cm^{-1}, 2950 cm^{-1}, and 1670 cm^{-1} are attributed to Zr-OH stretching modes, both CH_3 and CH_2 stretching modes, and C=O stretching modes, respectively. The increasing peak at 1190 cm^{-1} is assigned to both P=S stretching modes and P-S modes, respectively.

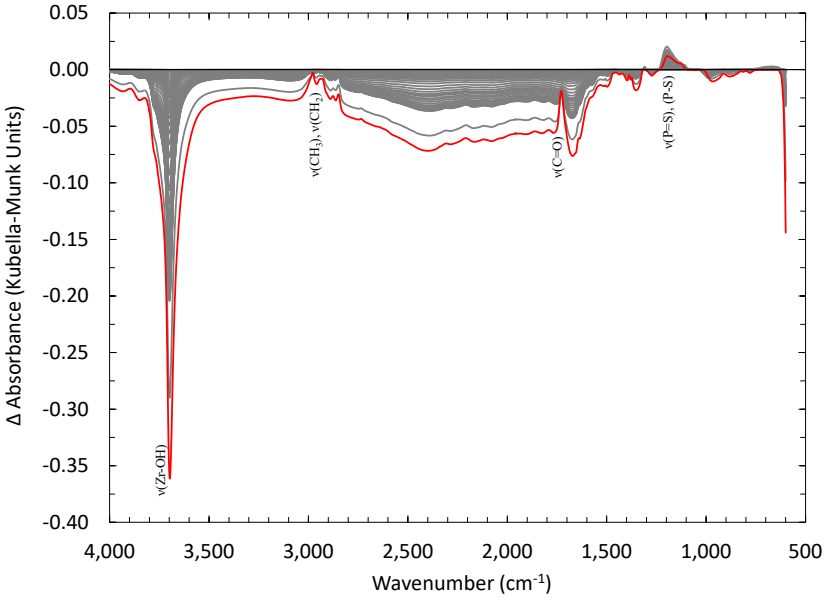

Figure 88. DRIFTS spectra of malathion on $Zr(OH)_4$

The DRIFTS spectra of VX on $Zr(OH)_4$ is shown in Figure 89. Losses at 3700 cm^{-1} and 2910 cm^{-1} are assigned to Zr-OH stretching modes and C-H stretching modes, respectively.

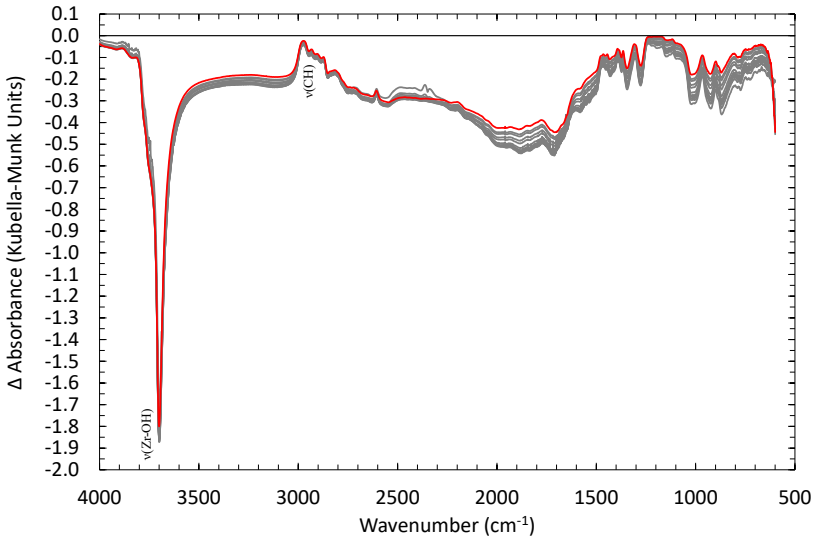

Figure 89. DRIFTS spectra of VX on $Zr(OH)_4$

5.3 FERRIHYDRITE AND GOETHITE

Iron oxides were analyzed in this effort due to their unique reaction chemistry shown in literature, as they are the only metal oxide family that has demonstrated capability to cleave the P-C bond in organophosphonates[45], demonstrating this ability with DMMP specifically. Two principal and relatively abundant analogues were investigated within this metal oxide family: ferrihydrite and goethite. Ferrihydrite ($Fe_5O_3(OH)_9$) has shown an excellent ability to adsorb toxic chemicals containing reduced As[46, 47] or P[48, 49] and performs well as an oxidizing agent on compounds containing sulfur[50]. Its reported band gap has ranged from 1.0 to 3.5 eV in literature[9], giving it excellent potential as a visible light photocatalyst. Goethite (FeO(OH)) is a much more ordered Fe^{+2} oxidation state oxide structure consisting of a hexagonally-close-packed array of O^{-2} and OH^- anions, depicted in Figure 90.

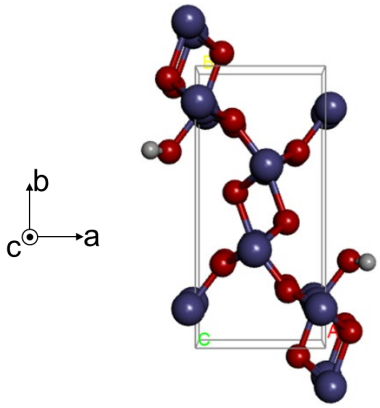

Figure 90. Unit cell of goethite

5.3.1 PHYSICAL PROPERTIES

The XRD patterns of ferrihydrite and goethite are shown in Figure xx. Ferrihydrite diffraction patterns typically consist of 2 to 6 broad peaks[51], with the most common types being referred to as "two-line" and "six-line" ferrihydrite, and the profile in Figure xx suggests the 6-line ferrihydrite is utilized, with modest but distinct peaks at 2-theta values of 36, 39, 45, 55, 61, and 63 degrees corresponding to the (110), (112), (113), (114), (115), and (300) surfaces of ferrihydrite, respectively[52]. Conversely, goethite has a highly ordered crystalline structure of sharp and narrow peaks, with the miller indices of its XRD peaks identified[53] in Figure 91. Peaks at 2-theta values of 20, 30, and 58 degrees are assigned to impurities in the sample.

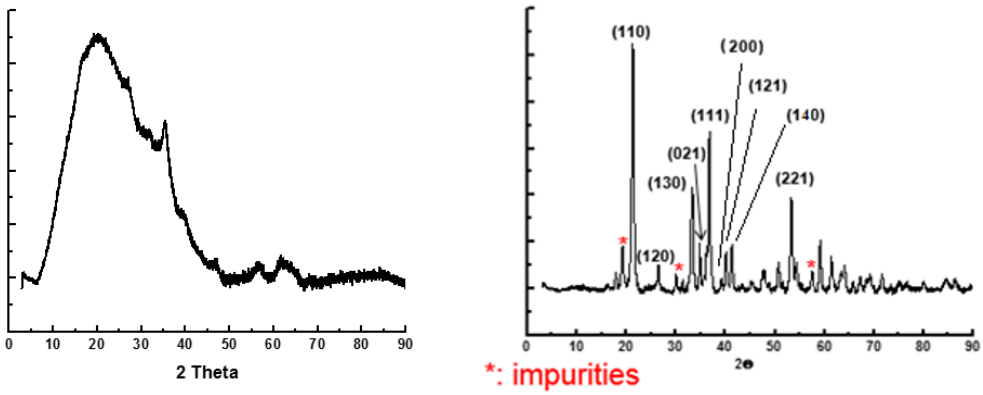

Figure 91. XRD patterns of ferrihydrite (left) and goethite (right)

The SEM images of ferrihydrite and goethite are depicted in Figure 92. Ferrihydrite is composed of densely packed spherical agglomerates consisting of submicron-sized particles, consistent with observations from previous studies[54]. In contrast, goethite crystals are needle-shaped and elongated along the crystallographic c-axis direction[3], as consistent with this effort.

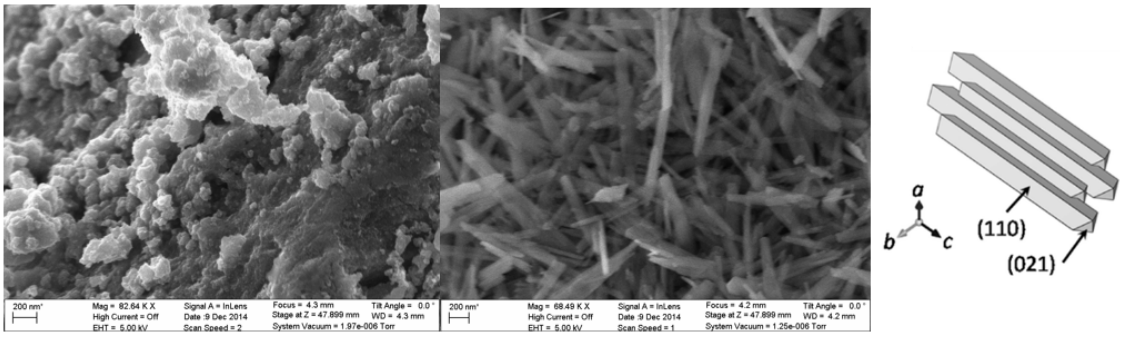

Figure 92. SEM of ferrihydrite (left) and goethite (middle),
with goethite crystal structure on right[3]

TGA and DSC profiles of ferrihydrite and goethite are depicted in Figure 93. Ferrihydrite exhibits most of its mass loss by 100 C, suggesting loss of bulk water and surface hydroxyl groups. The goethite TGA curve is more complex, however, with a mass loss of 2.5 wt.% at temperatures from 25°C to 200°C and a mass loss of 12.0 wt.% at temperatures from 200°C to 300°C, thought to be caused by the desorption of physically and chemically adsorbed water, respectively. One apparent endothermic peak (at 265.8°C) is observed in the heating process. This peak corresponds to goethite dehydration being hindered by the formation of hematite[55].

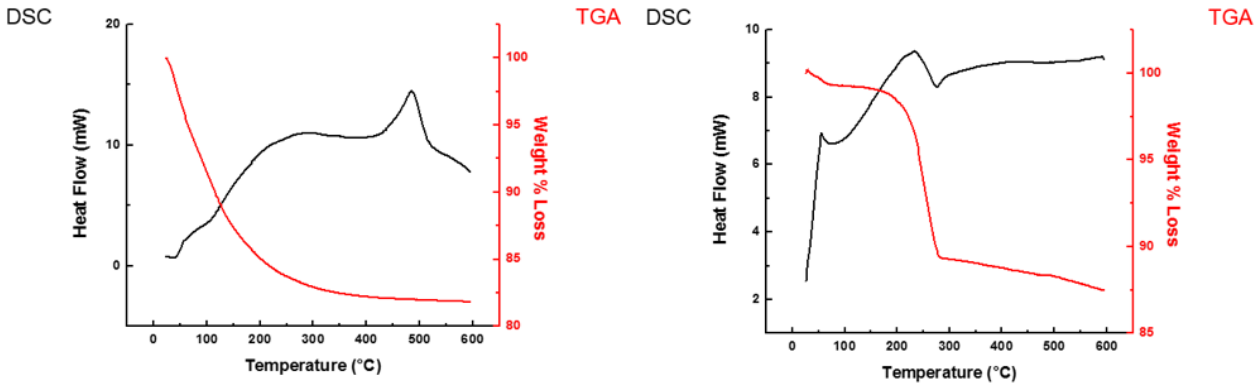

Figure 93. TGA and DSC profiles of ferrihydrite (left) and goethite (right)

5.3.2 SURFACE PROPERTIES

FTIR spectra of ferrihydrite and goethite are depicted in Figure 94. The FTIR spectra of ferrihydrite is dominated by broad –OH stretches from structural hydroxide around 3300 cm^{-1}. Other major peaks include the deformation mode of absorbed H_2O at 1630 cm^{-1}, assymetric and symmetric v3C-O stretching modes of absorbed atmospheric carbonate at 1475 cm^{-1} and 1345 cm^{-1}, respectively, C-O symmetric stretching modes at 1000 cm^{-1}, and Fe-O lattice stretching modes at 700 and 570 cm^{-1} [56]. Goethite also has a prominent, but much narrower, -OH stretching peak at 3150 cm^{-1}. Other prominent peaks include in-plane and out-of-plane Fe-O-OH bending modes at 890 cm^{-1} and 790 cm^{-1}, respectively, and Fe-O stretching modes of lattice FeO_6 around 640 cm^{-1}. There are three minor peaks which are attributed to a triplet of hydroxyl bending modes in the 1600-1800 cm^{-1} region[57, 58].

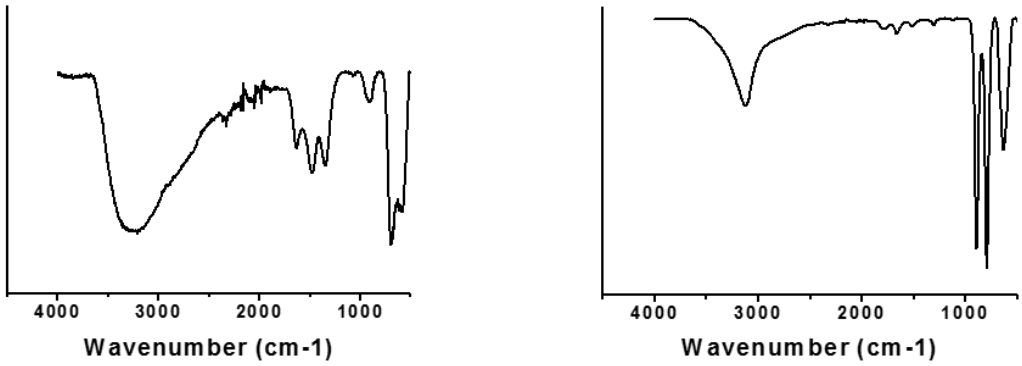

Figure 94. FTIR spectra of ferrihydrite (left) and goethite (right)

Raman spectra of ferrihydrite and goethite are depicted in Figure 95. The ferrihydrite sample showed raman peaks around 300, 500, 700, and 1300 cm^{-1}, which is consistent with literature data[59]. The three low wavenumber peaks are related to Fe-O stretching modes; specifically, there are 6 Fe-O modes in an isolated $Fe(O,OH)_6$ octahedron found in ferrihydrite, named v_1 through v_6, and it is the v_4, v_2, and v_1 modes that are postulated to correspond to the peaks at 300, 500, and 700 cm^{-1}, respectively[59]. The peak around 1300 cm^{-1} has been attributed to magnetically-ordered iron oxide analogues, such as maghemite or hematite impurities in the sample. For hematite, the strong peak at 1300 cm^{-1} has been attributed to two-

magnon scatterning resulting from the interaction of two magnons associated with proximate antiparallel spin sites. These bands are not observed in goethite, however.

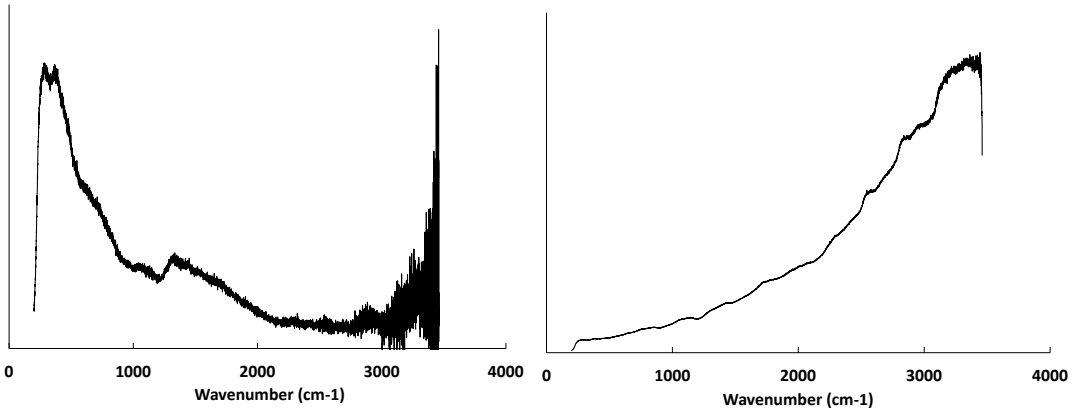

Figure 95. Raman spectra of ferrihydrite (left) and goethite (right)

5.3.3 ELECTRONIC AND OPTICAL PROPERTIES

UV-vis spectra of baseline ferrihydrite and goethite are depicted in Figure 96, and spectra of simulant-exposed ferrihydrite and goethite are depicted in Figure 98. The ferrihydrite UV-vis spectra showed high absorption over the entire visible and ultraviolet light region in a profile consistent with observations in literature[60, 61]. The positions of the minima of the second-derivative plot of the UV-vis absorbance values versus wavelength correspond to well-established crystal-field bands in iron oxides and have been identified in ferrihydrite to occur at 400 nm, 500 nm, and 700 nm, corresponding to the electron transition $^6A_1$ -> (^4E; $^4A_1$), the electron pair transition ($^6A_1$ + $^6A_1$) -> ($^4T_1$ + $^4T_1$), and the electron transition $^6A_1$ -> $^4T_2$, respectively[62].

The goethite UV-vis spectra result from three types of electronic transitions: (1) ligand field (Fe d-d) transitions, (2) interactions between magnetically coupled Fe(III) ions, and (3) O(2p) -> Fe(3d) charge transfer. For bulk goethite, the UV-vis second derivate minima have been assigned to the charge transfer $6T_{1u}$ -> $2T_{2g}$ around 250 nm , the electron transition $^6A_1$ -> (^4E; $^4A_1$) around 420 nm, the electron pair transition ($^6A_1$ + $^6A_1$) -> ($^4T_1$ + $^4T_1$) around 520 nm, and the electron transition $^6A_1$ -> $^4T_2$ around 680 nm[62, 63]. Tauc plots for ferrihydrite and goethite are shown in Figure 97. Calculated band gaps were 1.55 eV for ferrihydrite, comparing well with literature values ranging from 1.0 to 3.5 eV[9], and 2.0 eV for goethite, slightly lower than literature values ranging from 2.1 to 2.5 eV[64]. Exposure to simulants truncated the UV-Vis signal in the visible light range for both materials but did not change alter the overall profile or shift the absorption edge, suggesting that no changes in band structure occurred.

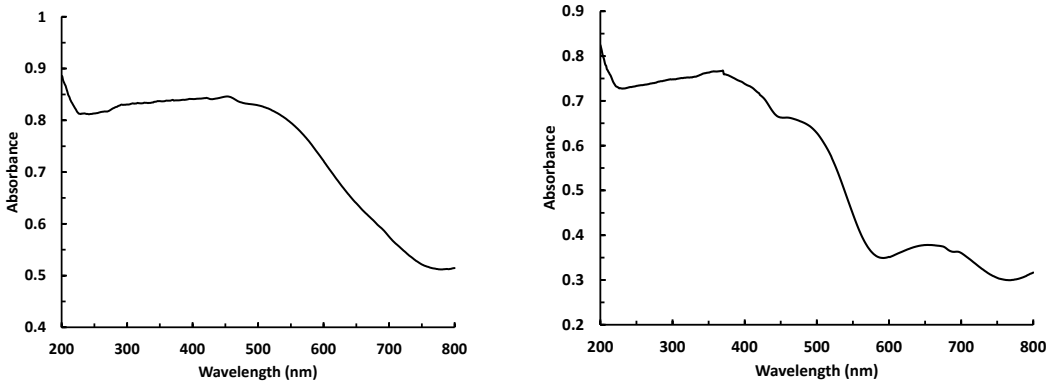

Figure 96. UV-Vis spectra of ferrihydrite (left) and goethite (right)

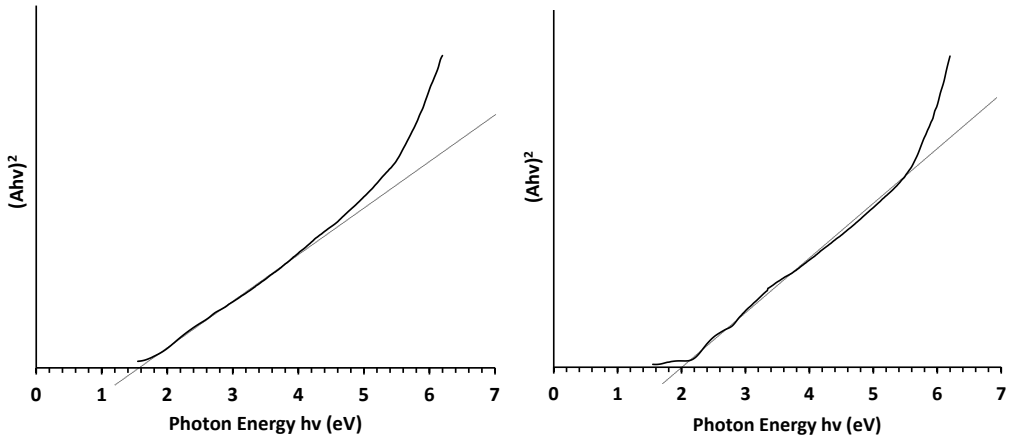

Figure 97. Tauc plots of ferrihydrite (left) and goethite (right)

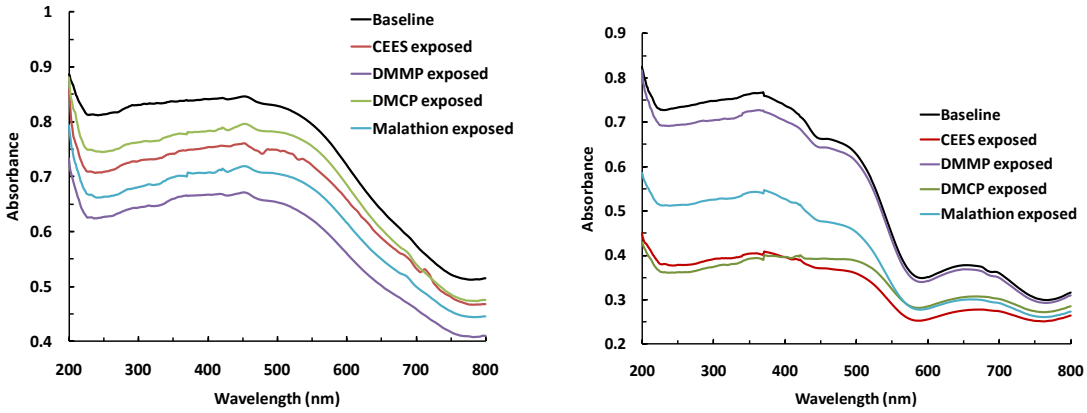

Figure 98. UV-Vis spectra of simulant-exposed ferrihydrite (left) and goethite (right)

Fluorescence spectra of baseline ferrihydrite and goethite are depicted in Figure 99, and spectra of stimulant-exposed ferrihydrite and goethite are depicted in Figure 100. Neither material exhibited any

excitation behavior in their fluorescence spectra over the visible light wavelength range, both in virgin and simulant-exposed form, which is expected as both are considered non-fluorescent.

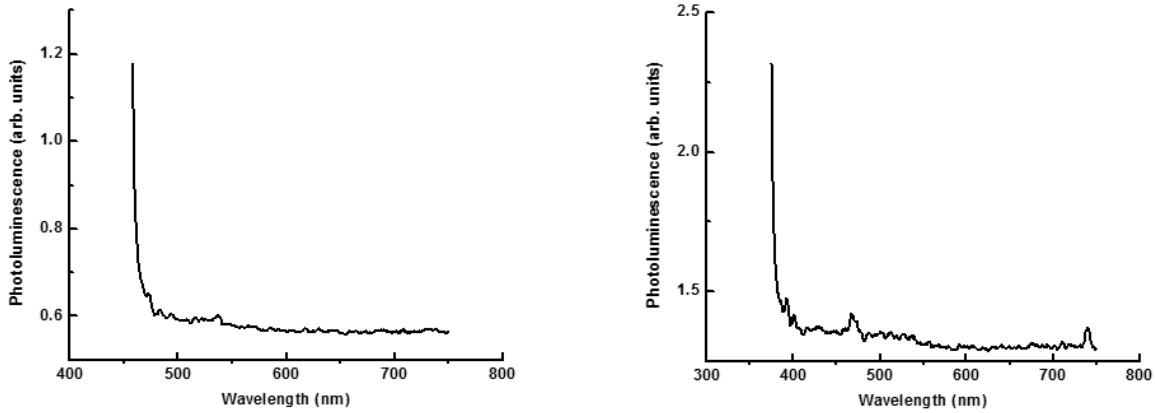

Figure 99. Fluorescence emission spectra of ferrhydrite (left) and goethite (right)

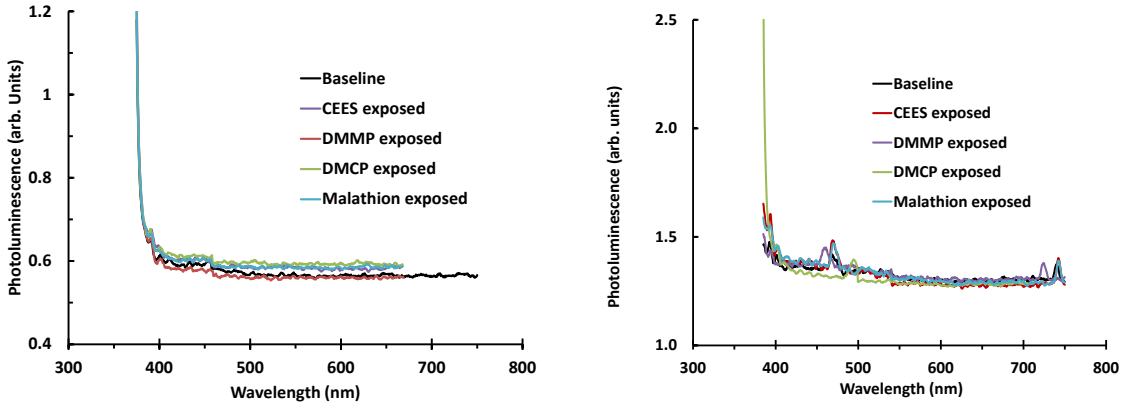

Figure 100. Fluorescence emission spectra of simulant-exposed ferrhydrite (left) and simulant-exposed goethite (right)

5.3.4 ADSORPTION AND REACTION CHARACTERIZATION

N_2 isotherms of ferrihydrite and goethite are depicted in Figure 101, and select physical properties of both materials are reported in Table 7. Both iron oxides exhibit type II isotherms with small H3 hysteresis loops. Measured surface areas are in line with literature values, as ferrihydrite has been reported between 200 and 400 m^2/g and goethite has been reported between 20 and 27 m^2/g [65].

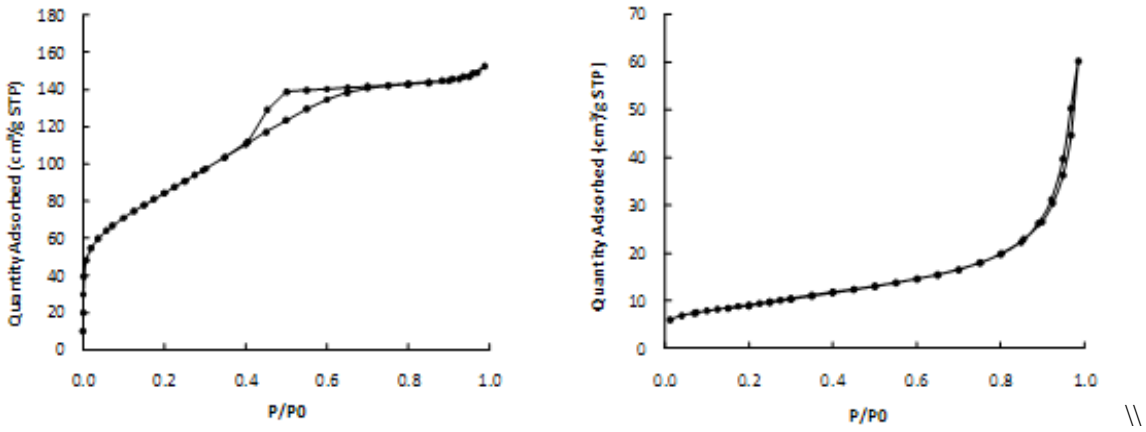

Figure 101. N_2 isotherms of ferrihydrite (left) and goethite (right)

Table 7. Physical properties of Ferrihydrite and Goethite

Material	BET SA (m^2/g)	Total PV (cc/g)	Micropore Volume (cc/g)
Ferrihydrite	297.7	0.2360	0.1092
Goethite	32.3	0.0931	0.0011

Water isotherms of ferrihydrite and goethite are depicted in Figure 102. Ferrihydrite shows moderate water uptake, likely due to its moderately high surface area and hydrogen bonding with its surface functional groups, but goethite exhibits very low ability, attributing to its very small surface area.

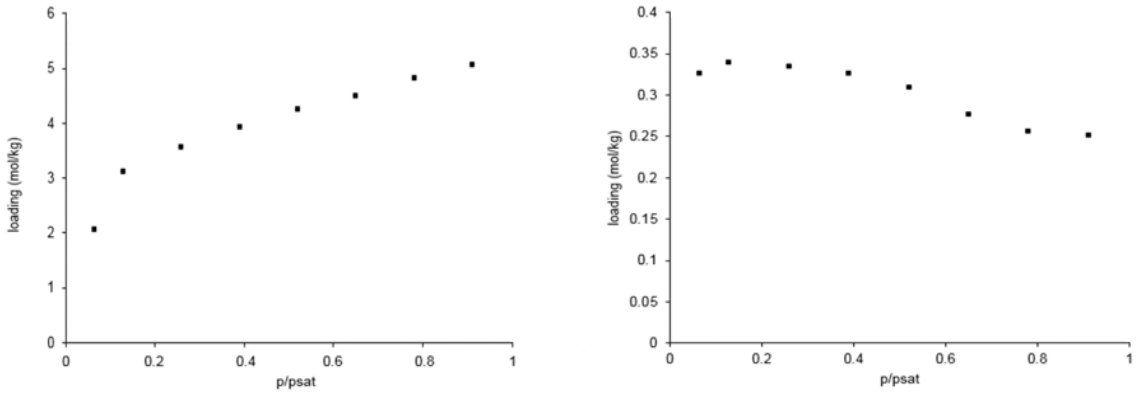

Figure 102. Water isotherms of ferrihydrite (left) and goethite (right)

The pKa distributions of ferrihydrite and goethite are depicted in Figure 103. Ferrihydrite yields three principal peaks in its pKa distribution around 7.5, 8.5, and 10.0, consistent with literature data[66]. The species around pKa of 7.5 and 8.5 have been hypothesized to correspond to the acidity constants of the protolysis reactions of the OH surface groups of ferrihydrite, and the peak at pKa of 10 has been attributed to the presence of polynuclear Fe(III) (hydroxyl) species[67]. Goethite yields two small peaks in its pKa distribution around 8.0 and 9.5, consistent with literature data for crystalline magnetite, the dehydration product of goethite[66]. These peaks have been hypothesized to correspond to the pKa values of the

dissociation constants of $FeOH^+$ in the material[66]. The calculated points of zero charge were found at a pH of 9.8 for ferrihydrite and 10.0 for goethite, slightly higher than literature values spanning from pH of 8.5 to 9.0 for both materials[29].

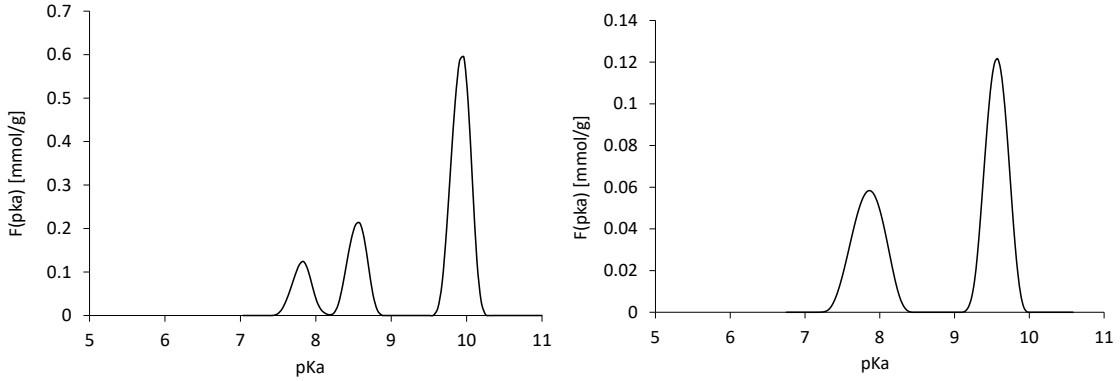

Figure 103. pKa distributions for ferrihydrite (left) and goethite (right)

5.3.5 CHEMICAL DOSE-EXTRACTION TECHNIQUE

The chemical dose-extraction removal abilities of ferrihydrite are shown in Table 8. Ferrihydrite exhibited notable removal capabilities across the spectrum of simulants and agents tested, as shown in figures X, X, and X. Its CEES and HD reactivity was among the highest measured of all materials tested, and CEES only mildly overpredicted HD. Reactivity among the G simulants progressed as DMMP < DFP < DMCP, with DFP most closely predicting GD performance and DMCP most closely predicting GB performance. Malathion greatly underpredicted VX performance.

Table 8. Dose-extraction results for ferrihydrite.

CEES		HD		DMCP		DFP		DMMP		GB		GD		Malathion		VX	
%R	SD	%R	SD	%R	SD	%R	SD	%R	SD	%R	SD	%R	SD	%R	SD	%R	SD
51.2	-	39.5	-	99.5	-	53.8	-	17.1	10.0	93.3	-	64	7.1	21.3	7.2	44	-

The chemical dose-extraction removal abilities of goethite are shown in Table 9. Goethite was much less reactive across the spectrum of simulants and agents than its ferrihydrite counterpart, as shown in figures X, X, and X. CEES and HD reactivity were both minimal, with CEES mildly overpredicting HD performance. Reactivity among the G simulants progressed as DFP < DMMP < DMCP, with DMCP most closely predicting GB reactivity and DMMP most closely predicting GD reactivity. Malathion removal greatly overpredicted VX performance.

Table 9. Dose-extraction results for goethite.

CEES		HD		DMCP		DFP		DMMP		GB		GD		Malathion		VX	
%R	SD	%R	SD	%R	SD	%R	SD	%R	SD	%R	SD	%R	SD	%R	SD	%R	SD
14.6	-	0	-	67.0	4.2	10.7	4.2	14.9	7.5	44.0	-	14.0	0.1	40.6	12.0	21.0	-

5.3.6 NMR

The reaction of DMMP with ferrihydrite was studied by ^{31}P NMR. In the first experiment, 2.5 µL DMMP was added to 25 mg ferrihydrite–either as-received or equilibrated to 50 % RH–in a 4-mL glass vial. As a control, a blank vial was also prepared containing only 2.5 µL DMMP (no ferrihydrite). The vials were allowed to stand for 1 h before extraction with 1.5 mL CH_3CN and analysis by ^{31}P NMR. The results are shown in Figure 104.

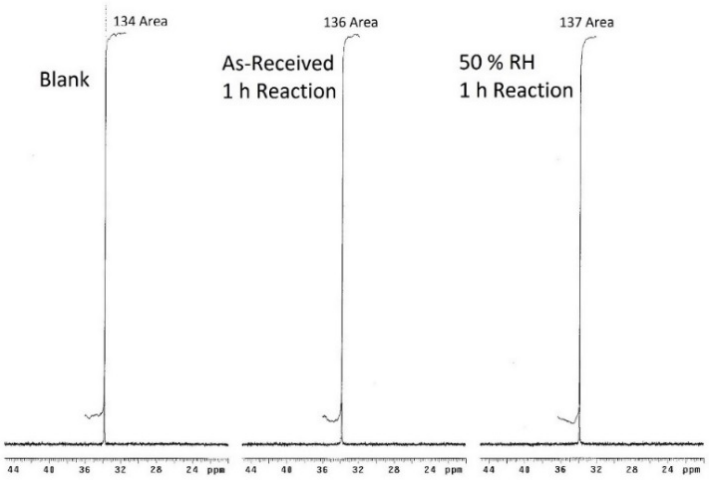

Figure 104. ^{31}P NMR spectra obtained for 2.5 µL DMMP added to 2.5 mg ferrihydrite; 1-h reaction.

Comparison of the amount of DMMP extracted from the ferrihydrite samples to the blank indicated negligible reaction occurring during the one hour period. In the hope of actually seeing product formation, a second DMMP sample prepared in an identical manner (including a blank) was allowed to stand for two months (Figure 105). Compared to the blank the CH_3CN extract exhibited a reduction in the amount of DMMP; however, no products were observed. The extracted ferrihydrite sample was allowed to air-dry to evaporate residual CH_3CN, and then extracted with 1.5 mL 0.2 N HCl (Figure 105). Besides residual DMMP a product was observed in the HCl extract. The product was subsequently identified as the hydrolysis product MMPA (Figure 106) as described below.

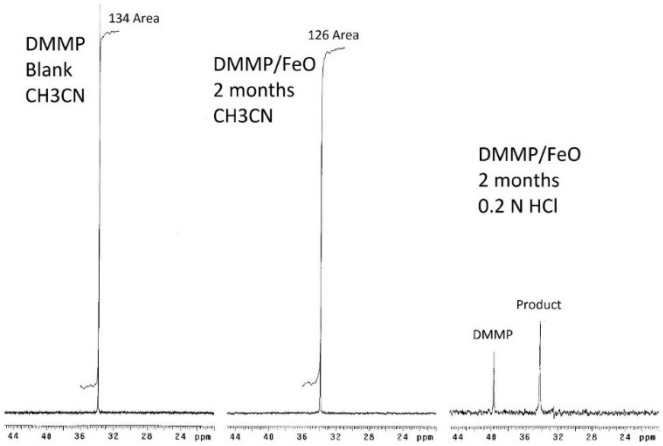

Figure 105. ^{31}P NMR spectra obtained for 2.5 µL DMMP added to 2.5 mg ferrihydrite; 2-month reaction.

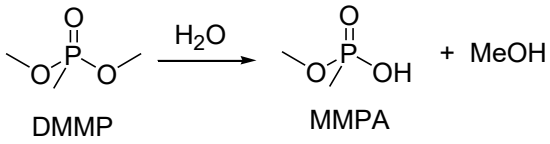

Figure 106. Hydrolysis of DMMP to MMPA

To determine whether the product was formed due to acid-hydrolysis of DMMP during the HCl extraction step, 2.5 µL DMMP was added to 0.75 mL 0.2 N HCl (Figure 107). No hydrolysis of the DMMP occurred, confirming its stability during 0.2 N HCl-extraction of the ferrihydrite.

To determine whether the product formed during the 2-month reaction on ferrihydrite was the hydrolysis product MMPA (Figure 106), authentic MMPA was first made by adding 2.5 µL DMMP to 0.75 mL 1.9 N NaOH (Figure 107). Nearly quantitative conversion of DMMP to MMPA was achieved as ^{1}H NMR detected cleaved MeOH; signals for MMPA methyl groups; and only small, residual peaks for the methyl groups of DMMP. The authentic MMPA was then used to spike the HCl extract of the 2-month DMMP/ferrihydrite reaction (Figure 108). An increase in the product peak indicated it was indeed the MMPA hydrolysis product. Thus, the reaction of DMMP with ferrihydrite occurred via hydrolysis (not oxidation).

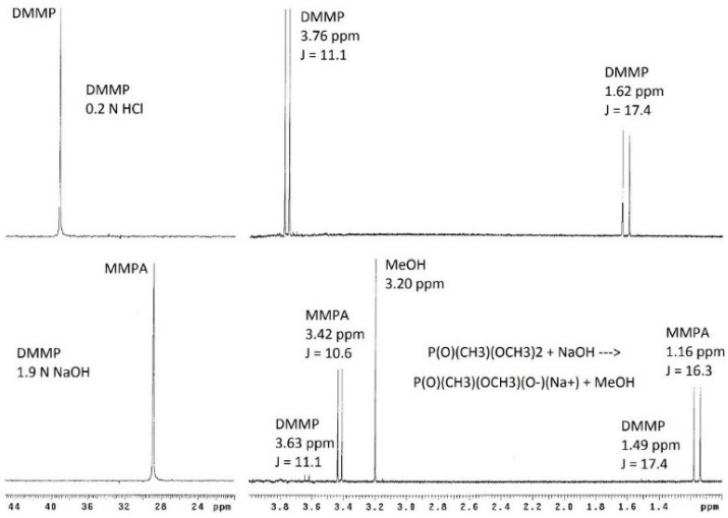

Figure 107. ^{31}P (left) and ^{1}H (right) NMR spectra obtained for 2.5 µL DMMP in 0.75 mL 0.2 N HCl (top) and 0.75 mL 1.9 N NaOH (bottom; see text).

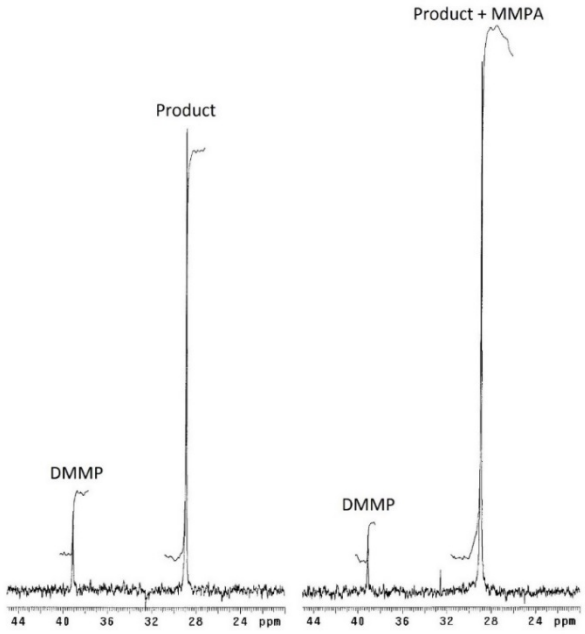

Figure 108. ^{31}P NMR spectra obtained for 0.2 N HCl extract of the 2-month DMMP/ferrihydrite reaction sample before (left) and after (right) spiking with authentic MMPA.

5.3.7 DRIFTS

The DRIFTS spectra of CEES on ferrihydrite is shown in Figure 109. Losses at 3650 cm^{-1}, 1380 cm^{-1}, 1090 cm^{-1}, and 654 cm^{-1} are attributed to Fe-OH stretching modes, in-plane CH_3 bending modes, out-of-plane S-CH_2 bending (wagging) modes, and C-Cl stretching modes, respectively. Increasing peaks at 2930 cm^{-1}, 2880 cm^{-1}, 1430 cm^{-1}, 1220 cm^{-1}, and 1210 cm^{-1} are assigned to CH_2 stretching modes, CH_2

stretching modes, in-plane CH_3 bending modes, out-of plane CH_2 bending (wagging) modes, and out-of-plane CH_2 bending (wagging) modes, respectively.

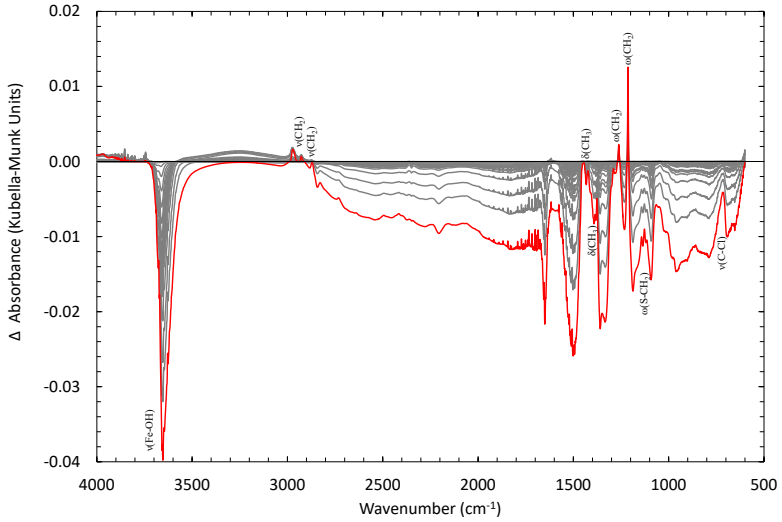

Figure 109. DRIFTS spectra of CEES on ferrihydrite

The DRIFTS spectra of HD on ferrihydrite is shown in Figure 110. Increasing peaks at 3700 cm^{-1} and 1680 cm^{-1} are attributed to Fe-OH stretching modes and in-plane H_2O bending modes, respectively.

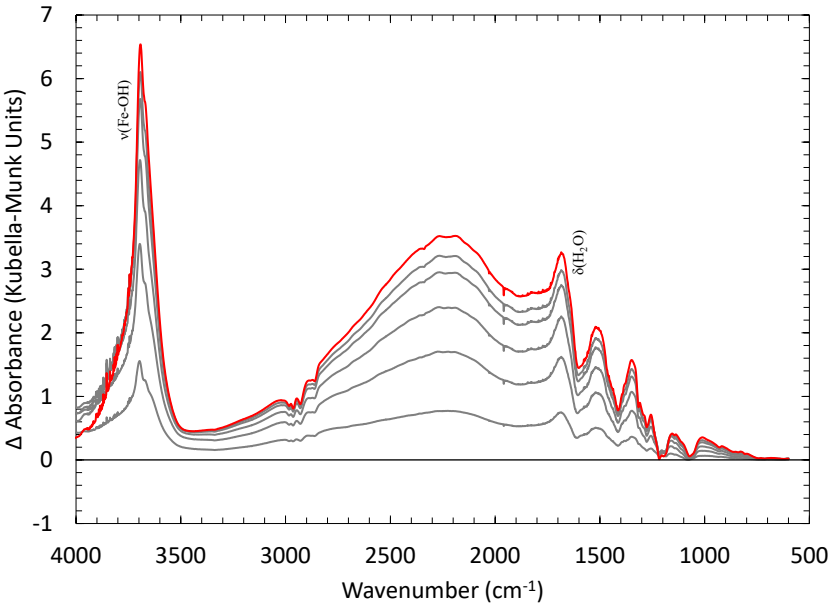

Figure 110. DRIFTS spectra of HD on ferrihydrite

The DRIFTS spectra of DMMP on ferrihydrite is shown in Figure 111. Adsorption of DMMP on FeO in the IR spectra shows losses in the isolated OH bands. Adsorption of DMMP can be seen by the increase and blueshift in the P=O band from gas phase (~1230 cm^{-1}). The adsorption site is most likely an Fe^{2+} site. In comparison with the Fe_2O_3 catalyst, the P=O band redshifts from 1269 cm^{-1} to 1255 cm^{-1} as the

Fe oxidation state decreases from +3 to +2. The DMMP molecule looks to also decompose as peaks can be seen for formate (-OOCH) bands, which most likely are formed from a $-OCH_3 \rightarrow -OCH_2 \rightarrow -OOCH$ mechanism.

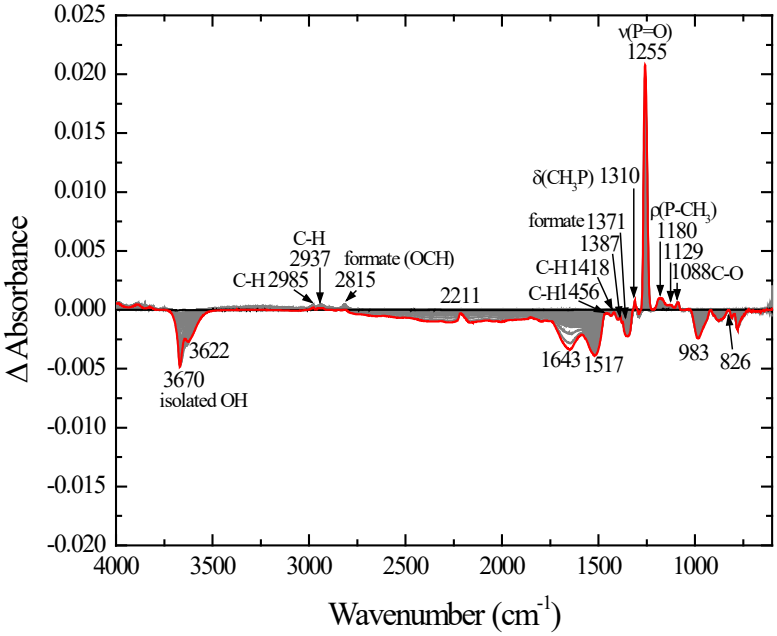

Figure 111. DRIFTS spectra of DMMP on ferrihydrite

The DRIFTS spectra of DFP on ferrihydrite is shown in Figure 112. Losses at 3650 cm^{-1} and 1400 cm^{-1} are attributed to Fe-OH stretching modes and in-plance CH_3 bending modes, respectively. Increasing peaks at 1230 cm^{-1} and 1100 cm^{-1} are assigned to P=O stretching modes and C-O stretching modes, respectively.

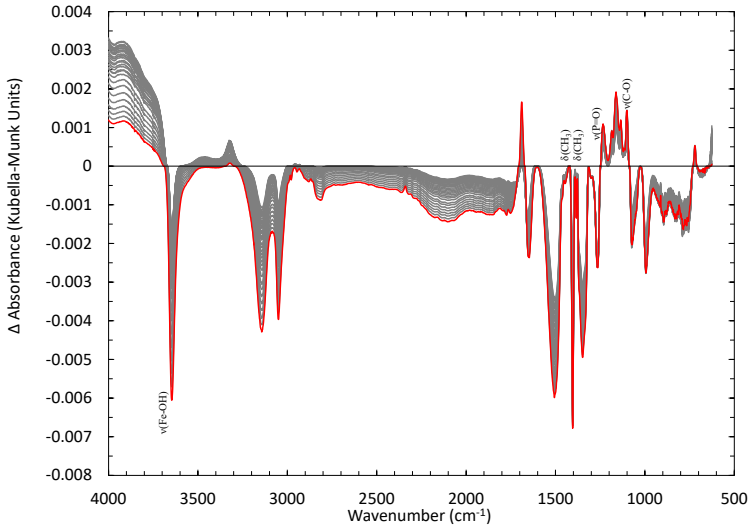

Figure 112. DRIFTS spectra of DFP on ferrihydrite

The DRIFTS spectra of DMCP on ferrihydrite is shown in Figure 113. Losses at 3550 cm^{-1} and 1610 cm^{-1} are attributed to H_2O stretching modes and in-plane H_2O bending modes, respectively. Increasing peaks at 1450 cm^{-1} and 1280 cm^{-1} are assigned to in-plane CH_3 bending modes and P=O stretching modes, respectively.

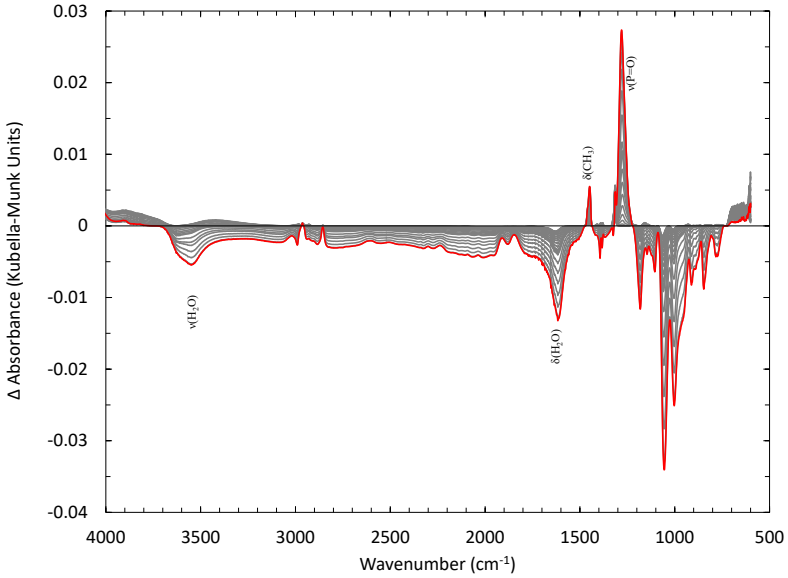

Figure 113. DRIFTS spectra of DMCP on ferrihydrite

The DRIFTS spectra of malathion on ferrihydrite is shown in Figure 114. Losses at 3690 cm^{-1}, 1650 cm^{-1}, and 1420 cm^{-1} are attributed to Fe-OH stretching modes, C=O stretching modes, and in-plane CH_3 bending modes, respectively. Increasing peaks at 2950 cm^{-1}, 1140 cm^{-1}, and 1070 cm^{-1} are assigned to both CH_3 and CH_2 stretching modes, P-S modes, and C-O stretching modes, respectively.

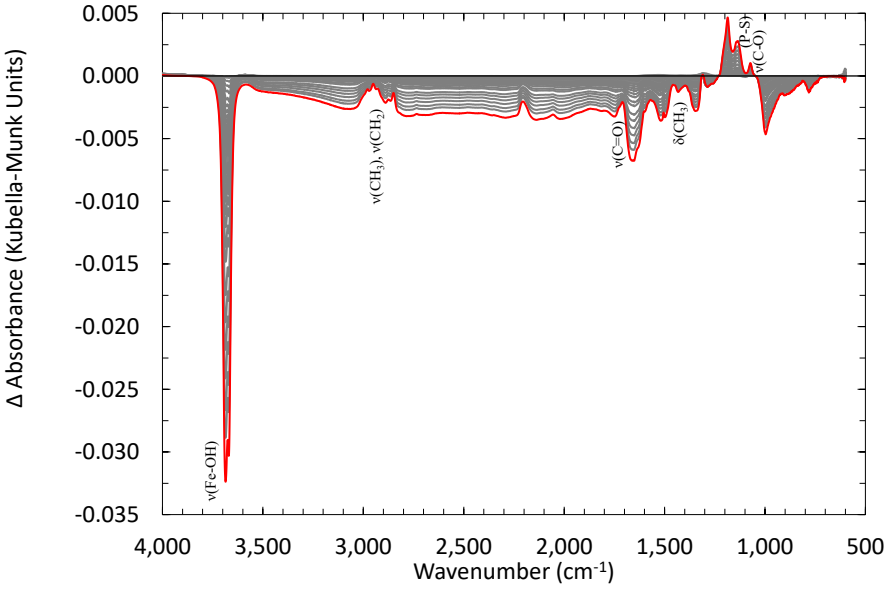

Figure 114. DRIFTS spectra of malathion on ferrihydrite

The DRIFTS spectra of DMMP on goethite is shown in Figure 115. Adsorption of DMMP on Fe_2O_3 in the IR spectra shows losses in the isolated and associated OH bands in conjunction with loss in the water bending-band. Adsorption of DMMP can be seen by the increase and blueshift in the P=O band from gas phase (~1230 cm^{-1}). The adsorption site is most likely an Fe^{3+} site. The DMMP molecule looks to also decompose as peaks can be seen for isolated methoxy groups on iron as well as formate (-OOCH) bands, which most likely are formed from $-OCH_3 \rightarrow -OCH_2 \rightarrow$ -OOCH mechanism.

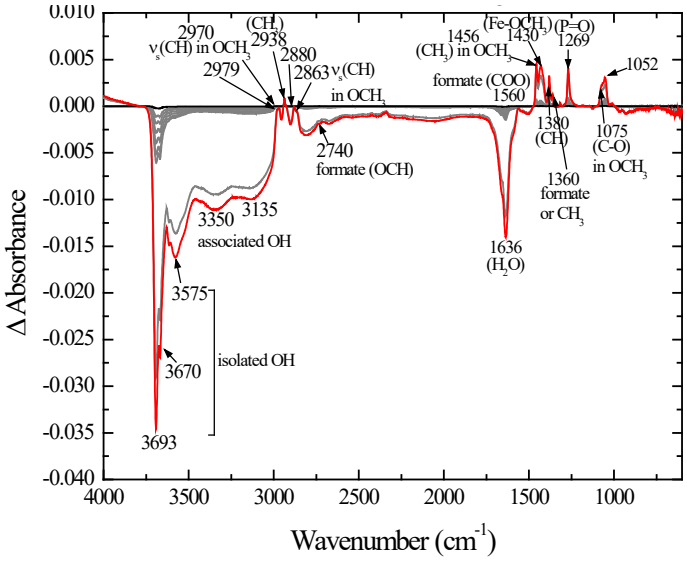

Figure 115. DRIFTS spectra of DMMP on goethite

The DRIFTS spectra of GB on goethite is shown in Figure 116. The loss at 3690 cm^{-1} is attributed to Fe-OH stretching modes. Increasing peaks at 1210 cm^{-1}, 1150 cm^{-1}, and 1060 cm^{-1} are assigned to P=O stretching modes, O-P-O stretching modes, and O-P-O stretching modes, respectively.

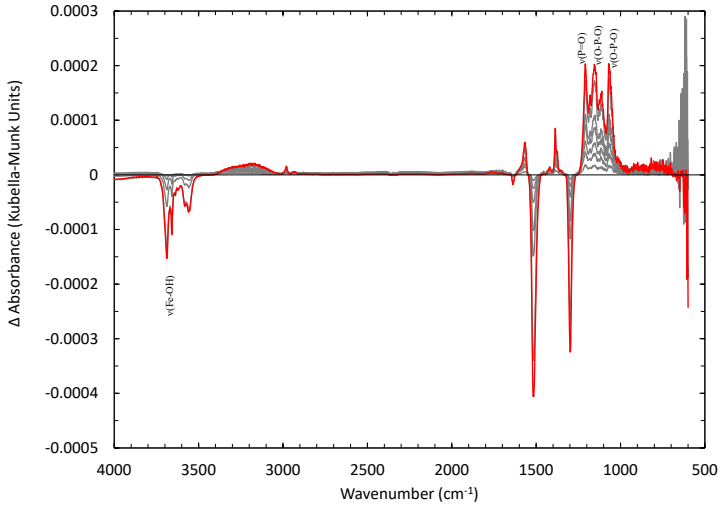

Figure 116. DRIFTS spectra of GB on goethite

5.4 UiO-66

UiO-66 is a robust metal-organic framework (MOF) that exhibits high thermal and chemical stability. UiO-66 is readily synthesized by the in situ hydrolysis of $ZrCl_4$ with a 1,4-benzenedicarboxylate linker (BDC). The inorganic secondary binding unit (SBU) is key to the inherent stability of this MOF. UiO-66 adopts a cubic framework of cationic $Zr_6O_4(OH)_4$ nodes. The triangular faces of the Zr_6-octahedron in these nodes are alternately capped by μ_3-O and μ_3-OH groups. Each of the polyhedron edges is bridged by a carboxylate (μ_2-(CO_2)) originating from the dicarboxylic acid in the organic linkers to form a $Zr_6O_4(OH)_4(CO_2)_{12}$ cluster. This structure results in each zirconium atom being bound in a square-antiprismatic geometry to eight oxygen atoms in which one face of the square antiprism is formed by oxygen atoms from the carboxylates while the second square face is formed by oxygen atoms from the μ_3-O and μ_3-OH groups. The porosity of the UiO-66 structure consists of narrow triangular windows with a free diameter close to 6 Å, octahedral cavities with a diameter of 11 Å, and tetrahedral cavities with a diameter of 8 Å[68]. In addition, UiO-66 exhibits a high BET surface area (1,100 m^2/g)[69]. The high degree of symmetry and interlinking of the SBUs coupled with the strong zirconium-oxygen bonds in the SBU allow the MOF to retain its structure under a variety of experimental conditions, including exposure to extremely acidic (low pH) and basic (high pH) conditions and exposures to elevated relative humidity[70-72].

The high stability of UiO-66 under humid conditions coupled with its high surface area makes it an attractive candidate for filtration applications and recent work has proven its ability to adsorb and react with molecules of interest. UiO-66 has been shown to adsorb NO_2 by breaking the bond between the organic linker and metallic oxide center such that nitrate and nitrite species are formed[73]. UiO-66 has also exhibited the ability to effectively hydrolyze soman (o-pinacolyl methylphosphofluoridate or GD) with a half-life of approximately 3.5 minutes, with a TOF of ~ 20, under buffered conditions[74]. However, UiO-66 has had limited success in adsorbing many other chemical warfare agents (CWAs) and toxic industrial chemicals (TICs) that are of interest for filtration applications. This limitation has been largely attributed to its microporous structure that does not allow for facile diffusion of larger molecules of interest in addition to a lack of reactive moieties on the organic linker that could facilitate adsorption and reaction of the molecules of interest[75].

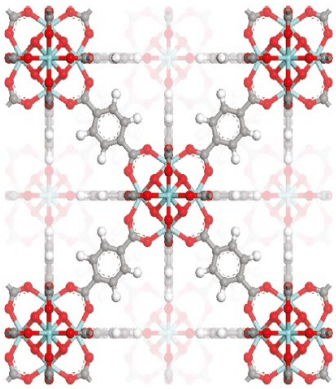

Figure 117. Depiction of UiO-66[4]

5.4.1 PHYSICAL PROPERTIES

The x-ray diffraction pattern of UiO-66 is shown in figure 118 with Miller indices of crystalline structure identified over the relevant peaks. XRD patterns of MOFs in general are largely comprised of low-2Θ angle peaks, as the long range order of the materials occurs on a very large scale relative to metal oxides.

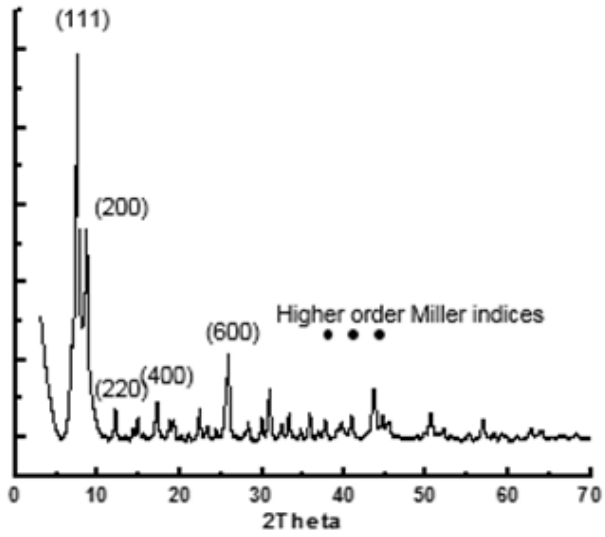

Figure 118. XRD pattern of UiO-66

SEM images of UiO-66 are depicted in Figure 119. These images show that UiO-66 particles have a cubic shape with a size in the 100-200 nm range, consistent with literature data[76, 77].

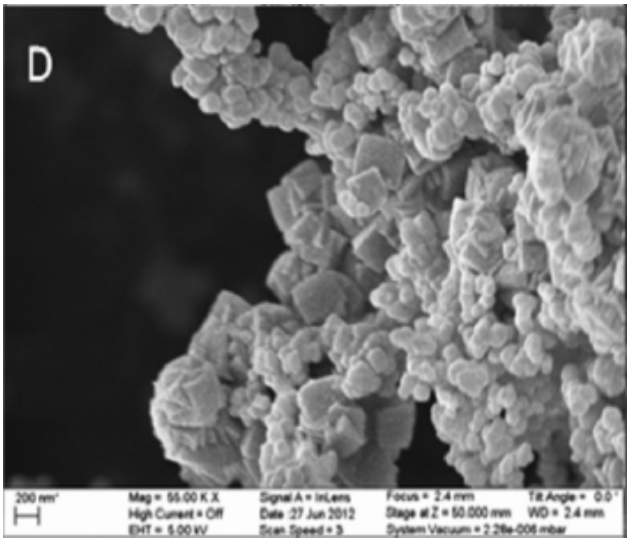

Figure 119. SEM of UiO-66

The TGA/DSC profile of UiO-66 is shown in Figure 120. TGA showed a gradual weight loss up to about 100 C, consistent with the loss of physically absorbed water, a second weight loss between 150 C

and 200 C attributed to DMF decomposition, and lastly a sharp decrease around 500 C, indicative of collapse of the structure and degradation to ZrO_2[76,77].

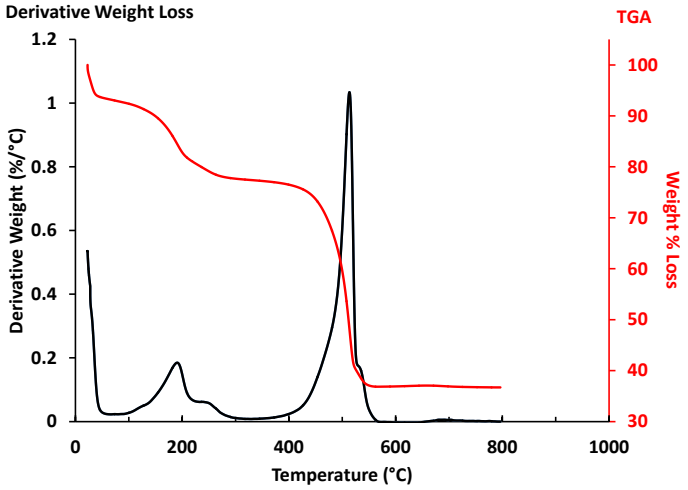

Figure 120. TGA/DSC profile of UiO-66

5.4.2 SURFACE PROPERTIES

The FTIR spectra of UiO-66 is shown in Figure 121. It shows a large peak at 1410 cm^{-1}, attributed to O-C-O symmetric stretching. Secondary peaks at 1540 and 810 cm^{-1} are attributed to C-C ring and O-H bending/C-H bending modes, respectively. The peak at 560 cm^{-1} corresponds to Zr-(O-C) assymetric stretching modes [78].

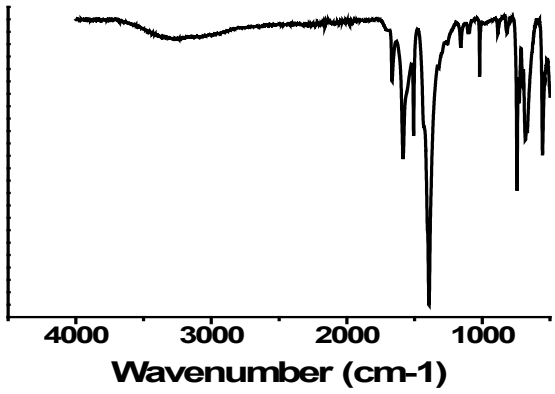

Figure 121. FTIR spectra of UiO-66.

Raman spectra of UiO-66 is shown in Figure 122. Vibrations containing benzene ring and carboxylate modes have been shown to be most active in raman spectroscopy for UiO-66, and this is also observed here. Particlarly, the C-C ring vibration at 1540 cm^{-1} is strongest, followed by peaks at 1420 cm^{-1} (O-C-O symmetric stretching), 1100 cm^{-1} (C-C ring), 850 cm^{-1} (O-H bend + C-H bending), and 630 cm^{-1} (Zr-O-C symmetric stretching)[79].

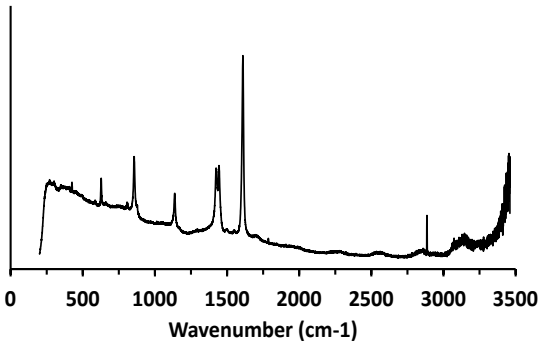

Figure 122. Raman spectra of UiO-66

5.4.3 ELECTRONIC AND OPTICAL PROPERTIES

The UV-Vis spectrum of UiO-66 is depicted in figure 123. The sample yielded no absorbance at wavelengths greater than 300 nm and a sharp peak around 250 nm, consistent with literature data[80, 81]. Two UV absorption peaks are observed at 260 nm and 290 nm, which are attributed to the UV adsorption of Zr-O oxo-clusters and ligand-based adsorption influenced by the nearby metal centers, respectively[82]. Tauc plot analysis in Figure 124 calculated a band gap of 3.8 eV, slightly lower than the literature value of 3.94 eV[79]. UV-vis spectra of simulant-exposed UiO-66 is shown in Figure 125. Absorbance in the UV region is truncated upon exposure to DMCP and the absorption edge is shifted slightly towards lower wavenumber (higher energy) wavelengths for all chemicals.

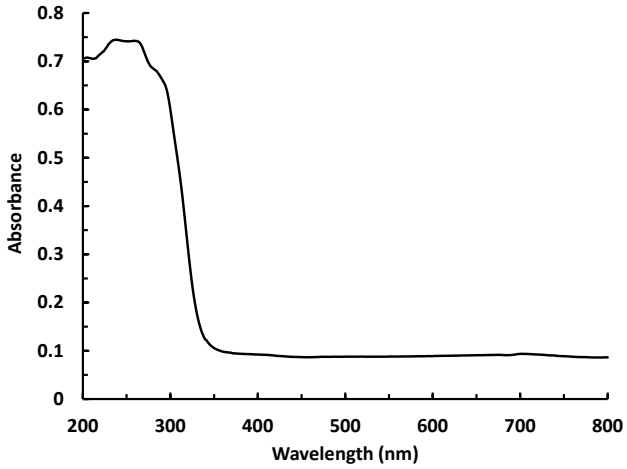

Figure 123. UV-Vis spectra of UiO-66.

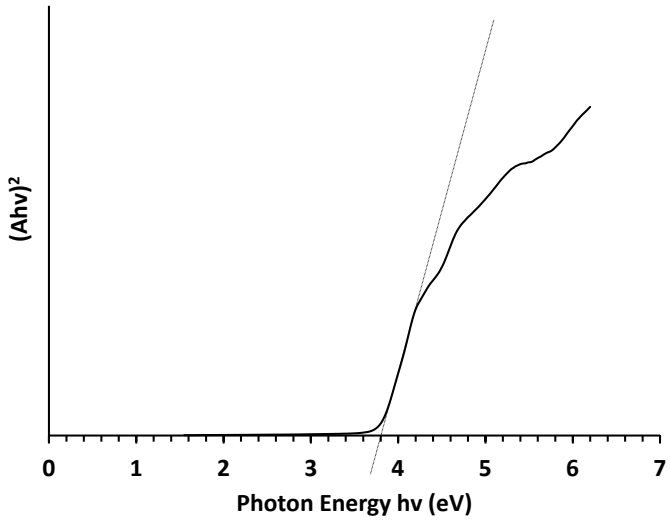

Figure 124. Tauc plot of UiO-66

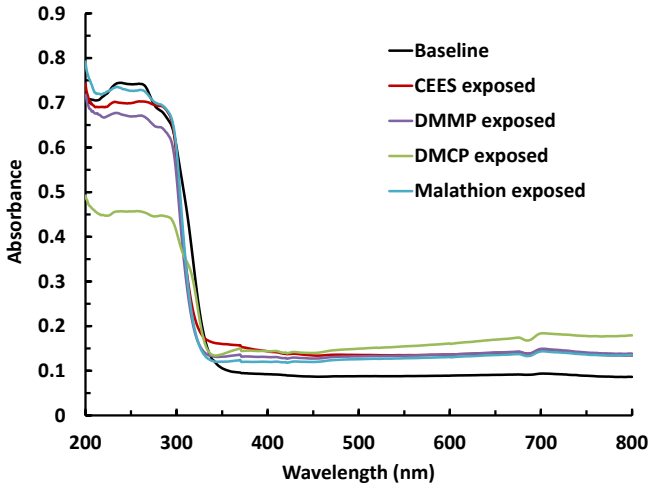

Figure 125. UV-Vis spectra of simulant-exposed UiO-66.

Fluorescence spectra of UiO-66 is depicted in Figure 126, and fluorescence spectra of simulant-exposed UiO-66 are depicted in Figure 127. The baseline UiO-66 spectra yields a strong intensity peak around 400 nm, consistent with literature data[82], and has been intrinsically attributed to metal-to-ligand charge transfer in the material[83]. The terephthalic acid linker used in UiO-66 synthesis has also yielded a strong fluorescence peak in this region (388 nm) which has been attributed to π^*-> n transitions[84]. Exposure to simulant universally produces a stronger peak in the fluorescence spectrum that is shifted towards the 300-350 nm range, consistent with the UV spectra showing absorption edge shifting in that direction as well. This suggests a change in band structure may have occurred upon simulant exposure which produced a greater concentration of electron-hole pairs and slightly increased the band gap energy required to excite these electrons from the valence band to the conduction band of the material. Additionally, CEES exposure also yielded a minor and lower-energy peak in the fluorescence spectrum around 450 nm.

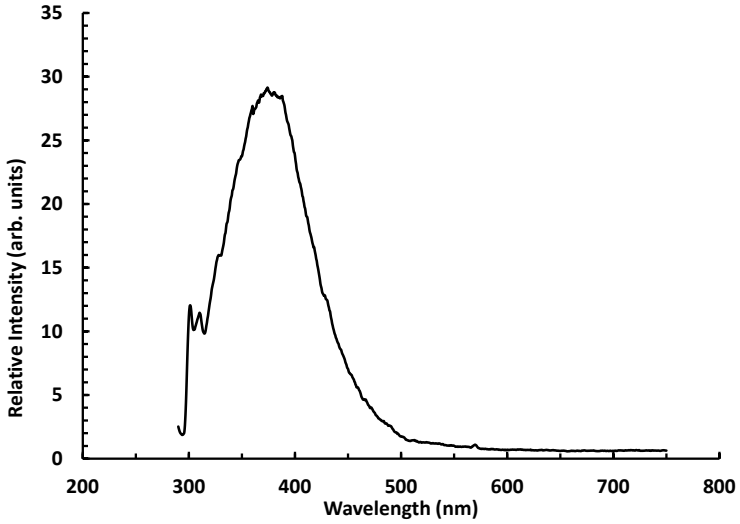

Figure 126. Fluorescence spectra of UiO-66

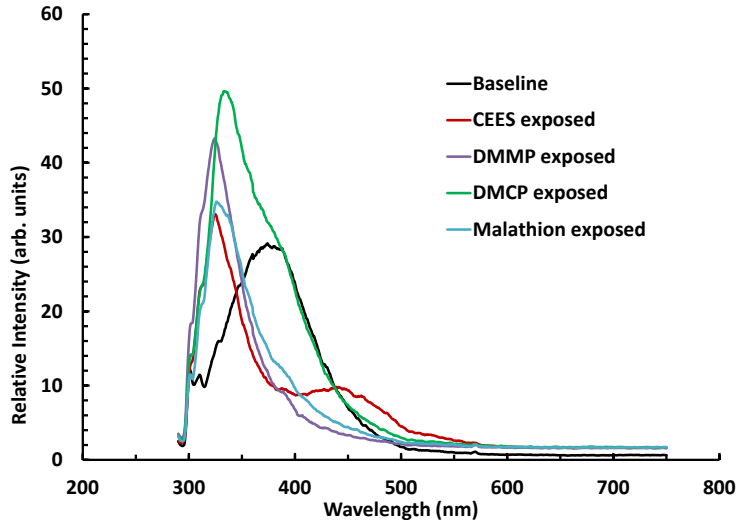

Figure 127. Fluorescence spectra of simulant-exposed UiO-66

5.4.4 ADSORPTION AND REACTION CAPABILITIES CHARACTERIZATION

The N_2 isotherm of UiO-66 is shown in Figure 128. UiO-66 exhibited a type II isotherm with minimal hysteresis and a BET surface area of 1464.6 m^2/g, consistent with literature values[77].

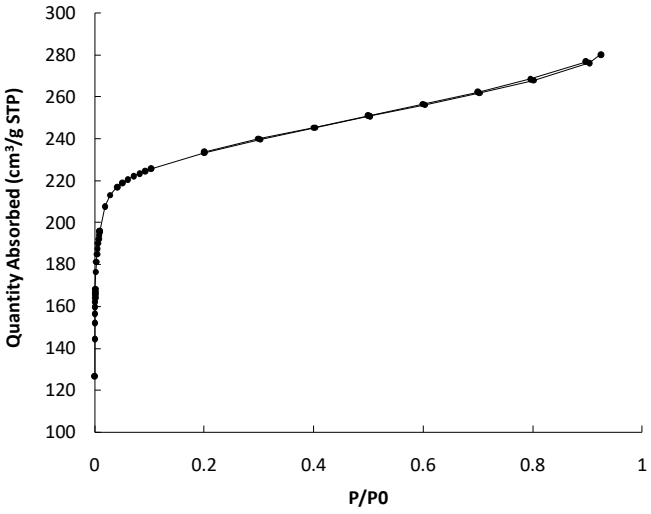

Figure 128. N_2 isotherm of UiO-66.

Table 10. Physical properties of UiO-66

BET SA (m^2/g)	Total PV (cc/g)	Micropore Volume (cc/g)
1465	0.9478	0.4659

The water isotherm of UiO-66 is shown in Figure 129. UiO-66 is moderately hydrophilic due to its high surface area and surface hydroxyl groups on the Zr-based structure building unit providing the means for hydrogen bonding.

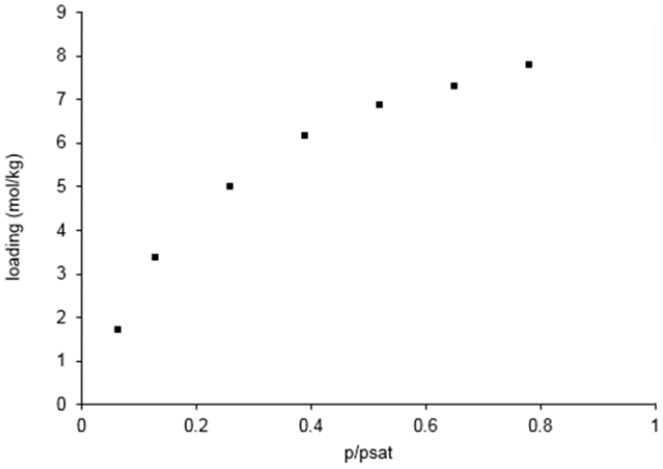

Figure 129. Water isotherm of UiO-66

The pKa distribution for UiO-66 is shown in figure 130. Three distinct peaks are observed in the pKa distribution. These correspond to three distinct types of protons found in this MOF: u_3-OH protons found around pKa of 3.5 , Zr-OH_2 protons found around pKa of 6.8, and Zr-OH protons found around a

pKa of 8.3[5]. The latter two protons are considered to form from defect sites in the node of UiO-66, depicted in Figure 131, thus suggesting a particularly high amount of Zr-OH defects in the sample. The point of zero charge of UiO-66 was calculated to be 8.4 but has been found to occur at a pH ranging from of 3.9 to 5.5 in literature[85, 86].

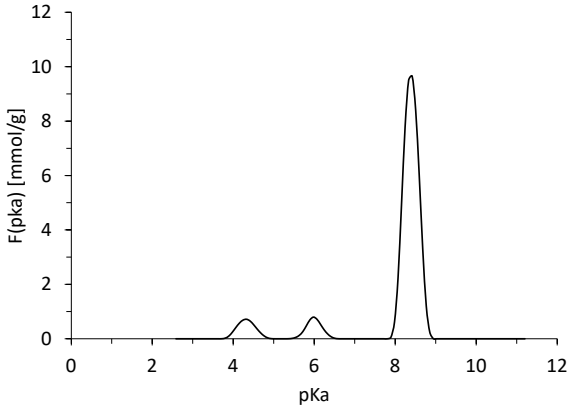

Figure 130. pKa distribution of UiO-66

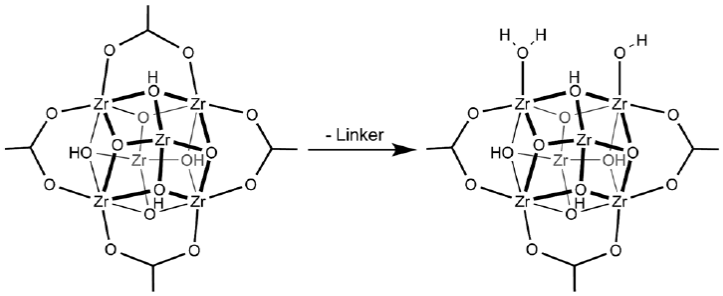

Figure 131. Types of protons on UiO-66[5]

5.4.5 CHEMICAL DOSE-EXTRACTION REMOVAL ABILITY

Results of chemical dose extraction for UiO-66 are shown in Table 11. With the exception of VX, UiO-66 demonstrated low reactivity across the spectrum of simulants and agents tested. CEES and HD removal were both negligible. G simulant reactivity progressed as DFP < DMMP < DMCP, with DFP most closely predicting GD removal and DMMP most closely predicting GB removal. Malathion greatly underpredicted VX removal.

Table 11. Dose-extraction results for UiO-66

CEES		HD		DMCP		DFP		DMMP		GB		GD		Malathion		VX	
%R	SD	%R	SD	%R	SD	%R	SD	%R	SD	%R	SD	%R	SD	%R	SD	%R	SD
0	-	0	-	99.0	-	22.0	-	55.0	-	44.0	-	13.8	4.9	12.0	-	46.3	-

5.4.6 NMR

NMR was used to investigate the catalytic activity of UiO-66 for GD and HD. ^{31}P NMR spectra for GD with UiO-66 in 0.5 M (pH 10) ethylmorpholine (EM) buffer and on the solid itself are shown in Figures 132 and 134, respectively. Kinetic plots are also shown (Figures 133, 135). Kinetic parameters found are shown in Table 12.

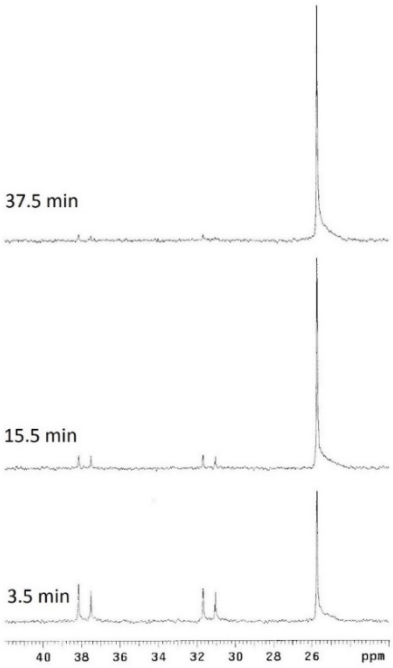

Figure 132. Select ^{31}P NMR spectra obtained for 2.6 µL GD added to 2.5 mg UiO-66 in 0.75 mL 0.5 M EM buffer.

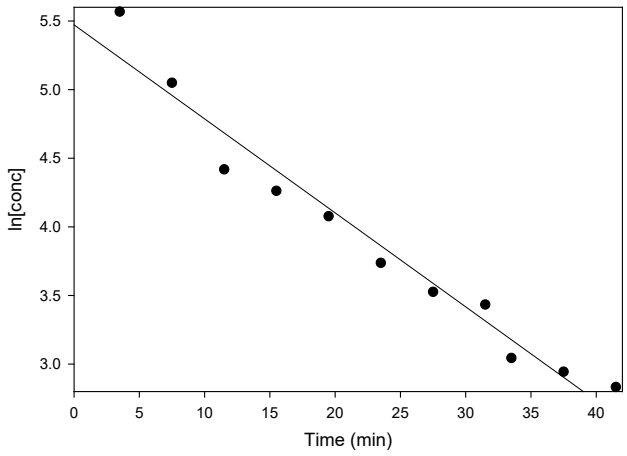

Figure 133. Plot of [GD] vs. time for ^{31}P NMR spectra obtained for 2.6 µL GD added to 2.5 mg UiO-66 in 0.75 mL 0.5 M EM buffer.

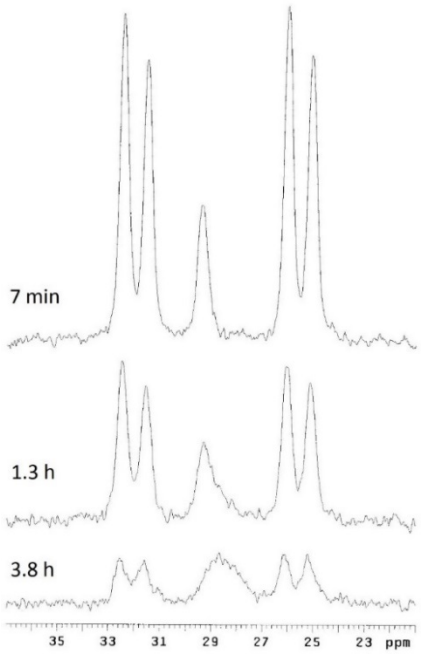

Figure 134. Select ^{31}P MAS NMR spectra obtained for 5 µL GD added to 100 mg UiO-66.

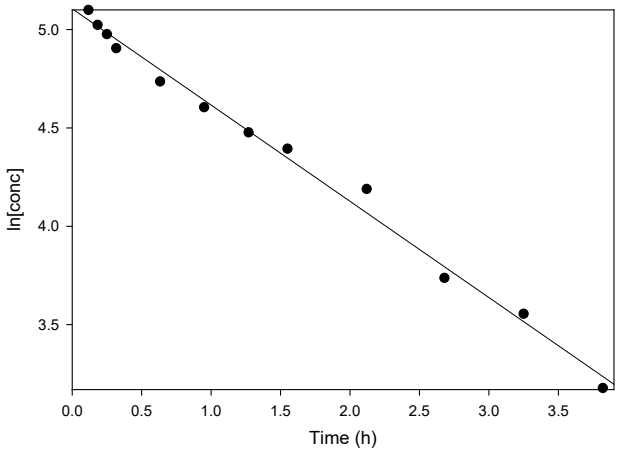

Figure 135. Plot of [GD] vs. time for ^{31}P MAS NMR spectra obtained for 5 µL GD added to 100 mg UiO-66.

Table 12. Reactions with UiO-66

Chemical and conditions	Performance with UiO-66	Performance with buffer only	Notes
GD, pH 10 EM Buffer	$t_{1/2}$ = 10 min	$t_{1/2}$ = 26 min	
GD on UiO-66 solid	$t_{1/2}$ = 1.4 h	-	
HD on UiO-66 Solid	Limited reaction	-	-Less than 3 % reaction observed over the course of 21 h
HD in $CHCl_3$ on UiO-66 solid	$t_{1/2}$ = 2.5 days	-	-25 % reaction over the course of 21 h -$CHCl_3$ leached out residual CH_2Cl_2 and DMF[a] solvents[b]
HD in CH_3CN on UiO-66 solid	Limited reaction	-	-Less than 2 % reaction observed over the course of 21 h
CH_3CN Extraction of HD from UiO-66 Solid	Limited reaction	-	-Less than 2 % reaction observed over the course of 24 h

[a] Dimethyl formamide.
[b] The UiO-66 contained considerable amounts of these solvents, apparently left over from synthesis of the material.

GD is catalyzed by UiO-66 in pH 10 EM buffer as the rate of this reaction is faster than in pH 10 buffer alone. GD reacts rather slowly on the UiO-66 solid itself. In both instances, GD is hydrolyzed (Figure 41, Section 6.1.6). The HD reaction with UiO-66 was examined in a variety of ways – reaction with the solid using neat HD and HD in $CHCl_3$ and CH_3CN solvents, and by CH_3CN extraction – to compare the results (Table 12). NMR spectra and accompanying kinetic plots are shown in Figures 136-143.

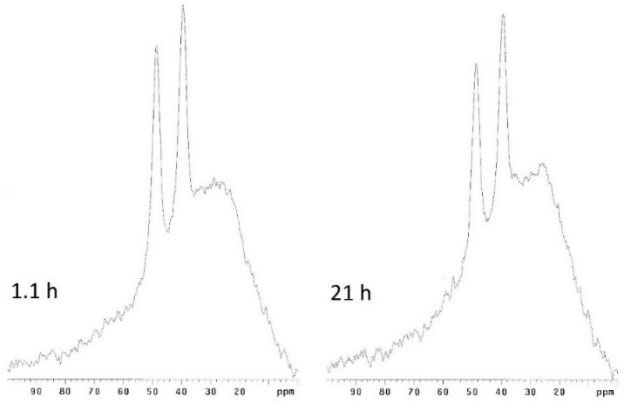

Figure 136. Select ^{13}C NMR spectra obtained for 20 µL HD added to 50 mg UiO-66 at the indicated times.

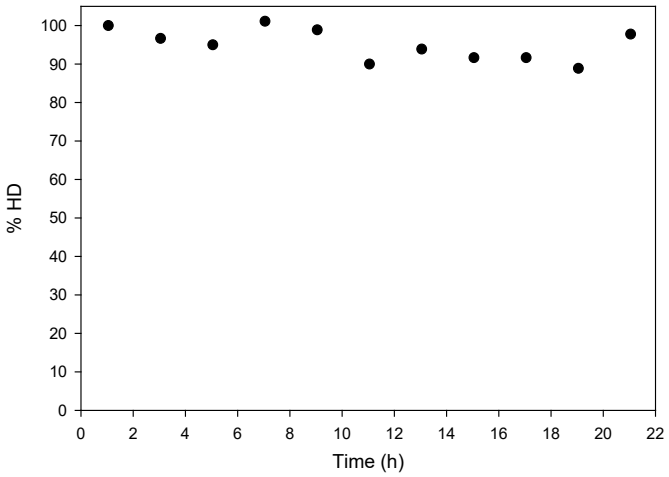

Figure 137. Plot of [HD] vs. time for ^{13}C NMR spectra obtained for 20 µL HD added to 50 mg UiO-66.

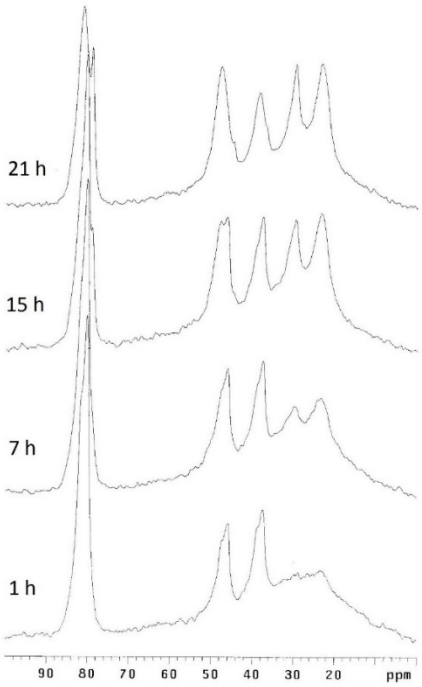

Figure 138. Select ^{13}C NMR spectra obtained for 20 µL HD/160 µL $CHCl_3$ added to 50 mg UiO-66 at the indicated times.

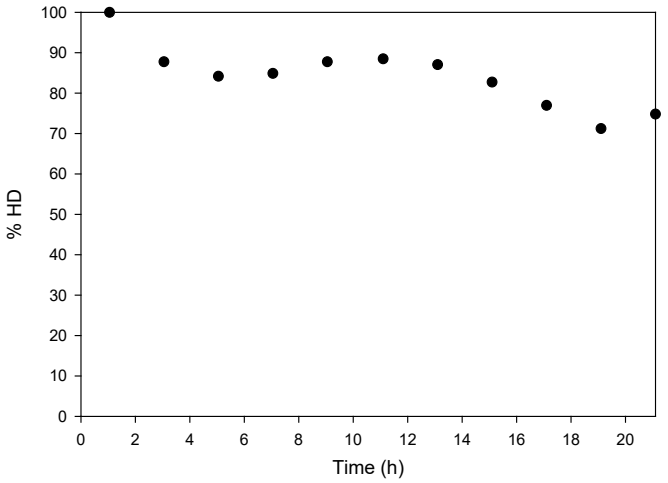

Figure 139. Plot of [HD] vs. time for ^{13}C NMR spectra obtained for 20 μL HD/160 μL $CHCl_3$ added to 50 mg UiO-66.

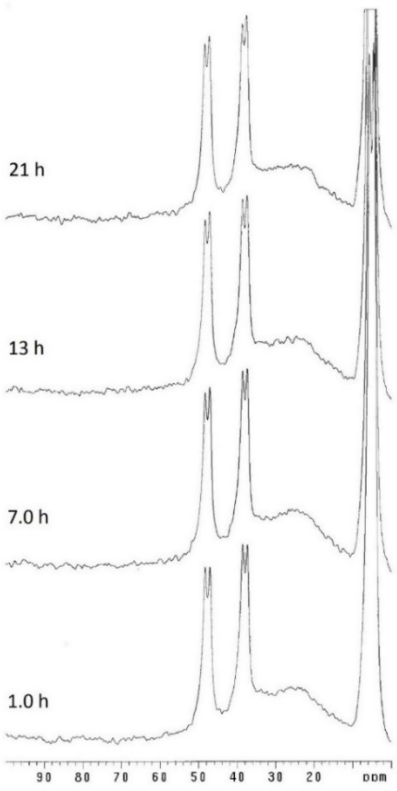

Figure 140. Select ^{13}C NMR spectra obtained for 20 μL HD/160 μL CH_3CN added to 50 mg UiO-66at the indicated times. The large peak near 5 ppm is due to the CH_3CN solvent.

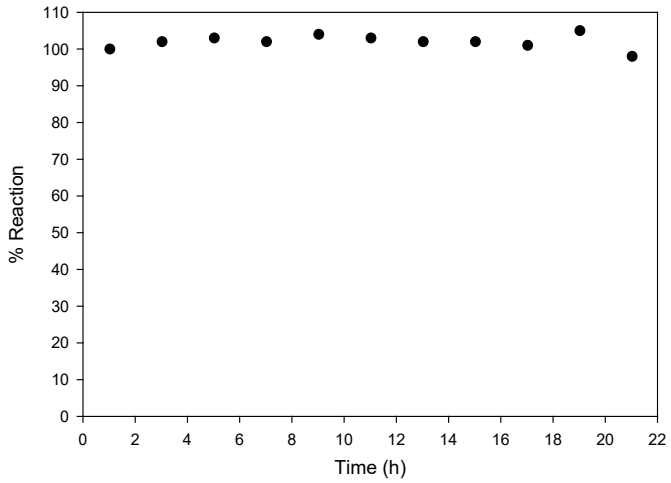

Figure 141. Plot of [HD] vs. time for ^{13}C NMR spectra obtained for 20 µL HD/160 µL CH_3CN added to 50 mg UiO-66.

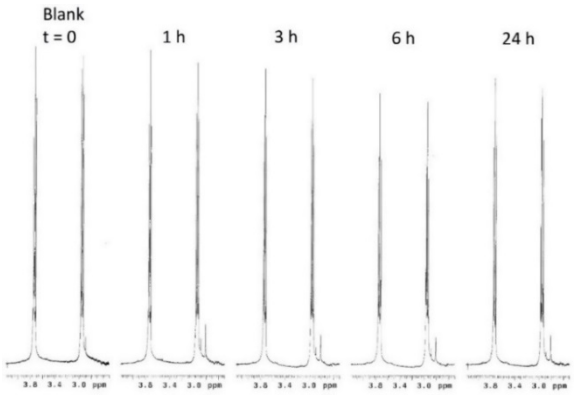

Figure 142. ^{13}H NMR spectra obtained for 20 µL HD to 50 mg UiO-66 and CH_3CN extracted at the indicated times.

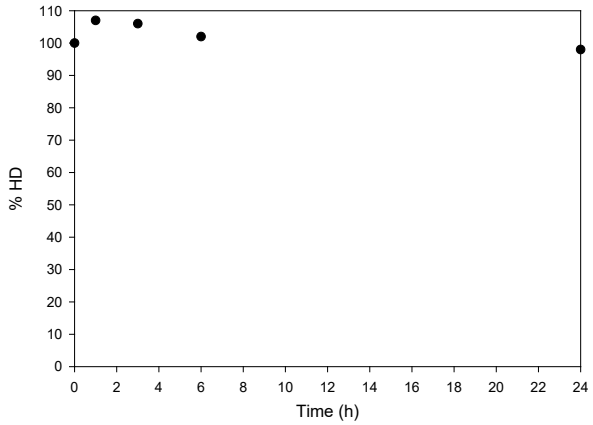

Figure 143. Plot of [HD] vs. time for ^{13}C NMR spectra obtained for CH_3CN-extractions of 20 µL HD added to 50 mg UiO-66.

Very little reaction occurred for neat HD on solid UiO-66, with 97 % remaining after 21 h. For HD in $CHCl_3$ the reaction was somewhat faster, such that about 75 % HD remained after 21 h as evidenced by the diminished HD peak at 37.4 ppm. Besides the slow disappearance of this peak, the other HD peak at 46.0 ppm appeared to increase in intensity over time, and two new peaks at 29.6 and 23.3 ppm emerged; these are due to extraction of EtOH by $CHCl_3$ from the microcentrifuge tube as detailed above. Similar to the reaction of neat HD, HD in CH_3CN showed very little reaction with less than 2 % reacting after 21 h. The HD reaction studied by CH_3CN-extraction also showed less than 2 % reacting after 24 h.

5.4.7 DRIFTS

The DRIFTS spectra of CEES on UiO-66 is shown in Figure 144. The loss at 3680 cm^{-1} is attributed to Zr-OH stretching modes. Increasing peaks at 1400 cm^{-1} and 1210 cm^{-1} are assigned to in-plane CH_3 bending modes and out-of-plane CH_2 bending (wagging) modes, respectively.

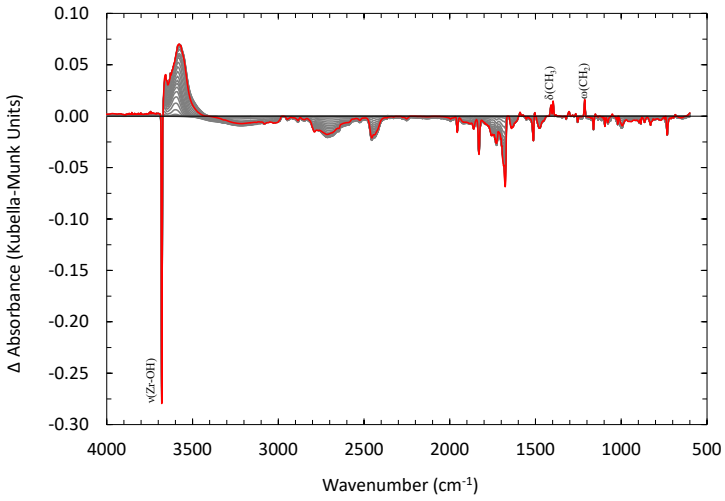

Figure 144. DRIFTS spectra of CEES on UiO-66

The DRIFTS spectra of HD on UiO-66 is shown in Figure 145. Losses at 3680 cm^{-1} and 2860 cm^{-1} are attributed to Zr-OH stretching modes and CH_2 stretching modes, respectively. Increasing peaks at 1620 cm^{-1}, 1230 cm^{-1}, and 680 cm^{-1} are assigned to in-plane H_2O bending modes, both in-plane $S(CH_2)$ bending modes and in-plane $Cl(CH_2)$ bending modes, and both C-Cl and C-S stretching modes, respectively.

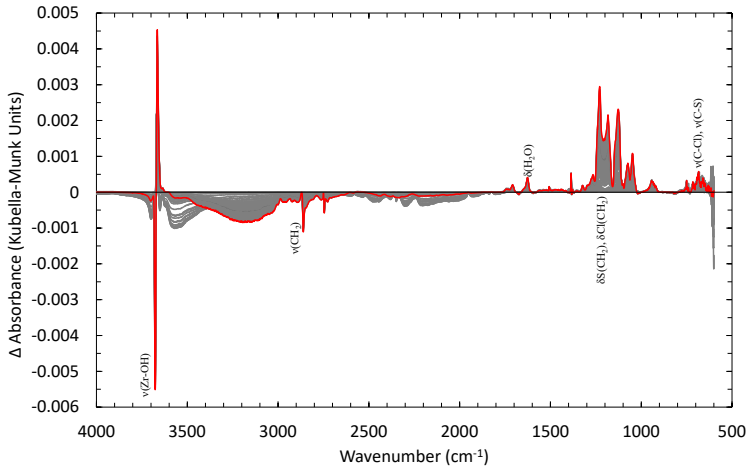

Figure 145. DRIFTS spectra of HD on UiO-66

The DRIFTS spectra of DMMP on UiO-66 is shown in Figure 146. Adsorption of DMMP on UiO-66 in the IR spectra shows a loss in the isolated OH band indicating one adsorption site. Adsorption of DMMP can be seen by the increase and blueshift in the P=O band up to 1265 cm^{-1} and relatively weak adsorption at 1231 cm^{-1}. In comparison with the UiO-66-NH_2 P=O adsorption band at 1216 cm^{-1}, the DMMP molecule adsorbs on OH sites mainly on UiO-66 and on NH_2 sites on UiO-66-NH_2. The DMMP molecule looks to stay relatively intact and does not dissociate or react with the surface.

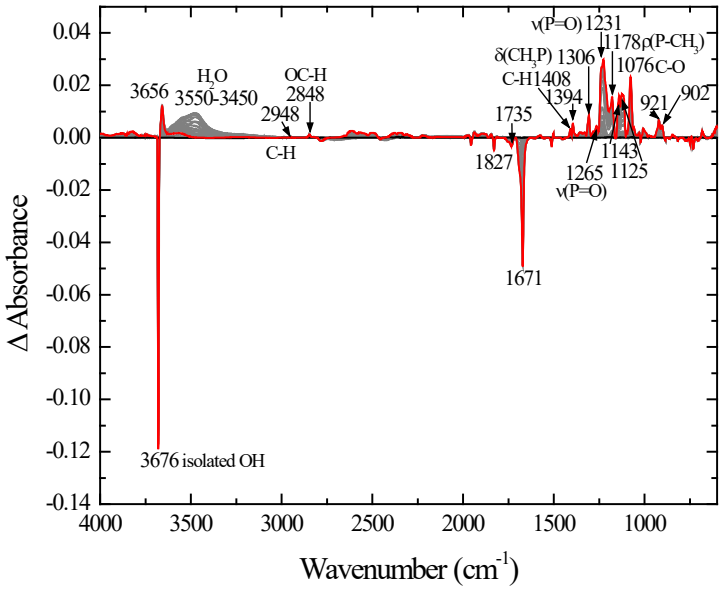

Figure 146. DRIFTS spectra of DMMP on UiO-66

The DRIFTS spectra of DMCP on UiO-66 is depicted in Figure 147. The loss at 3680 cm^{-1} is attributed to Zr-OH stretching modes. Increases at 1310 cm^{-1}, 1210 cm^{-1}, and 1070 cm^{-1} are assigned to in-plane P-CH_3 bending modes, P=O stretching modes, and O-P-O stretching modes, respectively.

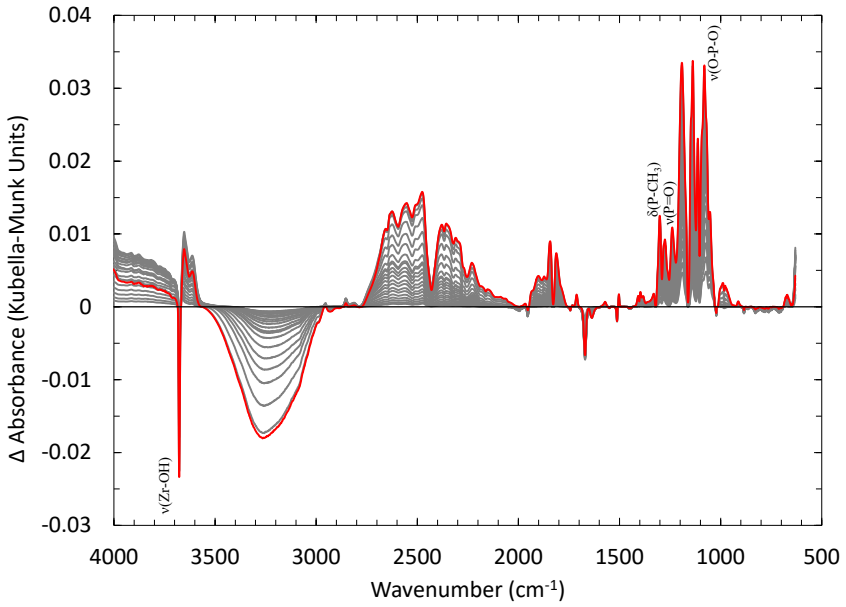

Figure 147. DRIFTS spectra of DMCP on UiO-66

The DRIFTS spectra of GB on UiO-66 is shown in Figure 148. The loss at 3680 cm^{-1} is attributed to Zr-OH stretching modes. Increasing peaks at 1200 cm^{-1}, 1120 cm^{-1}, and 1060 cm^{-1} are assigned to P=O stretching modes, O-P-O stretching modes, and O-P-O stretching modes, respectively.

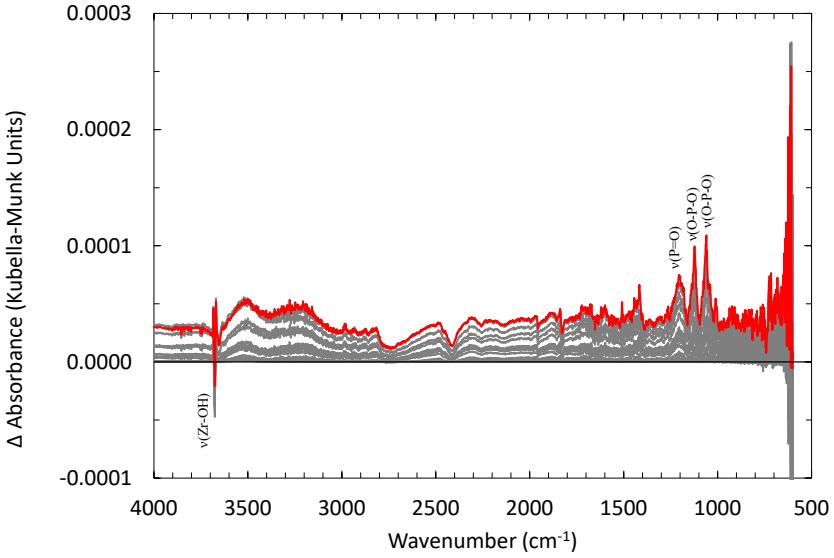

Figure 148. DRIFTS spectra of GB on UiO-66

The DRIFTS spectra of malathion on UiO-66 is shown in Figure 149. The loss at 3680 cm^{-1} is attributed to Zr-OH stretching modes. Increasing peaks at 1190 cm^{-1} and 1040 cm^{-1} are assigned to both P=S stretching modes and P-S modes and C-O stretching modes, respectively.

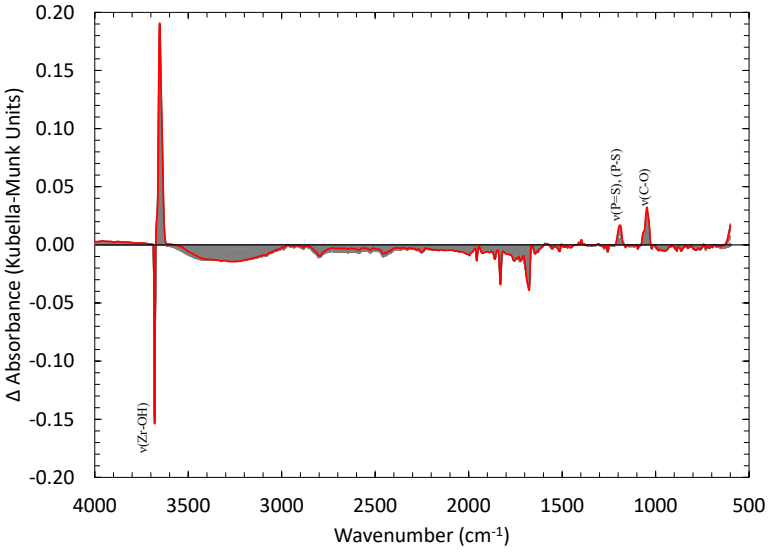

Figure 149. DRIFTS spectra of malathion on UiO-66

The DRIFTS spectra of VX on UiO-66 is shown in Figure 150. The loss at 3680 cm^{-1} is assigned to Zr-OH stretching modes.

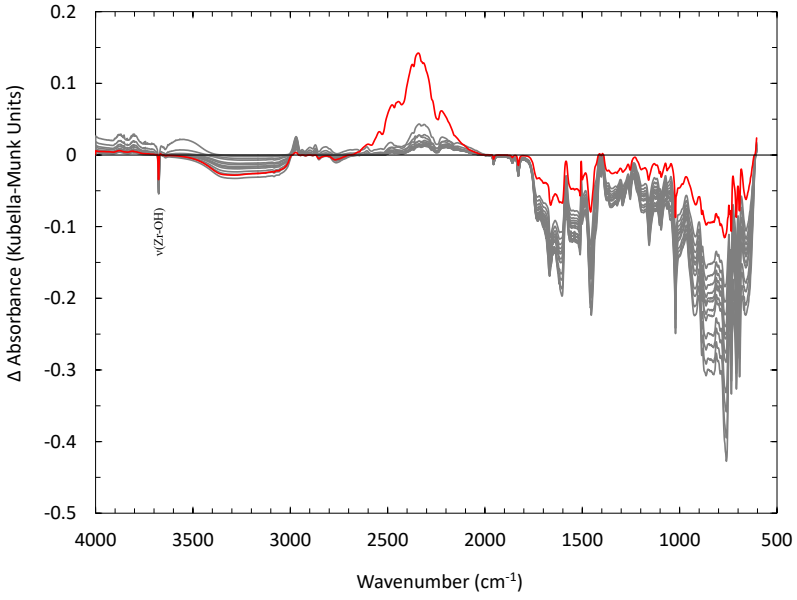

Figure 150. DRIFTS spectra of VX on UiO-66

5.5 UiO-66-NH_2

The organic linker in UiO-66 can be readily exchanged for organic linkers with pendant groups to facilitate reactivity of the UiO-66 MOF towards TICs and CWAs. As such, an amine group has been installed on the phenyl portion of the organic linker by an in situ hydrolysis of $ZrCl_4$ with 2-aminoterephthalic acid to form UiO-66-NH_2. The amine functionality is particularly attractive for filtration applications due to its acid-base properties and its potential for hydrogen bonding. The resulting PXRD data showed that the MOF is topologically equivalent to that of UiO-66 and N_2 isotherms show a similar, but slightly lower, BET surface area (1070 m^2/g). The thermal stability of UiO-66-NH_2 is lower than that of UiO-66, decomposing at 350 °C versus 540 °C, respectively. The thermal decomposition of both UiO-66 and UiO-66-NH_2 is attributed to the breakdown of the bond between the SBU and carboxyl group on the linker indicating that the linker is not only key to the reactivity of the MOF but also contributes significantly to its stability as well[87].

UiO-66-NH_2 has shown remarkable reactivity towards CWAs and TICs. UiO-66-NH_2 readily removes chlorine gas by an electrophilic aromatic substitution mechanism at a capacity of 17.5 mol/kg[75]. In addition, UiO-66-NH_2 has proven to be very effective in ammonia (NH_3) and cyanogen chloride (CNCl) sorption due to the hydrogen bonding sites on the amine group[88]. Carbon dioxide (CO_2) and methane (CH_4) adsorption is also doubled in UiO-66-NH_2 over UiO-66 due to the additional hydrogen bonding that the amine groups provide[89]. While the amine group on UiO-66-NH_2 increases its activity towards TICs and CWAs, it also decreases the already small pore size in the MOF. The small pore size remains the primary limitation in further increasing the activity of UiO-66-NH_2 which has been proven in the engineered forms of the MOF[88].

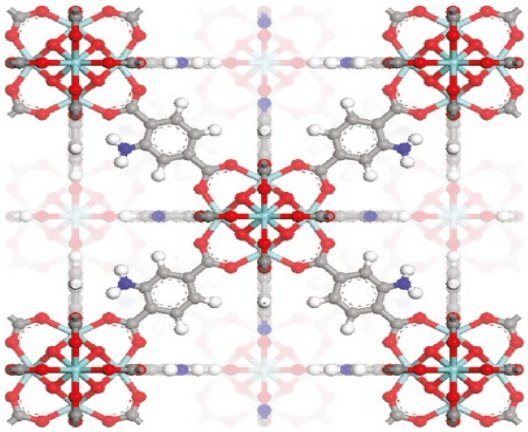

Figure 151. Structure of UiO-66-NH_2

5.5.1 PHYSICAL PROPERTIES

The XRD pattern of UiO-66-NH_2 is shown in Figure 152. XRD patterns of UiO-66-NH_2 are fully identical to those of UiO-66, with the peaks at 2-theta values around 7, 8, 12, 17, 22, and 26 degrees corresponding to the (111), (200), (220), (400), (511), and (600) surfaces of the MOF, respectively[90]. This isostructural relationship with UiO-66 is consistent with previous efforts[4, 81, 91].

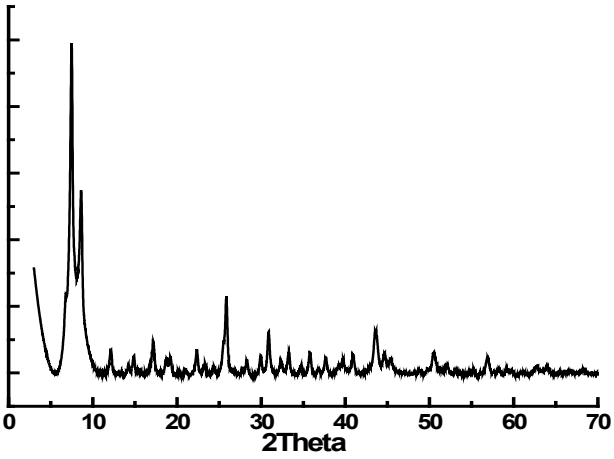

Figure 152. XRD pattern of UiO-66-NH_2

SEM images of UiO-66-NH_2 are shown in Figure 153. The images confirm the standard ball-shape morphology of UiO-66-NH_2 crystals, with particle sizes in the 200-500 nm range, consistent with literature values[71, 92-94].

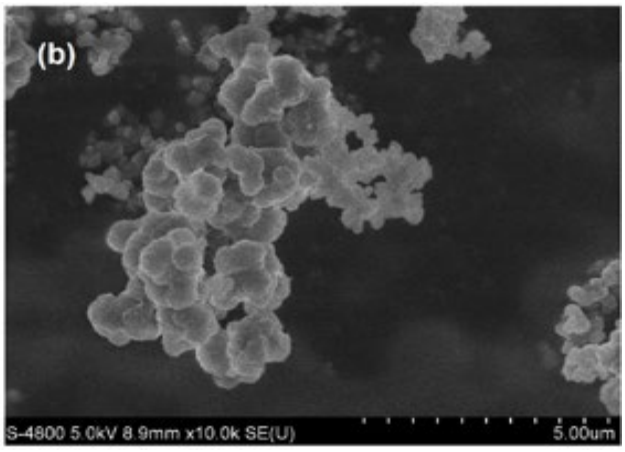

Figure 153. SEM image of UiO-66-NH_2

The TGA profile of UiO-66-NH_2 is shown in Figure 154. Three distinct weight losses are observed, as reported in literature, and are attributed to loss of physisorbed water in the 0-100 C range, dehydroxylation of OH^- moieties in the 200-300 C range, and collapse of the structure to ZrO_2 around 350 C, which also corresponds to the exothermic peak in the DSC profile[92].

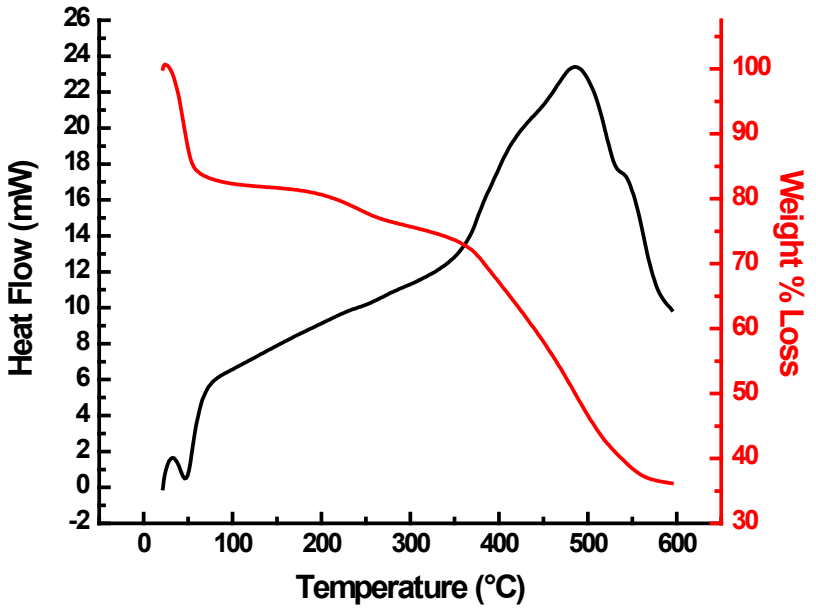

Figure 154. TGA and DSC profiles of UiO-66-NH_2

5.5.2 SURFACE PROPERTIES

FTIR spectra of UiO-66-NH_2 are shown in Figure 155. Many peaks are identical to its UiO-66 analogue and can be assigned analogously. Major peaks unique to the amine derivative are assigned to C-N stretching modes around 1356 cm^{-1} and N-H bending (scissoring) vibrational modes around 1626 cm^{-1} [4]. Small peaks due to symmetric and asymmetric NH_2 stretching modes have been observed in the 3300-3600 cm^{-1} range as well[4], but here they are enveloped by the broad –OH stretching peak in that region.

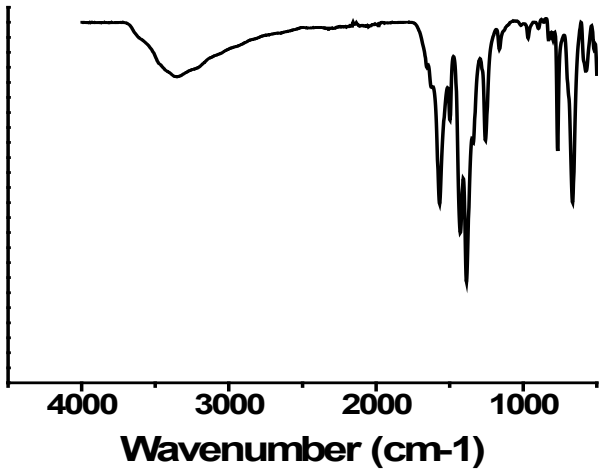

Figure 155. FTIR spectra of UiO-66-NH_2

Raman spectrum for UiO-66-NH_2 is shown in Figure 156. No distinct peaks are observed, as is consistent with literature efforts[4]. This dearth of raman signature is due to the fluorescence capabilities of UiO-66-NH_2, which will be outlined specifically in the following sections. Briefly, fluorescence interference from relevant samples is often a severe problem in raman spectroscopy, because this generates a very large background signal that is often stronger than the distinct raman scattering peaks of structural components of the sample and thus cannot be subtracted out to reveal characteristic structural signatures[95].

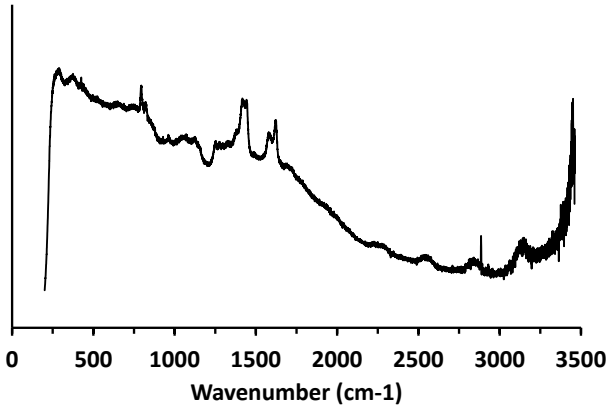

Figure 156. Raman spectra of UiO-66-NH_2

5.5.3 ELECTRONIC AND OPTICAL PROPERTIES

The UV-Vis spectra of UiO-66-NH_2 is depicted in Figure 157. It showed no absorption at wavelengths greater than 450 nm and distinct peaks around 250 and 360 nm, consistent with literature data[81,93]. In comparison to the baseline UiO-66, the new absorption band at 360 nm with UiO-66-NH_2 is associated with the chromophore of the BDC-NH_2 linker, specifically assigned to ligand-to-metal charge transfer in the material[81] and the appearance of the photoabsorption edge of the 360 nm peak within the visible light region conforms with the yellow appearance of the sample, as opposed to the white appearance of UiO-66[80]. Analogously, UV-vis spectra of the isolated aminoterephthalic acid linker used in UiO-66-NH_2 synthesis reveals a similar peak at 381 nm that has been assigned to $\pi \rightarrow \pi^*$ electronic transitions in the aromatic ring[96]. Tauc plot analysis in Figure 158 calculated a band gap of 2.8 eV, slightly lower than the literature band gap of 2.95 eV[78].

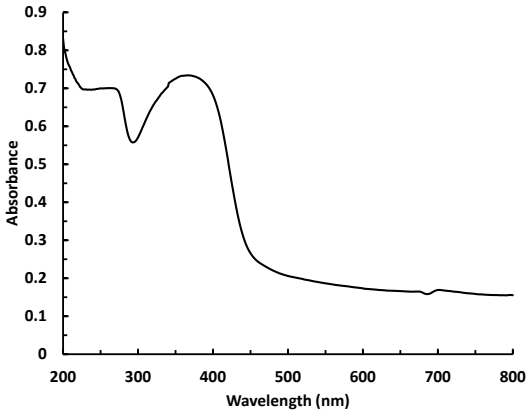

Figure 157. UV-Vis spectra of UiO-66-NH_2

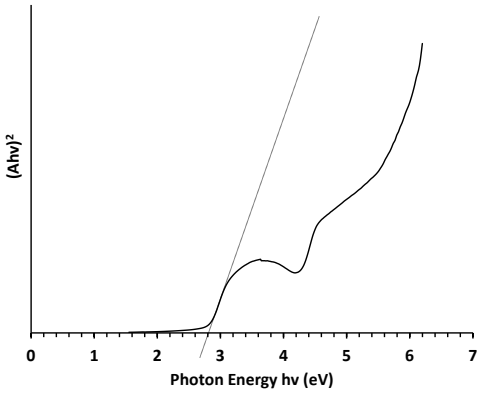

Figure 158. Tauc plot of UiO-66-NH_2

UV-vis spectra of simulant-exposed UiO-66 is shown in Figure 159. The absorption baseline is slightly elevated upon malathion exposure, and a red shift in the absorption edge is observed with malathion and CEES. This suggests that exposure to these simulants slightly lowered the band gap of the resulting material.

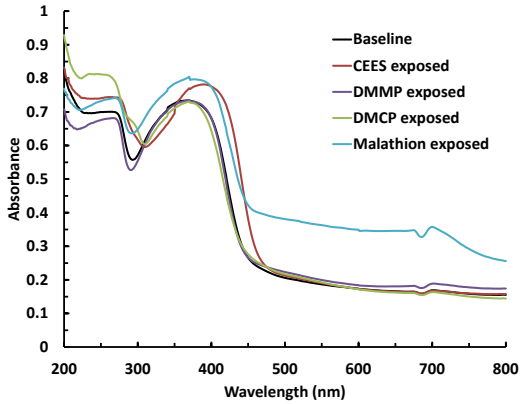

Figure 159. UV-Vis spectra of simulant-exposed UiO-66-NH_2

Fluorescence spectra of UiO-66-NH_2 is shown in Figure 160. A strong fluorescence peak is observed around 450 nm, with a wider right photoabsorption edge extending to roughly 550 nm, consistent with literature data and also attributed to metal-to-ligand charge transfer in the material[97]. Exposure to simulants dramatically increased the intensity of the fluorescence peak (Figure 161) but, unlike UiO-66, did not dramatically shift the corresponding wavelength of the peak, with the malathion and CEES-exposed material peaks shifted slightly to lower-energy wavelengths. This suggests that a higher density of electron-hole pairs was created in the material upon simulant exposure and again confirms just a slight reduction in band gap with CEES and malathion only.

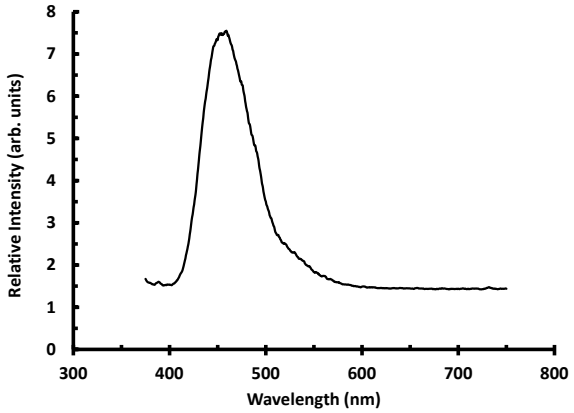

Figure 160. Fluorescence spectra of UiO-66-NH_2

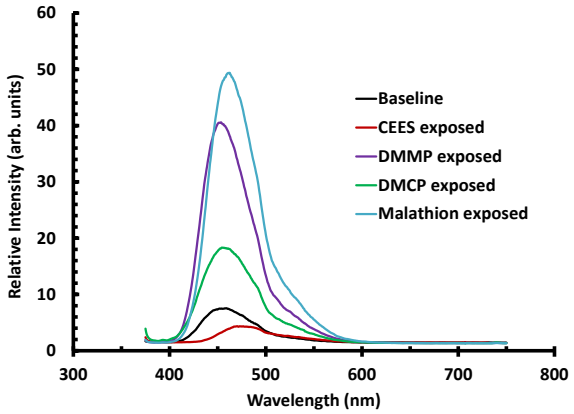

Figure 161. Fluorescence spectra of simulant-exposed UiO-66-NH_2

5.5.4 ADSORPTION AND REACTION CHARACTERIZATION

The N_2 isotherm of UiO-66-NH_2 is shown in Figure 162, and selected physical parameters are shown in Table 13. Surface area was 1382 m^2/g, which is consistent with previous literature values around 1300 m^2/g [98].

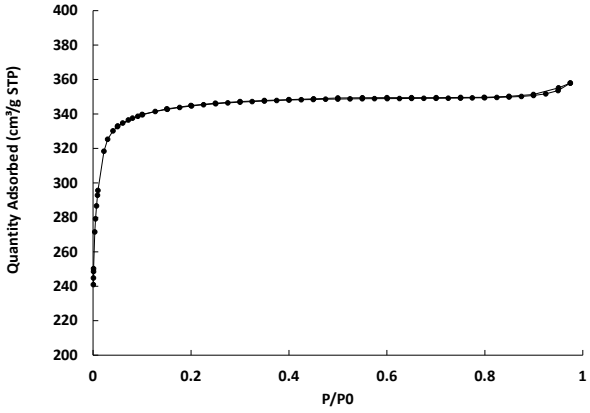

Figure 162. N_2 isotherm of UiO-66-NH_2

Table 13. Physical properties of UiO-66-NH_2

BET SA (m^2/g)	Total PV (cc/g)	Micropore Volume (cc/g)
1382	0.5495	0.4873

Water isotherm data for UiO-66-NH_2 is depicted in Figure 163. It showed to have the highest water absorption among all the referee materials evaluated, which is likely a combination of its very high surface area coupled with its favorable surface chemistry for hydrogen bonding with the amine functionality.

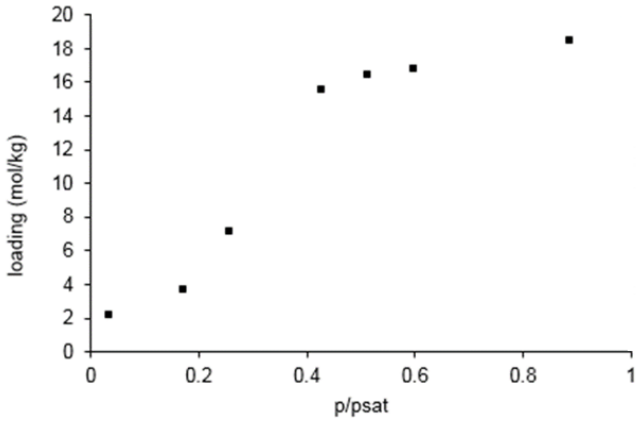

Figure 163. Water isotherm of UiO-66-NH_2

The pKa distribution of UiO-66-NH_2 is shown in Figure 164. Three distinct peaks are observed in the pKa distribution and can be analyzed analogously to the assignment for UiO-66. The major difference with UiO-66-NH_2 occurs with the high-pKa peak, which is shifted past 9 and has twice the intensity of the high-pKa UiO-66 peak. This is likely a contribution from the amine protons in the material. The point of zero charge of UiO-66-NH_2 was calculated to be 8.8, much higher than literature values around 6.5[86].

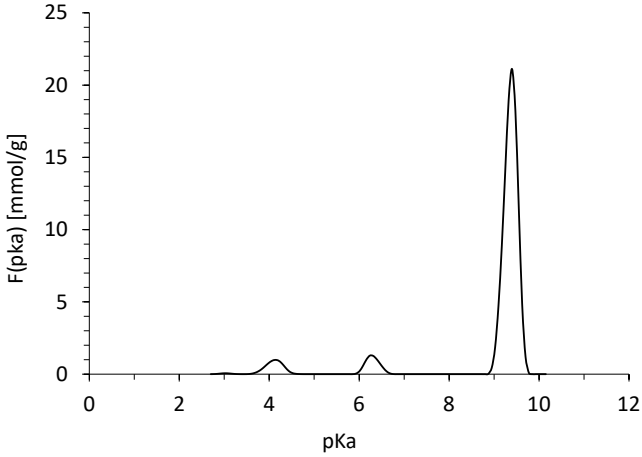

Figure 164. pKa distribution of UiO-66-NH_2

5.5.5 DOSE AND EXTRACTION TECHNIQUE

UiO-66-NH_2 exhibited the highest CEES removal of any material tested, but this dramatically overpredicted HD removal abilities. G series simulant conversions progressed in the order DFP < DMMP < DMCP, with GB removal most closely predicted by DMCP and GD removal overpredicted by all simulants by a wide margin. Malathion removal was high at 58% but vastly overpredicted VX removal capabilities.

Table 14. Dose-extraction results for UiO-66-NH_2

CEES		HD		DMCP		DFP		DMMP		GB		GD		Malathion		VX	
%R	SD	%R	SD	%R	SD	%R	SD	%R	SD	%R	SD	%R	SD	%R	SD	%R	SD
99.9	0.1	21.0	6.0	100	-	52.7	-	55.6	4.2	88.0	-	18.1	7.2	58.1	6.2	4.4	-

5.5.6 NMR

NMR was used to investigate the reactivity of GD and HD with UiO-66-NH_2. ^{31}P NMR spectra obtained for GD added to UiO-66-NH_2 in water, with and without EM buffer, and to sorbent itself are shown in Figures 165, 167, and 169, with kinetic plots given in Figures 166, 168, and 170. NMR spectra obtained for HD added to UiO-66-NH_2 and characterized in situ (^{13}C) or CH_3CN-extraction (^{1}H) and their kinetic plots are shown in Figures 171-174. Kinetic results are shown in Table 15.

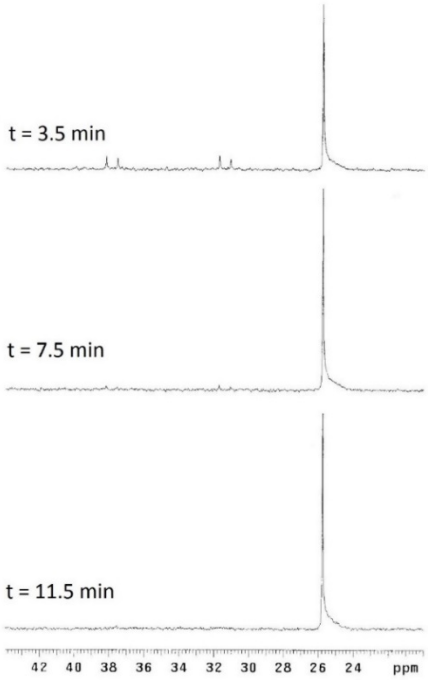

Figure 165. Select ^{31}P NMR spectra obtained for 2.6 µL GD added to 2.6 mg UiO-66-NH_2 in 0.75 mL 0.5 M EM buffer.

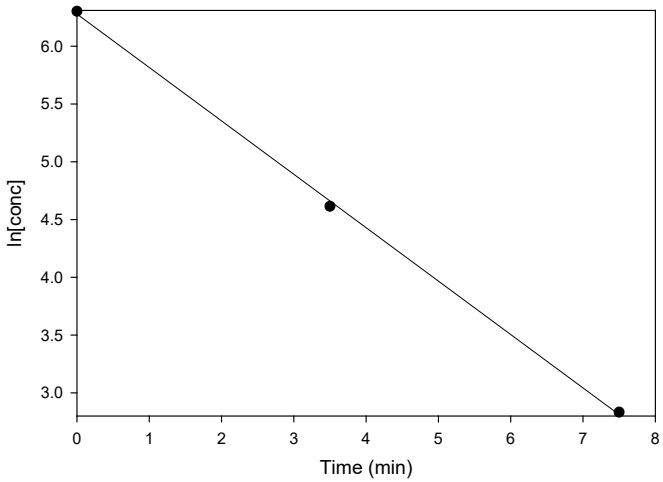

Figure 166. Plot of [GD] vs. time for ^{31}P NMR spectra obtained for 2.6 µL GD added to 2.6 mg UiO-66-NH_2 in 0.75 mL 0.5 M EM buffer.

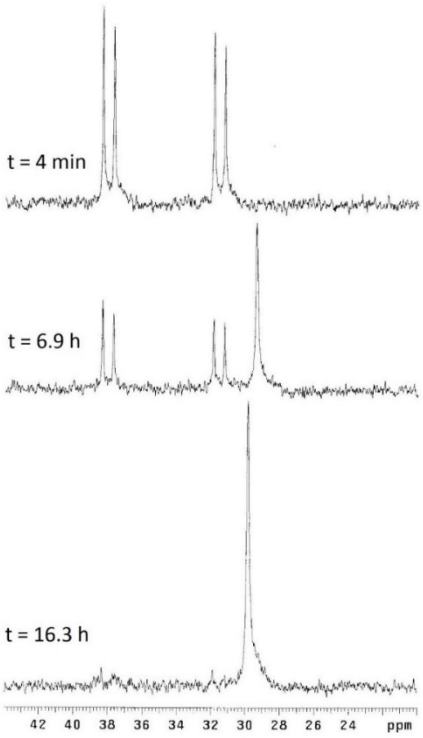

Figure 167. Select ^{31}P NMR spectra obtained for 2.6 µL GD added to 2.6 mg UiO-66-NH_2 in 0.75 mL water.

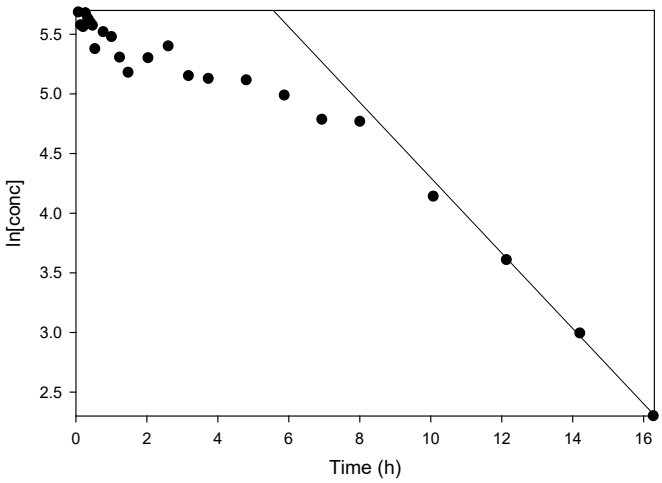

Figure 168. Plot of [GD] vs. time for ^{31}P NMR spectra obtained for 2.6 µL GD added to 2.6 mg UiO-66-NH_2 in 0.75 mL water.

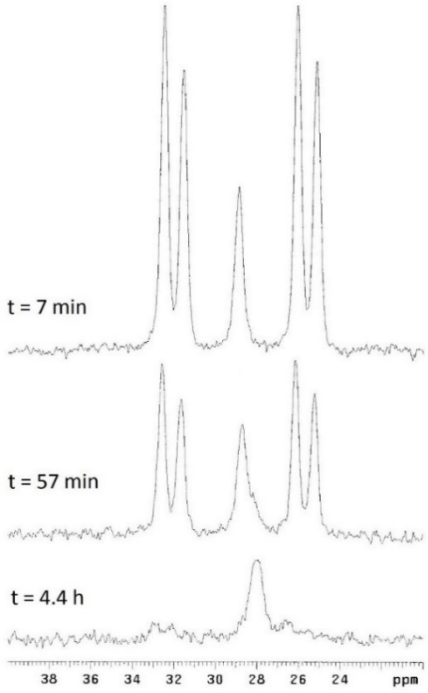

Figure 169. Select ^{31}P MAS NMR spectra obtained for 5 µL GD added to 100 mg UiO-66-NH_2.

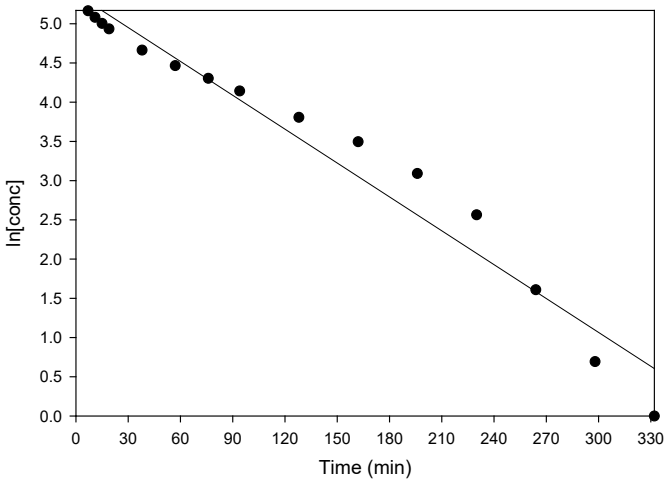

Figure 170. Plot of [GD] vs. time for ^{31}P MAS NMR spectra obtained for 5 µL GD added to 100 mg UiO-66-NH_2.

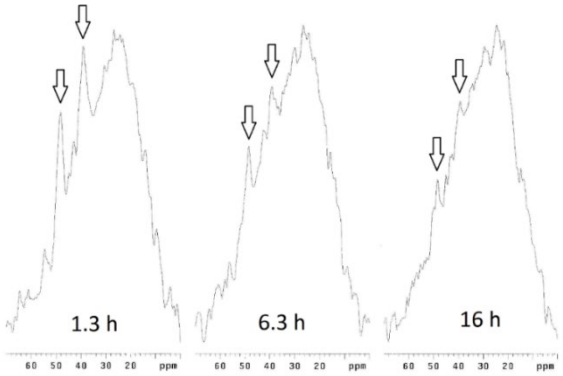

Figure 171. Select ^{13}C NMR spectra obtained for 5 µL HD added to 41 mg UiO-66-NH_2. Arrows indicate the two HD peaks (see text).

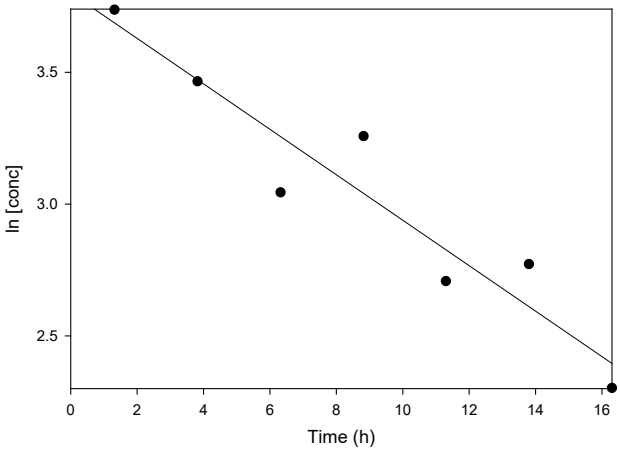

Figure 172. Plot of [HD] vs. time for ^{13}C NMR spectra obtained for 5 µL HD added to 41 mg UiO-66-NH_2.

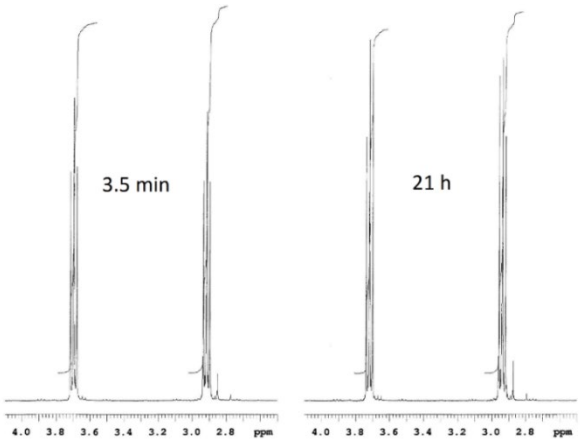

Figure 173. Select ^{1}H NMR spectra obtained for 5 µL HD added to 5 mg UiO-66-NH_2 in 0.75 mL CD_3CN. Integrals are shown for the two HD peaks (see text).

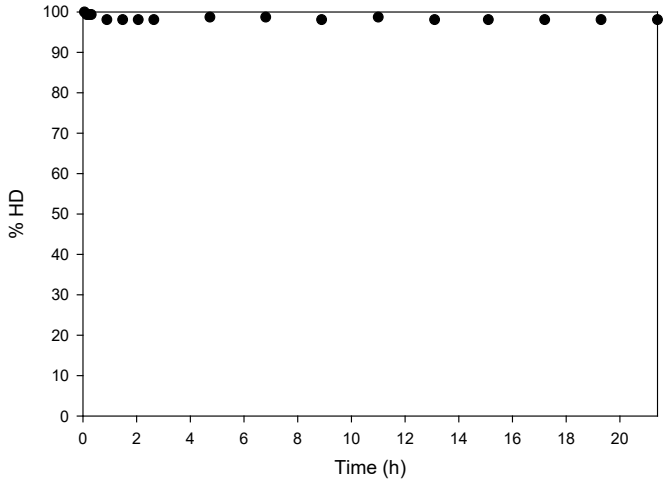

Figure 174. Plot of [HD] vs. time for ^{1}H NMR spectra obtained for 5 µL HD added to 5 mg UiO-66-NH_2 in 0.75 mL CD_3CN.

Table 15. Results for Reactions of GD and HD with UiO-66-NH_2

Chemical and Conditions	Performance
GD with 0.5 M EM buffer of pH 10	$t_{1/2}$ = 1.5 min
GD in water (no buffer)	Final $t_{1/2}$ = 2.2 h
GD on neat solid	$t_{1/2}$ = 48 min
HD on neat solid	$t_{1/2}$ = 8.0 h
HD in CH_3CN	98 % HD left after 21 h

GD reacts very quickly in the presence of EM buffer at pH 10, but the reaction is very slow in neutral water. The half-life on the neat solid is 48 min. HD reacts quite slowly with the neat solid, exhibiting a half-life of 8.0 h. This is confirmed by the HD in CH_3CN solution experiment which showed 98 % HD remaining after 21 h.

5.5.7 DRIFTS

The DRIFTS spectra of CEES on UiO-66-NH_2 is shown in Figure 175. The loss at 3670 cm^{-1} is attributed to Zr-OH stretching modes. The increasing peak at 1290 cm^{-1} is assigned to out-of-plane CH_2 bending (wagging) modes.

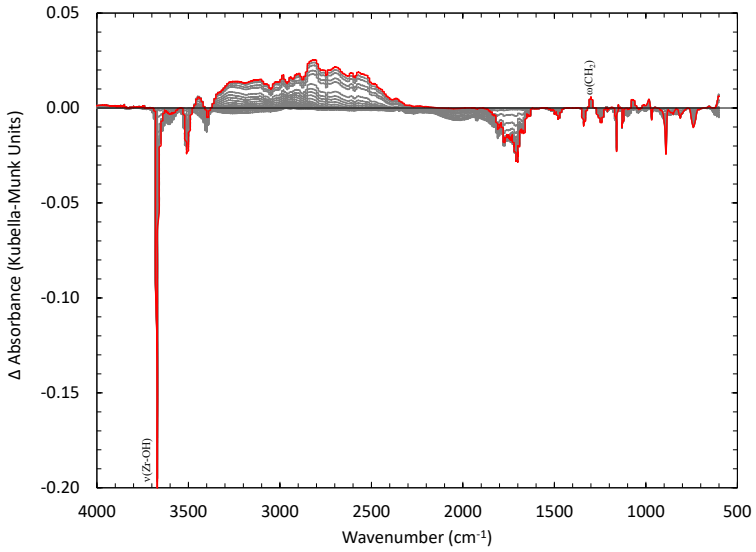

Figure 175. DRIFTS spectra of CEES on UiO-66-NH_2

The DRIFTS spectra of HD on UiO-66-NH_2 is shown in Figure 176. The loss at 3670 cm^{-1} is attributed to Zr-OH stretching modes. The positive peak at 1180 cm^{-1} is assigned to both in-plane $S(CH_2)$ bending modes and in-plance $Cl(CH_2)$ bending modes.

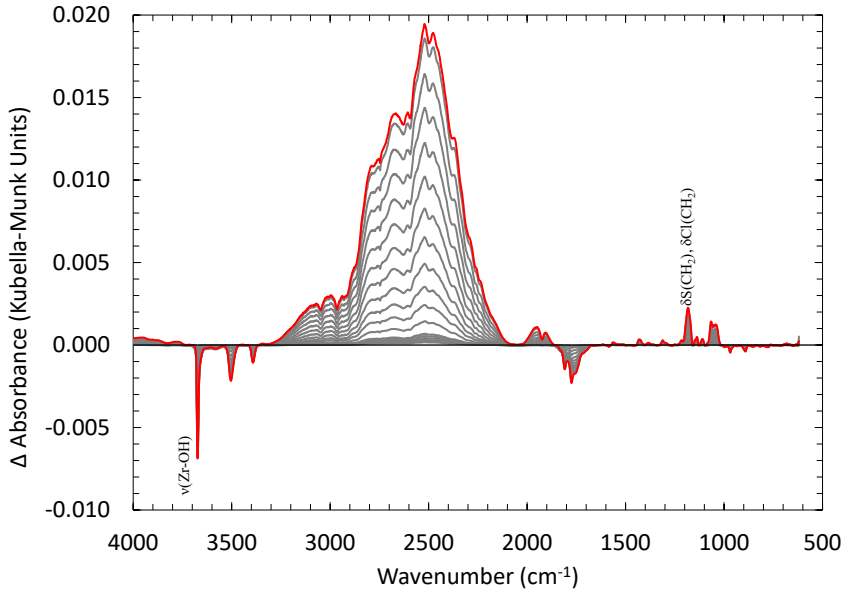

Figure 176. DRIFTS spectra of HD on UiO-66-NH_2

The DRIFTS spectra of DMMP on UiO-66-NH_2 is shown in Figure 177. Adsorption of DMMP on UiO-66-NH_2 in the IR spectra shows a loss in the isolated OH band and NH_2 bands indicating two adsorption sites. Adsorption of DMMP can be seen by the increase and redshift in the P=O band down to 1216 cm^{-1}. The DMMP molecule looks to stay relatively intact and does not dissociate or react with the surface. Possible methoxy-species might be present around 2800 cm^{-1}.

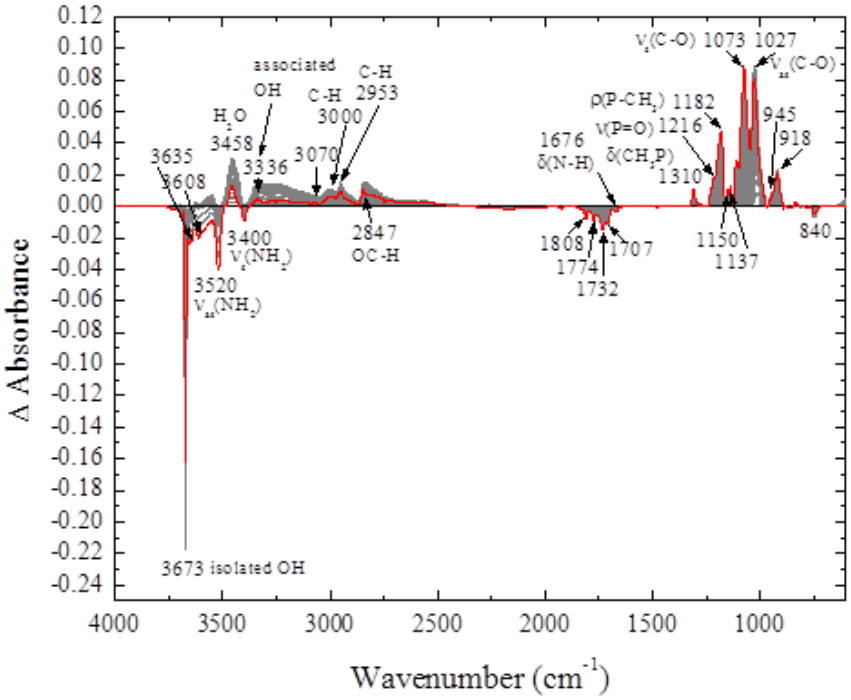

Figure 177. DRIFTS spectra of DMMP on UiO-66-NH_2

The DRIFTS spectra of GB on UiO-66-NH_2 under dry conditions is shown in Figure 178. Losses at 3670 cm^{-1}, 3520 cm^{-1}, and 3410 cm^{-1} are attributed to Zr-OH stretching modes, NH_2 stretching modes, and NH_2 stretching modes, respectively. Increasing peaks at 1190 cm^{-1}, 1180 cm^{-1}, and 1030 cm^{-1} are assigned to P=O stretching modes, in-plane CH_3 bending modes, and C-O stretching modes, respectively.

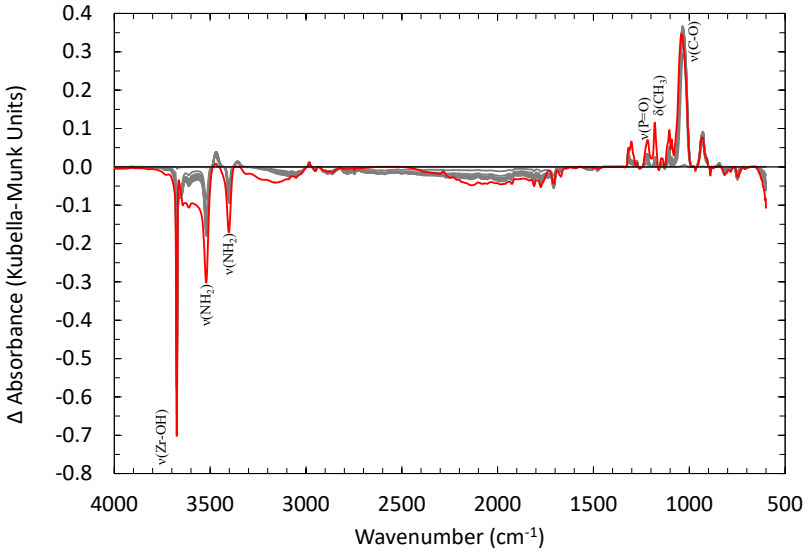

Figure 178. DRIFTS spectra of dry GB on UiO-66-NH_2

The DRIFTS spectra of GB on UiO-66-NH_2 under wet conditions is shown in Figure 179. The loss at 3680 cm^{-1} is attributed to Zr-OH stretching modes. Increasing peaks at 1220 cm^{-1}, 1150 cm^{-1}, and 1090 cm^{-1} are assigned to P=O stretching modes, in-plane CH_3 bending modes, and O-P-O stretching modes, respectively.

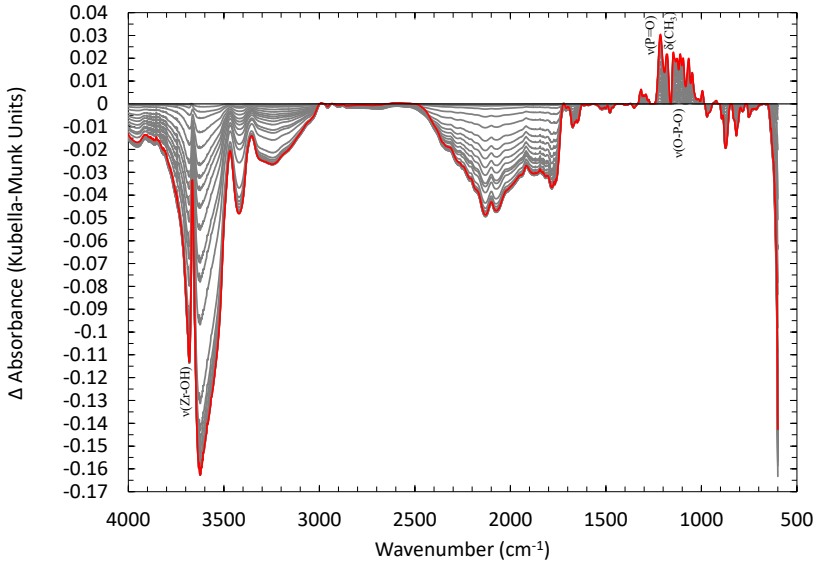

Figure 179. DRIFTS spectra of wet GB on UiO-66-NH_2

The DRIFTS spectra of GD on UiO-66-NH_2 is shown in Figure 180. Losses at 3670 cm^{-1}, 3510 cm^{-1}, and 3410 cm^{-1} are attributed to Zr-OH stretching modes, NH_2 stretching modes, and NH_2 stretching modes, respectively. Increasing peaks at 1210 cm^{-1}, 1180 cm^{-1}, and 1070 cm^{-1} are assigned to P=O stretching modes, in-plane CH_3 bending modes, and O-P-O stretching modes, respectively.

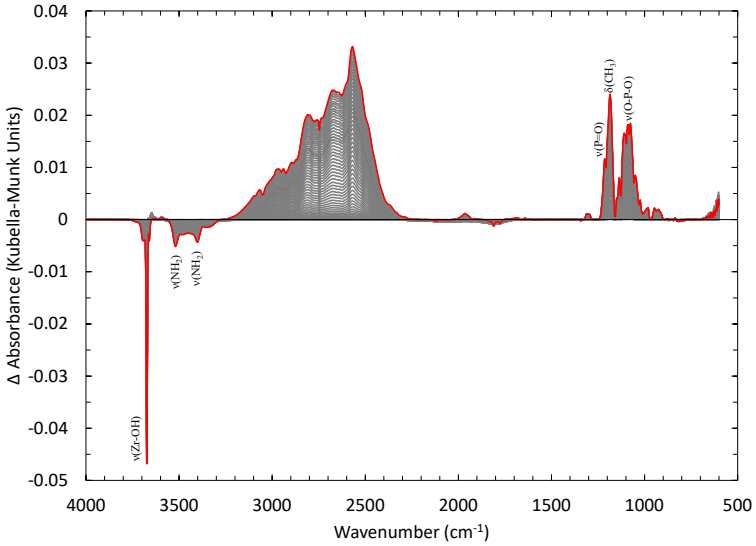

Figure 180. DRIFTS spectra of GD on UiO-66-NH_2

The DRIFTS spectra of malathion on UiO-66-NH_2 is shown in Figure 181. Losses at 3670 cm^{-1}, 3520 cm^{-1}, and 3400 cm^{-1} are attributed to Zr-OH stretching modes, NH_2 stretching modes, and NH_2 stretching modes, respectively. Increasing peaks at 1180 cm^{-1} and 1020 cm^{-1} are assigned to both P=S stretching modes and P-S modes, and C-O stretching modes, respectively.

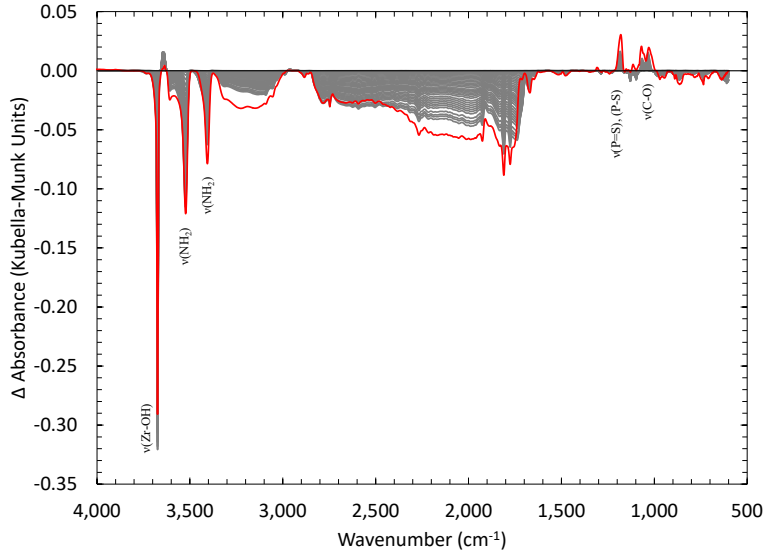

Figure 181. DRIFTS spectra of malathion on UiO-66-NH_2

The DRIFTS spectra of VX on UiO-66-NH_2 is shown in Figure 182. Losses at 3670 cm^{-1}, 3530 cm^{-1}, and 3400 cm^{-1} are assigned to Zr-OH stretching modes, NH_2 stretching modes, and NH_2 stretching modes, respectively.

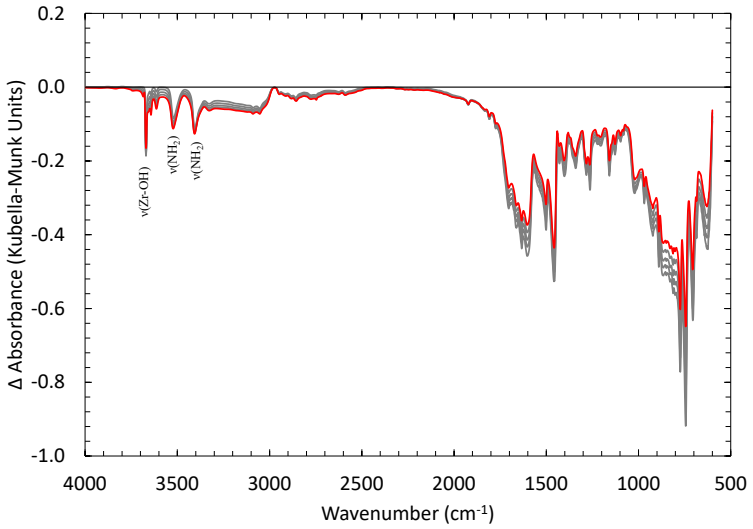

Figure 182. DRIFTS spectra of VX on UiO-66-NH_2

5.6 NU-1000

While zirconium-based MOFs are promising for filtration applications due to their high thermal and chemical stability, many of these MOFs have pore apertures that are too small to allow for diffusion of molecules of interest to the interior space of the MOF where a majority of the reactive sites are located. A novel Zr_6-based MOF, NU-1000, has been recently synthesized to overcome these challenges[99, 100]. NU-1000 is built up from eight connected $Zr_6(\mu_3\text{-}O)_4(\mu_3\text{-}OH)_4(H_2O)_4(OH)_4$ nodes and tetratopic 1,3,6,8(p-benzoate)pyrene ($tbapy^{4-}$) linkers. The resulting structure consists of wide channels (31 Å) into which are directed a total of four terminal-zirconium-ligated aquo and hydroxo groups per node along with an additional four in smaller 10 Å channels. The larger channels and increased number of exposed reactive sites relative to the UiO-66 MOFs make this MOF an ideal candidate for gas sorption and catalysis applications.

While this MOF is still relatively new and limited studies have been done on the capacity of NU-1000 for removal of TICs and CWAs, the work that has been done shows that this MOF is indeed promising. NU-1000 has already shown a high degree of activity for soman with a half-life of only 3 minutes, under buffered conditions. Additionally, it has been shown that NU-1000 can be readily modified through solvent-assisted ligand incorporation (SALI) to incorporate different functionalities onto the exposed hydroxyl groups. Incorporation of perfluoroalkanes to NU-1000 through SALI significantly increased the CO_2 uptake of the MOF and proved the ability to modify the exposed hydroxyl groups of the SBU[101]. The remarkably wide pores and ability to functionalize the hydroxyl groups to tune the chemical make up inside of the pores makes this MOF an exceptionally versatile and attractive material for gas sorption and catalysis applications.

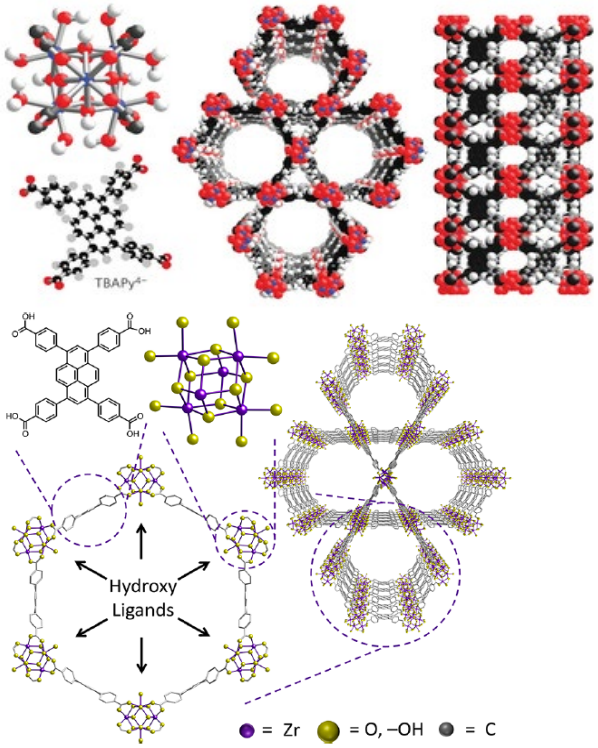

Figure 183. Structure of NU-1000[99]

5.6.1 PHYSICAL PROPERTIES

The x-ray diffraction spectrum of NU-1000 is shown in Figure 184. NU-1000 has three major XRD peaks over the range evaluated, consistent with simulated spectra[102]. Peaks at 2-theta values around 5, 7.5, and 10.5 degrees correspond to the (200), (201), and (400) faces of NU-1000, respectively. Of note is that a major peak also exists at a 2-theta value of 2.5 degrees, corresponding to the (100) face of NU-1000, which is outside the range evaluated.

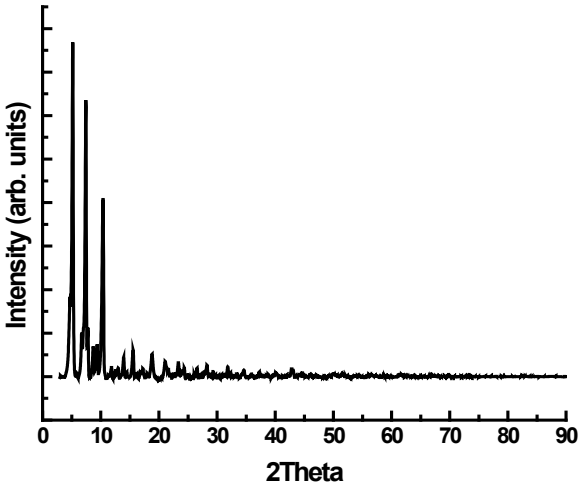

Figure 184. XRD spectra of NU-1000

SEM images of NU-1000 are depicted in Figure 185. NU-1000 is known to have a morphology resembling hexagonally-shaped rod crystals[99, 103, 104], and this is also observed here. Particle sizes were roughly 15-20 um in length, within range of previously reported literature values[99].

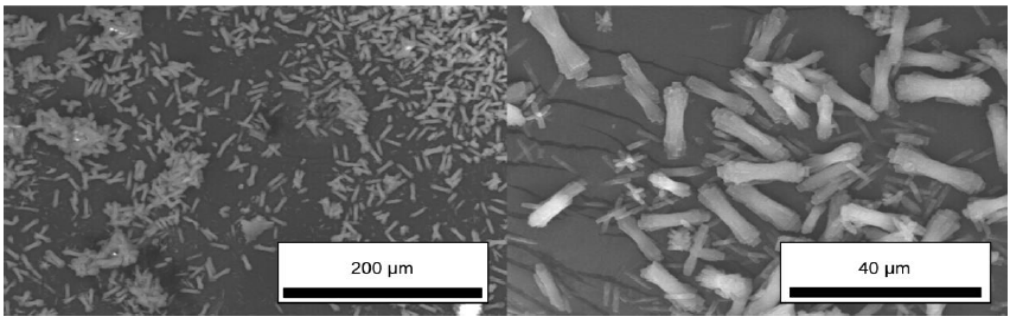

Figure 185. SEM images of NU-1000

The TGA profile for NU-1000 is consistent with literature[105] where only bulk physisorbed water is emitted up to 100 C, and the collapse of the structure to ZrO_2 proceeds around 450-500 C, analogously to the UiO MOFs.

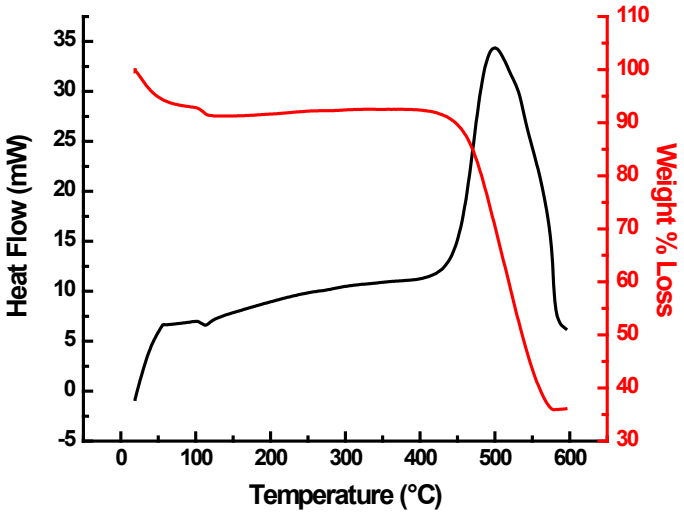

Figure 186. TGA profile of NU-1000

5.6.2 SURFACE PROPERTIES

FTIR spectra of NU-1000 are depicted in Figure 187. The profile is very similar to UiO-66, as the structures have very similar chemical framework and connectivity, and so assignment can be inferred analogously. Namely, the peak around 1400 cm^{-1} can be attributed to O-C-O symmetric stretching, the peak around 1600 cm^{-1} can be attributed to C-C ring bending modes, and the broad peak around 800 cm^{-1} can be attributed to O-H bending and C-H bending modes in the structure.

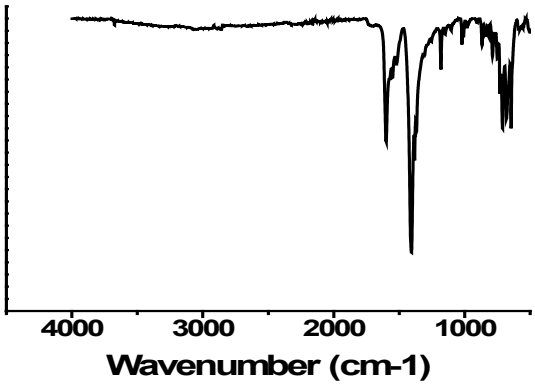

Figure 187. FTIR spectra of NU-1000

Raman spectra for NU-1000 are depicted in Figure 188. Analogous to UiO-66, vibrations containing benzene ring and carboxylate modes are most active in Raman spectroscopy. Strong C-C ring vibrations at 1540 cm^{-1}, followed by peaks at 1420 cm^{-1} (O-C-O symmetric stretching), 1100 cm^{-1} (C-C ring), and 850 cm^{-1} (O-H bend + C-H bending) are analogous to UiO-66. Additionally, however, there are exceptionally strong peaks at 1250 cm^{-1} and 400 cm^{-1}. The peak at 1250 cm^{-1} may be a collective mode of the 1,3,6,8(p-benzoate)pyrene linker, as UiO-67 possesses a peak around this wavelength attributed to a

collective mode of its biphenyl dicarboxylate linker[78] and the NU-1000 linker is a similarly large aromatic system. The high number of benzene rings comprised within this linker would easily justify the strength of this peak. The peak around 400 cm^{-1} may be due to out-of-plane C-C ring deformations, as similar peaks in this region been attributed to UiO-66 and UiO-67 to a much lower intensity[78], and they possess much fewer C-C ring bonds.

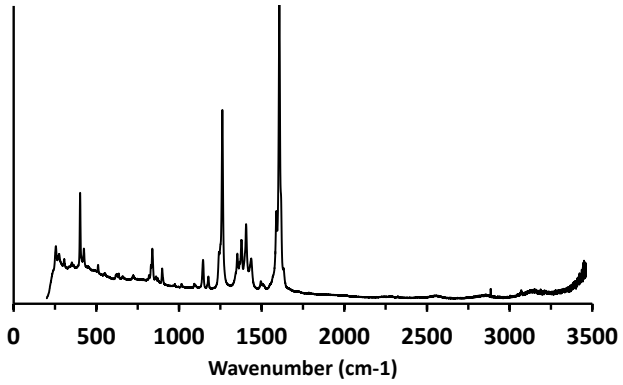

Figure 188. Raman spectra of NU-1000

5.6.3 ELECTRONIC AND OPTICAL PROPERTIES

The UV-Vis spectra of NU-1000 is shown in Figure 189. While similar to the UiO-66 spectra in its general profile, the absorption edge occurs at much higher wavelength (lower energy) in NU-1000. This is likely attributed to ease of ligand-to metal UV adsorption of Zr-O oxo-clusters and ligand-based adsorption influenced by the nearby metal centers due to the extensive aromatic network present in the linker. The Tauc plot of NU-1000 is shown in Figure 190, with a calculated band gap of 2.45 eV. Simulant-exposed UV-vis spectra of NU-1000 are shown in Figure 191. Quenching is observed in the UV region upon exposure with all chemicals with a slight red shift in the absorption edge of the spectra for all simulants, indicative of a slightly reduced band gap of the resulting material.

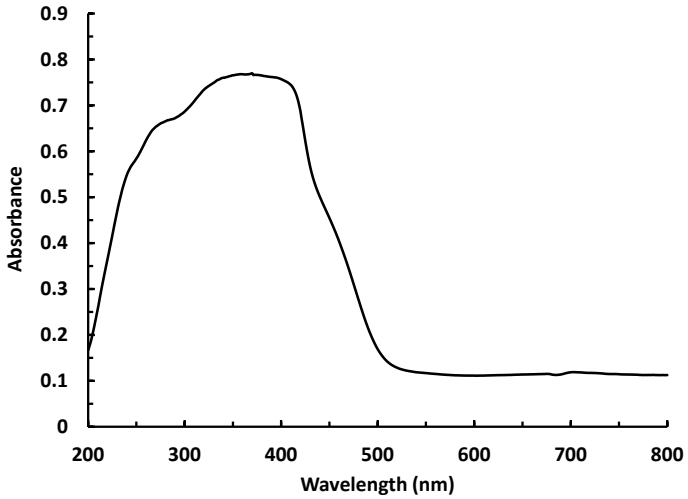

Figure 189. UV-Vis spectra of NU-1000

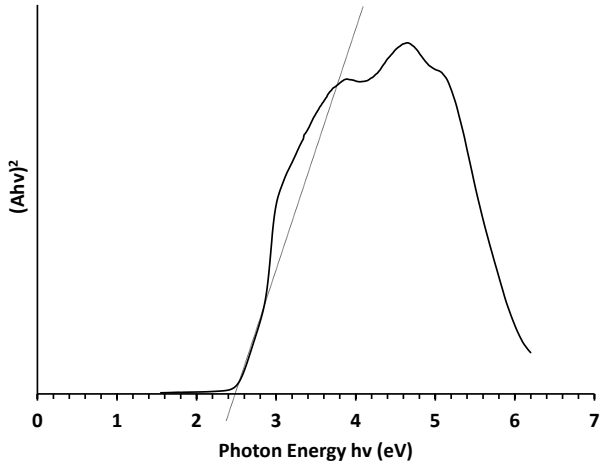

Figure 190. Tauc plot of NU-1000

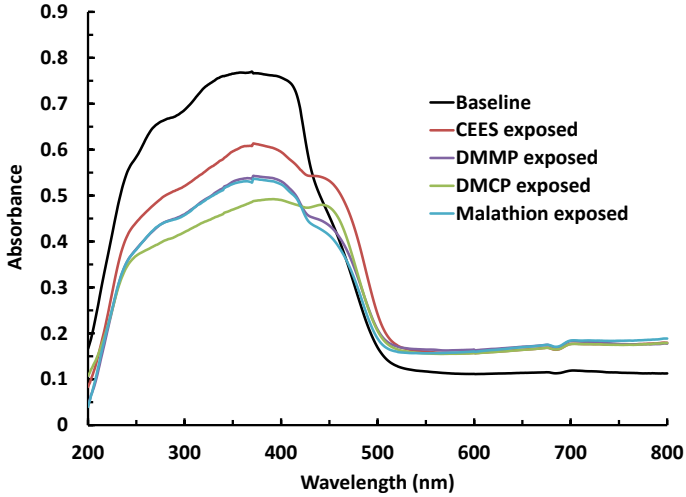

Figure 191. UV-Vis spectra of simulant-exposed NU-1000

Fluorescence spectra of NU-1000 is shown in Figure 192. An extremely intense doublet peak around 500 nm and 525 nm is observed, the magnitude of which is anticipated as compounds containing aromatic groups with low-energy $\pi \rightarrow \pi^*$ transitions, found in the NU-1000 linker, are known to exhibit strong fluorescence, with quantum efficiency increasing with increasing number of rings in the compound. Fluorescence spectra of simulant-exposed NU-1000 are shown in Figure 193. With the exception of DMCP, all chemicals produced an overall fluorescence intensity similar to the baseline NU-1000; however, the ratio of the intensity of the 500 nm peak to the 525 nm peak varies with each chemical. With malathion and DMMP exposure, the 500 nm peak is of greater intensity than the 525 nm peak, similar to the unexposed material, but with CEES and DMCP exposure, the 525 nm peak is of greater intensity than the 500 nm peak. This suggests that exposure to chlorine may play a role in altering this ratio.

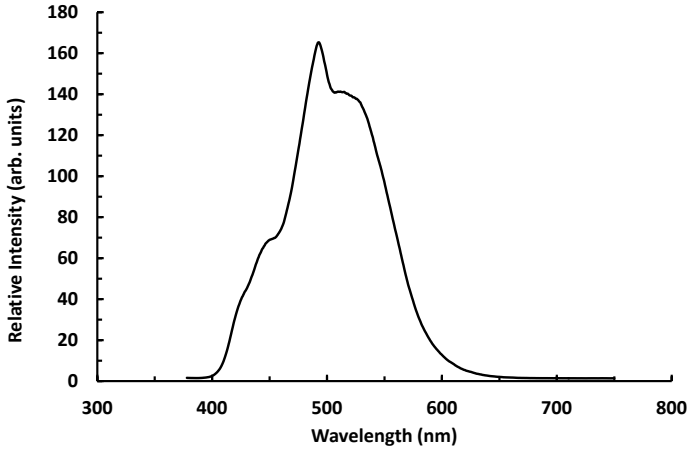

Figure 192. Fluorescence spectra of NU-1000

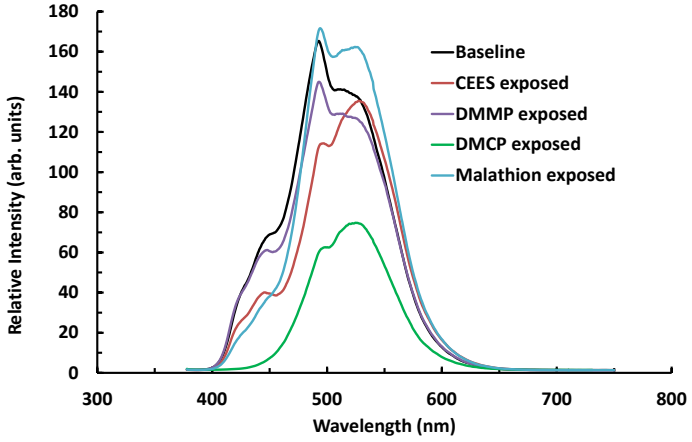

Figure 193. Fluorescence spectra of simulant-exposed NU-1000

5.6.4 ADSORPTION AND REACTION CHARACTERIZATION

The N_2 isotherm of NU-1000 is shown in Figure 194, with selected physical parameters shown in Table xx. NU-1000 exhibited a type IV isotherm, consistent with literature data[106]. BET surface area was 1713 m^2/g, slightly lower than literature values, which have typically been reported in the 2000-2300 m^2/g range[107, 108].

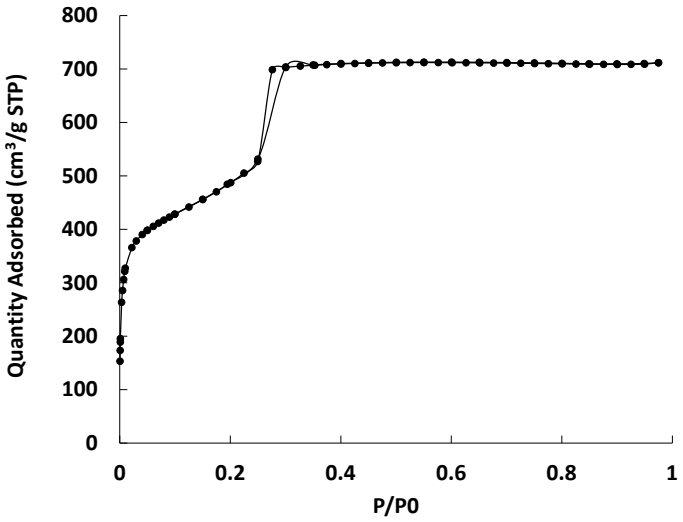

Figure 194. N_2 isotherm of NU-1000

Table 16. Physical properties of NU-1000

BET SA (m^2/g)	Total PV (cc/g)	Micropore Volume (cc/g)
1713	1.3020	0.6824

Water isotherm data for NU-1000 is shown in Figure 195. Despite its high surface area, very low water uptake is observed for NU-1000. This is likely due to its low concentration of hydrogen-bonding surface moieties, as depicted in the pKa distribution in the following section.

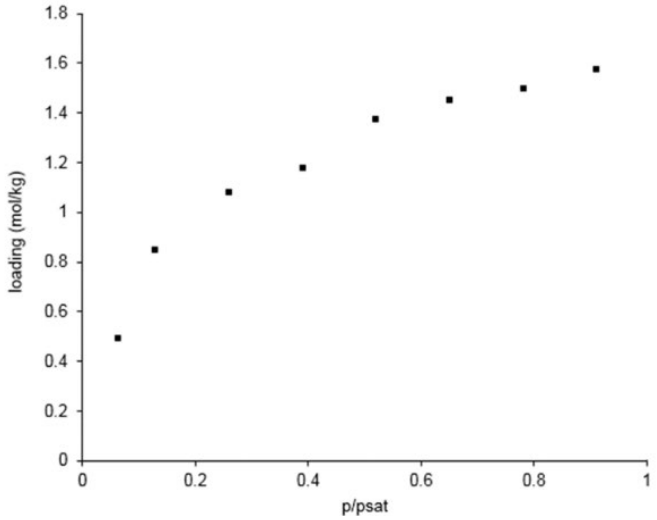

Figure 195. Water isotherm for NU-1000

The pKa distribution for NU-1000 is shown in Figure 196. The three main peaks present at pKa values of 3.6, 6.0, and 8.2 have been assigned to u3-OH protons, -OH_2 protons, and –OH protons in the node, respectively[5]. A fourth pKa peak at 9.5, shown here, was also reported in literature supporting

information but not considered a real and distinct pKa value[5]. That peak, as well as the peak around pKa of 5, may be due to a combination of $Zr(OH)_2$, $Zr(OH)(OH_2)$, or $Zr(OH_2)_2$ groups that is analogously found on zirconium hydroxide and can be assigned to peaks in those regions[2]. The calculated point of zero charge of the material was 7.2.

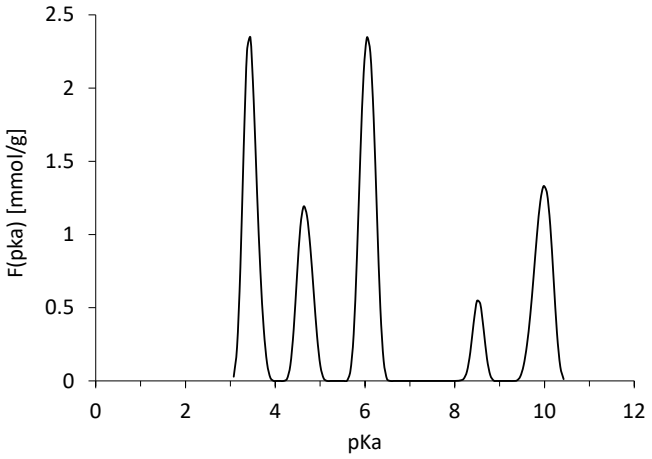

Figure 196. pKa distribution of NU-1000

5.6.5 DOSE AND EXTRACTION TECHNIQUE

CEES and HD removal were both low on NU-1000 with CEES mildly overpredicting HD performance. G simulant performance progressed in the order DMMP < DFP < DMCP, with all 3 materials overpredicting GB and GD reactivity by a wide margin. Malathion performance largely underpredicted VX capabilities.

Table 17. Dose-extraction results for NU-1000

CEES		HD		DMCP		DFP		DMMP		GB		GD		Malathion		VX	
%R	SD	%R	SD	%R	SD	%R	SD	%R	SD	%R	SD	%R	SD	%R	SD	%R	SD
17.4	9.3	7.0	-	79.8	1.3	79.8	2.6	49.3	2.8	16.0	-	0	0	14.6	1.1	53.0	-

5.6.6 NMR

^{31}P NMR was used to investigate the catalytic activity of NU-1000 in water, with and without 0.5 M EM buffer (pH 10), and on the sorbent itself. ^{31}P NMR spectra and kinetic plots are shown in Figures 197-202. Results are given in Table 18.

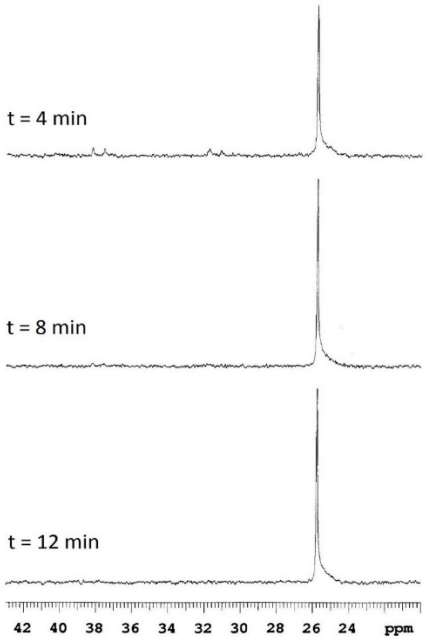

Figure 197. Select ^{31}P NMR spectra obtained for 2.6 µL GD added to 3.3 mg NU-1000 in 0.75 mL 0.5 M EM buffer.

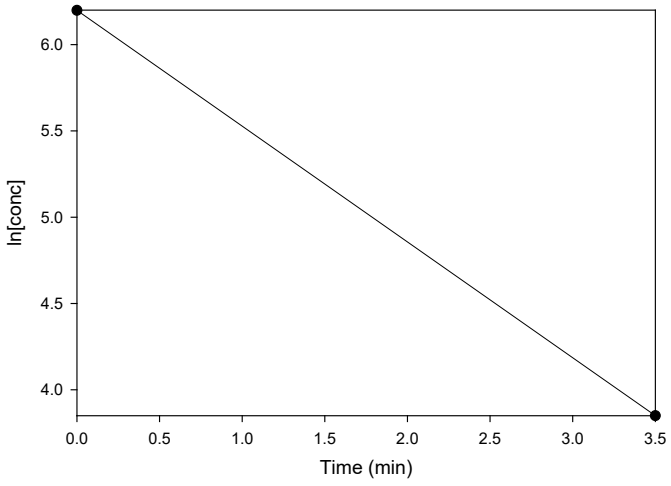

Figure 198. Plot of [GD] vs. time for ^{31}P NMR spectra obtained for 2.6 µL GD added to 3.3 mg NU-1000 in 0.75 mL 0.5 M EM buffer.

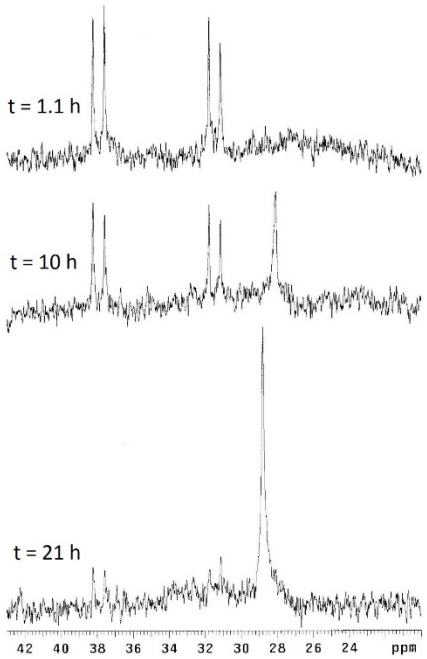

Figure 199. Select ^{31}P NMR spectra obtained for 2.6 µL GD added to 3.3 mg NU-1000 in 0.75 mL water.

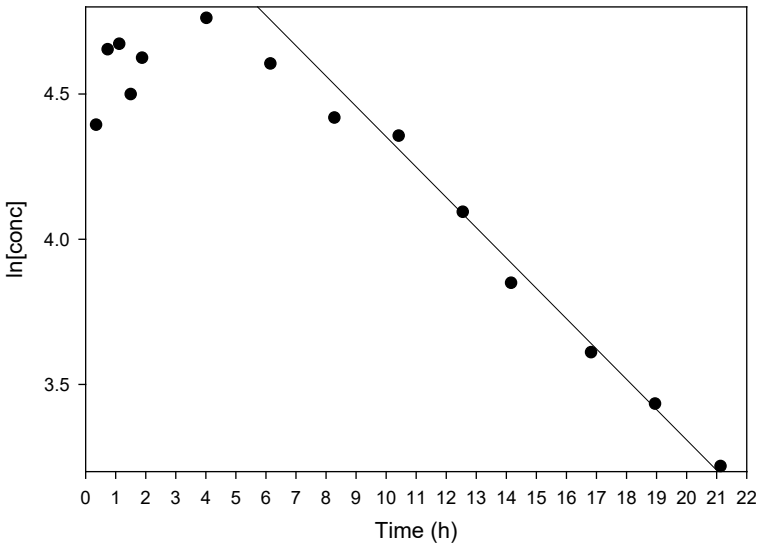

Figure 200. Plot of [GD] vs. time for ^{31}P NMR spectra obtained for 2.6 µL GD added to 3.3 mg NU-1000 in 0.75 mL water.

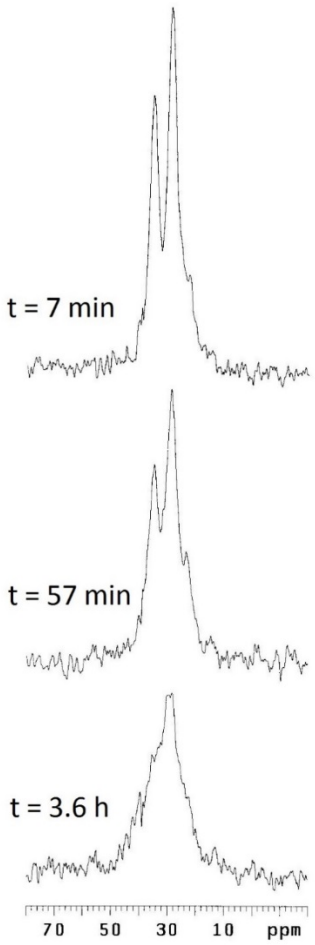

Figure 201. Select ^{31}P NMR MAS NMR spectra obtained for 5 μL GD added to 19.4 mg NU-1000.

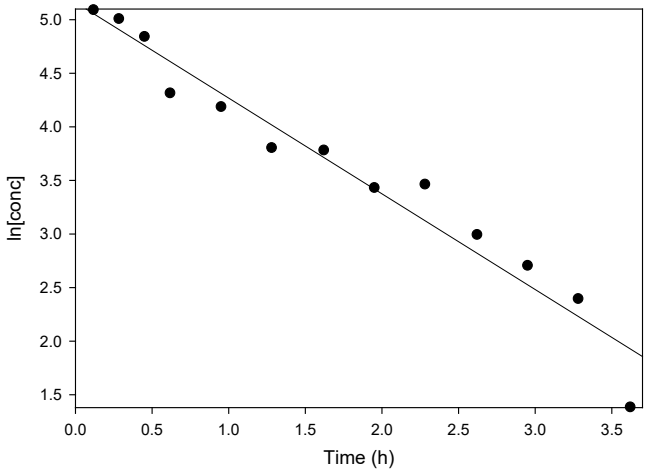

Figure 202. Plot of [GD] vs. time for ^{31}P NMR MAS NMR spectra obtained for 5 μL GD added to 100 mg NU-1000.

Table 18. Reactivity of GD with NU-1000

Conditions	Performance
0.5 M EM Buffer, pH 10	$t_{1/2}$ = 1 min
Neutral water (no buffer)	Final $t_{1/2}$ = 6.6 h
Neat GD on sorbent	$t_{1/2}$ = 36 min

GD with NU-1000 in water buffered at pH 10 with EM buffer reacts very fast, with a half-life of 1 min. However, in neutral water with no buffer, a final half-life of 6.6 h is observed. On the neat sorbent, GD reacts with a half-life of 36 min.

5.6.7 DRIFTS

The DRIFTS spectra of CEES on NU-1000 is shown in Figure 203. The loss at 3670 cm^{-1} is attributed to Zr-OH stretching modes. Increasing peaks at 2920 cm^{-1} and 1210 cm^{-1} are assigned to CH_2 stretching modes and out-of-planing CH_2 bending (wagging) modes, respectively.

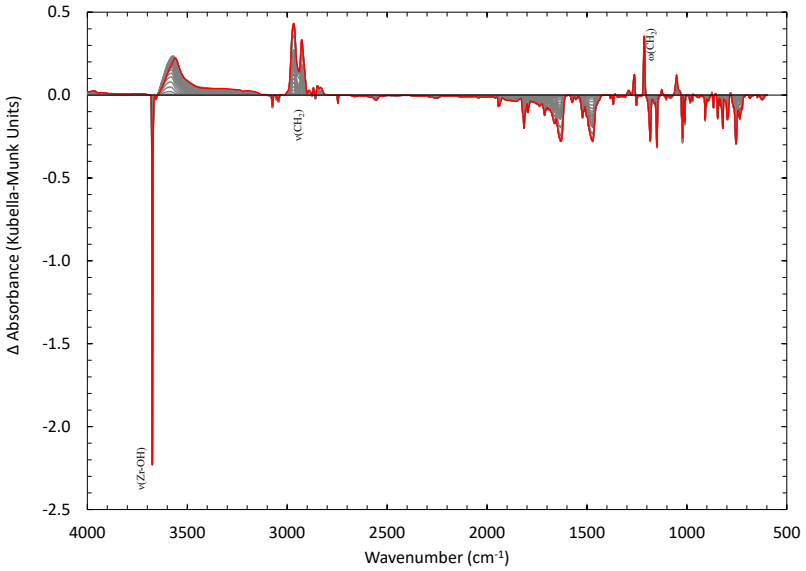

Figure 203. DRIFTS spectra of CEES on NU-1000

The DRIFTS spectra of DMMP on NU-1000 is shown in Figure 204. Adsorption of DMMP on NU-1000 in the IR spectra shows a loss in the isolated OH band and an increase in the associated NH and OH band region indicating two possible adsorption sites. Adsorption of DMMP can be seen by the increase and blue shift in the P=O band up to 1263 cm^{-1}. Methoxy-species are present around 2800-2750 cm^{-1}. Carbonates/carboxylate species could also be present around 1570-1450 cm^{-1}.

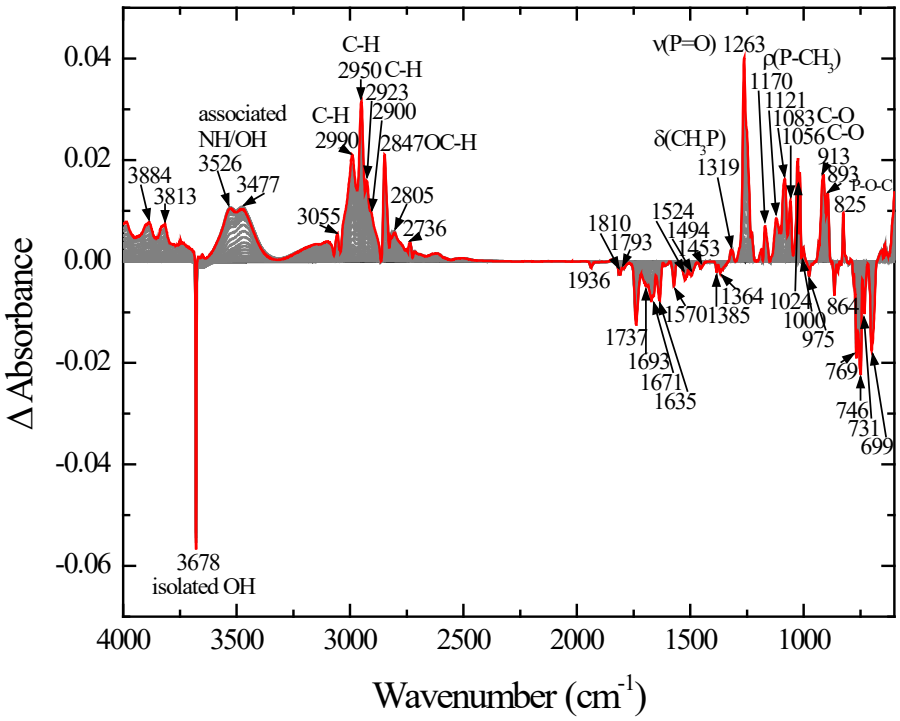

Figure 204. DRIFTS spectra of DMMP on NU-1000

The DRIFTS spectra of DMCP on NU-1000 is shown in Figure 205. The loss at 3680 cm^{-1} is attributed to Zr-OH stretching modes. Increasing peaks at 1300 cm^{-1}, 1200 cm^{-1}, and 1070 cm^{-1} are assigned to in-plane P-CH_3 bending modes, P=O stretching modes, and O-P-O stretching modes, respectively.

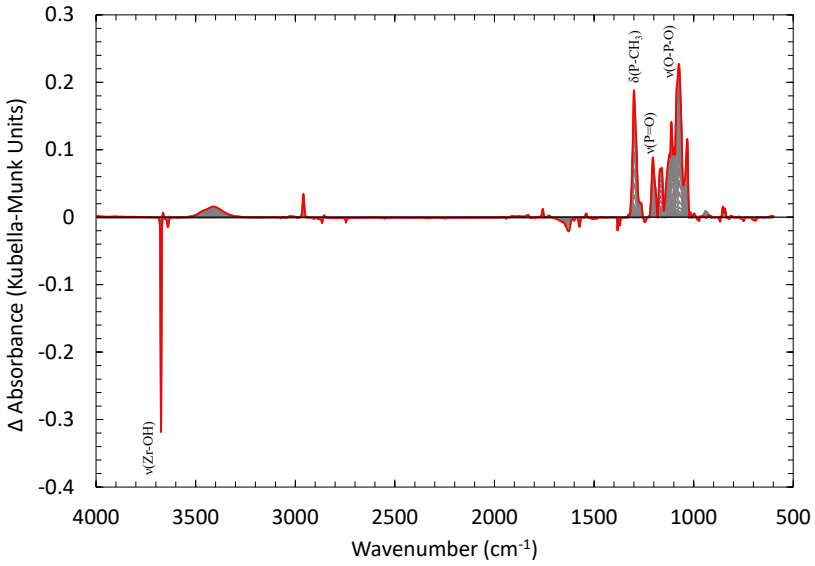

Figure 205. DRIFTS spectra of DMCP on NU-1000

The DRIFTS spectra of malathion on NU-1000 is shown in Figure 206. The loss at 3670 cm^{-1} is attributed to Zr-OH stretching modes. Increasing peaks at 2960 cm^{-1}, 1190 cm^{-1}, and 1040 cm^{-1} are assigned

to both CH_3 and CH_2 stretching modes, both P=S stretching modes and P-S modes, and C-O stretching modes, respectively.

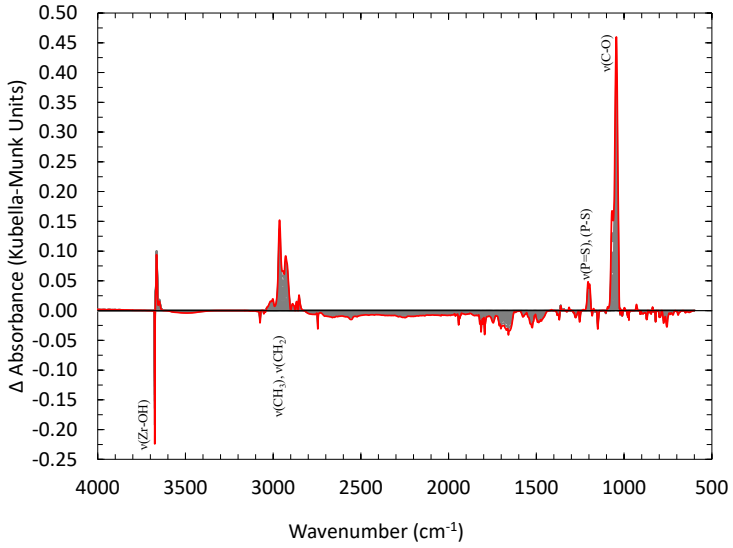

Figure 206. DRIFTS spectra of malathion on NU-1000

The DRIFTS spectra of VX on NU-1000 is shown in Figure 207. The loss at 3670 cm^{-1} is attributed to Zr-OH stretching modes. Increasing peaks at 2970 cm^{-1} and 1410 cm^{-1} are assigned to C-H stretching modes and in-plane C-H bending modes, respectively.

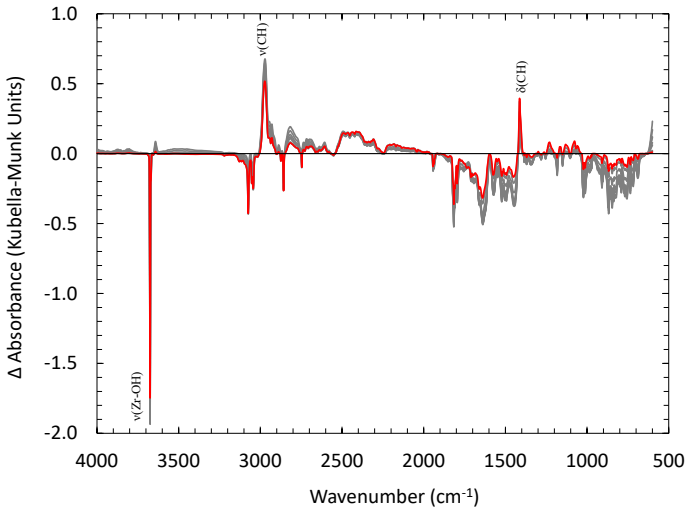

Figure 207. DRIFTS spectra of VX on NU-1000

6. ANALYSIS AND DISCUSSION

6.1 CHEMICAL SENSING

6.1.1 ASSESSMENT OF SPECTRAL PROPERTIES OF SIMULANT-EXPOSED MATERIALS

As previously discussed, fluorescence occurs fundamentally when a material absorbs a photon, elevating a valence electron to a higher-energy quantum state, and then, on the nanosecond time scale, the absorbing molecule loses some of the energy acquired via internal conversion and/or vibrational relaxation events, and the photon is emitted through the process of the electron making a transition back to its original quantum state. The aforementioned energy loss causes the emitted photon to be of lower energy and longer wavelength than the absorbed photon, which typically shifts its properties further towards the visible light spectrum. There are typically a large number of vibrational levels that can be coupled into the transition between electronic states in a material, and so photon emission is usually distributed over a range of wavelengths.

In order for a valence electron of a material to be excited to a higher energy level, the absorbed photon must be of an energy greater than or equal to the energy difference required to excite the aforementioned electron to its next level, also referred to as its band gap. Typically, for valence electrons in sigma molecular orbitals or localized pi molecular orbitals, this energy gap can only be bridged by photons of energy corresponding to the ultraviolet light wavelength spectrum. Delocalized pi electrons found in extensive conjugated aromatic systems, however, can be excited by lower-energy light in the visible wavelength range through $n \rightarrow \pi^*$ and $\pi \rightarrow \pi^*$ transitions, as shown in Figure 8. This type of electron network is found in the linkers of UiO-66, UiO-66-NH_2, and especially NU-1000, and this explains the high degree of spectral responsiveness of those three materials to simulant exposure.

Substitution in an aromatic network, through either adsorption or chemical reaction with its components, causes shifts in the wavelength of absorption maxima and corresponding changes in the fluorescence bands. Specifically, electron-donating substitutents have a favorable effect on fluorescence intensity, and electron-withdrawing substituents have an adverse effect. The three MOFs in this study all displayed this property with a high degree of specificity, as the 4 different simulants evaluated displayed unique fluorescence signatures in the spectra. This suggests that they all have high potential in detection applications and merits further analysis in future work to fully elucidate the electron transfer mechanisms involved and the exact sensitivy to gas-phase exposure specifically, as opposed to saturation by neat liquid challenge.

6.2 CHEMICAL PERFORMANCE

6.2.1 COMPARISON OF DOSE-EXTRACTION SIMULANT DATA TO DOSE-EXTRACTION AGENT DATA

6.2.1.1 COMPARISON BY CHEMICAL SET

6.2.1.1.1 COMPARISON OF CEES TO HD

Referee material performance against CEES and HD is compared in Figures 208, 209, and 210. In order to assess the full value of a simulant for representation of its corresponding agent performance, both quantitative and qualitative comparisons must be analyzed. An ideal simulant will yield performance data that both closely predicts agent performance and accurately depicts relative performance across a set of materials. Figures 208, 209, and 210 all show that CEES performance overpredicts HD performance by a substantial margin in many cases. The differences in reactivity can likely be explained as follows. CEES and HD both can be removed via a hydrolysis mechanism which involves the rate-determining step of forming a cyclic sulfonium ion intermediate[109]. Electron-donating groups such as the CH_3CH_2 moiety in CEES would stabilize the positive charge on the sulfur, but the $ClCH_2CH_2$ group of HD, containing the electron-withdrawing Cl, would be expected to be much less electron donating than an ethyl group, resulting in less stabilization of the sulfonium ion and therefore lower reactivity.

Figure 210 shows moderate correlation between CEES and HD reactivity, though it is not completely flawless. The major exception to this correlation is ferrihydrite, as the ratio between CEES and HD removal is much lower with that material than the others.

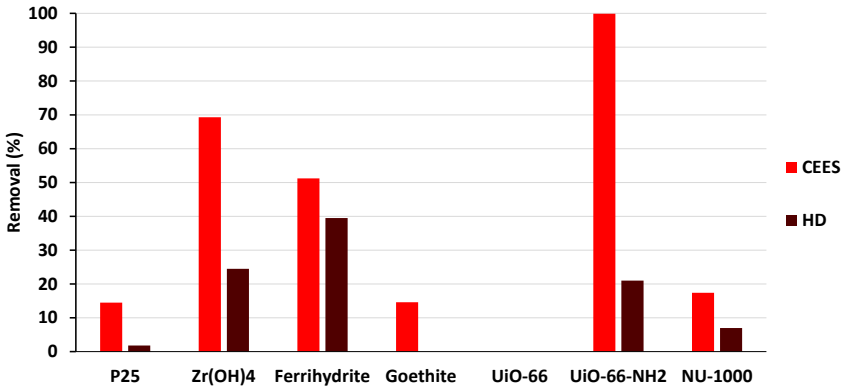

Figure 208. CEES and HD dose-extraction removal data for referee materials

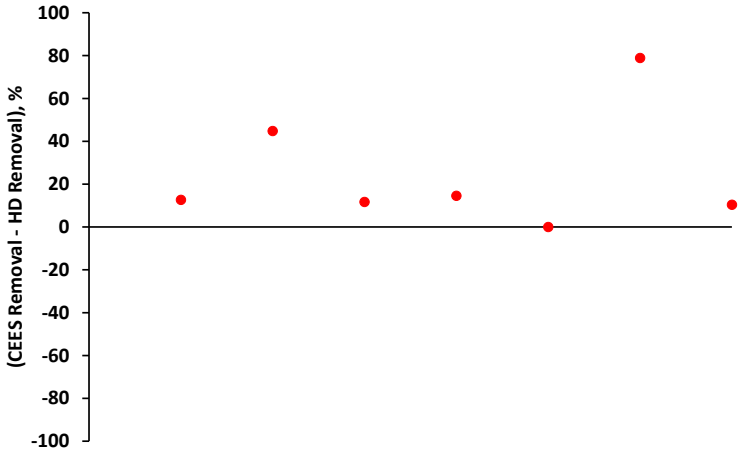

Figure 209. Differential data between CEES and HD dose-extraction removal percentage

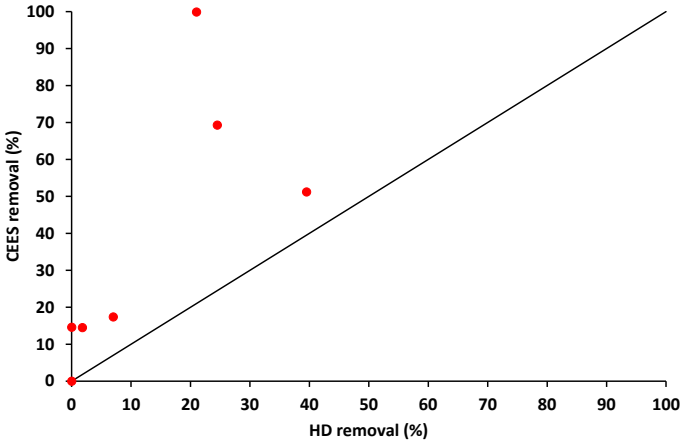

Figure 210. Plot of CEES dose-extraction removal versus HD dose-extraction removal. A line of slope equal to one passing through the origin is included to represent perfect correlation

6.2.1.1.2 COMPARISON OF DMMP, DFP, DMCP TO GB AND GD

Referee material performance against DMMP, DFP, and DMCP compared to GB is shown in Figures 211, 212, and 213, and performance against DMMP, DFP, and DMCP compared to GD is shown in Figures 214, 215, and 216. Several conclusions can be drawn from this data. First, the general removal trend among the G simulants for the referee materials progressed as DMMP < DFP < DMCP. This can be explained in terms of bond strengths, as reaction with these chemicals typically involves cleaving of P=O, P-F, and P-Cl bonds, with corresponding strengths of 544, 490, and 326 kJ/mol, respectively. Also, the simulant providing the best qualitative and quantitative predictability was not the same for both GB and GD. For GD, DFP was both the best quantitative removal predictor (in terms of lowest sum of squared deviations from agent removal data) and best qualitative removal predictor (in terms of highest R^2 value of the linear best-fit line, allowing for exclusion of one outlier value for each chemical). Conversely, for GB, DFP was still the best qualitative removal predictor, but DMCP was the best quantitative removal predictor. Therefore, this suggests that for GB, the choice of simulant should depend on the specific goal of the

experiment, whether to closely mimic the absolute removal performance or to correctly identify a removal trend among a set of materials.

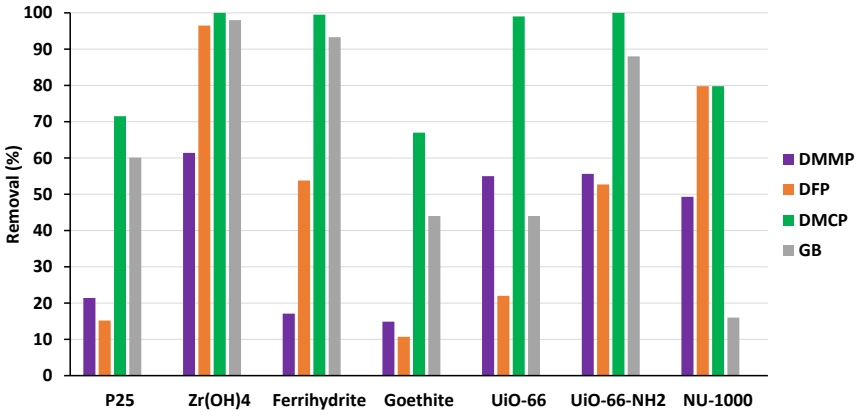

Figure 211. DMMP, DFP, DMCP, and GB dose-extraction removal data for referee materials

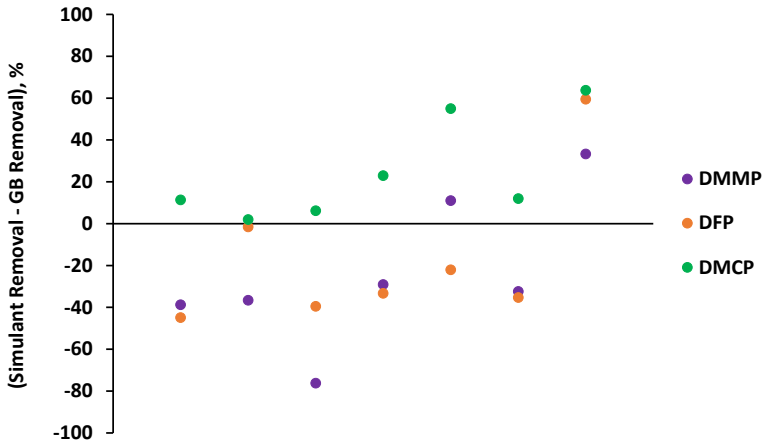

Figure 212. Differential data between DMMP, DFP, and DMCP and GB dose-extraction removal percentage

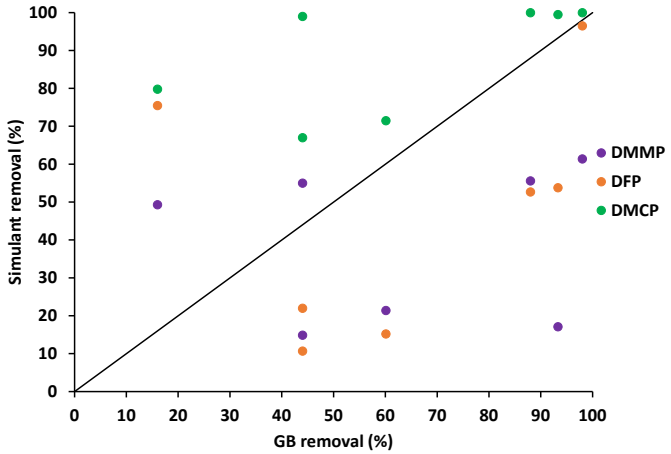

Figure 213. Plot of DMMP, DFP, and DMCP dose-extraction removal versus GB dose-extraction removal.

A line of slope equal to one passing through the origin is included to represent perfect correlation

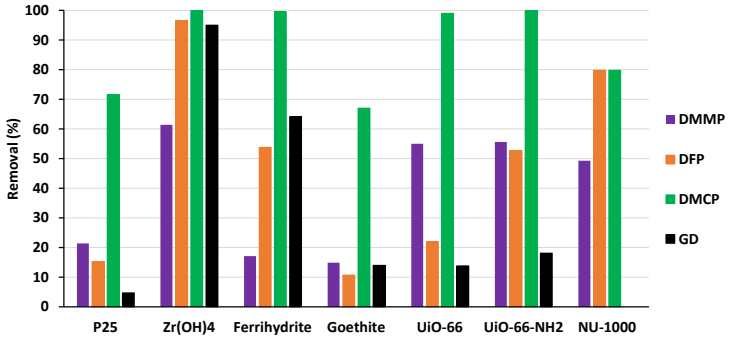

Figure 214. DMMP, DFP, DMCP, and GD dose-extraction removal data for referee materials

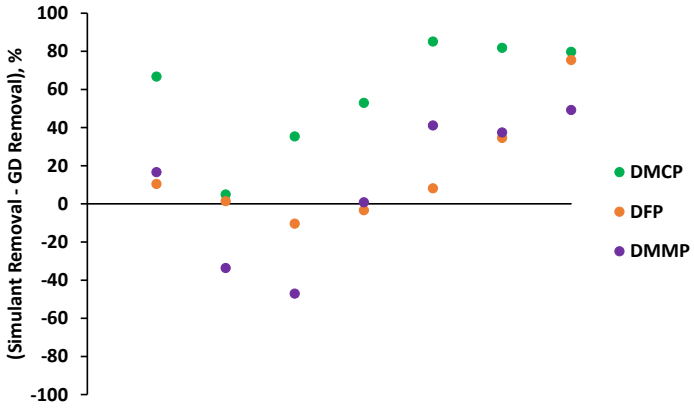

Figure 215. Differential data between DMMP, DFP, and DMCP and GD dose-extraction removal percentage

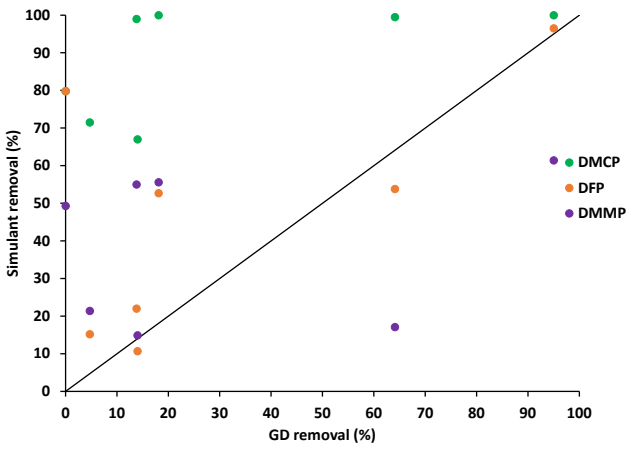

Figure 216. Plot of DMMP, DFP, and DMCP dose-extraction removal versus GD dose-extraction removal. A line of slope equal to one passing through the origin is included to represent perfect correlation

6.2.1.1.3 COMPARISON OF MALATHION TO VX

Referee material performance against malathion and VX is shown in Figures 217, 218, and 219. Generally, it is shown that malathion is a poor simulant for VX on both qualitative and quantitative grounds. This may be a function of the heteroatom chemistry being too dissimilar between the two chemicals, as malathion has a P=S bond whereas VX has a P=O bond. Selection of a chemical with more similar structure around the phosphorous atom, such as malaoxon, may yield results with better predictability.

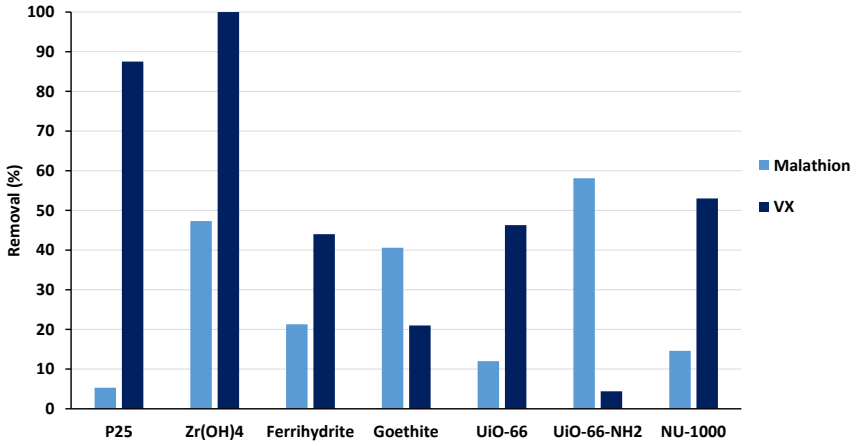

Figure 217. Malathion and VX dose-extraction removal data for referee materials

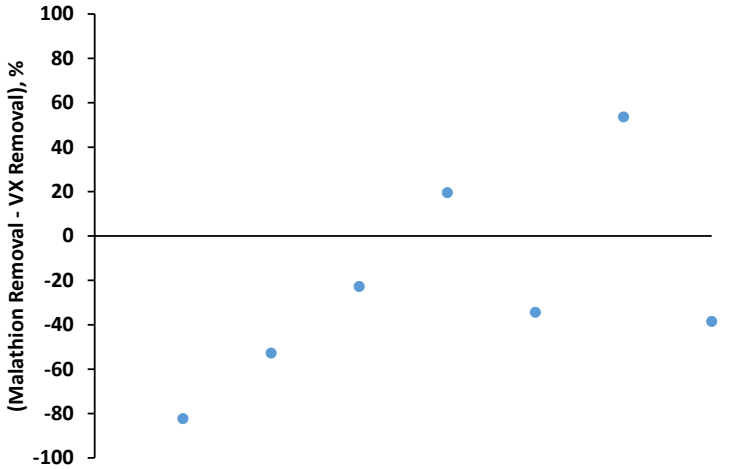

Figure 218. Differential data between malathion and VX dose-extraction removal percentage

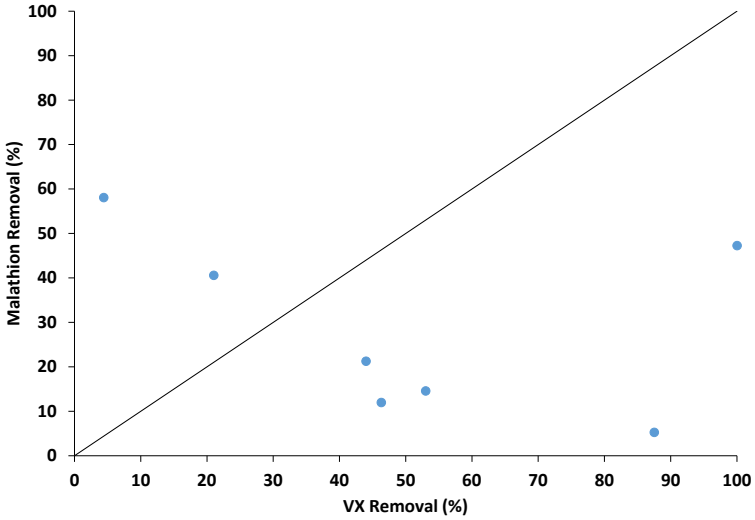

Figure 219. Plot of malathion dose-extraction removal versus VX dose-extraction removal. A line of slope equal to one passing through the origin is included to represent perfect correlation

6.2.1.2 COMPARISON BY MATERIAL

Dose-extraction removal data was also analyzed collectively for each material, and the results are shown in Figures 220 and 221. For this comparison, only the deviation from the best quantitative predictor for GB and GD was used in depicting the removal differentials. For example, in the case of GB, only the DMCP to GB removal differential was used and not the differentials involving DFP and DMMP. It can be seen that the two iron oxides, ferrihydrite and goethite, had by far the best overall simulant-to-agent removal correlation among all chemicals evaluated. If the malathion-VX data is ignored due to malathion being considered insufficiently similar chemically to be an adequate VX simulant, then the four metal oxides/hydroxides overall showed strong correlation between simulant and agent removal data. The MOFs, however, showed poor quantitative predictability across the entire spectrum of chemicals, with all simulants in general greatly overpredicting agent removal data.

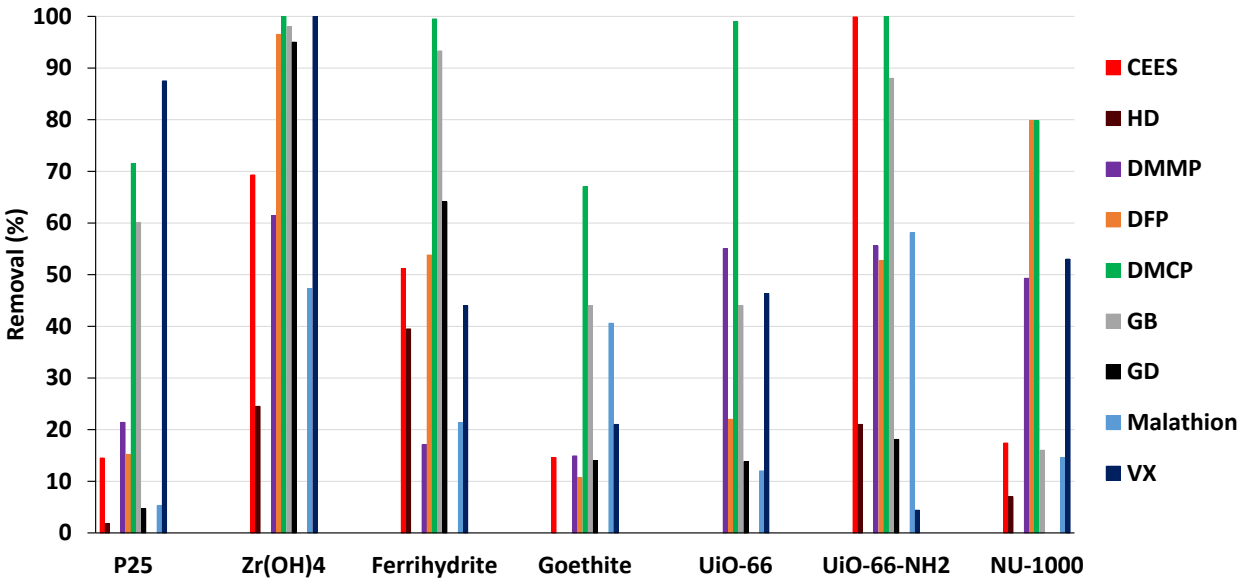

Figure 220. Dose-extraction percent removal data for all chemicals, grouped by material

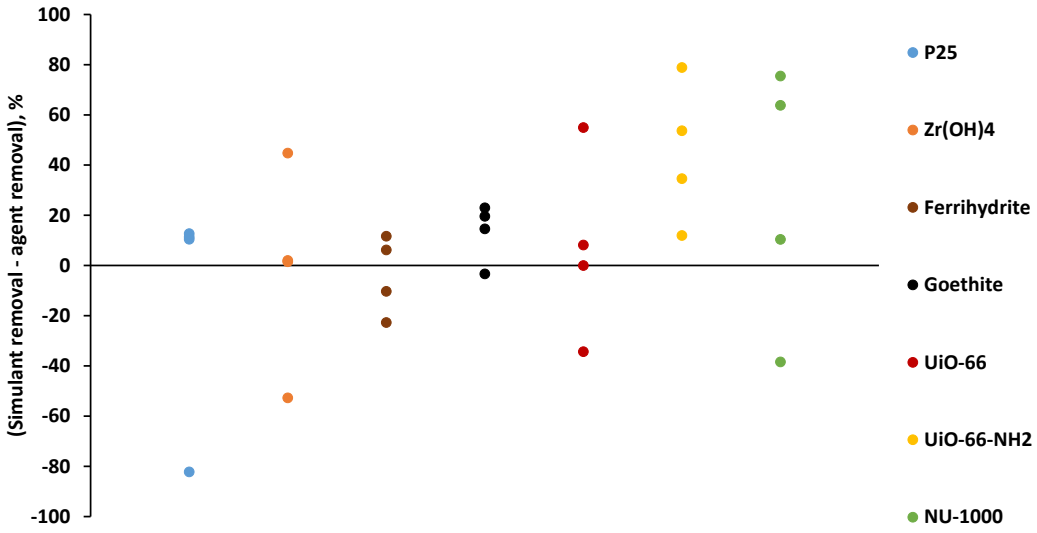

Figure 221. Differential data between simulant to corresponding agent dose-extraction removal percentage, grouped by material. Simulant-agent differentials used are CEES - HD, DMCP - GB, DFP - GD, and malathion – VX.

6.2.2 COMPARISON OF NMR AGENT DATA TO DOSE-EXTRACTION AGENT DATA

Comparison between NMR data and dose-extraction data is shown in Figures 222, 223, and 224. The objective of this specific analysis is to show the degree of relatability between the two major methods employed in this study for gauging reactivity of a material. The dose-extraction parameter of percent remaining was used instead of percent removal in the effort to show a direct correlation where both variables would be increasing at the same time. In theory, a longer half-life observed in reaction via NMR would

correlate with a lower amount of agent removed in the dose-extraction experiments and thus a higher amount of agent remaining. A direct correlation is indeed shown with HD and VX in this regard; however, only two data points exist for comparison, and so limited confidence can be applied to the relatability of these methods from those comparisons alone.

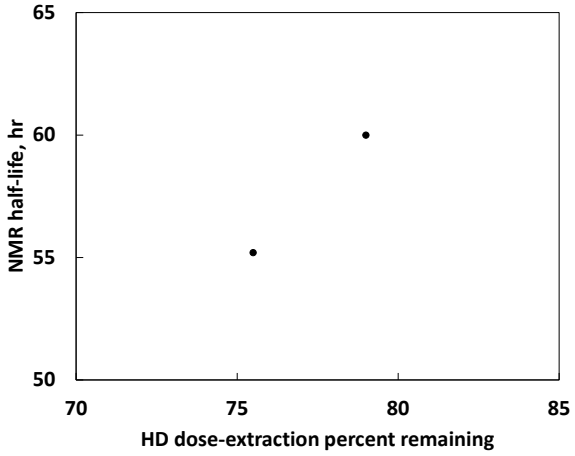

Figure 222. Comparison of NMR half-life for HD in $CHCl_3$ versus HD dose-extraction percent remaining for applicable referee materials. Note that percent remaining, = 100 – percent removal, is used here as that parameter would ideally increase directly with the measured NMR half-life

With GD, limited to no correlation is observed between NMR and dose-extraction data. A couple of explanations can be made for this behavior. First, the data is tightly grouped for the most part, with all the calculated half-lives being less than 30 minutes and all but one of the dose-extraction experiments calculating between 80 and 100 percent of agent remaining. Both of these parameters represent rather narrow ranges that, when considering margin of error, could reconcile the data into a more direct trend. Another explanation involves the reliability of the dose-extraction method for predicting true reactivity. As the dose-extraction method relies on measurement of the characteristic peak of GD of the gas chromatogram of the extract to determine percent removal, it is plausible that byproducts from GD reaction could present a similar retention time and thus would be misinterpreted as corresponding to GD, which in turn would underpredict GD removal. Alternatively, for larger-pore-size molecules, physisorption of GD in the pores may occur, which would be difficult to sufficiently extract out. This would lead to an overprediction of GD removal. Therefore, it is likely a combination of poor sensitivity/selectivity of the extraction method and difficulties in fully extracting all solute that is not chemisorbed or chemically reacted that accounts for the differences in method performance evaluation.

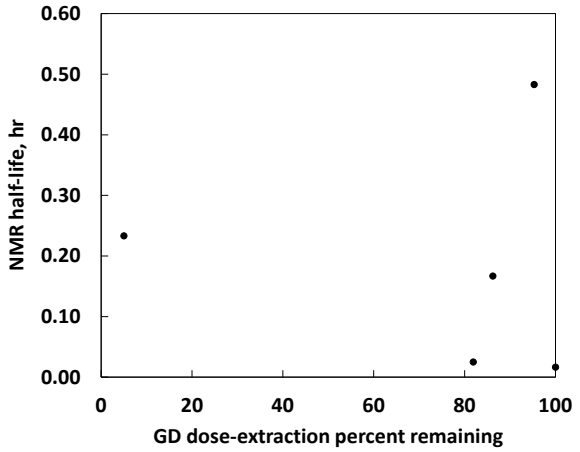

Figure 223. Comparison of NMR half-life for GD in a 0.5M ethylmorpholine buffer at pH 10 versus GD dose-extraction percent remaining for applicable referee materials. Note that percent remaining, = 100 – percent removal, is used here as that parameter would ideally increase directly with the measured NMR half-life

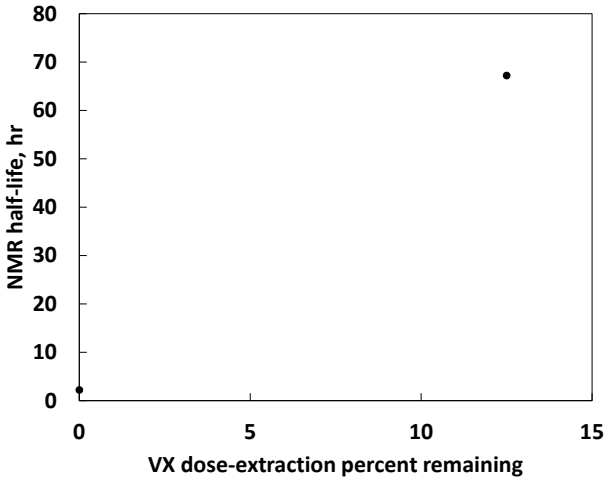

Figure 224. Comparison of NMR half-life for VX in a 0.5M ethylmorpholine buffer at pH 10 versus VX dose-extraction percent remaining for applicable referee materials. Note that percent remaining, = 100 – percent removal, is used here as that parameter would ideally increase directly with the measured NMR half-life

6.3 CHEMICAL REACTION MECHANISMS

With a few exceptions, the DRIFTS spectra peaks of this paper have only been cryptically identified in terms of the major chemical groups involved in the reactions of the referee materials with selected simulants and chemical warfare agents. Nevertheless, this data offers a path forward for future investigation into specific reaction mechanisms that can be expanded upon in future studies and elucidates some general noteworthy observations. All materials show strong interaction with simulants and nerve agents via surface hydroxyl species, and thus these sites should be given astute consideration when evaluating reactivity. The general time profile of simulant and nerve agent heteroatom activity has been

identified for each referee material-chemical combination, as specific peaks have been assigned to most of the P=O vibrational modes for G and V agents/simulants and the S-CH_2 and Cl-CH_2 vibrational modes for the vesicants. This offers a starting point for further investigation into the ultimate fate of the agent on each referee material and, coupled with the other characterization data of this paper, helps to clarify the full detection and decontamination capabilities of the materials evaluated against the greatest of chemical threats.

7. LITERATURE CITED

1. Lopez, R.; Gomez, R., Band-gap energy estimation from diffuse reflectance measurements on sol-gel and commercial TiO2: a comparative study. *Journal of Sol-Gel Science and Technology* **2012,** *61* (1), 1-7.

2. Bandosz, T. J.; Laskoski, M.; Mahle, J.; Mogilevsky, G.; Peterson, G. W.; Rossin, J. A.; Wagner, G. W., Reactions of VX, GD, and HD with Zr(OH)(4): Near Instantaneous Decontamination of VX. *Journal of Physical Chemistry C* **2012,** *116* (21), 11606-11614.

3. Kakuta, S.; Numata, T.; Okayama, T., Shape effects of goethite particles on their photocatalytic activity in the decomposition of acetaldehyde. *Catalysis Science & Technology* **2014,** *4* (1), 164-169.

4. Kandiah, M.; Nilsen, M. H.; Usseglio, S.; Jakobsen, S.; Olsbye, U.; Tilset, M.; Larabi, C.; Quadrelli, E. A.; Bonino, F.; Lillerud, K. P., Synthesis and Stability of Tagged UiO-66 Zr-MOFs. *Chemistry of Materials* **2010,** *22* (24), 6632-6640.

5. Klet, R. C.; Liu, Y.; Wang, T. C.; Hupp, J. T.; Farha, O. K., Evaluation of Bronsted acidity and proton topology in Zr- and Hf-based metal-organic frameworks using potentiometric acid-base titration. *Journal of Materials Chemistry A* **2016,** *4* (4), 1479-1485.

6. Barton, D. G.; Shtein, M.; Wilson, R. D.; Soled, S. L.; Iglesia, E., Structure and electronic properties of solid acids based on tungsten oxide nanostructures. *Journal of Physical Chemistry B* **1999,** *103* (4), 630-640.

7. Oshani, F.; Marandi, R.; Rasouli, S.; Farhoud, M. K., Photocatalytic investigations of TiO2-P25 nanocomposite thin films prepared by peroxotitanic acid modified sol-gel method. *Applied Surface Science* **2014,** *311*, 308-313.

8. Flage-Larsen, E.; Royset, A.; Cavka, J. H.; Thorshaug, K., Band Gap Modulations in UiO Metal-Organic Frameworks. *Journal of Physical Chemistry C* **2013,** *117* (40), 20610-20616.

9. Colton, J. S.; Erickson, S. D.; Smith, T. J.; Watt, R. K., Sensitive detection of surface- and size-dependent direct and indirect band gap transitions in ferritin. *Nanotechnology* **2014,** *25* (13).

10. Zhang, H. Z.; Bayne, M.; Fernando, S.; Legg, B.; Zhu, M. Q.; Penn, R. L.; Banfield, J. F., Size-Dependent Bandgap of Nanogoethite. *Journal of Physical Chemistry C* **2011,** *115* (36), 17704-17710.

11. Jagiello, J., STABLE NUMERICAL-SOLUTION OF THE ADSORPTION INTEGRAL-EQUATION USING SPLINES. *Langmuir* **1994,** *10* (8), 2778-2785.

12. Contescu, C.; Popa, V. T.; Miller, J. B.; Ko, E. I.; Schwarz, J. A., PROTON AFFINITY DISTRIBUTIONS OF TIO2-SIO2 AND ZRO2-SIO2 MIXED OXIDES AND THEIR RELATIONSHIP TO CATALYST ACTIVITIES FOR 1-BUTENE ISOMERIZATION. *Journal of Catalysis* **1995,** *157* (1), 244-258.

13. Roy, A.; Srivastava, A. K.; Singh, B.; Mahato, T. H.; Shah, D.; Halve, A. K., Degradation of sulfur mustard and 2-chloroethyl ethyl sulfide on Cu-BTC metal organic framework. *Microporous and Mesoporous Materials* **2012,** *162*, 207-212.

14. Janus, M.; Morawski, A. W., New method of improving photocatalytic activity of commercial Degussa P25 for azo dyes, decomposition. *Applied Catalysis B-Environmental* **2007,** *75* (1-2), 118-123.

15. Tobaldi, D. M.; Pullar, R. C.; Seabra, M. P.; Labrincha, J. A., Fully quantitative X-ray characterisation of Evonik Aeroxide TiO2 P25 (R). *Materials Letters* **2014,** *122*, 345-347.

16. Han, H. W.; Zan, L.; Zhong, J. S.; Zhang, L. N.; Zhao, X. Z., The preparation of high-surface-area nanocrystalline TiO2 films using easy-reaggregation particles in solution. *Materials Science and Engineering B-Solid State Materials for Advanced Technology* **2004,** *110* (2), 227-232.

17. Hanaor, D. A. H.; Sorrell, C. C., Review of the anatase to rutile phase transformation. *Journal of Materials Science* **2011,** *46* (4), 855-874.

18. Swamy, V., Size-dependent modifications of the first-order Raman spectra of nanostructured rutile TiO(2). *Physical Review B* **2008,** *77* (19).

19. Papp, S.; Korosi, L.; Meynen, V.; Cool, P.; Vansant, E. F.; Dekany, I., The influence of temperature on the structural behaviour of sodium tri- and hexa-titanates and their protonated forms. *Journal of Solid State Chemistry* **2005,** *178* (5), 1614-1619.

20. Xiang, Q. J.; Yu, J. G.; Jaroniec, M., Synergetic Effect of MoS2 and Graphene as Cocatalysts for Enhanced Photocatalytic H-2 Production Activity of TiO2 Nanoparticles. *Journal of the American Chemical Society* **2012,** *134* (15), 6575-6578.

21. Wang, G. H.; Xu, L.; Zhang, J.; Yin, T. T.; Han, D. Y., Enhanced Photocatalytic Activity of TiO2 Powders (P25) via Calcination Treatment. *International Journal of Photoenergy* **2012**.

22. Szilagyi, I. M.; Santala, E.; Heikkila, M.; Pore, V.; Kemell, M.; Nikitin, T.; Teucher, G.; Firkala, T.; Khriachtchev, L.; Rasanen, M.; Ritala, M.; Leskela, M., Photocatalytic Properties of WO3/TiO2 Core/Shell Nanofibers prepared by Electrospinning and Atomic Layer Deposition. *Chemical Vapor Deposition* **2013,** *19* (4-6), 149-155.

23. Jin, Z.; Duan, W. B.; Liu, B.; Chen, X. D.; Yang, F. H.; Guo, J. P., Fabrication of efficient visible light activated Cu-P25-graphene ternary composite for photocatalytic degradation of methyl blue. *Applied Surface Science* **2015,** *356*, 707-718.

24. Jayabharathi, J.; Karunakaran, C.; Thanikachalam, V.; Ramanathan, P., Binding and fluorescence enhancing behaviour of phenanthrimidazole with different phases of TiO2. *New Journal of Chemistry* **2014,** *38* (9), 4321-4335.

25. Masolo, E.; Meloni, M.; Garroni, S.; Mulas, G.; Enzo, S.; Baro, M. D.; Rossinyol, E.; Rzeszutek, A.; Herrmann-Geppert, I.; Pilo, M., Mesoporous Titania Powders: The Role of Precursors, Ligand Addition and Calcination Rate on Their Morphology, Crystalline Structure and Photocatalytic Activity. *Nanomaterials* **2014,** *4* (3), 583-598.

26. Spanos, N.; Georgiadou, I.; Lycourghiotis, A., INVESTIGATION OF RUTILE, ANATASE, AND INDUSTRIAL TITANIA WATER SOLUTION INTERFACES USING POTENTIOMETRIC TITRATION AND MICROELECTROPHORESIS. *Journal of Colloid and Interface Science* **1995,** *172* (2), 374-382.

27. Ludwig, C.; Schindler, P. W., SURFACE COMPLEXATION ON TIO2 .1. ADSORPTION OF H+ AND CU2+ IONS ONTO TIO2 (ANATASE). *Journal of Colloid and Interface Science* **1995,** *169* (2), 284-290.

28. Hiemstra, T.; Vanriemsdijk, W. H.; Bolt, G. H., MULTISITE PROTON ADSORPTION MODELING AT THE SOLID-SOLUTION INTERFACE OF (HYDR)OXIDES - A NEW APPROACH .1. MODEL DESCRIPTION AND EVALUATION OF INTRINSIC REACTION CONSTANTS. *Journal of Colloid and Interface Science* **1989,** *133* (1), 91-104.

29. Kosmulski, M., pH-dependent surface charging and points of zero charge. IV. Update and new approach. *Journal of Colloid and Interface Science* **2009,** *337* (2), 439-448.

30. Han, S. T.; Xi, H. L.; Fu, X. Z.; Wang, X. X.; Ding, Z. X.; Lin, Z. C.; Su, W. Y., Study on the photocatalytic degradation of a simulate agent (2-CEES) of mustard gas. *Acta Physico-Chimica Sinica* **2004,** *20* (3), 296-301.

31. Obee, T. N.; Satyapal, S., Photocatalytic decomposition of DMMP on titania. *Journal of Photochemistry and Photobiology a-Chemistry* **1998,** *118* (1), 45-51.

32. Southon, P. D.; Bartlett, J. R.; Woolfrey, J. L.; Ben-Nissan, B., Formation and characterization of an aqueous zirconium hydroxide colloid. *Chemistry of Materials* **2002,** *14* (10), 4313-4319.

33. Mogilevsky, G.; Karwacki, C. J.; Peterson, G. W.; Wagner, G. W., Surface hydroxyl concentration on Zr(OH)(4) quantified by H-1 MAS NMR. *Chemical Physics Letters* **2011,** *511* (4-6), 384-388.

34. Stefanic, G.; Popovic, S.; Music, S., THE EFFECT OF MECHANICAL TREATMENT OF ZIRCONIUM(IV) HYDROXIDE ON ITS THERMAL-BEHAVIOR. *Thermochimica Acta* **1995,** *259* (2), 225-234.

35. Peterson, G. W.; Karwacki, C. J.; Feaver, W. B.; Rossin, J. A., Zirconium Hydroxide as a Reactive Substrate for the Removal of Sulfur Dioxide. *Industrial & Engineering Chemistry Research* **2009,** *48* (4), 1694-1698.

36. Peterson, G. W.; Rossin, J. A.; Karwacki, C. J.; Glover, T. G., Surface Chemistry and Morphology of Zirconia Polymorphs and the Influence on Sulfur Dioxide Removal. *Journal of Physical Chemistry C* **2011,** *115* (19), 9644-9650.

37. Peterson, G. W.; Rossin, J. A., Removal of Chlorine Gases from Streams of Air Using Reactive Zirconium Hydroxide Based Filtration Media. *Industrial & Engineering Chemistry Research* **2012,** *51* (6), 2675-2681.

38. VanCantfort, O.; Michaux, B.; Pirard, R.; Pirard, J. P.; Lecloux, A. J., Synthesis and characterization of monodisperse spherical zirconia particles. *Journal of Sol-Gel Science and Technology* **1997,** *8* (1-3), 207-211.

39. Glover, T. G.; Peterson, G. W.; DeCoste, J. B.; Browe, M. A., Adsorption of Ammonia by Sulfuric Acid Treated Zirconium Hydroxide. *Langmuir* **2012,** *28* (28), 10478-10487.

40. Boulfrad, S.; Djurado, E.; Fouletier, J., Electrochemical characterization of nanostructured zirconias. *Solid State Ionics* **2009,** *180* (14-16), 978-983.

41. Guo, G. Y.; Chen, Y. L.; Ying, W. J., Thermal, spectroscopic and X-ray diffractional analyses of zirconium hydroxides precipitated at low pH values. *Materials Chemistry and Physics* **2004,** *84* (2-3), 308-314.

42. Kumari, L.; Li, W. Z.; Xu, J. M.; Leblanc, R. M.; Wang, D. Z.; Li, Y.; Guo, H. Z.; Zhang, J. D., Controlled Hydrothermal Synthesis of Zirconium Oxide Nanostructures and Their Optical Properties. *Crystal Growth & Design* **2009,** *9* (9), 3874-3880.

43. Mitchell, J. K.; Arcibar-Orozco, J. A.; Bandosz, T. J., Reactive removal of 2-chloroethyl ethyl sulfide vapors under visible light irradiation by cerium oxide modified highly porous zirconium (hydr) oxide. *Applied Surface Science* **2016,** *390*, 735-743.

44. Kosmulski, M., The significance of the points of zero charge of zirconium (hydr)oxide reported in the literature. *Journal of Dispersion Science and Technology* **2002,** *23* (4), 529-538.

45. Tesfai, T. M.; Sheinker, V. N.; Mitchell, M. B., Decomposition of dimethyl methylphosphonate (DMMP) on alumina-supported iron oxide. *Journal of Physical Chemistry B* **1998,** *102* (38), 7299-7302.

46. Mohapatra, D.; Singh, P.; Zhang, W.; Pullammanappallil, P., The effect of citrate, oxalate, acetate, silicate and phosphate on stability of synthetic arsenic-loaded ferrihydrite and Al-ferrihydrite. *Journal of Hazardous Materials* **2005,** *124* (1-3), 95-100.

47. Jain, A.; Raven, K. P.; Loeppert, R. H., Arsenite and arsenate adsorption on ferrihydrite: Surface charge reduction and net OH- release stoichiometry. *Environmental Science & Technology* **1999,** *33* (8), 1179-1184.

48. Weaver, C. M.; Schulze, D. G.; Peck, L. W.; Magnusen, H. M.; Martin, B. R.; Gruenhagen, S. E., Phosphate-binding capacity of ferrihydrite versus calcium acetate in rats. *American Journal of Kidney Diseases* **1999,** *34* (2), 324-327.

49. Wang, X.; Li, W.; Harrington, R.; Liu, F.; Parise, J. B.; Feng, X.; Sparks, D. L., Effect of Ferrihydrite Crystallite Size on Phosphate Adsorption Reactivity. *Environmental Science & Technology* **2013,** *47* (18), 10322-10331.

50. Poulton, S. W., Sulfide oxidation and iron dissolution kinetics during the reaction of dissolved sulfide with ferrihydrite. *Chemical Geology* **2003,** *202* (1-2), 79-94.

51. Jansen, E.; Kyek, A.; Schafer, W.; Schwertmann, U., The structure of six-line ferrihydrite. *Applied Physics a-Materials Science & Processing* **2002,** *74*, S1004-S1006.

52. Drits, V. A.; Sakharov, B. A.; Salyn, A. L.; Manceau, A., STRUCTURAL MODEL FOR FERRIHYDRITE. *Clay Minerals* **1993,** *28* (2), 185-207.

53. Ford, R. G.; Bertsch, P. M.; Seaman, J. C., Goethite morphologies investigated via X-ray diffraction of oriented samples. *Clays and Clay Minerals* **1997,** *45* (5), 769-772.

54. Stengl, V.; Marikova, M.; Bakardjieva, S.; Subrt, J.; Oplustil, F.; Olsanska, M., Reaction of sulfur mustard gas, soman and agent VX with nanosized anatase TiO2 and ferrihydrite. *Journal of Chemical Technology and Biotechnology* **2005,** *80* (7), 754-758.

55. Chen, Y. H., Thermal properties of nanocrystalline goethite, magnetite, and maghemite. *Journal of Alloys and Compounds* **2013,** *553*, 194-198.

56. Hausner, D. B.; Bhandari, N.; Pierre-Louis, A. M.; Kubicki, J. D.; Strongin, D. R., Ferrihydrite reactivity toward carbon dioxide. *Journal of Colloid and Interface Science* **2009,** *337* (2), 492-500.

57. Prasad, P. S. R.; Prasad, K. S.; Chaitanya, V. K.; Babu, E. V. S. S. K.; Sreedhar, B.; Murthy, S. R., In situ FTIR study on the dehydration of natural goethite. *Journal of Asian Earth Sciences* **2006,** *27* (4), 503-511.

58. Parida, K.; Das, J., Studies on ferric oxide hydroxides .2. Structural properties of goethite samples (alpha-FeOOH) prepared by homogeneous precipitation from Fe(NO3)(3) solution in the presence of sulfate ions. *Journal of Colloid and Interface Science* **1996,** *178* (2), 586-593.

59. Mazzetti, L.; Thistlethwaite, P. J., Raman spectra and thermal transformations of ferrihydrite and schwertmannite. *Journal of Raman Spectroscopy* **2002,** *33* (2), 104-111.

60. Xu, T. Y.; Zhu, R. L.; Liu, J.; Zhou, Q.; Zhu, J. X.; Liang, X. L.; Xi, Y. F.; He, H. P., Fullerol modification ferrihydrite for the degradation of acid red 18 under simulated sunlight irradiation. *Journal of Molecular Catalysis a-Chemical* **2016,** *424*, 393-401.

61. Grygar, T.; Hradil, D.; Bezdicka, P.; Dousova, B.; Capek, L.; Schneeweiss, O., Fe(III)-modified montmorillonite and bentonite: Synthesis, chemical and UV-vis spectral characterization, arsenic sorption, and catalysis of oxidative dehydrogenation of propane. *Clays and Clay Minerals* **2007,** *55* (2), 165-176.

62. Scheinost, A. C.; Chavernas, A.; Barron, V.; Torrent, J., Use and limitations of second-derivative diffuse reflectance spectroscopy in the visible to near-infrared range to identify and quantify Fe oxide minerals in soils. *Clays and Clay Minerals* **1998,** *46* (5), 528-536.

63. Zhang, H.; Bayne, M.; Fernando, S.; Legg, B.; Zhu, M.; Penn, R. L.; Banfield, J. F., Size-Dependent Bandgap of Nanogoethite. *Journal of Physical Chemistry C* **2011,** *115* (36), 17704-17710.

64. Tunega, D., Theoretical Study of Properties of Goethite (alpha-FeOOH) at Ambient and High-Pressure Conditions. *Journal of Physical Chemistry C* **2012,** *116* (11), 6703-6713.

65. Das, S.; Hendry, M. J.; Essilfie-Dughan, J., Transformation of Two-Line Ferrihydrite to Goethite and Hematite as a Function of pH and Temperature. *Environmental Science & Technology* **2011,** *45* (1), 268-275.

66. Arcibar-Orozco, J. A.; Wallace, R.; Mitchell, J. K.; Bandosz, T. J., Role of Surface Chemistry and Morphology in the Reactive Adsorption of H2S on Iron (Hydr)Oxide/Graphite Oxide Composites. *Langmuir* **2015,** *31* (9), 2730-2742.

67. Arcibar-Orozco, J. A.; Bandosz, T. J., Visible light enhanced removal of a sulfur mustard gas surrogate from a vapor phase on novel hydrous ferric oxide/graphite oxide composites. *Journal of Materials Chemistry A* **2015,** *3* (1), 220-231.

68. Barcia, P. S.; Guimaraes, D.; Mendes, P. A. P.; Silva, J. A. C.; Guillerm, V.; Chevreau, H.; Serre, C.; Rodrigues, A. E., Reverse shape selectivity in the adsorption of hexane and xylene isomers in MOF UiO-66. *Microporous and Mesoporous Materials* **2011,** *139* (1-3), 67-73.

69. Katz, M. J.; Brown, Z. J.; Colon, Y. J.; Siu, P. W.; Scheidt, K. A.; Snurr, R. Q.; Hupp, J. T.; Farha, O. K., A facile synthesis of UiO-66, UiO-67 and their derivatives. *Chemical Communications* **2013,** *49* (82), 9449-9451.

70. DeCoste, J. B.; Peterson, G. W.; Schindler, B. J.; Killops, K. L.; Browe, M. A.; Mahle, J. J., The effect of water adsorption on the structure of the carboxylate containing metal-organic frameworks Cu-BTC, Mg-MOF-74, and UiO-66. *Journal of Materials Chemistry A* **2013,** *1* (38), 11922-11932.

71. Cavka, J. H.; Jakobsen, S.; Olsbye, U.; Guillou, N.; Lamberti, C.; Bordiga, S.; Lillerud, K. P., A new zirconium inorganic building brick forming metal organic frameworks with exceptional stability. *Journal of the American Chemical Society* **2008,** *130* (42), 13850-13851.

72. Wissmann, G.; Schaate, A.; Lilienthal, S.; Bremer, I.; Schneider, A. M.; Behrens, P., Modulated synthesis of Zr-fumarate MOF. *Microporous and Mesoporous Materials* **2012,** *152*, 64-70.

73. Ebrahim, A. M.; Levasseur, B.; Bandosz, T. J., Interactions of NO2 with Zr-Based MOF: Effects of the Size of Organic Linkers on NO2 Adsorption at Ambient Conditions. *Langmuir* **2013,** *29* (1), 168-174.

74. Peterson, G. W.; Moon, S.-Y.; Wagner, G. W.; Hall, M. G.; DeCoste, J. B.; Hupp, J. T.; Farha, O. K., Tailoring the Pore Size and Functionality of UiO-Type Metal-Organic Frameworks for Optimal Nerve Agent Destruction. *Inorganic Chemistry* **2015,** *54* (20), 9684-9686.

75. DeCoste, J. B.; Browe, M. A.; Wagner, G. W.; Rossin, J. A.; Peterson, G. W., Removal of chlorine gas by an amine functionalized metal-organic framework via electrophilic aromatic substitution. *Chemical Communications* **2015,** *51* (62), 12474-12477.

76. Cao, Y.; Zhao, Y.; Lv, Z.; Song, F.; Zhong, Q., Preparation and enhanced CO2 adsorption capacity of UiO-66/graphene oxide composites. *Journal of Industrial and Engineering Chemistry* **2015,** *27*, 102-107.

77. Abid, H. R.; Tian, H.; Ang, H.-M.; Tade, M. O.; Buckley, C. E.; Wang, S., Nanosize Zr-metal organic framework (UiO-66) for hydrogen and carbon dioxide storage. *Chemical Engineering Journal* **2012,** *187*, 415-420.

78. Chavan, S.; Vitillo, J. G.; Gianolio, D.; Zavorotynska, O.; Civalleri, B.; Jakobsen, S.; Nilsen, M. H.; Valenzano, L.; Lamberti, C.; Lillerud, K. P.; Bordiga, S., H-2 storage in isostructural UiO-67 and UiO-66 MOFs. *Physical Chemistry Chemical Physics* **2012,** *14* (5), 1614-1626.

79. Valenzano, L.; Civalleri, B.; Chavan, S.; Bordiga, S.; Nilsen, M. H.; Jakobsen, S.; Lillerud, K. P.; Lamberti, C., Disclosing the Complex Structure of UiO-66 Metal Organic Framework: A Synergic Combination of Experiment and Theory. *Chemistry of Materials* **2011,** *23* (7), 1700-1718.

80. Shen, L.; Liang, S.; Wu, W.; Liang, R.; Wu, L., Multifunctional NH2-mediated zirconium metal-organic framework as an efficient visible-light-driven photocatalyst for selective oxidation of alcohols and reduction of aqueous Cr(VI). *Dalton Transactions* **2013,** *42* (37), 13649-13657.

81. Silva, C. G.; Luz, I.; Xamena, F.; Corma, A.; Garcia, H., Water Stable Zr-Benzenedicarboxylate Metal-Organic Frameworks as Photocatalysts for Hydrogen Generation. *Chemistry-a European Journal* **2010,** *16* (36), 11133-11138.

82. Wang, A. N.; Zhou, Y. J.; Wang, Z. L.; Chen, M.; Sun, L. Y.; Liu, X., Titanium incorporated with UiO-66(Zr)-type Metal-Organic Framework (MOF) for photocatalytic application. *Rsc Advances* **2016,** *6* (5), 3671-3679.

83. Lee, T.; Chang, Y. H.; Lee, H. L., Crystallization process development of metal-organic frameworks by linking secondary building units, lattice nucleation and luminescence: insight into reproducibility. *Crystengcomm* **2017,** *19* (3), 426-441.

84. Chen, W.; Wang, J. Y.; Chen, C.; Yue, Q.; Yuan, H. M.; Chen, J. S.; Wang, S. N., Photoluminescent metal-organic polymer constructed from trimetallic clusters and mixed carboxylates. *Inorganic Chemistry* **2003,** *42* (4), 944-946.

85. Wang, C.; Liu, X.; Chen, J. P.; Li, K., Superior removal of arsenic from water with zirconium metal-organic framework UiO-66. *Scientific Reports* **2015,** *5*.

86. Lv, G.; Liu, J.; Xiong, Z.; Zhang, Z.; Guan, Z., Selectivity Adsorptive Mechanism of Different Nitrophenols on UIO-66 and UIO-66-NH2 in Aqueous Solution. *Journal of Chemical and Engineering Data* **2016,** *61* (11), 3868-3876.

87. DeCoste, J. B.; Peterson, G. W., Metal-Organic Frameworks for Air Purification of Toxic Chemicals. *Chemical Reviews* **2014,** *114* (11), 5695-5727.

88. Peterson, G. W.; DeCoste, J. B.; Fatollahi-Fard, F.; Britt, D. K., Engineering UiO-66-NH2 for Toxic Gas Removal. *Industrial & Engineering Chemistry Research* **2014,** *53* (2), 701-707.

89. Cam Loc, L.; Tri, N.; Tien Cuong, H.; Minh Nam, H.; Cam Anh, H., The role of carriers in properties and performance of Pt-CuO nanocatalysts in low temperature oxidation of CO and p-xylene. *Advances in Natural Sciences-Nanoscience and Nanotechnology* **2015,** *6* (1).

90. Chen, Q.; He, Q.; Lv, M.; Xu, Y.; Yang, H.; Liu, X.; Wei, F., Selective adsorption of cationic dyes by UiO-66-NH2. *Applied Surface Science* **2015,** *327*, 77-85.

91. Garibay, S. J.; Cohen, S. M., Isoreticular synthesis and modification of frameworks with the UiO-66 topology. *Chemical Communications* **2010,** *46* (41), 7700-7702.

92. Cam Loc, L.; Thi Thuy Van, N.; Tri, N.; Tien Cuong, H., Synthesis, characterization and adsorption ability of UiO-66-NH2. *Advances in Natural Sciences-Nanoscience and Nanotechnology* **2015,** *6* (2).

93. Kardanpour, R.; Tangestaninejad, S.; Mirkhani, V.; Moghadam, M.; Mohammadpoor-Baltork, I.; Zadehahmadi, F., Efficient alkene epoxidation catalyzed by molybdenyl acetylacetonate supported on aminated UiO-66 metal - organic framework. *Journal of Solid State Chemistry* **2015,** *226*, 262-272.

94. Wu, L.; Zhang, X.-F.; Li, Z.-Q.; Wu, F., A new sensor based on amino-functionalized zirconium metal-organic framework for detection of Cu2+ in aqueous solution. *Inorganic Chemistry Communications* **2016,** *74*, 22-25.

95. Kagan, M. R.; McCreery, R. L., REDUCTION OF FLUORESCENCE INTERFERENCE IN RAMAN-SPECTROSCOPY VIA ANALYTE ADSORPTION ON GRAPHITIC CARBON. *Analytical Chemistry* **1994,** *66* (23), 4159-4165.

96. He, J.; Wang, J. Q.; Chen, Y. J.; Zhang, J. P.; Duan, D. L.; Wang, Y.; Yan, Z. Y., A dye-sensitized Pt@UiO-66(Zr) metal-organic framework for visible-light photocatalytic hydrogen production. *Chemical Communications* **2014,** *50* (53), 7063-7066.

97. Yang, J.; Dai, Y.; Zhu, X.; Wang, Z.; Li, Y.; Zhuang, Q.; Shi, J.; Gu, J., Metal-organic frameworks with inherent recognition sites for selective phosphate sensing through their coordination-induced fluorescence enhancement effect. *Journal of Materials Chemistry A* **2015,** *3* (14), 7445-7452.

98. Zlotea, C.; Phanon, D.; Mazaj, M.; Heurtaux, D.; Guillerm, V.; Serre, C.; Horcajada, P.; Devic, T.; Magnier, E.; Cuevas, F.; Ferey, G.; Llewellyn, P. L.; Latroche, M., Effect of NH2 and CF3 functionalization on the hydrogen sorption properties of MOFs. *Dalton Transactions* **2011,** *40* (18), 4879-4881.

99. Mondloch, J. E.; Bury, W.; Fairen-Jimenez, D.; Kwon, S.; DeMarco, E. J.; Weston, M. H.; Sarjeant, A. A.; Nguyen, S. T.; Stair, P. C.; Snurr, R. Q.; Farha, O. K.; Hupp, J. T., Vapor-Phase Metalation by Atomic Layer Deposition in a Metal-Organic Framework. *Journal of the American Chemical Society* **2013,** *135* (28), 10294-10297.

100. Mondloch, J. E.; Katz, M. J.; Isley, W. C., III; Ghosh, P.; Liao, P.; Bury, W.; Wagner, G.; Hall, M. G.; DeCoste, J. B.; Peterson, G. W.; Snurr, R. Q.; Cramer, C. J.; Hupp, J. T.; Farha, O. K., Destruction of chemical warfare agents using metal-organic frameworks. *Nature Materials* **2015,** *14* (5), 512-516.

101. Deria, P.; Mondloch, J. E.; Tylianakis, E.; Ghosh, P.; Bury, W.; Snurr, R. Q.; Hupp, J. T.; Farha, O. K., Perfluoroalkane Functionalization of NU-1000 via Solvent-Assisted Ligand Incorporation: Synthesis and CO2 Adsorption Studies. *Journal of the American Chemical Society* **2013,** *135* (45), 16801-16804.

102. Kung, C.-W.; Mondloch, J. E.; Wang, T. C.; Bury, W.; Hoffeditz, W.; Klahr, B. M.; Klet, R. C.; Pellin, M. J.; Farha, O. K.; Hupp, J. T., Metal-Organic Framework Thin Films as Platforms for Atomic Layer Deposition of Cobalt Ions To Enable Electrocatalytic Water Oxidation. *Acs Applied Materials & Interfaces* **2015,** *7* (51), 28223-28230.

103. Hod, I.; Deria, P.; Bury, W.; Mondloch, J. E.; Kung, C.-W.; So, M.; Sampson, M. D.; Peters, A. W.; Kubiak, C. P.; Farha, O. K.; Hupp, J. T., A porous proton-relaying metal-organic framework material that accelerates electrochemical hydrogen evolution. *Nature Communications* **2015,** *6*.

104. Li, P.; Klet, R. C.; Moon, S.-Y.; Wang, T. C.; Deria, P.; Peters, A. W.; Klahr, B. M.; Park, H.-J.; Al-Juaid, S. S.; Hupp, J. T.; Farha, O. K., Synthesis of nanocrystals of Zr-based metal-organic frameworks with csq-net: significant enhancement in the degradation of a nerve agent simulant. *Chemical Communications* **2015,** *51* (54), 10925-10928.

105. Platero-Prats, A. E.; Mavrandonakis, A.; Gallington, L. C.; Liu, Y.; Hupp, J. T.; Farha, O. K.; Cramer, C. J.; Chapman, K. W., Structural Transitions of the Metal-Oxide Nodes within Metal-Organic Frameworks: On the Local Structures of NU-1000 and UiO-66. *Journal of the American Chemical Society* **2016,** *138* (12), 4178-4185.

106. Wang, T. C.; Vermeulen, N. A.; Kim, I. S.; Martinson, A. B. F.; Stoddart, J. F.; Hupp, J. T.; Farha, O. K., Scalable synthesis and post-modification of a mesoporous metal-organic framework called NU-1000. *Nature Protocols* **2016,** *11* (1), 149-162.

107. Yang, D.; Bernales, V.; Islamoglu, T.; Farha, O. K.; Hupp, J. T.; Cramer, C. J.; Gagliardi, L.; Gates, B. C., Tuning the Surface Chemistry of Metal Organic Framework Nodes: Proton Topology of the

Metal-Oxide-Like Zr-6 Nodes of UiO-66 and NU-1000. *Journal of the American Chemical Society* **2016,** *138* (46), 15189-15196.

108. Deria, P.; Bury, W.; Hupp, J. T.; Farha, O. K., Versatile functionalization of the NU-1000 platform by solvent-assisted ligand incorporation. *Chemical Communications* **2014,** *50* (16), 1965-1968.

109. Wang, Q. Q.; Begum, R. A.; Day, V. W.; Bowman-James, K., Sulfur, oxygen, and nitrogen mustards: stability and reactivity. *Organic & Biomolecular Chemistry* **2012,** *10* (44), 8786-8793.

Blank

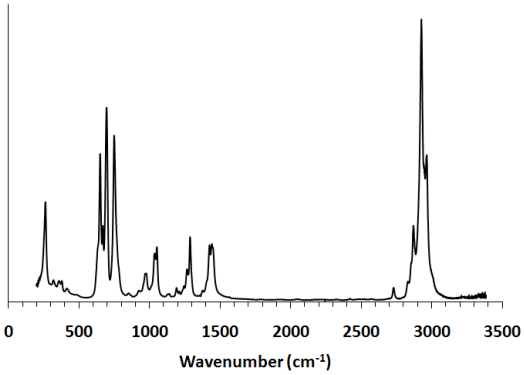

Figure 225. Raman spectra of neat CEES

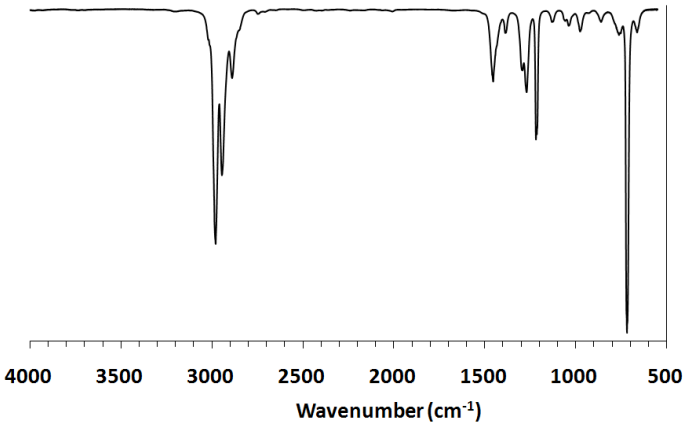

Figure 226. FTIR spectra of neat CEES

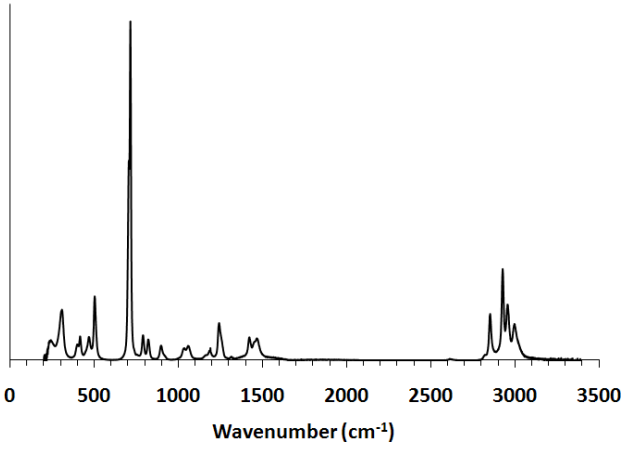

Figure 227. Raman spectra of neat DMMP

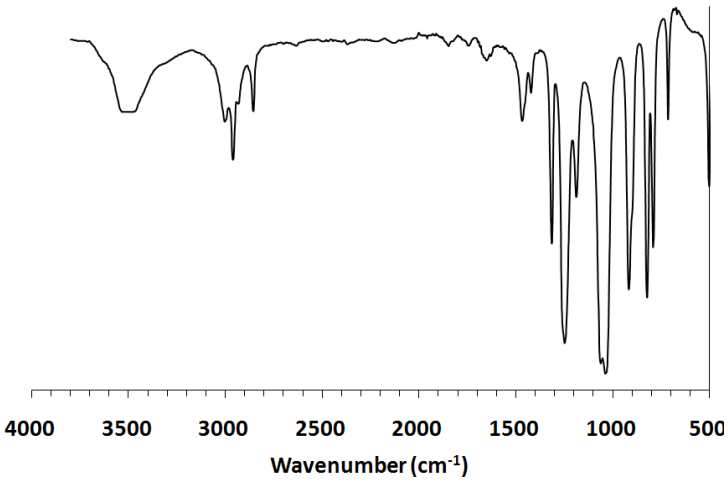

Figure 228. FTIR spectra of neat DMMP

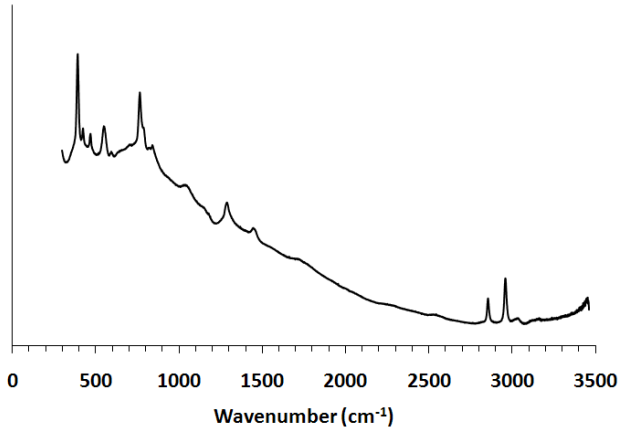

Figure 229. Raman spectra of neat DMCP

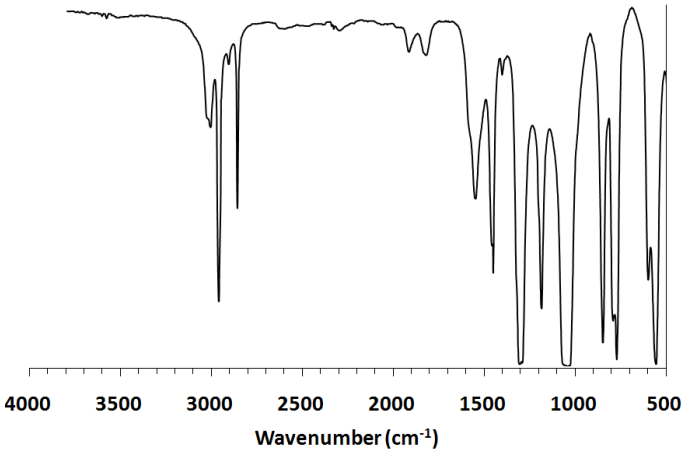

Figure 230. FTIR spectra of neat DMCP

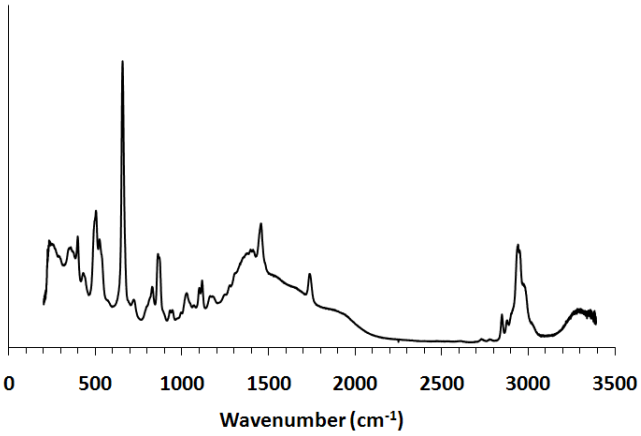

Figure 231. Raman spectra of neat Malathion

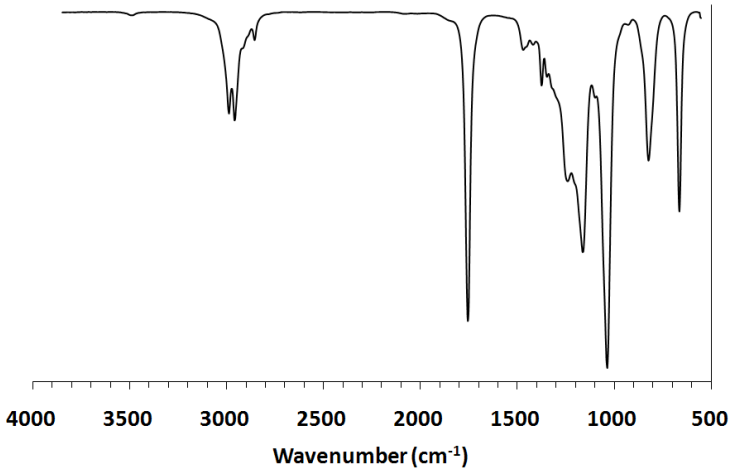

Figure 232. FTIR spectra of neat malathion

DISTRIBUTION LIST

The following individuals and organizations were provided with one Adobe portable document format (pdf) electronic version of this report:

U.S. Army Edgewood Chemical
Biological Center (ECBC)
RDCB-DRP
ATTN: Karwacki, C.

ECBC Technical Library
RDCB-DRB-BL
ATTN: Foppiano, S.
Stein, J.

ECBC
RDCB-DRP-F
ATTN: Maxwell, A.
Browe, M.

Office of the Chief Counsel
AMSRD-CC
ATTN: Upchurch, V.

Defense Threat Reduction Agency
J9-CBS
ATTN: Cronce, D.

Defense Technical Information Center
ATTN: DTIC OA

Department of Homeland Security
RDCB-PI-CSAC
ATTN: Mearns, H.

ECBC Rock Island
RDCB-DES
ATTN: Lee, K.
RDCB-DEM
ATTN: Grodecki, J.

G-3 History Office
U.S. Army RDECOM
ATTN: Smart, J.

EDGEWOOD CHEMICAL BIOLOGICAL CENTER
A U.S. Army RDECOM Laboratory